UNIVERSITY OF SOUTHAMPTON

FACULTY OF ENGINEERING AND THE ENVIRONMENT

Department of Aeronautics, Astronautics and Computational Engineering

Satellite Measurement of Ocean Turbulence

by

Simon Gareth George

Thesis for the degree of Doctor of Philosophy

June 2014

UNIVERSITY OF SOUTHAMPTON

<u>ABSTRACT</u>

FACULTY OF ENGINEERING AND THE ENVIRONMENT

<u>Aeronautics, Astronautics and Computational Engineering</u>

Thesis for the degree of Doctor of Philosophy

SATELLITE MEASUREMENT OF OCEAN TURBULENCE

Simon Gareth George

Turbulence and mixing in the surface layer of the ocean is a significant element in the combined ocean-atmosphere system, and plays a considerable role in the transfer of heat, gas and momentum across the air-sea boundary. Furthermore, improving knowledge of the evolution of energy within the ocean system, both globally and locally, holds importance for improving our understanding of the dynamics of the ocean at large- and small-scales. As such, insight into turbulence and turbulent flows at the ocean surface is becoming increasingly important for its role in ocean-atmosphere exchange and, from a wider perspective, climate change.

A research project was initiated to understand the role that spacecraft remote-sensing may play in improving observation of "turbulence" (in a broad sense) in the ocean, and for identifying how steps towards such observation may be made. An initial, exploratory study identified the potential benefit of Synthetic Aperture Radar in "bridging the gap" between in-situ and remote observations of $O(10 \text{ m})$ turbulence and flows. A simulation procedure was followed to derive theoretical profiles of radar backscattering cross-section arising from a candidate flow field (that of the turbulent wake arising from a surface moving body) in order to postulate the role of instrument configuration and ambient conditions on visibility and resolvability of turbulent flow structure.

The results demonstrate the potential to observe and characterise surface turbulent wake flows in terms of radar backscattering: a range of simulated backscatter images are presented for a turbulent surface current field derived from flow moving past a towed sphere, yielding investigation of the impact of turbulent currents on simulated radar backscattering. This has developed insights into the feasibility of resolving small-scale turbulence with remote-sensing radar and highlights the potential for extracting details of the flow structure and characteristics of turbulence near the surface of the ocean using current and future SAR capability.

Contents

List of Tables

List of Figures

Declaration of Authorship

I, *Simon Gareth George*, declare that the thesis entitled *Satellite Measurement of Ocean Turbulence* and the work presented in the thesis are both my own, and have been generated by me as the result of my own original research. I confirm that:

- this work was done wholly or mainly while in candidature for a research degree at this University;

- where any part of this thesis has previously been submitted for a degree or any other qualification at this University or any other institution, this has been clearly stated;

- where I have consulted the published work of others, this is always clearly attributed;

- where I have quoted from the work of others, the source is always given. With the exception of such quotations, this thesis is entirely my own work;

- I have acknowledged all main sources of help;

- where the thesis is based on work done by myself jointly with others, I have made clear exactly what was done by others and what I have contributed myself;

- parts of this work have been published as:

    o George, S. G., Tatnall, A. R. L.; *Measurement of Turbulence in the Oceanic Mixed Layer using Synthetic Aperture Radar*; 2011; in Proceedings of the ESA, SOLAS & EGU Joint Conference 'Earth Observation for Ocean-Atmosphere Interactions Science' (Eds. L. Ouwehand), ESA SP-703 (CD-ROM), ESA Communications, European Space Agency, Noordwijk, The Netherlands.

    o George, S. G., Tatnall, A. R. L.; *Simulation of SAR Ocean Turbulence Signatures using Direct Numerical Simulation and Radar/Hydrodynamic Modelling*; 2012; in 9th European Conference on Synthetic Aperture Radar, Electronic Proceedings, 23-26 April 2012, Nürnberg, Germany, ISBN 978-3-8007-3404-7.

    o George, S. G., Tatnall, A. R. L.; *Measurement of Turbulence in the Oceanic Mixed Layer using Synthetic Aperture Radar (SAR)*; 2012; in Ocean Science Discussions, Vol. 9, No. 5, pp. 2851-2883. doi:10.5194/osd-9-2851-2012. http://www.ocean-sci-discuss.net/9/2851/2012/osd-9-2851-2012.html

Signed: …………………………………………………………………..

Date:………………………………………………………………….

Acknowledgements

The process of research is often a complex, syrupy substance and without the frequent, helpful advice and guidance of my friends and colleagues, I would most likely still be stuck somewhere in the fog. Gratitude must first go to my supervisors Dr. Adrian Tatnall and Dr. Gary Coleman (now at NASA Langley Research Center), along with those who became prolific advisors on many aspects of my work: the guidance offered by my generous colleagues was more than I could hope for, providing both stimulating academic discussion and constant reassurance. Other academics who aided in soothing the worries and focusing the research were Dr. Watchapon Rojanaratanangkule, Dr. Glyn Thomas and Dr. Hugh Lewis. I must also thank the assistance of Prof. Roland Romeiser (University of Miami) and Prof. Vladimir Kudryavtsev (Nansen International Environmental and Remote Sensing Center, St. Petersburg) for permitting use of their numerical codes for ocean radar image modelling (*M4S* and *RIM*, respectively) and invaluable guidance to my seemingly endless queries.

Of course, my fellow students in the Astronautics Research Group also provided exciting and entertaining discussions both about research and the world at large, such as Ben Schwarz, Adam White, Rhys Clements, Dan Greenhalgh, Warinthorn Kiadtikornthaweeyot etc. I wish everyone all the best; for both those who've finished their postgraduate journey ("we made it!") and those who're still marching on ("keep going!").

They say music soothes even the savage beast, and for that the friendly Southampton RockSoc crew deserves recognition for their constant encouraging support and wise words throughout the course of my research: in particular, Dave Joce(*), Jenny Josephs(*), Dan Illingworth, Antony James, Andrew Day, Bob Rimington(*), Charlie Hargood(*), Adam Sobey(*), Angela Tack and Kirsty Mills, along with many others; (*) also representing survivors (or current foot soldiers) of the PhD machine. Cap-doffing must also go to the raft of bands whose music maintained my focus and drive during my studies, notably AFI, Daft Punk, Rush, Nine Inch Nails, Less Than Jake, Foo Fighters, Turisas, The Ataris, Karnivool, Jimmy Eat World and Andrew WK. You guys rock.

Old friends never die, and as such there's a whole raft of chaps who've kept me afloat through these long few years with exciting distractions or wise words: Jeremy Gadfield for constant encouragement ("KEEP PUSHING"), Kim Lipscombe, Kate Thackeray, Timmy Peters, Louise Roberts, Pete Boorman, Oliver Kibblewhite, Ananda Hill and anyone else whom I've not explicitly mentioned here. My family also deserve immense recognition for their continued support and encouragement, and for being a rock of normality in my whirlwind research career.

Lastly but by no means leastly, I must thank my dedicated partner, Bryony, for her constant support through all the stresses, struggles and stickiness, and for always believing in me.

Symbols and Abbreviations

Roman Symbols

A	Area of a single resolution cell (m²)
A_w	Wave amplitude
B	Virtual surface describing immersed boundary object
B_r	Radar bandwidth of antenna
c_0	Speed of an electromagnetic wave in a vacuum ($= 2.998 \times 10^8$ ms⁻¹)
c_g	Ocean wave group velocity (ms⁻¹)
c_p	Ocean wave phase velocity (ms⁻¹)
D	Height of real aperture (m)
dt	Time-step of DNS
$E(k)$	Wave energy spectral density at wavenumber k
f	Spectral modulation of wave system
F_i	Body force term for immersed boundary object
F_R	Pattern propagation factor for target-to-receiving-antenna path
F_T	Pattern propagation factor for transmitting-antenna-to-target path
g	Acceleration due to gravity (= 9.81 ms⁻²)
$G_{pq}(\theta_i, \alpha, \phi)$	Polarisation scattering coefficient for $p = H, V$ transmit (horizontal and vertical) waveforms and $q = H, V$ receive waveforms
G_T	Gain of transmitting antenna
h	Altitude of SAR platform (km)
J_{IBM}	Forcing intensity of immersed boundary object
$k, \boldsymbol{k}$	Ocean wavenumber (scalar, vector) (s⁻¹)
$k_0, \boldsymbol{k_0}$	Radar wavenumber (scalar, vector) (s⁻¹)
$k_B, \boldsymbol{k_B}$	Bragg wavenumber (scalar, vector) (s⁻¹)
K_B	Boltzmann constant (= 1.38 × 10⁻²³ J°K⁻¹)
l_w	Relaxation length of ocean waves (m)
L	Length of real aperture (m)
L^*	Reference length scale
L_{DNS}	Reference length scale in DNS
L_{SA}	Length of synthetic aperture (km)
L'	Horizontal length scale of rms turbulence

$N(k)$	Wave action spectral density at wavenumber k
$\boldsymbol{p} = p_x, p_y, p_z$	Pressure (Nm-2)
$P(\alpha, \phi)d\alpha d\phi$	Probability that 2-D surface tilt angles (α and ϕ) lie within specific limits
P_T	Power transmitted by radar
Q	Second invariant of velocity gradient tensor
r	Radius of immersed boundary sphere in DNS
R_0	Radar (slant) range to target (km)
R_{sphere}	Radius of a perfectly-reflecting sphere
Re	Reynolds number
Re_{DNS}	Simulated Reynolds number in DNS
$S(k)$	Wave action balance source function – contribution of external forces
$S_{Turb}(k)$	Wave action balance source function – dissipation by turbulent velocity fluctuations
$S_v(k)$	Wave action balance source function – dissipation by viscosity
t	Time (s)
T	Noise temperature of radar antenna
U_{DNS}	Reference velocity scale in DNS
U_∞	Freestream velocity in DNS
$\boldsymbol{u} = u, v, w$	Cartesian velocities
u'	Turbulent rms velocity
$u_{wind} = (u, v, w)_{wind}$	Cartesian wind velocities
$\forall$	Fluid volume
v_r	Radial velocity of ocean surface scatterer (ms-1)
v_S	Flight velocity of SAR platform (ms-1)
$\boldsymbol{x} = x, y, z$	Cartesian coordinates

Greek Symbols

α	Surface tilt angle (angle between vertical and projection of the normal to the plane of the patch onto the vertical plane containing the microwave propagation direction)
β	Wave amplitude decay rate (s-1)
δ_{IBM}	Gaussian half-width of immersed boundary object
δ_{az}	Azimuth displacement of moving scatterer due to radial velocity (m)

δ_{rg}	Range displacement of moving scatterer due to radial velocity (m)
δx	Distance over which a single resolution cell of moving scatterers is "smeared" in the azimuth direction of a SAR image
ε	Turbulent dissipation rate of TKE into thermal energy (Jkg^{-1} or m^{2}s^{-3})
Δ_{az}	Azimuth resolution (m)
Δ_{rg}	Range resolution (m)
Δz	Fluid height change due to hydrostatic approximation (m)
θ_i	Incidence angle (degrees)
λ_0	Operating wavelength (m)
λ_B	Bragg wavelength (m)
λ_w	Ocean wavelength (m)
ν	Kinematic viscosity (m^{2}s^{-1})
ν_{DNS}	Reference kinematic viscosity in DNS
ρ	Fluid density (kgm^{-3})
σ	Radar Cross-Section (m^2)
σ_0	Normalised Radar Cross-Section (dB)
$\sigma_{0,\,Bragg}$	Normalised Radar Cross-Section, Bragg-scattering component only (dB)
σ_v	Standard deviation of radial velocities of ocean surface scatterers in a single resolution cell
τ_p	Pulse width (s)
τ_w	Relaxation time of ocean waves (s)
ϕ	Surface tilt angle (angle between vertical and projection of the normal to the normal to the patch onto the vertical plane containing the microwave propagation direction)
ϕ_{wind}	Angle made between simulated wind direction and x-axis
$\psi(k)$	Wave height spectral density at wavenumber k
ω	Apparent (Doppler-shifted) ocean wave frequency (Hz); angular frequency (rads^{-1})
ω_0	Intrinsic ocean wave frequency (Hz)

Abbreviations

AATSR	Advanced Along-Track Scanning Radiometer
AIRSAR	NASA/JPL Airborne Synthetic Aperture Radar system
AirSWOT	Airborne Surface Water and Ocean Topography test/validation campaign
ALOS-2	*Advanced Land Observation Satellite 2*, operated by JAXA
AMSR-E	Advanced Microwave Scanning Radiometer (Earth Observing System)
ASCAT	Advanced Scatterometer
ATI	Along-Track Interferometry
AVHRR	Advanced Very-High Resolution Radiometer
CCRS	Canadian Center for Remote Sensing
CFD	Computational Fluid Dynamics
CgLES	the DNS model of Dr. Thomas (Uni. Southampton)
CSA	Canadian Space Agency
CTD	Conductivity, Temperature & Depth instruments
CWA	principle of the Conservation of Wave Action
CZCS	Coastal Zone Color Scanner
DEM	Digital Elevation Map
DBI	Dual-Beam Interferometer
DLR	Deutsches Zentrum für Luft- und Raumfahrt (German Aerospace Centre)
DM	Discrepancy area Measure
DNS	Direct Numerical Simulation
DNSR	MATLAB visualisation tool for displaying computed NRCS signatures (author's code, Uni. Southampton)
DTI	Dynamics Technology Inc.
EMSE	Extended Mild-Slope Equation of McKee (1996)
EOM	ERIM Ocean Model
EPS MetOp	EUMETSAT Polar System fleet of *MetOp* satellites
ERIM	Environmental Research Institute of Michigan
ERS-1/2	*European Remote-Sensing* satellites 1 and 2, operated by ESA
ESA	European Space Agency
EUMETSAT	European Organisation for the Exploitation of Meteorological Satellites
FLUENT	CFD modelling software of ANSYS, Inc.
GEO	Geostationary Earth Orbit
GEO-CAPE	GEOstationary Coastal and Air Pollution Events mission study

GOES	*Geostationary Operational Environmental Satellite*, operated by the United States National Environmental Satellite, Data and Information Service
GUI	Graphical User Interface
HF	High-Frequency (radar)
HICO	Hyperspectral Imager for the Coastal Ocean instrument
HSW	the radar backscattering model of Holliday, St-Cyr & Woods (1986)
IEEE	Institute of Electrical and Electronics Engineers
InSAR	Interferometric SAR
IRIDIS3	the high-performance computing cluster at Uni. Southampton
ITU	International Telecommunication Union
JAXA	Japanese Aerospace Exploration Agency
JERS-1	*Japanese Earth Resources S*atellite, operated by JAXA
JPL	NASA Jet Propulsion Laboratory
LEO	Low Earth Orbit
LES	Large-Eddy Simulation
M4S	the RAR/SAR/InSAR image model of Prof. Romeiser (Uni. Miami)
M4Sr320	Radar backscatter computation model of M4S
M4Sw320	Wave action computation model of M4S
MEDOC	Mediterranean Ocean Convection experiment
MSE	the Mild-Slope Equation of McKee (1987)
MSS	Mean-square Surface Slope of ocean surface in radar backscattering
MSS	Multi-Spectral Scanner instrument
NOAA	Fleet of satellites operated by the National Oceanic & Atmospheric Administration
NORCSEX	Norwegian Continental Shelf Experiment
NRCS	Normalised Radar Cross-Section
PALSAR-2	Phased-Array type L-band Synthetic Aperture Radar 2
PHILLS	Portable Hyperspectral Imager for Low-Lift Spectroscopy instrument (Naval Research Laboratory)
psu	Practical Salinity Unit
RA-2	Radar Altimeter 2
RADARSAT-1/2	*Radar Satellite 1/2*, operated by CSA
RAR	Real Aperture Radar
RDT	Rapid Distortion Theory
RIM	Radar Imaging Model, the RAR image model of Prof. Kudryavtsev (Nansen International Environmental and Remote Sensing Centre)
RCS	Radar Cross-Section

RF	Radio Frequency
SAR	Synthetic Aperture Radar
SARSEX	Synthetic Aperture Radar Internal Wave Signature Experiment
SeaWiFS	Sea-Viewing Wide Field-of-View Sensor
SIR-C/X-SAR	Spaceborne Imaging Radar C/X-band Synthetic Aperture Radar mission aboard Space Shuttle *Endeavour* flights STS-59 and STS-68
SMOS	*Soil Moisture and Ocean Salinity* satellite, operated by ESA
SNR	Signal-to-Noise Ratio
SSH	Sea-Surface Height
SSM/I	Special Sensor Microwave Imager
SST	Sea-Surface Temperature
SSTL	Surrey Satellites Technology Ltd.
SWOT	Surface Water and Ocean Topography, forthcoming mission planned by NASA
TKE	Turbulence Kinetic Energy
TM (*Landsat*)	Thematic Mapper
WKB	Wentzel-Kramers-Brillouin theory of geometrical optics
XBT	Expendable Bathythermograph instrument
XTI	Across-Track Interferometry

1.   Introduction

The ocean has long fascinated the inhabitants of Planet Earth. The development of satellite remote-sensing instrumentation during the 1970s substantially increased the application of Earth observation science; however, it was not until *Seasat* (1977) that a space mission was designed specifically for ocean study. Since then, remote-sensing missions to observe and measure the sea surface have vastly improved the ability to characterise ocean dynamics on a global scale and the availability of satellite data has significantly contributed to man's understanding of the ocean and its properties. There are, however, significant 'gaps' in the ability of remote-sensing techniques to adequately capture all scales of motion at the sea surface: the results presented in this thesis attempt to rectify these shortfalls, and to provide the basis for further study which will strengthen remote-sensing capabilities for turbulent oceanography.

1.1   Background

The turbulent nature of the ocean plays a key role in the ever-changing climate of the Earth. Fluid mixing over a wide variety of scales is an effective factor in the transport of heat, salinity and energy throughout the ocean, often over very large distances. Oceanic turbulence hence has considerable influence not only on distribution and mixing within the ocean climate but also on characteristics of the complex boundary layer between the air and sea. This boundary plays a crucial role in regulating the thermal and gaseous balance between ocean and atmosphere: turbulence at the upper ocean, present in the top 50 m of the sea (also known as the "oceanic mixed layer") heavily influences the properties of the fluid surface and hence has a strong impact on this ocean-atmosphere balance. "Large-scale" processes (a few kilometres to hundreds of kilometres in scale) in the upper ocean have impacts on the distribution and delivery of heat flux across the sea surface interface around the globe in accordance with global and regional ocean currents; whilst at the opposite end of the spectrum, molecular turbulence and small-scale mixing play a role in the stability and creation of micro-environments for small oceanic life forms and balancing stable phytoplankton populations, directly contributing to the ocean climate itself but also contributing to CO_2 exchange with the air, as discussed by Thorpe (2007).

Turbulence and mixing in the near-surface layer of the ocean can therefore have considerable influence on the transfer of properties such as heat, gas and momentum across this boundary. The rates of exchange of such properties are governed by the characteristics and dynamics of the ocean surface boundary layer (and, equally, the lower region of the atmosphere). There is currently increasing interest in the effect of the upper ocean layer on climate change studies, particularly in

the role of ocean turbulence in the exchange of carbon dioxide between air and sea as described by Zappa et al. (2007). It is estimated that up to 20-50% of anthropogenic CO_2 delivered into the air across the globe may be absorbed by the sea (Sabine et al., 2004; Khatiwala et al., 2009). Upper ocean turbulence appears to play a key role in this exchange, as shown in recent findings published by Zappa et al. (2007) which demonstrate that the rate of air-water gas transfer varies linearly with the near-surface rate of turbulence dissipation. Conditions in the oceanic mixed layer itself are dependent on the surface wave system and presence of upper-ocean mixing, meaning that near-surface turbulence is therefore an important component in the exchange processes of gas, heat and momentum between the ocean and atmosphere (Frew et al. [2004]; McKenna & McGillis [2004]; Soloviev et al. [2007]; Veron et al. [2011]). Such conditions are dependent on the surface wave system and fluid mixing, and near-surface turbulence is therefore a key constituent of this process. Ocean turbulence in the upper layer of the ocean may hence be considered a crucial element in the climate cycle, and is coming under increased scrutiny from a climate change perspective. Understanding oceanic activity and turbulence is also crucial for a range of human activities, including shipping, navigation, ocean forecasting, coastal activity and prediction of loads on oceanic structures (oil rigs, offshore turbines, etc.).

Advancing the methods by which turbulent phenomena and processes in the oceanic mixed layer can be observed by remote-sensing methods may improve the ability to quantify the impact of the ocean mixed layer on climate change, and improve understanding of this complex system. Increased observation and understanding the ocean and its dynamics both in isolation, and in tandem with ocean-atmosphere interaction studies, is essential: the availability of timely, global data for ocean turbulence analysis may be invaluable for the development of turbulent oceanography and climate study. This thesis draws some perspectives on how oceanic turbulence may be studied using remote instrumentation and present results which suggest that, with suitable configuration of remote-sensing antennas, steps towards improved observation of turbulent oceanographic phenomena may be made in the future using imaging radar techniques.

1.2   The Current Study

Mixing processes in the ocean cover a vast range of scales in both time and space. This spectrum of oceanographic (turbulent) phenomena may be divided into a number of classifications, presented in Table 1, which have been previously examined by a wide range of scientists and oceanographers in the last century. In study of the ocean, there typically exists a crucial 'gap' in what may be observed using contemporary techniques: spacecraft sensors typically observe large-scale, horizontal turbulence – polar-orbiting Sea-Surface Temperature (SST) sensors (such as AVHRR on the

EUMETSAT *MetOp* fleet) observe large-scale/mesoscale current systems through spatial distribution of surface temperature, whilst Synthetic Aperture Radar (SAR) and optical instruments can resolve the larger components of ship-wake and small-scale turbulence. In-situ instrumentation, on the other hand, predominantly obtains "fine-scale" measurements (in the case of buoys or microstructure instruments) or "intermediate-scale" processes (in the case of shore-based High-Frequency [HF] radar). Turbulent flows and flow features/phenomena on decimetre scales are, hence, not studied effectively or captured on a global scale and may benefit significantly from improved remote-sensing observation. Advances in instrument capability of remote sensors may allow finer details of the surface wave-current interaction to be extracted from remote image, and to address this 'gap' in routine ocean observation. Improved observations of the oceans by specially-tailored ocean sensors will pave the way for new insights into turbulent processes and heightened understanding of the cause and character of ocean turbulent behaviour.

Classification	Spatial Scale		Temporal Scale (typical)	Typical Phenomena
	Horizontal	Vertical		
Synoptic Processes	100-200 km	100 m +	3-12 months	Eddies; Large-Scale Currents; etc.
Mesoscale Processes	10-100 km	100 m +	1-12 weeks	Eddies; Oceanic Fronts
Submesoscale Processes	< 1-10 km	10 m	0.5-7 days	Eddies; Interaction with Ocean Bottom Topography; Langmuir Circulations; Internal Waves; etc.
Small-Scale Processes	1 – 100 m	1-10 m	0.5-12 hours	Upper Layer Processes; Internal Waves; Surface Wakes; Wave-Current Interaction ; etc.
Upper Ocean Mixing Processes	10 cm – 1 m	< 1 m	< 1 minute	Wave-Breaking Processes
Molecular Processes	< 10 cm	< 1m	< 1 minute	Turbulence Microstructure

Table 1. Classification of oceanic phenomena, compiled from Dickey (1990) and other classifications found in literature.

Large-Scale Processes   Intermediate-Scale Processes

Small-Scale Processes   Fine-Scale Processes

In the past few decades, the capacity for remote-sensing to observe the Earth has led to marked improvement in the method(s) and mean(s) by which the oceans may be studied. This trend is likely to rise in the future as the capability for ocean observation improves yet further. Quantifying the role that remote-sensing can play in the characterisation of oceanic flows at decimetre scale is crucial for exploiting future capabilities; in particular, how future instrument capabilities may benefit the study of ocean turbulence and mixing. In addition, identifying methods whereby desirable (and novel) instrument configurations – designed explicitly for study of specific oceanic conditions/flows – may be derived will assist in deriving maximum return from future ocean instruments. To this end, the current study analysed the feasibility of remote detection and measurement of turbulent processes in the ocean, and examining the potential strategies by which this may be achieved through spacecraft Earth observation.

The challenges associated with the study were primarily associated with understanding the feasibility of improving current remote observations of ocean turbulence, developing an end-to-end simulation strategy linking the generation of turbulence to observable changes which may be measured remotely, and examination of the remote-sensing instrumentation necessary to extract these measurements. The study was initiated in pursuit of exploratory research into the potential links between remote-sensing capabilities and oceanic turbulence, and represents a feasibility assessment of the ability of remote-sensing to aid characterisation of turbulence in the ocean. This led to development of a multi-disciplinary research study, encompassing a number of scientific fields:

1. Remote-Sensing: Application of spaceborne instrumentation to oceanography, extraction of parameters from remote-sensing data, development of remote-sensing spacecraft and missions, etc.
2. Oceanography: Identifying the role of turbulence in the ocean at various scales, measurement capabilities and requirements, identifying the potential, and novel, measurements of oceanic conditions and intermediary role in linking the remote-sensing field with the fluid dynamics domain; etc.
3. Fluid Dynamics: How turbulence in the ocean relates to canonical fluid dynamics, relationship between measurements and what can be learned, identifying how knowledge/understanding of turbulence can contribute to oceanography/climate study, etc.

This initially required an assessment to be made of the capability of measuring turbulence through Earth observation methods: a remote-sensing strategy was developed in order to examine the appropriateness of various remote-sensing instruments to the potential examination of ocean turbulence, revealing the potential for SAR instrumentation to fulfil these capabilities. The subsequent simulation procedure involved identifying candidate phenomena for study, performing radar backscattering simulation of the candidate flows and examining the ability to resolve such turbulence in the context of current and future SAR capabilities. To date, there has been limited study of this kind within the literature for a range of ocean & turbulent phenomena, therefore the current results represent first steps to address this shortfall.

The phases of work employed in this remote-sensing study were adopted and adapted from a similar study performed by Fischer & Shuchman (1996), performed for remote-sensing of large-scale ocean convection alone, and are described as follows:

1. Identify the current ability of remote-sensing instrumentation to observe and characterise oceanic turbulence
2. Identify the desired candidate application for a prospective 'future capability' remote-sensing mission to improve observation of small-scale and mesoscale dynamics and ocean turbulence
3. Identify candidate remote-sensing technique & phenomena of study
4. Integrate Direct Numerical Simulation techniques and SAR remote sensing models to generate simulated data
5. Develop results to identify future remote-sensing instrumentation capable of capturing those measurements

The current research examined the methods by which three-dimensional flow features and structures in the upper ocean may be identified and interpreted from space; identifying SAR as a candidate remote-sensing technique which could improve ocean observations. In particular, the research aimed to address the limitations of in-situ methods in delivering observations of turbulence at scales of the order of 10 m ("small scales"), looking at how future developments in instrumentation or procedures may improve how the turbulent ocean can be studied remotely. The benefits of improved spatial resolution or sensitivity for land observation are well-documented in the literature and a significant driver for future instruments, however there is typically little discussion or study into the benefits of improved instrumentation for oceanographic applications. Advances in sensor capabilities for ocean study could allow improved characterisation of

particularly small-scale or low-contrast features, and provide an alternative perspective of oceanic phenomena that affect the oceans at small, localised scales (i.e. decimetre flow features).

There has been little consideration of this approach in previous studies, and thus a novel aspect of the current work lies in the previously-unexplored research in this area in the context of an end-to-end system; from the generation of turbulent (velocity/flow) signature using Direct Numerical Simulation (DNS) techniques, to simulating radar backscattering and SAR signatures, and leading to recommendations for future remote-sensing instrumentation. This represents a unique operation of such a simulation strategy for understanding future requirements for spaceborne ocean sensors.

1.3   Outline of Thesis

The rest of the thesis is presented as follows: Chapter 2 discusses introductions to ocean turbulence and its study via remote-sensing and in-situ instrumentation. Chapter 3 focuses on the ability of remote-sensing instrumentation to observe and resolve oceanic turbulence, identifying the primary scales of ocean turbulence for study and evaluation of current capabilities of remote sensors, establishing the potential for future SAR instruments to observe of "small-scale" processes. Chapters 4 and 5 introduce and discuss the simulation strategy operated in the study, along with discussion of its validity and limitations. Chapter 6 discusses results from a case study into the simulation of NRCS signatures of surface wake turbulence, whilst Chapters 7 and 8 examine the capabilities for observing such signatures in the context of typical ambient conditions and instrument limitations. Chapter 9 considers recommendations for future study, drawing perspectives on the scope for improving the applied simulation methods and outlooks on future SAR instrumentation. A chapter of conclusions is provided at the culmination of the thesis, in addition to a discussion of desirable future work in this field. A series of appendices of relevant work are also provided to support the results presented in the main thesis. To provide context for the structure of this document, Figure 1 depicts the flow of work which was undertaken within the study, and describes graphically the outline of discussion of that work within the framework of this thesis.

Chapter 1

Introduction to Study

Chapter 2

Ocean Turbulence & Remote-Sensing - Overview and Discussion

Chapter 3

Identification of Remote-Sensing Requirements and Candidate Instrumentation

Chapter 4

Development of End-to-End Simulation Strategy and Selected Tools

Chapter 5

Validation of Selected Strategy and Discussion of Primary Challenges

Chapter 6

Radar Backscattering Simulation of Surface Wake Turbulence

Chapter 7

SAR/Remote-Sensing Signatures of Surface Wake Turbulence

Chapter 8

Modification to Technique and Recommendations for Future Work

Chapter 9

Conclusions

Figure 1. Schematic demonstrating the flow of work undertaken in the study.

2. Ocean Turbulence and Remote-Sensing

2.1 Turbulence in the Ocean

Turbulence is widespread throughout geophysical fluids; a persistent feature which is found at all depths of the ocean, and at a wide variety of scales from surface turbulence and eddies in the upper (~ 50 m) layer to turbulence and shear generated in the deep ocean or at the ocean floor. Turbulence may be generated internally due to processes such as current shear (at internal interfaces) or breaking internal waves, or initiated at the surface by wave-breaking, current motions or flow past objects or underwater bottom topography. Broadly speaking, 'turbulent' ocean processes may be considered to be those that involve energy transfer between scales, or from and to different parts of the ocean and can, broadly, be described as turbulence. In this vein, the concept of 'turbulence' may be applied to a wide variety of regimes in the ocean; extending beyond the sub-centimetre regime of dissipative turbulence to the motions of global eddies and currents at the scale of hundreds of kilometres.

Turbulence in a fluid is not a single regime, or parameter, that can be easily defined or quantified. This concept is summarised by Thorpe (2007):

"Turbulence is generally accepted to be an energetic, rotational and eddying state of motion that results in the dispersion of material and the transfer of momentum, heat and solutes at rates far higher than those of molecular processes alone."

Turbulence is thus a concept which simply defines a wide range of states that share a number of factors in common, such as three-dimensionality, unsteadiness, instability, strong vorticity, unpredictability and a broad spectrum of length and time scales (Baumert et al., 2005). The study of fluid turbulence itself is hence a broad subject that covers all kinds of fluid flows ranging from the large-scale, global currents in the ocean to engineering pipe flows. As such, it is a highly-documented field and introductions to its breadth and current level of study may be found in Pope (2000) and Davidson (2004). Thorpe (2007) provides a thorough introduction to the current limit of knowledge of turbulence in the oceanographic arena, including and introductions to measurement and modelling techniques. This accompanies the more in-depth publication, Thorpe (2005), which examines the rationale for studying ocean turbulence, and describes the methods by which it is performed. Monin & Ozmidov (1985) also remains an important summary of the nature and measurement of oceanic turbulence and mixing, from large-scale horizontal processes to fine-scale turbulence. The review articles of Gargett (1989) and Thorpe (2004) document the evolving

state of research into ocean turbulence, and are supported by the clear text by Smyth & Moum (2001) which concisely describes the key concepts surrounding fluid turbulence and its application to the ocean. Studies of ocean turbulence, and its implications for the balance of the air-sea interface, are reviewed effectively by Drennan et al. (1997), whilst Baumert et al. (2005) discuss the processes and theories for measuring and understanding marine turbulence, along with direct and computational measurement techniques.

Large-scale flows adhere to characteristics of turbulence which are sometimes referred to as "geostrophic" or "mesoscale" turbulence, where a mesoscale flow is strongly nonlinear, rapidly-rotating and stably-stratified. Ocean currents are typically turbulent in the range of ocean wavenumbers at 1-100 km and mesoscale eddies at scales of 10-100 km in the ocean contain most of the ocean's turbulent energy (Monin & Ozmidov, 1985). Mesoscale processes are typically defined by large-scale, rotating, horizontal motion created by instability or current flow past an obstacle (e.g. a landmass); the role of mesoscale turbulence and phenomena in the global climate is developed and presented by Klein & Lapeyre (2009). Due to ocean stratification, such processes are two-dimensional in the horizontal plane, and may be characterised by dispersion of surface properties such as temperature, salinity or colour; hence, they can become resolved in satellite measurements of, for example, SST (via Infra-Red instrumentation) or sea-surface height (through satellite altimetry). Because of their ability to transport warmer or cooler water to regions surrounding them, large-scale oceanic eddies are important for the heat balance of the globe, in addition to the transport of nutrients and organic products across large distances. Smaller-scale phenomena are fully three-dimensional and energetic, contributing to local conditions and mixing in the upper 50 metres of the ocean. Turbulence and instabilities occurring at small scales feed off, and likewise contribute to, the energetics and activity of larger-scale flows: small-scale turbulence is generally distributed intermittently within the main body of the ocean in patches of localised mixing. Interpreting turbulence itself and defining the measurement strategy which is required to fully characterise mixing processes (from fine-scale to synoptic phenomena, see Table 1) is not an easy task, since turbulence may possess a wide range of states and may produce diverse effects on parameters such as temperature or velocity under different turbulent regimes.

Typically, the oceanographic view of turbulence is separated between processes at mesoscale (and bordering into submesoscale) processes whereby horizontal surface eddies can be monitored by SST measurements available from routine remote-sensing observations at 1 km resolution (e.g. AVHRR); at the other end of the spectrum, observations of very small-scale turbulence and dissipation using in-situ instrumentation. While in-situ measurements reveal important information about turbulence contained in mixing and small-scale processes, this model is not capable of

widespread/global monitoring: the huge volume of the global oceans mean that measurement of turbulent interactions, even over the smallest proportion of the seas and its internal phenomena, is an impossible task. In addition, access to areas of frequent or persistent turbulent activity can often be limited by remoteness or inaccessibility, inhibiting deployment of ships or instruments to the active zone. This problem is compounded by the unpredictability which largely defines turbulence activity, and lifetimes of events may too short-lived to allow the delivery of measurement sensors to the site whilst the event is still actively turbulent. As a result, capturing data on active turbulent processes and the environmental conditions prior to, and following, turbulent action is extremely desirable for development of many oceanographic techniques and global studies of the ocean. The ability to resolve these processes on a global scale, by remote means, may substantially increase measurement capability.

Near-surface, small-scale processes may be generated by such agents as ocean current instabilities, interaction with ocean bottom topography and/or surface wakes, wave-breaking processes, wind interactions with the sea surface, or interaction of a current as it flows past a landmass or underwater topography. Sub-surface turbulent flow may be fully three-dimensional and modulate the ocean surface in a manner that may be detected from satellite imagery, as shown by the ability of SAR to observe turbulent effects generated by underwater bottom topography, for example as described by Hennings et al. (2001) and Alpers et al. (2004). While not inherently turbulent, internal waves and current fronts are important for oceanographic studies since they transfer energy (internally) in a similar manner, and may act as an initiator for a turbulent disturbance. Events related to open-ocean convection can also have a significant impact on climate change, and improving understanding of their distribution, frequency and activity is therefore becoming increasingly important.

Methods of quantifying turbulent motion through in-situ measurement are primarily performed through measurement of structure, stress, flux and dissipation characteristics of the observed flow regime (Thorpe, 2007). Parameters such as velocity, temperature, pressure, contaminant concentration, density, sound velocity, electrical conductivity, refractive index and more, can vary spatially and temporally due to the presence of turbulence (Monin & Ozmidov, 1985). Parameters which may be used to quantify turbulence numerically include the rate of dissipation of Turbulence Kinetic Energy (TKE), ε; the spectrum of velocity fluctuations; Reynolds stresses; eddy viscosity; or the visual structure of the turbulent flow. In-situ instruments focus primarily on the very small, diffusive scales ("fine-scale") of turbulence in the ocean, although networks of instruments can consider spatial variations. Estimation of the TKE dissipation rate, ε, can be typically obtained through measurements of turbulence spectra, and with ongoing developments of Particle Imaging

Velocimetry (PIV) techniques. Measurement of temporal velocity fluctuations through hot-film anemometry or probes can be used to understand the dissipation of kinetic energy at molecular and diffusive scales by viscosity. Aerofoil probes are typically the principal means of measuring turbulence at fine scales (2.5-10 mm) in the ocean. Free-fall instruments such as the Advanced Microstructure Profiler are used to examine fluctuations in vertical shear, temperature and conductivity with depth, and investigate ocean microstructure. There has been increasing use of acoustic instruments such as the Acoustic Doppler Current Profiler (ADCP) to transmit and measure the acoustic reflections from particles advected by turbulent flow to examine the Doppler response and estimate the rate of production of TKE. Large-scale turbulence (submesoscales and larger) have considerably larger horizontal scales than vertical scales, making them predominantly two-dimensional. Systems of buoys and surface & sub-surface drifters can be deployed over spatial scales of many kilometres. These instruments can deliver measurements of, for example, temperature, density, directional wave spectra, wind speeds & direction, salinity, etc. and tracking of 'drifting' instruments can examine circulation and current flows. The webpage hosted by Woods Hole Oceanographic Institute[1] describes and defines many of the instruments used for in-situ ocean study. Further information on in-situ instruments and measurement techniques may be found in Thorpe (2007).

2.2   Previous Remote Studies of Ocean Turbulence

Remote-sensing instruments exploit the electromagnetic (EM) wave spectrum to extract information from the ocean surface; either by detecting EM energy transmitted by the surface itself (passive instruments), or by transmitting EM waves from satellite and collected reflecting waveforms (active instruments). Table 2 provides a brief comparison of typical remote-sensing instrumentation, along with common uses, representative instruments/spacecraft and their position in the EM spectrum. Parameters that may be acquired remotely (from the ocean surface) include temperature at the sea surface, density of salt content (salinity) at the sea surface, sea-surface height, roughness of the surface, wind speed & direction and ocean colour; although a wide range of further information and parameters may be derived from these basic quantities.

In the following sections, the ability of remote-sensing techniques to provide "measurement" of turbulence at various spatial scales are discussed, and some perspectives drawn on the relative merits of different techniques to characterise different oceanic scales. For readers unfamiliar with the capabilities and operation of remote sensors, texts by Robinson (2004, 2010) may provide the novice with a superb introduction to the field: these deliver a broad overview of the methods and

---

[1] Information from: https://www.whoi.edu/science/instruments/ (last accessed 19/08/2013)

potential for observation and monitoring of the ocean from space along with the opportunities for observing a range of large-scale and small-scale features with remote instrumentation. In addition, a recent text by Barale et al. (2010) summarises the current state of satellite oceanography and postulates the future, whilst Johannessen et al. (2000) discusses the role of spacecraft remote-sensing in operational oceanography, such as marine safety, pollution control, fisheries and oil spill monitoring. Ufermann et al. (2001) consider the synergies between various spaceborne sensors for observation of ocean features, whilst Chapron et al. (2008) and Freeman et al. (2010) expand on these views to examine the future challenges for satellite oceanography.

Instrument	Typical Sensors/Satellites	Primary Ocean Measurement	Electromagnetic Frequency Range
Synthetic Aperture Radar	*ERS-1/2, Envisat, RADARSAT-1/2, TerraSAR-X*	Ocean currents, surface waves, fronts, eddies, etc.	1-10 GHz
Passive Microwave Radiometry (salinity)	*SMOS, Aquarius*	Sea-surface salinity	1.4 GHz
Radar Altimetry	*T*, RA-2 on *Envisat, Jason-1/2, Cryosat* [SAR altimetry]	Dynamic surface height	3-13 GHz
Scatterometry	*MetOp* (ASCAT), *QuickScat* (SeaWinds), ERS-1/2 (AMI)	Wind Speed & Direction	5-13 GHz
Passive Microwave Radiometry (other applications)	SSM/I, AMSR-E	Surface temperature, wind speed, precipitation, liquid water path	7-90 GHz
Thermal Infra-Red Radiometry	AVHRR, AATSR, *GOES*	Surface temperature, cloud cover	20-550 THz
Multispectral Imaging	*IKONOS, Landsat* (MSS, TM), MERIS, CZCS, SeaWiFS	Ocean colour, biology, coastal regions, etc.	Visible spectrum Near-Infra-Red

Microwave Spectrum

Infra-Red Spectrum

Visible Spectrum
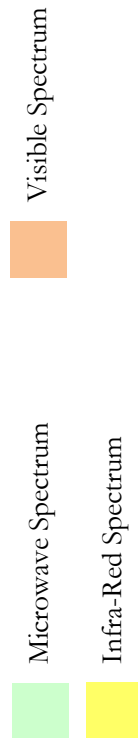
Table 2. Typical instrumentation used for satellite oceanography.

2.2.1   Remote-Sensing of Large-Scale Processes

Large-scale phenomena and "mesoscale" turbulence have been observed comprehensively by the full suite of instruments documented in Table 2, and a broad fleet of spacecraft. The launch of the *Seasat* satellite revealed the ability of remote-sensing instruments to resolve and detect a range of oceanic phenomena using a variety of instruments, and this heritage has proceeded through to current instruments in both Low Earth Orbit (LEO) and Geostationary Earth Orbit (GEO). Large-scale processes are most typically revealed in remote measurements by passive tracers which are dispersed and advected with the main flow: the transport of quantities such as temperature, salinity or colour along directions of the flow can demonstrate flow structure or delineate fluid of differing properties. In this thesis, the term *flow structure* is used to describe the instantaneous patterns and arrangements within a snapshot of a flow field marked by a tracer or advective sea surface property, such as temperature. Using remote-sensing instrumentation, characteristics of a flow (such as eddies and flow structure) can be revealed in a single snapshot of the surface through spatial distribution of derived quantity, and its evolution observed over time.

Large-scale surface flow features may be resolved by the distribution and dispersion of quantities such as SST, sea-surface salinity or measurements of ocean colour: such measurements may permit the structure or pattern of the turbulent flow to be observed, and details of the nature or source of the turbulence to be approximated. The study of ocean currents from spaceborne sensors has previously been reviewed by Dohan & Maximenko (2010). Motions of large-scale currents and eddy systems are routinely captured by thermal observations, demonstrating the transport of heat across the globe and the ability to obtain a synoptic view of these motions using satellite instruments sensitive to temperature: such observations are presented by, for example, Legeckis et al. (2002). Ocean colour is commonly characterised by the levels of biochemical material in the upper layer of the ocean, and eddying turbulent flow can act to entrain water masses of differing composition and cause the structure and dynamics of the flows to be revealed by variations in and advection of ocean colour. Materials such as algae, chlorophyll-A or phytoplankton concentrations may be advected by turbulence as passive tracers and reveal the structures present in the turbulent flow. A demonstration of the ability of SST and ocean colour measurements to capture large-scale dynamics is presented in Figure 2, reproduced from Klein & Lapeyre (2009). Methods by which information on currents and large-scale circulation may be extracted from, for example, SST and altimetry data using Maximum Cross-Correlation (MCC) techniques are discussed by Emery et al. (1986) and Tokmakian et al. (1990). An example of the MCC method used for SST, ocean colour and altimetry profiles is presented by Emery et al. (2005), and demonstrated in Figure 3. Measurement of surface salinity from an orbital platform has been obtained through the SMOS mission and in various

airborne microwave radiometer campaigns. The status of remote-sensing of ocean salinity is summarised in the review by Klemas (2011) and measurements of sea-surface salinity are showing increasing viability for observing large-scale dynamics following the launch of *SMOS* (2009) and *Aquarius* (2011). However, at present, significant science data from these spacecraft are only just beginning to enter the scientific literature, and new developments and data are awaited with great interest by the oceanographic community. Meanwhile, there have been a number of notable airborne salinity campaigns; for example, the campaigns in the Great Barrier Reef and Platos Lagoon described by Burrage (2003) and Burrage et al. (2008), respectively.

Where there is convergence or divergence of surface flow caused by currents or eddies, regions of flow structure may be illuminated and delineated by active radar backscattering. Such processes are commonly resolved as light and dark 'bands', as in Figure 4, which allow such flows (and their spatial structure) to be resolved. There is a considerable heritage of the visibility of mesoscale/submesoscale phenomena in SAR imagery which has proven the ability of such phenomena to be resolved by the effects on radar backscattering. Remote-sensing of large-scale features by SAR is examined by e.g. Vesecky & Stewart (1982), Fu & Holt (1983), Ivanov & Ginzburg (2002), Romeiser et al. (2003), Lyzenga et al. (2004) and Johannessen et al. (2005). The paths of current systems and eddies can also be revealed by distribution of surfactant materials over the surface, allowing features such as spiral eddies to be discriminated as shown by Redondo et al. (2011) and Johannessen et al. (2005). Lavrova (2005) also discusses the use of surfactants and sea-surface slicks (arising from biogenic/artificial materials or films present on the water surface) observed in radar imagery to estimate vorticity on the sea surface.

Deep ocean convection is a critical oceanic process responsible for large-scale regulation of the ocean climate (Marshall & Schott, 1999; Paluszkiewicz, Garwood & Denbo, 1994) and such events are comprised of both mesoscale activity and small/intermediate-scale turbulent motions. Since the results of the MEDOC (Mediterranean Ocean Convection experiment) study, published by Lacombe et al. (1970), there has been significant interest in deep water formation and open-ocean convection. However, despite best efforts, it remains poorly studied by remote-sensing due to its sporadic occurrence and short time scale of activity and as such, observations are limited. Measurements using SAR are presented by Carsey & Garwood (1993), Fischer et al. (1998) and Romeiser et al. (2002), whilst recent work published by Herrmann et al. (2009) discusses how use of spaceborne altimetry may allow large-scale convection to be detected through modest (2-3 cm) sea-surface height signatures. There has, however, been significant interest in numerical fluid modelling of convective processes and simulating satellite observations, such as Romeiser et al. (2004), and it

is hoped that future developments in instrumentation will improve observation of these elusive phenomena. Discussion of relevant simulation studies is made in §4.2.

Spatial distribution of sea-surface height may be used to extract information from large-scale systems such as geostrophic velocity and estimations of levels of large-scale TKE contained with ocean currents and eddies, as is summarised by Fu et al. (2010). In this respect, altimetric methods can offer valuable measurements of large-scale dynamics and eddy variability, revealed by measurement by instruments such as *TOPEX/Poseidon* (Stammer, 1997), with developments in the field summarised in the review paper of Morrow & Le Traon (2006). However, current altimetry sensors resolve sea-surface height only on the ground-track, and cannot resolve two-dimensional surface maps of ocean topography. Altimetry data is routinely used as input into ocean state models such as ECCO[2] and for measurement of CO_2 fluxes and mesoscale turbulence in the near-surface of the ocean (Soloviev et al., 2007).
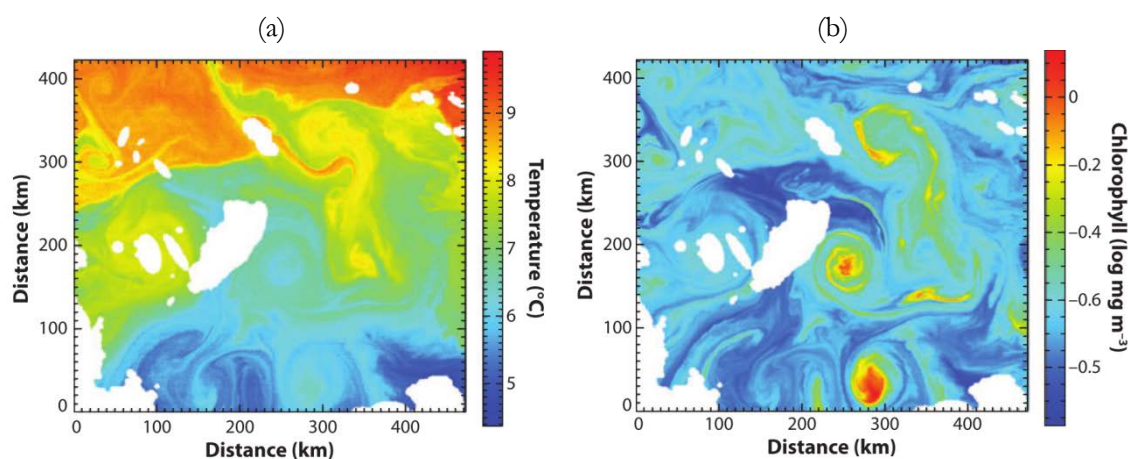
Figure 2. Large-scale oceanic eddies resolved in (a) sea-surface temperature and (b) ocean colour images (Chlorophyll concentration); from Klein & Lapeyre (2009).

---

[2] Estimating the Circulation and Climate of the Ocean; information from: http://www.ecco-group.org (last accessed 06/07/2011)
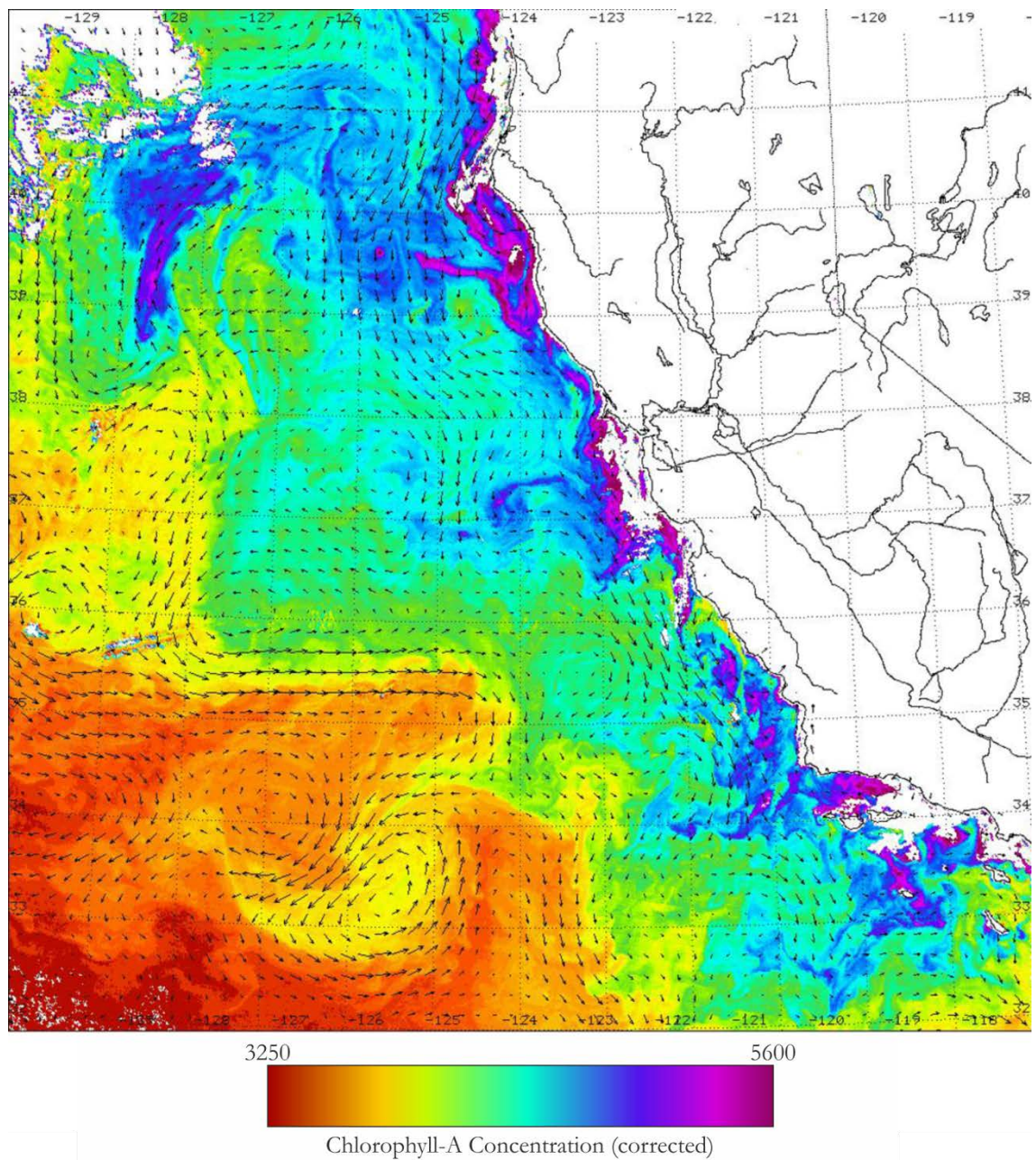
Figure 3. Surface currents computed using the MCC method from a pair of ocean colour images; adapted from Emery et al. (2005). The colour values used by Emery et al. (2005) are corrected based on ocean colour brightness temperature, and are not published as absolute values of Chlorophyll-A concentration.
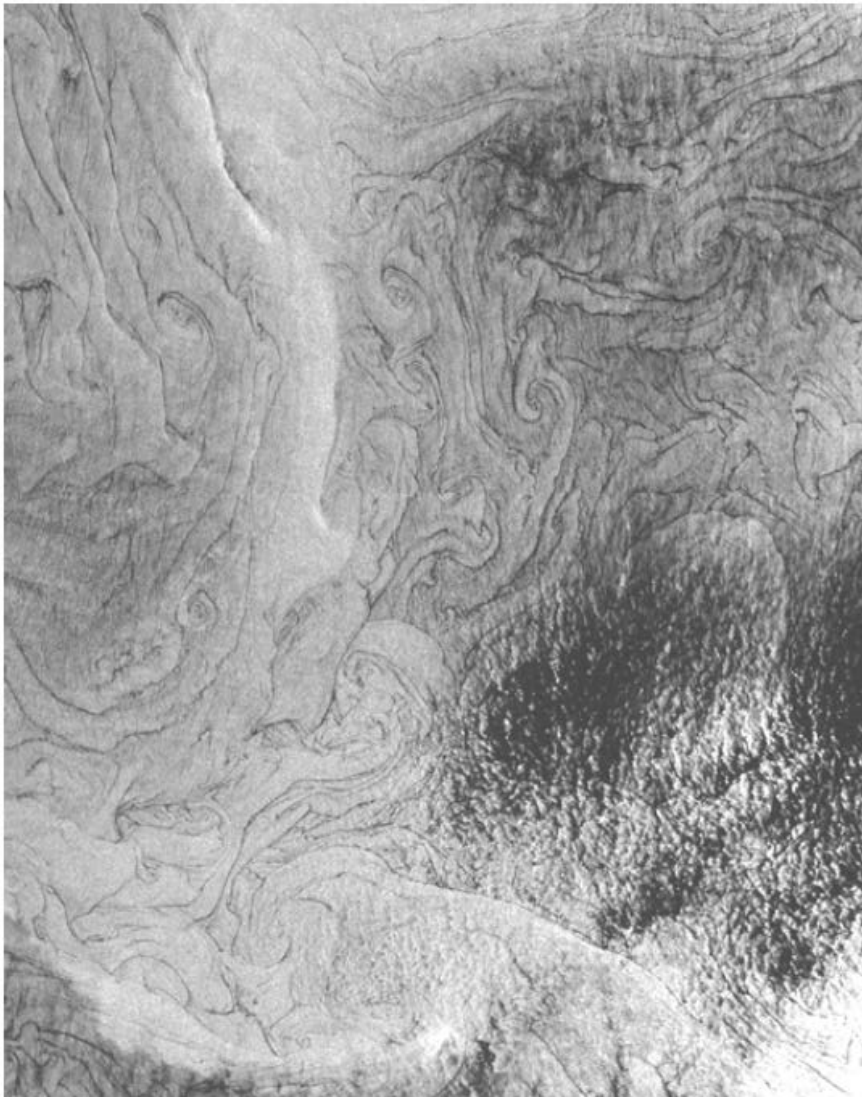
Figure 4. Chains of intermediate-scale cyclonic eddies (size 3-5 km) in the Japan Sea from *ERS-1* SAR ©ESA; from Ivanov & Ginzburg (2002).

2.2.2 Remote-Sensing of Intermediate-Scale Processes

In the domain of intermediate-scale ocean processes, there is a significant heritage to the observation of internal wave structures, ocean fronts and interaction of ocean flow systems with underwater bottom topography through SAR methods. Ocean fronts are oceanographic features which mark sharp boundaries between surface waters with very different properties (e.g. SST). Such processes are resolved through contrast of SST, whereby contrast across the front can be resolved in temperature variation; example SST and SAR images, reproduced from Ufermann et al. (2001), are presented in Figure 5. Very large-scale temperature fronts may be observed, for example, in

GEO SST measurements from *GOES*, such as those presented by Legeckis et al. (2002). In addition to visibility by temperature instruments, they may also be observable in radar backscatter imagery, as described by Johannessen et al. (1996) and Chubb et al. (1999), to provide improved understanding of frontal dynamics. Wu et al. (2000) and Johannessen (2000) examine use of SARs for monitoring of features such as ocean fronts, currents and internal waves; an example SAR image, reproduced from Apel (2004) and depicting internal waves observed by *RADARSAT-1*, is presented in Figure 6. Airborne observations of an upwelling patch, using a multifrequency SAR instrument aboard the NASA AIRSAR platform, have previously been presented by Johnson (2003).

Vesecky & Stewart (1982) offer observations of internal waves and are supported by many further studies, such as Gasparovic et al. (1988), Thompson & Jensen (1993), Ouchi, Stapleton & Barber (1997) and Li et al. (2000); a summary of the heritage of internal wave observations is presented by Apel (2004). The manifestation and effects of internal waves are analysed with clarity in Garrett & Munk (1979) and Gibson (1986): such processes occur due to interactions with bottom topography and stratification, causing large-scale, long-period subsurface waves which travel great distances and interact with the ocean surface, generating surface turbulence. The Bragg scattering mechanism of surface capillary waves can cause sub-surface process to be visible in satellite radar imagery: Clemente-Colón & Yan (2000) consider a number of low-backscatter oceanographic features which may be observed in radar imagery, such as surface winds, surfactants, upwelling and internal waves: such features typically have only a modest effect on radar backscattering, and this can present particular challenges for resolving their surface signatures using imaging radar. Interaction of underwater ocean currents with irregular or rough terrain on the sea floor can lead to instabilities and turbulence measurable at the surface, particularly by SAR; these techniques are summarised by Shuchman et al. (1985) and Alpers et al. (2004).

(a)   (b)
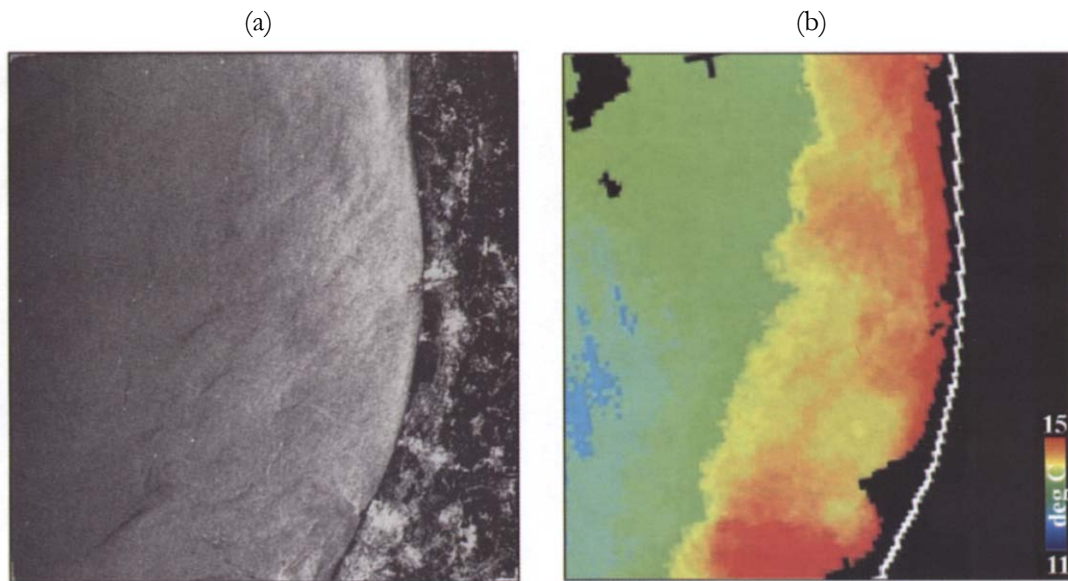
Figure 5. Comparison of (a) SAR and (b) SST data for an ocean thermal front; from Ufermann et al. (2001).
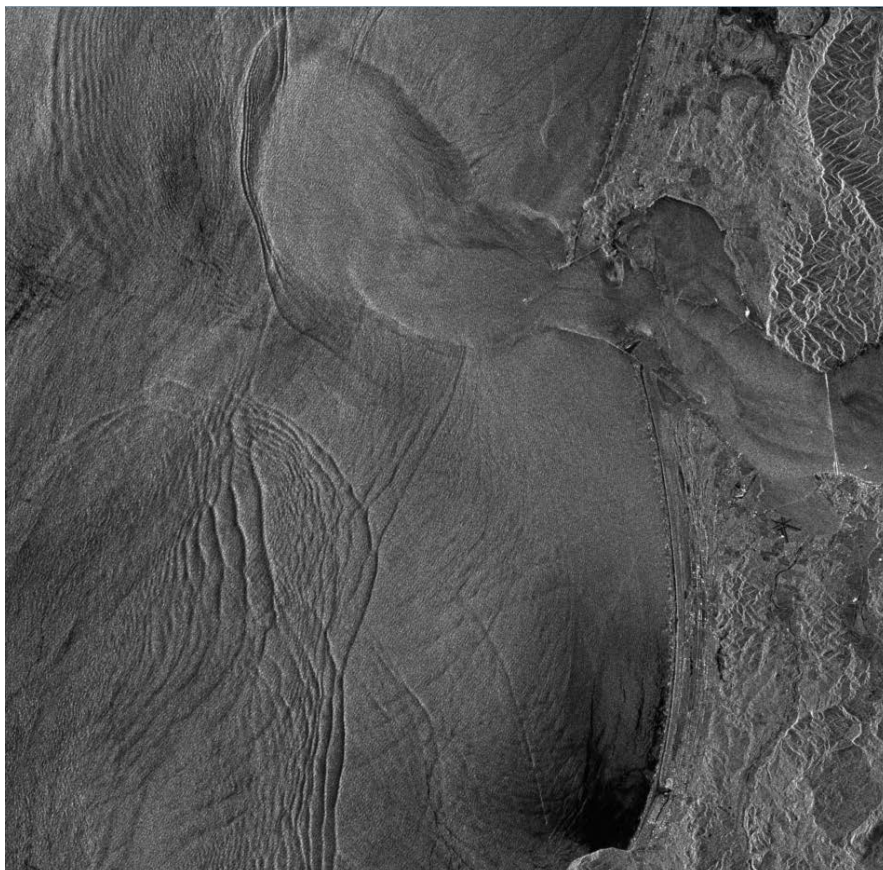
Figure 6. *RADARSAT-1* image showing internal waves off the coast of Washington State. Imaged area is 50 x 50 km. ©CSA; from Apel (2004).

2.2.3 Remote-Sensing of Small-Scale Processes

Observation of small-scale processes is primarily limited by resolution of the observing instrument, providing restrictions on visibility on visibility of those phenomena from prohibitive spacecraft orbits. The $O(1)$ km pixel size of, for example, typical thermal infra-red instrumentation, limit the scale at which processes can be adequately measured spatially. As such, existing (spaceborne) observation of small-scale processes is limited to high-resolution (sub-1 km) instruments, such as SAR or optical cameras.

Satellite data and observations of phenomena such as internal waves, turbulent ship wakes and interaction of ocean currents with bottom topography show that radar backscattering – measured in terms of Radar Cross-Section (RCS) – can respond to levels of small-scale, upper ocean turbulence and generate a measurable change in radar backscatter. Radar signatures of ship wakes are a common feature of many ocean SAR observations, and continue to see considerable study in order to understand how their signatures are resolved by SAR. Notable studies of radar images of turbulent ship wakes are those by Lyden et al. (1985), Reed et al. (1990), True et al. (1993), and Milgram et al. (1993). Research has been conducted from the point of both civil (safety, operations and navigation) and military (maritime tracking, surveillance, etc.). While continued, yet measured, progress has been made on remote-sensing of ship wakes since the mid-1990s, the arrival of data from radar on *TerraSAR-X* has led to renewed interest in ship wake flows observed at high resolution, showing encouraging results such as Soloviev et al. (2010a, 2010b): an example ship wake SAR image (reproduced from Soloviev et al. [2010a]) is presented in Figure 7.

Observed experimentally, the presence of fine-scale turbulence below the surface has been shown to interact with the ambient ocean wave system to modify the surface backscattering response under radar illumination, and has been studied by Reed et al. (1990), Ölmez & Milgram (1992) and Rozenberg et al. (1998). Simulation results published by Milgram et al. (1993) and True et al. (1993) also indicate measurable variations of RCS with presence of surface turbulence, and recent work on relationships between polarimetric SAR/RCS response and surface turbulence, such as by Rozenberg et al. (1998) and Morris et al. (2002), support the range of RCS measurements which may be obtained by radar backscatter techniques. Results from a chance observation of a ship wake from test flight of the Dual-Beam Interferometer were recently published by Toporkov et al. (2011), showing encouraging results for resolving turbulent ship wakes (including some details of internal flow structure) using Along-Track Interferometry (ATI) and for obtaining measurements of small-scale surface velocities.

A field that has seen prolific output from a subset of authors regards observation of submerged fossil turbulence by optical methods. The concept of fossil turbulence describes the case where a fluid is no longer turbulent, but (locally) contains remnants of previous turbulent activity: a summary of the key concepts of fossil turbulence are described in the article by Gibson (1988). Research of visible waveband observations from *IKONOS* and *QuickBird* satellites was published by Leung & Gibson (2004), whereby fossil Internal Soliton Waves arising from a wastewater outfall were observed to cause spectral brightness anomalies at the ocean surface. Potential observation of such phenomena through SAR is further discussed by Gibson et al. (2006).
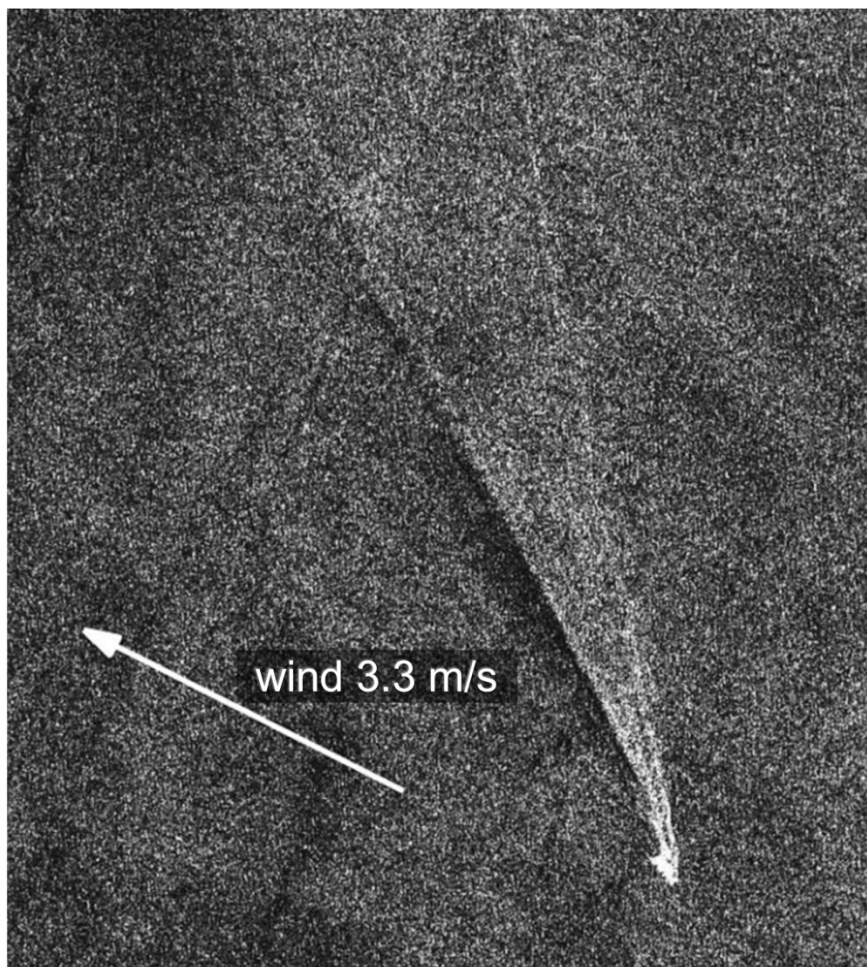
Figure 7. *TerraSAR-X* image of 09/06/2008 showing the wake of the *Eurus Paris* ©DLR; reproduced from Soloviev et al. (2010).

3.   Identification of Needs

A primary phase of investigative study was associated with identifying which scale of oceanic turbulence (according to the definitions presented in Table 1) would benefit most greatly from improvements in remote-sensing capability, and to ascertain the designated instrument method(s) with which to consider such improvements. A particular objective of the study was to match, where possible, the measurement requirements of the oceanographic community to remote-sensing capabilities.

It was considered desirable to maintain breadth over the range of turbulent processes to be considered, therefore focus was placed on addressing measurement of turbulence across all scales from large, mesoscale activity to small-scale turbulent flows. Sufficient sampling of ocean surface parameters remotely will improve the understanding of turbulent ocean processes and the dispersion of these parameters in advective, turbulent flows. Due to the limitation of EM radiation penetrating only the skin of the ocean[3], only the horizontal structure of the turbulence can be revealed to remote sensors by the patterns of temperature, salinity, etc. present at the surface. There are some limitations to using passive tracers to infer properties of large-scale turbulent processes: for example, there may not be a visible signature revealed by a particular parameter, perhaps because the fluid being horizontally mixed does not contain any contrast in, for example, surface temperature. Complications also arise since a single image provides only a snapshot of the surface, thus only an instantaneous indication of the horizontal structure of the variability, not dynamics; although this may be inferred from a time series of data. In addition, an ocean process may exist without a corresponding horizontal variation at the surface of parameters such as temperature, therefore observation of a single parameter or dispersant to resolve the turbulent structure may not be sufficient to detect the presence of a turbulent process alone. Observation of the surface with multiple sensors capable of extracting different dispersants (e.g. ocean colour or salinity), or direct extractions of the flow conditions (surface current vectors, surface height) may be required to increase the probability of observing an active phenomenon.

Chapter 5 ('Turbulent Dispersion') of Thorpe (2007) discusses the effects of tracer dispersion on large-scale turbulence, and how large-scale eddies may be characterised by the scale (and/or concentration) of a dispersant. Such motions may reveal coherent, characteristic structures deliminated by the tracer distribution: examples of this have previously been presented, for example, in Figure 2; demonstrating large-scale oceanic eddies resolved in (a) sea-surface

---

[3] Penetration depth of EM radiation into the ocean depends on the EM frequency. Whilst most spaceborne EM sensors cannot penetrate the upper surface 'skin' of the ocean, visible-wavelength instruments may "see" up to 15-30 m in the open ocean (Joseph, 2014).

temperature and (b) ocean colour (from Klein & Lapeyre [2009]). Typically, it is considered that a sampling frequency (spatial resolution of measurement) of one-half the frequency of variation (of the ocean process) is necessary to characterise the phenomenon according to the Nyquist criterion. To characterise the range of structure present in turbulent flow resolved by tracers, it is desirable to resolve not only the largest scale of variation of a particular turbulent eddy or phenomena, but the fabric of filaments and vortices (smaller scales of variation) which may be denoted by fine spatial structures with slender contrasts in surface temperature, salinity or height, etc.

For many remote-sensing instruments, there exists a trade-off between radiometric accuracy and spatial resolution or coverage, meaning that concurrent optimisation of both sensitivity and resolution may not be possible, particularly for spaceborne instrumentation. In a recent publication, Isern-Fontanet et al. (2008) discuss how three-dimensional (mesoscale) dynamics of the ocean may be recovered from sources of data such as high-resolution SST measurements using Surface Quasi-Geostrophy. Alternatively, Turiel et al. (2005) and Isern-Fontanet et al. (2007) considered methods by which the geometry of tracers in a single image may be used to infer information about the surface flow, or to derive an estimate of the velocity field, using multi-fractal methods: application of such techniques to remote-sensing images for observation of vertical structures and turbulence was pursued by Platonov et al. (2007).

3.1   Strategy and Findings

To investigate the ability of satellite instrumentation to obtain measurements of oceanic turbulence, a course of study was embarked upon to identify the parameters necessary, and the measurement accuracy required, with which to characterise ocean turbulence from space. A strategy, similar to that used by Fischer & Shuchman (1996), was implemented in identifying the measurement needs for a variety of remote-sensing instruments. This involved both a thorough literature survey of observed ocean turbulence processes and discussions with a range of researchers from the modelling, physical oceanography and remote-sensing communities in order to develop the measurement accuracies required to characterise turbulent processes. The study focussed on published data obtained from in-situ measurements.

In summary, the current investigation was performed with the aim of establishing the (measurement) needs of the ocean community, and to understand the requirements for deriving forward progress in observing ocean turbulence. First efforts to address this demand, through understanding the current capabilities of in-situ measures and requirements for remote observation of turbulence in the ocean, are presented in the following sub-sections.

3.1.1 Limitations and Challenges

A significant problem in this approach lay in the limited availability of existing data which relates to the horizontal variability of parameters such as temperature, salinity, colour, height, etc. at the sea surface for a considerable range of scales and oceanic phenomena. Not surprisingly, much of the literature pertaining to the horizontal variation of surface parameters (which may generate an observable surface signature from some turbulent ocean process) relates to data which has been previously acquired from existing remote sensors: for the purposes of the current study, this information cannot provide the necessary information on deriving future requirements, since it is sampled at the resolution and accuracy of existing instruments and hence cannot anticipate measurements at finer resolution. In this study, a focus was made on extracting data from in-situ and airborne campaign measurements of the ocean surface in order to understand potential requirements for future spaceborne instruments with improved resolution capabilities. Therefore in general, existing spaceborne data was not considered, since data is typically too coarse (and with limitations on sensitivity of measurement) to provide an unambiguous view of all of the scales of turbulence examined; only those at mesoscale and above. Since an improvement in spatial resolution is a desirable goal to capture finer scales (although not at the detriment of coverage or measurement sensitivity/accuracy), the use of measurements from coarser instruments does not assist in the definition of measurement needs.

For many ocean phenomena, vertical variations of parameters such as temperature, salinity and conductivity have been widely measured using depth profiles obtained from CTD (Conductivity, Temperature & Depth) or XBT (Expendable Bathythermograph) instruments. Such instruments reflect vertical changes very well, but do not capture horizontal variations. Furthermore, such instruments often do not measure surface properties within the skin of the ocean, which is the intermediary which is primarily observed by remote sensors: validation, therefore, of remote-sensing data with in-situ (surface) measurements is not a straightforward process. The nature of remote-sensing instrumentation to measure only the very upper layer of the ocean surface (0.01 – 2.0 cm, depending on the frequency of the instrument – see Footnote #3) means that, for example, temperature measurements captured by Infra-Red radiometers relate only the temperature of the 'skin' of the ocean, whereas in-situ instruments measure 'surface' temperature at some finite distance beneath the surface; but which may still described or published as 'sea surface' temperature. Differences between observed airborne/spaceborne measurements of SST and those obtained by in-situ instruments "can be attributed to thermal skin effects or to the cool skin layer and absorption of the surface radiance by the atmosphere between the [instrument platform] and the surface (equivalent to ≤ 0.1°K)," (Hagan et al., 1997). Furthermore, in their study, Pascual et al.

(2010) report spatial resolution of shipboard CTD tracks of 2.5 km (along-track) and 6.5 km (between tracks), which is larger than measurements offered by spaceborne sensors.

Measurement of surface parameters (and their horizontal variations) may instead be more accurately obtained by instruments which are towed or deployed by ships, or by arrays of moorings placed in a grid. Shipborne instruments typically permit measurements only along the ship's track, and as such cannot provide two-dimensional 'grid' of horizontal variation at the surface, yet can deliver useful data. Glider instruments are autonomous underwater vehicles which may collect data (of characteristics such as "temperature, salinity [conductivity], turbidity, chlorophyll, rhodamine, fluorescin and passive acoustic signals," as described by Wood [2008]) along sub-surface tracks: Pascual et al. (2010) report operation of a gliders with an along-track resolution of 0.3 km (coastal glider) and 1.1 km (deep glider), with resolution of 4 km between glider tracks over a 50 x 40 km area. However, gliders are designed to operate sub-surface, at varying depths (the study by Pascual et al. [2010] conduct measurements over a glider track varying between 0 and 200 m depth), and therefore do not characterise surface quantities. Similarly drifter instruments typically move with surface currents along uncontrolled paths; Pascual et al. (2010) report operation of such instruments at a depth of 15 m.

Networks of buoys/instrument can provide instantaneous data on a two-dimensional grid, but in general such networks have significant separation which may be too large to capture variations of small- to submesoscale turbulence: for example, the United States National Data Buoy Center (part of the National Weather Service Organisation) catalogues a vast range of moored measurement buoys around the USA and across the globe and marks buoys with typical separation of the order of 20-100 km[4], whereas the Global Tropical Moored Buoy Array[5] which shows a 10° separation in longitude and 1.5-3° in latitude. Therefore, a significant challenge was encountered in that in-situ (moored buoy) data rarely exists with sufficient horizontal resolution (in two dimensions) to display a clear understanding of horizontal spatial variations for a range of ocean (turbulent) processes.

Surface data may be instead acquired through airborne test campaigns, typically in a similar manner to spaceborne instruments but with advantages of improved spatial resolution arising from closer proximity to the ocean surface. Such validation activities can typically be of significant benefit in quantifying benefits in remote-sensing capabilities from space, and may be used in tandem with a

---

[4] NOAA National Data Buoy Center; data acquired by using the Google Maps distribution of buoys in the Gulf of Mexico; available online at: http://www.ndbc.noaa.gov/, last accessed 22/08/2013
[5] NOAA Global Tropical Moored Buoy Array; available online at: http://www.pmel.noaa.gov/tao/global/global.html, last accessed 22/08/2013

prospective or new spaceborne instrument to calibrate or validate data. Challenges were, however, encountered in the limited accessibility of in-situ or airborne test data for the spatial variability of ocean colour, sea-surface height and surface currents: as a result, deriving measurement requirements for some parameters was very difficult. In addition, for data which was acquired or extracted from the published literature, it was not possible to derive all information in this chapter from absolute values (either in tables or text); therefore, some data was required to be read from figures or graphs, and hence some details of spatial distance and/or variation of parameters are approximated by eye.

Further issues that were encountered during the study were related to the balance of explicit measurement requirements, and the expectations of future instrument performance, which was experienced during survey of ocean scientists: in many cases, it was difficult to isolate explicit measurement needs from preconceptions on achievable capabilities, and this permeated through many of the received responses. Previous work by Fischer & Shuchman (1996), performing a similar survey of the oceanographic community, was associated with a workshop at which the published set of measurement requirements were derived, with applications for study of mesoscale/submesoscale processes associated with open-ocean convection. In this respect, it was necessary to evaluate requirements for varying applications: for example, the instrument capability required for coastal study differs from that required for observing processes in the open-ocean, since there is generally higher spatial variability along with variation in contrast(s) between different water masses. For future work in this field or extension of the current investigation, it is recommended that a similar strategy is pursued, albeit with a single, explicit application (or ocean process) in mind.

3.1.2 Ocean Colour and Biochemical Tracers

For general measurement of ocean colour data, a report by the International Ocean-Colour Coordinating Group (IOCCG, 2000) indicates that imaging of near-coastal regions may require spatial resolution better than 30 m (an achievable specification for optical cameras, but ambitious for multi-spectral instruments) for observation of shallow-bottom effects (for purpose of navigation, etc.), with open-ocean features requiring spatial resolution finer than 250 m. These requirements, however, are based on general ocean remote-sensing and are not focussed on characterising particular turbulent processes or focussing on a particular scale of phenomena; rather, this investigation is restricted to more general ocean remote-sensing requirements, with some generalised comments regarding the application of ocean turbulence. A comprehensive list of the ocean colour sources which were consulted as part of this study is presented in B.2 of Appendix B.

In development of the ESA *Sentinel-3* spacecraft, requirements for ocean colour observations have been previously been published and discussed by Drinkwater & Rebhan (2005); this data has been reproduced and presented in Table B1 of Appendix B. Spatial resolution is specified as 2-4 km for global monitoring and 0.2-0.5 km for coastal regions. In coastal regions, requirements are significantly reduced due to the high biological activity and variation in these regions, which lead to enhanced spatial variation. A minimum of 15 spectral bands is prescribed to cover the wavelength region of 400-1050 nm. Open-ocean requirements are supported by recommendations by Robinson (2010) and the World Meteorological Organization (WMO)[6], stipulating spatial resolution better than 5 km, although this appears very conservative and already feasible using the 1 km resolution data which can be derived by *SeaWiFS*. The values derived by Drinkwater & Rebhan (2005) for coastal regions are supplemented by more optimistic requirements of 30-1000 m and 45 m documented by the IOCCG (2000) and Freeman et al. (2010), whilst Robinson (2010) proposes an ambitious spatial resolution of "a few metres" for observing ocean colour in coastal regions. With regard to capturing temporal variations, Drinkwater & Rebhan (2005) recommend a temporal resolution of 1 day to observe coastal and fast-developing processes, but this may necessitate a considerable spacecraft constellation with short repeat-period and temporal separation to derive rapid time-series of measurement.

A recent report prepared by the Committee on Assessing Requirements for Sustained Ocean Color Research and Operations (National Research Council; Yoder et al. [2011]) focussed mainly on the requirements for continuing data on ocean colour from space, but made brief (qualitative) comments on the desired spatial and spectral accuracy of future, hyperspectral sensors: although not installed on a long-term mission, the HICO (Hyperspectral Imager for the Coastal Ocean) instrument was operated on the International Space Station in 2009, achieving a 100 m spatial resolution at 5.7 nm bandwidth (equivalent spatial resolution from airborne platform: 90 m)[7], hinting at the potential capabilities of future spaceborne missions. The GEO-CAPE (GEOstationary Coastal and Air Pollution Events) mission study present a draft document of ocean colour science requirements, requesting hyperspectral instruments in GEO with spatial resolution of 250 m (threshold: 375 m) and 0.25 nm spectral resolution (threshold: 2 nm); derived from NASA (2012). With respect to airborne capabilities of (hyperspectral) ocean colour sensors, the airborne PHILLS (Ocean Portable Hyperspectral Imager for Low-Light Spectroscopy) developed by the Naval Research Laboratory (Mobley et al., 2005) is a pushbroom scanner capable of spatial resolution of 1-2 m and spectral resolution of 4.6 nm. Meanwhile, regarding visible

---

[6] World Meteorological Organization – OSCAR (Observing Systems Capability Analysis and Review Tool); available online at: http://www.wmo-sat.info/oscar/requirements, last accessed 18/06/2013

[7] Information from: http://hico.coas.oregonstate.edu/ (last accessed 23/11/2013)

waveband sensors, airborne/spaceborne optical instruments may be operated for applications such as coral reef observation (Hochberg & Atkinson, 2003), with spatial resolution (< 1-2 m) capable from aircraft and 1-4 m achievable from spacecraft such as IKONOS; Mumby et al. (1997) have previously delivered a qualitative discussion of spatial resolution requirements for coral reef study, although significant progress in instrument capability has been made since its publication.

Considering published data on ocean colour and chlorophyll-A measurement, results from observation of a cold-core eddy are published by Robinson (2010), showing a variation of chlorophyll concentration of 0.2-0.5mg^{-3} across an eddy of diameter 30-40 km. From Buranapratheprat et al. (2010), Chlorophyll-A distributions show a variation of 0.1 mgm^{-3} over a eddy spanning 25 km. However, limited data exists regarding how turbulent processes are observed/measured in combination with in-situ measurements of ocean colour in the open literature and as such, a full data survey was not possible. The results of this study therefore remain inconclusive regarding the measurement needs of ocean colour tracers for capturing and resolving large-scale turbulent processes. There is great evidence of such turbulence scales resolved in imagery obtained from *SeaWiFS* or *CZCS*, but there is currently insufficient in-situ or airborne test data with which to corroborate remote-sensing measurements based on surface data or to postulate the implications for improvements in spatial or measurement resolution. Only a limited range of source material has been consulted with respect to future requirements for remote ocean colour sensors, and it is recommended that future work probe the potential benefits and measurement needs for such study. With regards to this exploratory investigation, however, the identified measurement requirements for ocean study are presented in Table 3 which follows at the end of this chapter.

3.1.3 Sea-Surface Temperature

Sea-surface temperature is one of the most heavily-studied oceanographic parameters from both airborne and in-situ perspectives, and as such, a considerable volume of results (and discussion of requirements) exists in the current literature. A comprehensive list of the sources consulted in survey of the literature, along with key information extracted from those sources, is presented in Table B3 of Appendix B.

With respect to future measurement needs, Drinkwater & Rebhan (2005) indicate that requirements for spatial resolution are, least surprisingly, most constricting for observing coastal zones, where rapid spatial or temporal processes occur: a spatial resolution of 0.5 km (or finer) is recommended. Considering more broad ocean applications, spatial resolution requirements for SST are specified at 1-5 km for a range of applications by the WMO[6], meanwhile Schiller & Brassington (2011)

reproduce results previously presented by Le Traon (2006) considering general requirements for weather prediction (10-50 km), climate monitoring (20-50 km) and ocean forecasting (1-10 km) applications. In a requirements study focussed on improved instrumentation for monitoring mesoscale eddies and open-ocean convection plumes, Fischer & Shuchman (1996) published recommended mission requirements developed at a dedicated workshop for such processes. They define a desirable spatial resolution for SST measurement of 2-5 km is set for mesoscale eddies, whilst a more slender 100 m for capturing convective plumes (typically much smaller in scale; perhaps 0.1-2 km in diameter): measurement accuracy for these processes is defined as 0.01-0.05 K and 0.0005-0.01 K respectively. For comparison, Drinkwater & Rebhan (2005) define a desirable measurement resolution of 0.025 °K for various application, with relative and absolute accuracies of 0.05 K and 0.1 K. Bourassa et al. (2010) consider more restrictive requirements, defining sampling accuracy desired to 0.005 K for monitoring global climate change, and 0.1 K for considering upper ocean heat content and open-ocean upwelling, supported by less stringent requirements defined by the WMO[6] (0.5 K at 100 m resolution). Considering more broad applications, Le Traon (2006) presents desirable measurement accuracies for applications such as weather prediction (0.2-0.5 K), climate monitoring (0.1 K) and ocean forecasting (0.2 K). Freeman et al. (2010) discuss sampling requirements for regions of ocean fronts and upwelling zones at 1-2 km or finer, although this may seem coarse in light of some strong temperature contrasts such as those observed by Askari et al. (1993) and Robinson (2010).

Through examination of SST studies published in the literature, it may be observed that some turbulent phenomena exhibit slender temperature contrasts; for example ocean eddies demonstrate temperature contrasts as small as 0.2 K over distance of 1-2 km, whereas surface temperature contrasts of an ocean front may be up to 10-15 K (Askari et al., 1993; Robinson, 2010). In terms of the current capability of airborne SST sensors, details of the CBLAST-Low (Coupled Boundary Layers, Air-Sea Transfer in Low Winds) study discussed by Zappa & Jessup (2005) demonstrate a 1 m spatial resolution and 0.02 K thermal resolution of an airborne IR camera, observing meriodonal variability of 0.23 K/km and zonal variability of 0.27 K/km. In an earlier airborne campaign (summarised by Hagan et al. [1997]), an airborne instrument with 100 m spatial resolution and 0.1 K observed horizontal gradients of SST of 1 K in 10 km; although Zappa & Jessup (2005) describe observation gradients in excess of 2 K in 10 km, and SST data published in graphical form demonstrate significantly higher gradients of temperature at small-scales.

Concluding this investigation of potential future capabilities of ocean temperature remote sensors, a compiled definition of measurement needs for observing sea-surface temperature are presented in Table 3. Through the heritage of twenty years of SST observation from space, there is a significant

level of discussion of SST data and future perspectives held within the literature and amongst the oceanographic community. However, there have not been significant steps in spaceborne capability to measure ocean surface temperature in this time, and so understanding the feasibility of deriving such progress (or extrapolating from airborne capabilities) remains a complex task.

3.1.4 Sea-Surface Salinity

Sea-surface salinity is typically quantified in terms of the psu (Practical Salinity Unit), equivalent to parts per thousand of salt in seawater, and due to its dispersive properties can reveal the variability of large-scale eddies and turbulent processes. For such phenomena, data for the variation of sea-surface salinity (in a similar manner to SST) over a range of observed eddy processes is presented in Table B4 of Appendix B. The findings of a similar previous study by Srokosz (1995) have been reproduced in this table, along with data acquired from other sources.

A very coarse spatial resolution requirement of 10-150 km is specified by Srokosz (1995) for observing mesoscale eddies, while Swift & McIntosh (1983) denote a range of spatial resolutions depending on application; 0.01-0.05 km for estuary regions, 1 km for bay areas and 1-10 km in the open ocean. Swift & McIntosh (1983) also comment that "some oceanographers cite that it is necessary to know the density of seawater to within an accuracy of five decimal places, which in turn requires a 10 ppm accuracy on measurement of salinity," which is extremely ambitious, even with state-of-the art sensors. Following their study, Fischer & Shuchman (1996) indicate that remote measurement of mesoscale eddies should be made at spatial resolution 2-5 km, with desirable resolution of 0.1 km for understanding the plume dynamics of open-ocean convection phenomena. Regarding accuracy of psu measurement for observing mesoscale eddies associated with deep ocean convection, Fischer & Shuchman (1996) propose a value of 0.005-0.02 psu are necessary; a more stringent requirement of 0.0001-0.001 psu is recommended for observing the individual convective plumes. Srokosz's (1995) recommendation for examining mesoscale eddies is a desired measurement accuracy of 0.05-1.7 psu, whilst Swift & McIntosh (1983) suggest a more restrictive measurement accuracy of 0.01 psu for studies of estuarine, coastal and open-ocean areas. Near coastal regions, where freshwater run-off may mix with saline water and lead to strong contrasts, Thomann (1976) and Blume et al. (1978) indicate that coarser measurement accuracy (of up to 1-2 psu) may be permissible to capture eddy motions. Although this may appear somewhat counter-intuitive, this is because typically, larger contrasts in surface salinity occur where fresh- and salt-water mix, thus coarser discrimination is required to demarcate fluid of differing properties. For sufficient coverage of open-ocean turbulence, however, a more slender measurement accuracy be required. For general ocean measurement of sea-surface salinity, the WMO[6] specifies a desirable

requirement of 0.07-0.2 psu for salinity measurement, although this figure is not specifically targeted at extracting information on the salinity distributions of eddies or turbulent dispersion.

These combined results suggest that measuring mesoscale eddies requires instrumentation capable of measuring to 0.01 psu accuracy at spatial resolution considerably finer than 1 km in order to generate satisfactory sampling of sea-surface salinity across the eddy field. Where Srokosz (1995) suggests a requirement for measuring salinity changes of 0.05-1.7 psu, on space scales of 10-150 km, for large-scale eddies there has so far been limited analysis of the spatial variability of sea-surface salinity in resolving eddy flow patterns. However, since observation and measurement of sea-surface salinity from space are comparatively recent (within the last five years) and with only a limited amount data so far processed and published from *SMOS* and *Aquarius*, the conclusions of this investigation remain slightly unclear. At the present time, spaceborne salinity capability remains rather coarse in terms of spatial resolution (50-150 km) and salinity retrieval accuracy; furthermore, airborne measurements also suffer similar limitations when compared to, for example, airborne SST sensors. This result means that, extraction of sea-surface salinity at similar resolution as sea-surface temperature is distant, and that a true set of requirements for sea-surface salinity (either for a range of applications or for study of particular ocean processes) are yet to emerge.

3.1.5 Sea-Surface Height

Large-scale turbulent phenomena such as eddies, currents, fronts and deep convection may sometimes be associated with measurable changes in the surface height across the horizontal extent; although typically with very infinitesimal gradient slopes. Variations in sea level height observed for various mesoscale phenomena were recovered from the open literature and are presented in Table B.5 of Appendix B. Despite the large amounts of data on large-scale processes derived from spaceborne altimeters, there exists little data regarding the spatial variation of such processes (at least not where validated against in-situ observation networks), largely due to the sampling problems of current radar altimeters and in-situ measurement limitations. Traditional (nadir-pointing) radar altimetry obtains an along-track measurement only (point measurement beneath the satellite ground track); although two-dimensional geostrophic information can be obtained. Ideally, a finite swath width of SSH is ultimately desired for robustness of measurement and improving the sampling capability; Pascual et al. (2007) report that even mesoscale structures of O(100 km) are not fully resolved by measurements from two nadir-looking altimeters, and to date there remains limited study of two-dimensional SSH maps derived from remote instruments, although future

missions such as Surface Water & Ocean Topography[8] (*SWOT*, expected launch 2020) may address this shortfall.

Meanwhile, coverage of in-situ sensors and measurement accuracy holds significant limitations which preclude robust (mean) SSH data from being obtained; typically, SSH derived from such instruments are estimated by converting temperature/pressure data to a prediction of mean SSH. Altimetry is typically not performed from airborne platforms due to the difficulty of maintaining stable, accurate flight using aircraft; however, early results from the *SWOT* airborne test/calibration campaign (AirSWOT) are expected to be forthcoming during 2014. Deriving the requirements for measuring sea-surface height is therefore not a straightforward exercise. In the *Sentinel-3* mission requirements study, Drinkwater & Rebhan (2005) identify principle goals of SSH measurement are set at 2-8 cm for coverage of large- to meso-scale processes, whilst identifying that more stringent goals may be required for climate analysis. Defining acceptable accuracy of SSH measurement to capture characteristics of individual processes, based on the data compiled during the literature survey, is challenging. The general trend that emerges from this limited investigation suggests that centimetre-level accuracy of SSH measurement is necessary in order to measure and monitor oceanic processes such as large-scale ocean eddies and open-ocean convection. With regards to mesocale eddies of $O(100$ km$)$, Pascual et al. (2007) describe that altimetric signals observed for such structures in the Mediterranean are typically weak, ~7-8 cm rms; however, defining acceptable accuracy of surface surface height for finer structures is more challenging.

3.1.6   Discussion

From analysis of the literature and a range of sources examining the visibility of ocean phenomena in current ocean sensors (airborne and spaceborne; and in some cases, future) and the measurement requirements, some conclusions may now be drawn regarding the potential developments in sensor capability which may be necessary to make significant progress in the measurement or understanding of the turbulent ocean. This analysis was progressed with the aim of deriving a set of measurement needs and matching the defined needs with potential opportunities to improve current capability; thereby focussing further research on a selected instrument and associated application. These requirements, specified by instrument for extraction of observation of turbulence over a broad range of scales, are proposed in Table 3, which summarise the primary findings of §3.1.

---

[8] Information from: http://swot.jpl.nasa.gov/mission/ (last accessed 04/11/2013)

In construction of these requirements, a range of sources and academics were consulted in order to cover a breadth of oceanic applications, processes and instrumentation. However, a focus was made on the measurements needs relating to observing intermediate- and large-scale ocean processes, and in this respect, mainly to the requirements necessary for capturing spatial distribution of surface characteristics and only minorly towards the (spectral/measurement) resolution at which parameters may be extracted from sea surface data. In this respect, Table 3 does not represent a comprehensive tabulation of the complete requirements necessary to observe any particular process; but instead, represents the desirable capabilities for future ocean-sensing instruments in order to make progress in turbulent ocean science.

Ocean (Surface) Parameter	Spatial Resolution	Data Accuracy
Sea-Surface Temperature	< 100 m (25-50 m)	up to 0.0005 °K
Ocean Colour (multispectral imaging)	< 100 m (25-50 m)	less than < 0.1 mgm^{-3}
Sea-Surface Salinity	< 100 m (25-50 m)	0.01 psu (better than 0.0001 psu)
Sea-Surface Height	< 10 m	< 1 cm

Table 3. Measurement requirements for observation of ocean turbulence over a range of scales. Values contained in brackets represent particularly goals which are particularly challenging, but most desirable for future progress.

In addition to the surface properties discussed in §3.1 previously, there are additional characteristics whose role(s) are more complex and are not merely sole characteristics of the ocean surface which are measured directly. In this respect, the findings of this investigation for such parameters have not been included in Table 3, although the implications for these measurements will be discussed in the following paragraphs.

The ability of RAR/SAR instruments to observe radar backscatter cannot be defined by a single surface property but in essence is relevant to characteristics of sea-surface roughness. The visibility of phenomena such as ship wakes, internal waves, eddies and ocean fronts in radar imagery has proven the ability of such phenomena to be resolved through modulation of the surface wave spectrum and, as a result, radar backscattering. Since radar backscattering cross-section is not an inherent property of the ocean surface (when compared to parameters such as temperature or salinity content) but reliant on the observing radar configuration and coincident conditions, there is no opportunity to explore or validate in-situ measurement requirements and hence deriving acceptable tolerances for spatial accuracy and measurement of radar backscatter is problematic: they are dependent on numerous factors including the strength and scale of the phenomena, the ambient conditions (wind state, sea state) and the radar used to observe the process, along with

reliance on beneficial viewing conditions. Although there is currently no direct relationship between turbulence and radar backscattering cross-section (RCS), the presence of flow structure of resolved eddy/turbulence phenomena can be observed in current imagery, in addition to surface current deformation (convergence/divergence, shear, strain, rotation) which may be affiliated with turbulent motion. An improvement in spatial resolution of SAR instrumentation is typically desirable for improving sampling/resolution of small-scale phenomena. *TerraSAR-X* currently offers spatial resolution of 3-5 m, with a 1 m Spotlight mode: recent results published from this instrument have shown satisfactory ability to resolve a range of phenomena, such as those published by Soloviev et al. (2010) and Lehner et al. (2012). On observing ocean bottom topography, Hennings et al. (2007) define requirements of up 1 m spatial resolution and 1.5 dB radiometric resolution necessary. Meanwhile, Fischer & Shuchman (1996) observe variations of NRCS (in simulated radar imagery) of as little as 0.4-0.8 dB for open-ocean convection signatures. From this perspective, the measurement sensitivity desired for observing ocean turbulence may then be required for less than 1 dB, which poses some challenges; the summary article by Clemente-Colón & Yan (2000) describes the implications for observing a range of low-backscatter features on the ocean surface, such as the effects of rainfall, surfactants, sea ice, upwelling and other oceanographic phenomena. Current spatial resolution capabilities may be adequate to resolve a range of mesoscale (and submesoscale) ocean features, but improved resolution could offer significant benefits and allow finer details of surface motions to be observed and characterised.

In addition, the measurement of surface currents, at least in terms of large-scale or mean motions, have heritage of observation using both in-situ and remote instrumentation: in the former, observations from buoys or moorings can provide point measurements of surface currents, whilst large-scale current motions may be inferred from time series of remote images (e.g. the MCC technique as described previously in §2.2.1), extrapolated from altimetric data, or obtained using techniques such as Surface Quasi-Geostrophic (SQG) theory as discussed by Isern-Fontanet et al. (2008). Furthermore, the potential to obtain direct ocean surface velocity measurements from Doppler characteristics of a received SAR signal is a developing field and may be applied to large-scale currents to estimate line-of-sight velocity of current systems (Johannessen et al., 2008). Requirements for monitoring mesoscale eddy currents are discussed by Fischer & Shuchman (1996), desiring accuracy of 5-10 cms[-1] at 2-5 km spatial resolution, while open-ocean convection plume dynamics may require 5 cms[-1] at 100 m resolution. Bourassa et al. (2010) discuss requirements for monitoring surface currents to 20 cms[-1] for measuring upper ocean heat content and regions of open ocean upwelling, with a desire for accuracy of 10 cms[-1] for global climate change applications. The WMO[6] specifies requirements of current accuracy of 10 cms[-1] and 20 cms[-1] for coastal, and open-ocean regions, respectively. Due to limited information about which

to draw conclusions, the requirements for measuring large-scale processes using surface current data remain open at this time.

3.1.7　　　　Summary

Following study of the available literature and identification of required needs, it is clear that a significant 'gap' exists in the oceanographic canon for observing, and characterising, submeso- and small-scale processes in the ocean. Capturing improved observation of these processes, on a global scale and associated particularly with understanding of the role turbulence and mixing plays on the air-sea climate at these scales, could lead to advances in modelling the motion and energy balance of the ocean as a whole: for example, adequate parameterisation(s) of submesoscale mixing processes are critical in simulating and predicting ocean circulation and changes in climate; such considerations are highlighted by Waugh (2006). In this respect, it is clear that improved observation of small- and submesoscale turbulent/ocean processes could lead to significant benefit for the oceanographic/modelling community, and therefore it is relevant to posit the implications for deriving (achievable) progress in the capability of current sensors in the future, and to attempt to align these with the predicted needs of the ocean community.

A primary conclusion of this investigation is that there is still a significant need for future ocean remote-sensing missions to address the lack of synoptic measurements of oceanic turbulence at a broad range of scales whilst capturing high-resolution structure of small-scale processes. In particular, the capability to observe ocean processes in the observation 'gap' between in-situ measurement(s) and remote-sensing of intermediate-scale processes is still a severe limitation, and steps towards matching the needs of the oceanographic community in this measurement intervals are required across all categories of remote-sensing instrument. From this perspective, it is recommended that significant efforts towards airborne testing of high-resolution sensors be continued in order to prepare for the next generation of specialised ocean sensors. The current *ad hoc* review of necessary observation requirements is by no means comprehensive in its agenda or results, but is indicative enough to understand the breadth of the 'gap' which exists between needs of the ocean community and current spaceborne capabilities.

For reinforcement of the identified requirements, it would be highly desirable to engage more thoroughly with ocean scientists in order to obtain a more comprehensive view of mission/measurement requirements from a scientific standpoint: a suggested activity would follow the example of Fischer & Shuchman (1996), involving a workshop among the oceanographic community to specify desirable measurement requirements. In 2007, a challenge workshop was organised in the UK by the Centre for Earth Observation Instrumentation (CEOI) to identify

scientific drivers for ocean study, and the findings of this event were published online by Remedios et al. (2007). It is greatly recommended that a similar event be held for further refinement of the derived measurement requirements for ocean turbulence study. Alternatively, this could be performed in the context of a comprehensive online, or digital, survey of relevant ocean scientists.

The remainder of this thesis considers selection of a remote-sensing technique which, with further potential future advances in capability, may be able to address this shortfall and improve the understanding of turbulent processes and scales between 1 metre and 1 kilometre in extent.

3.2   The Selected Study

Considering the current fleet of spacecraft instrumentation which may be operated for satellite oceanography, and the potential for future advances in capability, the response of radar backscattering to both small-scale turbulence and large-scale motion highlights imaging radar as a technique which, with future technical advance, may be instrumental in improving global study of ocean turbulence over a range of scales. With regard to the use of SAR for observation of the ocean, the review of Holt (2004) provides an efficient overview of current operations, however key details are also summarised later in §4.1. Since fine spatial resolution from RAR (Real Aperture Radar) instruments is infeasible from space due to the restrictive antenna length requirements, the allocation of RCS as the designated measurement method implies use of spaceborne SAR, exploiting the Doppler echoes using aperture synthesis techniques. The fine spatial resolution available from SAR-type instruments (from 20 m, to potentially sub-metre, resolution) offer improvements over the RCS measurements achievable with RAR, and can provide measurements of a number of additional parameters of interest (surface roughness, wave spectrum, surface strain, etc.) for observing surface signatures of various ocean processes through the medium of radar backscatter. Due to the extensive studies performed into ocean wave/current imaging by SAR by authors such as Fu & Holt (1983) and Ivanov & Ginzburg (2002), the relationship between hydrodynamic wave-current modulation and the Bragg and full-spectrum NRCS is well-developed, which facilitates operation of simulation models. The heritage of *Seasat* through *ERS-1/2* to modern instruments like *TerraSAR-X* has proven the ability to resolve mesoscale eddies (see Figure 4) down to ship wake turbulence (see Figure 7), and extract parameters such as spatial & temporal scales, and the source and nature of the turbulence.

Whilst the explicit selection of 'SAR' makes some generalisations about the capability and operation of imaging radar, synthetic aperture techniques have seen renewed interest in the past decade – particularly from an oceanographic perspective – and there is a significant momentum being carried

forward with an exciting range of future spaceborne SARs entering operation in the coming years. Historically, the principal spaceborne SAR systems have been primarily operated at L-, C- and X-band frequencies, yet there is a current need for increasing the range of spaceborne SAR instruments at a wide range of diverse frequencies and polarisation capabilities, at high resolution, for dedicated ocean study. This study therefore offers an accessible opportunity to consider the effects of unconventional instrument configurations, and prospective performance in observing and resolving small- to submesoscale turbulence in the ocean, and to understand the implications and requirements for future instruments.

From this preliminary feasibility study, it was clear that the primary limits on SAR for observing the effects of surface turbulence would lie in the ability to resolve fine backscatter variations arising from wave-current interaction(s): limitations would arise from the ability to observe the presence of modest surface flow features based on the available spatial resolution of the instrument, along with the ability to distinguish slender differences in radar backscatter from surface signatures which may show only faint spatial variation. Undoubtedly, benefits in operation will be observed with advances in spatial resolution, yet it is perhaps the domain of measurement accuracy, and sensitivity to low-backscatter sea surface features, which poses the greatest challenge for accommodating improved ocean-sensing capability. In addition, a trade-off must be made to ensure that improved resolution capability is not at the expense of coverage, as there is a significant desire (if not a necessity) for measurement(s) to be made over wide areas of the ocean at a time in order to maximise data capture.

As a result, the selected study considered the role of SAR in addressing the shortfall in observation of small- and submesoscale oceanic turbulence, and to further understand how future modifications to SAR performance may facilitate improved characterise turbulent processes in this region of the ocean spectrum. Where measurement requirements of other instruments have been defined and considered in this chapter – and desirable 'needs' identified for future ocean study with prospective instrumentation – the situation for future imaging radar requirements is less clear, and the implications for observing the ocean with novel SAR configurations are yet to be fully understood. A simulation strategy, which is defined in the following chapter, was coordinated in order to derive simulated radar surface signatures of a small-scale ocean process and improve understanding of the role of SAR in future ocean study of turbulence.

4.   Applied (End-To-End) Simulation Strategy

4.1   Basics of Synthetic Aperture Radar

Radar (Radio Detection and Ranging) systems are devices which transmit and receive pulses of electromagnetic waves through a microwave antenna, measuring characteristics of the wave reflected back to the instrument and calculations based on the time delay (and in the case of SAR, the Doppler characteristics). Imaging radar is a technique for Earth observation which requires the instrument to transmit a constant stream of pulses towards the surface of the Earth as the antenna platform travels over the scene, measuring accurately the time delay and strength of the echo reflecting back toward the instrument. Imaging radars are typically side-looking instruments, transmitting the radar beam in the range direction towards the surface of the Earth, demonstrated in Figure 8. Typical radio frequencies of operation are within L- to X-bands (1-10 GHz), transmitting EM waves of wavelength, λ_0, of 30 cm to 3 cm, respectively. For a detailed description of the SAR technique, the reader is directed to the comprehensive texts by Jackson & Apel (2004) and Henderson & Lewis (1998); however, a brief summary of instrument operation and current capability is presented here.
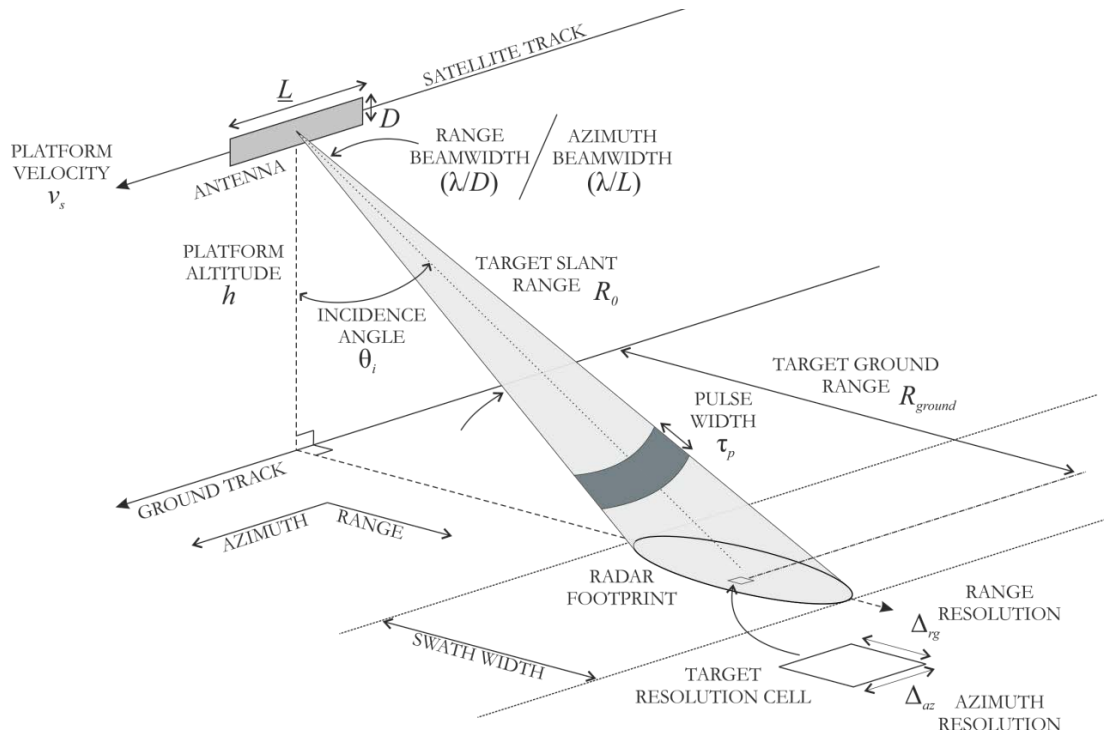
Figure 8. Observation geometry of side-looking radar.

It is important here to introduce a number of various terminologies used in the remainder of this report, and their implications for remote-sensing:

o *Spatial Resolution* defines the minimum distance at which two adjacent objects, or measurements, may be discriminated in an image – two features lying closer than this distance may be resolved individually and only one, single feature will be visible in the resulting image. This measurement typically forms one pixel of the final, (corrected) image, whereby two objects closer together will not be distinguishable from a single object. Where SAR may observe with a pixel resolution in the range 3-25 m (e.g. *TerraSAR-X* and *Envisat* respectively), supporting data of surface temperature may only be present with a much coarser resolution of around 1km pixel resolution.

o *Radiometric Resolution* is an instrument characteristic defining the accuracy to which a particular remote measurement can be made. The accuracy of the instrument to detect minute changes in the measured parameter is typically defined by the number of digital levels used to express measurements (more levels yields greater detail). A finer resolution permits greater discrimination between two data points with magnitudes separated by only a small variation.

o *Signal-to-Noise Ratio* (*SNR*) defines the ability of the instrument to measure a response over background noise generated by the instrument itself. A high SNR allows the instrument to detect reduced values of NRCS and to distinguish these detections from noise.

o *SAR Image Intensity* is the primary measurement of a SAR instrument. The basic measurements of a SAR antenna are in amplitude and phase; combining to derive a *complex image*. Through SAR processing, an *intensity image* is derived, which is the squared amplitude of NRCS across the observed scene.

o *Speckle* is a phenomenon associated with SAR which arises due to the coherent nature of the instrument. If the ocean surface, and the distribution of short waves upon it, is thought of as a collection of individual point scatterers, then it is possible that radar returns arrive at the antenna simultaneously but arising from different scatterers and pulses, thus possessing different phase values. When constructing a SAR image from the echo history, this means that these returns may add up constructively, or destructively, leading to a statistical (although appearing non-deterministic) variation in amplitude of the signal over the surface

which can degrade the clarity of the image. The effect of speckle can be reduced by averaging independent looks of the same scene, known as "multi-looking"; although this degrades the observed spatial resolution. For an example SAR image affect by speckle noise, see the *TerraSAR-X* image presented in Figure 7, which displays the characteristics 'salt-and-pepper' effect created by image speckle.

A Real Aperture Radar (RAR) antenna constructs a radar image through motion of the scene through the radar beam footprint, using the systematic phase change of the target's signal as it moves across the footprint to resolve the image. Azimuth resolution, Δ_{az}, is dependent on the product of the azimuth beamwidth and the slant range to target; hence azimuth resolution is diffraction-limited, requiring unfeasibly large antenna aperture size, of the order of a kilometre to achieve a resolution of around 25 m. Range resolution, Δ_{rg}, is dependent on the effective pulse width, τ_p, (with application of range compression), given by

$$\Delta_{rg} = \frac{c_0 \tau_p}{2} \tag{i}$$

where c_0 is the speed of an electromagnetic wave (in a vacuum). Discussion of radar operation and range compression may be found in Skolnik (1980) and Skolnik (1990).

The SAR technique improves the RAR limitations on azimuth resolution by exploiting the motion of the antenna platform, using the Doppler history of the pulse echoes backscattered to the radar to reconstruct the phase history via motion of the radar beam over a target area of the surface. This is made possible by the coherency (in-phase summation) of subsequent backscattered echoes measured at positions along a distance of the flight path, as shown in Figure 9. This process is known as aperture synthesis, yielding a synthetic aperture, L_{SA}, of perhaps 1-2 km in distance, which is significantly greater than the real aperture size, L, typically 10-15 m. The larger aperture size L_{SA} therefore creates a thinner (azimuth) beamwidth, and hence finer angular resolution compared with the instrument aperture (L) alone. This provides opportunity to obtain a fine azimuth resolution, Δ_{az}, which is independent of the target slant range, and related only to the size of the radar antenna (McCandless & Jackson, 2004):

$$\Delta_{az} = \frac{L}{2} \tag{ii}$$

This is theoretically valid at infinite slant range, but in practice limited by the available radar transmit power and the requirement for satisfactory reflected signal strength to be received by the

antenna. Range resolution for SAR is identical to that achievable through RAR, subject to the same requirements for range compression.
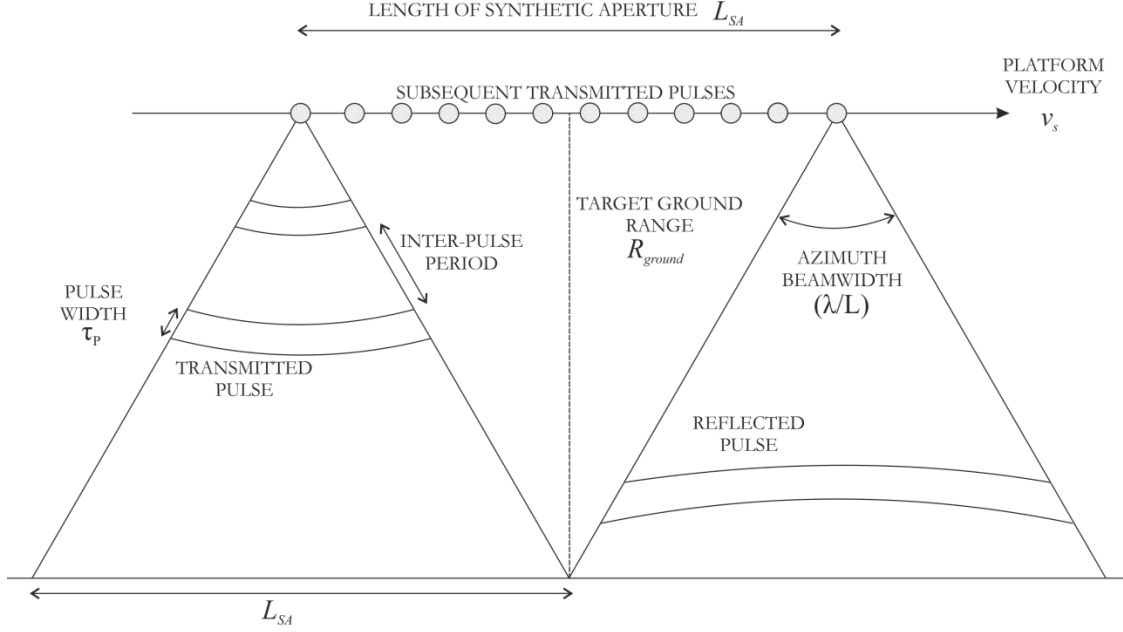
Figure 9. Principle of aperture synthesis.

At 1-10 GHz frequencies, radar waves do not penetrate into the ocean itself, but are instead scattered by the surface interface with the air. Smooth surfaces cause waves to be reflected specularly from the surface, in the manner shown in Figure 10, whilst rough surfaces cause components of the transmitted radar energy to be reflected back towards the radar antenna. For imaging of the ocean, SAR hence primarily measures the roughness of the sea surface at scales of 1-30 cm, measured in terms of the energy backscattered from the surface toward the instrument. The magnitude of this energy, with respect to the incident radar energy, determines the brightness of the surface in the resulting image. Broadly speaking, the Radar Cross-Section (RCS), σ, of an imaging radar is the effective area of a rough surface (or scattering object) which reflects radar power back to an antenna, and is a function of the ratio of scattered, E_s, to incident, E_i, radar energy as follows:

$$\sigma = 4\pi R_{sphere}^2 \frac{E_s}{E_i} \qquad \text{(iii)}$$

where the $4\pi R_{sphere}^2$ term represents the size of a perfectly-reflecting sphere (of radius R_{sphere}) which would produce the same strength of reflection as the surface; hence, RCS refers to a unit of area, in m². The amount of scattered energy is dependent on the geometric and electrical characteristics of the surface, such as the mean local slope of waves and dielectric constant of

seawater. The Normalised Radar Cross-Section (NRCS), σ_0 (also known as 'sigma zero'), is the RCS normalised by an area given by the power ratio

$$\sigma_0 = 10\log_{10}\left(\frac{\sigma}{A}\right) \qquad \text{(iv)}$$

where A is typically the area of an image pixel achieved by the instrument. NRCS is typically reported in terms of decibels, whereby the sigma zero power is the square of the processed image (amplitude) values[9]:

$$\sigma_0 \text{ (dB)} = 10\log_{10}\sigma_0 \qquad \text{(v)}$$

The Signal-to-Noise Ratio equation describes the power ratio between the echo signal received and the power level noise of the instrument:

$$\text{SNR} = \frac{P_{Signal}}{P_{Noise}} = \frac{P_T G_T{}^2 \lambda_0{}^2 \sigma_0 F_T{}^2 F_R{}^2}{(4\pi)^3 R_0{}^4 K_B T B_n} \qquad \text{(vi)}$$

where P_T is the transmitted signal power, G_T is the power gain of the transmitting/receiving radar antenna, F_T and F_R are the pattern propagation factors for antenna-to-target and target-to-antenna paths respectively, K_B is the Boltzmann constant ($= 1.38 \times 10^{-23}$ J°K^{-1}), T is the noise temperature of the receiving system and B_n is the noise bandwidth of the receiver's pre-detection filter.

An alternative terminology commonly used by antenna designers and operators is the Noise-Equivalent Sigma Zero (NESZ), measuring sensitivity to areas of low-backscatter. NESZ defines the RCS (sigma zero, σ_0) at which the received signal power is equal to the background noise, where SNR = 1; i.e. the minimum RCS which can be detected above the thermal noise floor. NESZ is given by the following relation, obtained by re-arranging the standard radar equation from Skolnik (1990). NESZ of a current spaceborne SAR is typically of the order of -20 to -30 dB[10].

$$\text{NESZ} = \frac{(4\pi)^3 R_0{}^4 K_B T B_n}{P_T G_T{}^2 \lambda_0{}^2 F_R{}^2 F_T{}^2} \qquad \text{(vii)}$$

Alignment of the antenna with the Earth's surface normal describes the polarisation of the waveforms it can transmit and receive: typically, SARs use linear polarisation, whereby the wave's

---

[9] Information from: http://www.eorc.jaxa.jp/JERS-1/en/GFMP/SEA-2A/docs/html/tutorial.htm; last accessed: 23/05/2013

[10] Information from: http://www.eorc.jaxa.jp/ALOS/en/about/palsar.htm; http://esamultimedia.esa.int/multimedia/publications/SP-1322_1/ (last accessed 15/02/2013)

electric field is aligned either with the horizontal surface plane (horizontally-polarised), or perpendicular to the surface (vertically-polarised). With H and V representing horizontal and vertical polarisation respectively, an antenna may be classified as 'HV' if it transmits horizontally-polarised pulses (represented by the first letter) and receives vertically-polarised ones (represented by the second letter). A typical quad-polarised antenna (e.g. *TerraSAR-X*) can transmit and receive both horizontal and vertical polarisations, allowing measurement in four polarimetric modes: HH, HV, VH and VV.

A range of scattering regimes, appropriate to the ocean surface, are presented in Figure 10. Bragg scattering is commonly the primary mechanism for radar backscatter from the ocean: assuming that radar waves at the ocean surface arrive approximately parallel, if surface roughness holds a scale of the order of the Bragg wavelength, λ_B, then the two reflected returns will arrive at the receiver aperture simultaneously. The critical (resonant) Bragg wavelength is related to the radar wavelength, λ_0, and the radar incidence angle, θ_i, by

$$\lambda_B = \frac{\lambda_0}{2\sin\theta_i} \tag{viii}$$

A schematic of the Bragg scattering regime is presented in Figure 11. Analogous to the theory of interference patterns in diffraction theory, multiple waves (from consequent transmitted pulses) arrive at the antenna simultaneously and coherently summate to yield a strong radar response. This is hence attributed to the target resolution cell from where the returns arose, causing it to appear 'bright' in the NRCS image. Increasing amounts of specular reflection (and reduced levels of diffused backscatter) are observed when the surface smoothens, as shown in Figure 10 (a). With respect to the ocean, there is typically little (pure) specular reflection of radar waves directly back to the antenna, except in the case of steep and/or breaking waves. A comprehensive discussion of the effect of radar/SAR imaging of ocean waves is presented in the text by Kanevsky (2009).
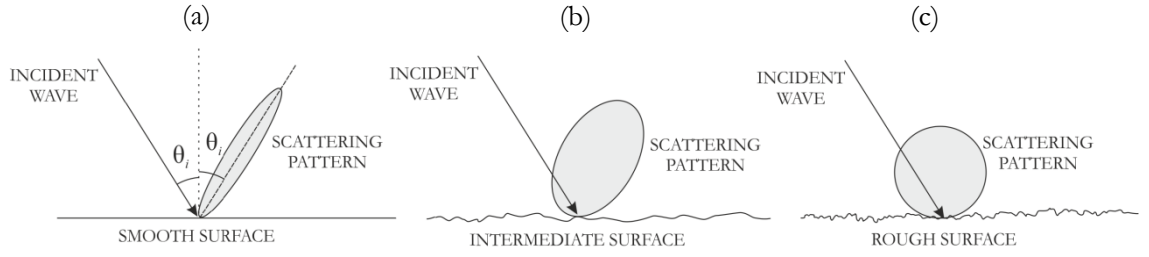
Figure 10. Surface scattering regimes: (a) specular reflection; (b) specular diffusion from intermediate surface; (c) isotropic diffusion from rough surface.
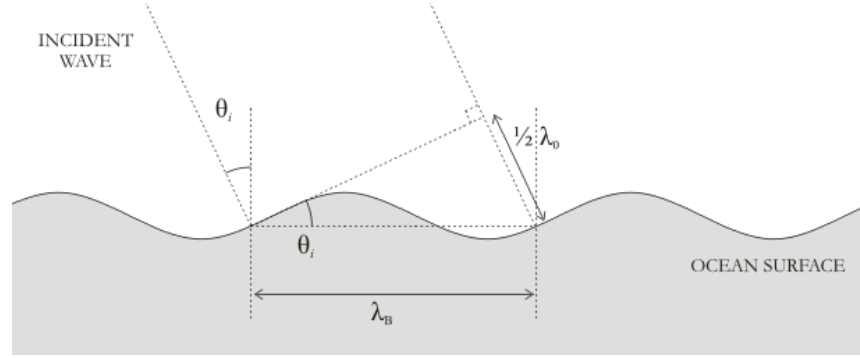
Figure 11. Bragg scattering regime at the ocean surface.

Whilst SAR observes purely the top-layer of the ocean (since water is opaque to EM waves in the microwave spectrum), underlying fluid motions affect the surface wave system, allowing these motions to become visible in the radar backscattering profile due to modulation of the background surface profile. The ocean surface is formed of a spectrum of superposed waves of varying wavelength: centimetre-level roughness is primarily driven by wind-generated capillary waves, which are distributed atop gravity waves with wavelength in the range of metres. Oceanographic phenomena (even sub-surface processes such as internal waves) are rendered visible due to their impact on the wave spectrum and hence on the distribution of Bragg-backscattering waves. Spatial variation of this pattern therefore causes bright and dark regions to form across the scene, denoting areas of wave-current interaction.

Contribution to the NRCS from Bragg scattering alone is defined by $\sigma_{0,\text{Bragg}}$; hereby referred to as 'Bragg NRCS'. The contribution of long waves (of wavelength 1 m and larger, typically gravity waves) is introduced in the local slope upon which the Bragg waves reside, modifying the radar energy which is scattered back towards the antenna: this is known as the 'Two-Scale' approach, and

the backscattering response of the combined system is the full NRCS, σ_0, taking account of the contribution of the whole wave spectrum to radar backscattering: this will hereby referred to as 'Composite Surface NRCS'.

The fine spatial resolution which can be achieved using the SAR technique is of considerable interest for all Earth remote-sensing applications, but is of particular benefit for satellite oceanography due to the ability to resolve small- (and at upper limit, intermediate-) scale phenomena which typical sea-surface height or temperature measurements may not capture adequately (although there are challenges posed by the motion of the ocean surface, which are addressed in §8.2). Active microwave operation also has the benefits of all-day/all-weather operation unhindered by solar illumination or cloud cover[11]. The primary ability of SAR which is relevant to this application, however, remains the sensitivity of NRCS to sea surface straining of capillary waves, which is a phenomenon not visible in high-resolution optical sensors but which may be generated by modulation of the surface by subsurface processes. Subsurface motions can hence influence the surface waves: NRCS modulation observed by SAR can provide insights into subsurface phenomena, capturing fluid motions that exist at depths which can be captured through electromagnetic penetration (of the ocean surface) alone – this explains why features of underwater bottom topography (e.g. sandbanks, shelves, etc.) are observed to produce surface effects, as summarised by Alpers et al. (2004).

The presence of O(10 m) turbulence (and similar flow features) have a twofold impact on the radar surface signature: firstly, the macro-scale ("integral-scale") flow structure causes wave-current interaction which strains the surface distribution of radar-scattering waves; and secondly, the presence of fine-scale turbulence and turbulent velocity fluctuations near the sea surface act to attenuate and redistribute surface wave energy at scales of the order of the radar wavelength through viscous dissipation and downward convection of wave energy (Kitaigorodskii and Lumley 1983, Kitaigorodskii et al. 1983). Where the integral scale causes modulation of the wave spectrum and disturbs the spatial distribution of Bragg-scale waves, the fine-scale turbulence extracts wave energy from the surface, causing the root mean square (rms) amplitude of the short surface waves to be attenuated and wave motions to be dampened. The observed result is reduced levels of Bragg scattering from short, centimetre-level waves and increased levels of specular reflection;

---

[11] Whilst this may be true in theory, a practical SAR instrument is subject to limitations which will prevent operation of the instrument at all times. Patches of rain may sometimes cause signal losses and attenuation (e.g. Melsheimer et al. [1998a]) and whilst SAR can, in principle, operate in any wind conditions, only a narrow window of viable ocean surface will deliver observable surface signatures (see §7.2 for further discussion of the effect of wind speed on active radar operation). Furthermore, active microwave instruments typically have high power demands which inhibit continuous, all-day operation from space.

demonstrated schematically in Figure 12. Hence, regions of fine-scale near-surface turbulence appear as low levels of NRCS and thus 'dark' in SAR imagery. This process was observed experimentally by Green et al. (1972), and later by Ölmez & Milgram (1992) who observed relationships between characteristics of turbulent mixing and decay in the amplitude of short, surface waves; details of these observations are addressed in Appendix D. Unfortunately, there has been limited experimental investigation on the impact of turbulence on short ocean surface waves, primarily due to the difficulty of measuring these effects operationally. Particularly in the case of ship wakes, turbulence is also associated with near-surface mixing that cause surfactant materials to accumulate at the sea surface to cause further dampening of short waves. The presence of surfactants and oil films floating on the sea surface can often disguise the effect of turbulence, due to their greater dampening impact on radar-scattering waves.
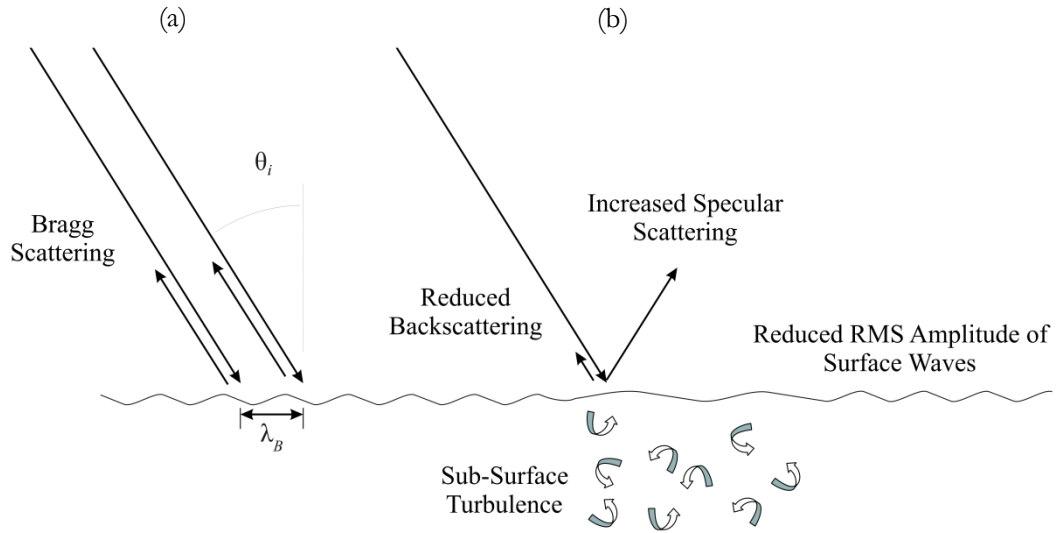
Figure 12. Effect of turbulence near the sea surface on radar backscattering of active microwaves.

The current state-of-the art in spaceborne SAR is represented by *TerraSAR-X*, developed by DLR and launched in 2007. The spacecraft operates a circular polar orbit at 514 km altitude, with a 4.8 m antenna operating at a frequency of 9.6 GHz (X-band). Spatial resolution of 3 m is achieved in StripMap mode, with up to 1 m resolution feasible in the High Resolution Spotlight mode. In 2010, a nearly-identical spacecraft, *TanDEM-X*, was launched into formation orbit of 250-500 m separation for Across-Track Interferometic (XTI) measurement and Digital Elevation Map (DEM) generation. Future SAR systems of note for ocean study include *ALOS-2* (JAXA, expected launch 2014) containing the *PALSAR-2* instrument operating a polarimetric L-band antenna; the *Sentinel-1* mission (ESA, expected launch 2014) with a dual-frequency antenna at C-/ Ku-bands and a multi-spacecraft constellation; and the *NovaSAR-S* (SSTL, expected launch 2015) spacecraft with a novel

S-band antenna. Preliminary results from these missions are eagerly awaited for the potential benefits for ocean SAR observation.

4.2 Review of Previous Simulation Studies

In the literature, a number of previous studies have considered integration of fluid modelling techniques with radar imaging algorithms to derive simulated remote-sensing signatures for various ocean phenomena. A review of the principal studies, associated with the scales of "small-scale" ocean phenomena which are considered here, and summarised in Table 4. A more comprehensive database of simulation studies and details of these studies are presented in Appendix C.

Fischer & Shuchman (1996) provide a comprehensive review of potential methods by which spacecraft remote-sensing may be employed to measure large-scale ocean convection (although relevant to other mesoscale/intermediate processes), and conducts a range of preliminary computational simulations in radar scattering. Focus is made on both the large-scale motions (using a 50 x 50 km fluid mesoscale model of Garwood, Isakari & Gallacher [1994]) and small-scale activity (using a 6 x 6 km LES model) which is associated with deep convection events, and how both components may be resolved by imaging radar. Results from the ERIM ocean model (*ERIM*) simulate the surface signatures likely to manifest from convective plumes, how they may appear in SAR images and how such signatures may be identified in future high-resolution SAR imagery. This work was later extended and expanded by Fischer et al. (1999), demonstrating further computational study using ocean radar imaging models to simulate the radar scattering characteristics of convective surfaces. The authors draw some conclusions about the applicability of simulations to real SAR data and expectations of the performance of future SAR systems (at time of publication) such as *TerraSAR-X*. Simulations are performed for a range of spaceborne (*ERS-1, RADARSAT-1, JERS-1*) and airborne (3000 m altitude, 200 ms^{-1} flight velocity, HH/VV-polarisation, $\theta_i = 30/40/50°$) cases, and for 1/3.5/10 ms^{-1} wind speeds. The authors considered values of mean NRCS, and maximum contrast of NRCS, across transects of the simulated images made in the range direction.

Following the visibility of internal waves in radar images obtained by the *Seasat* mission, there has been significant interest in the observation of internal wave structures within radar images attained from space, and hence in radar backscatter simulation of such features. Lyzenga & Bennett (1988) provided an early basis in internal wave detection theory using one-dimensional fluid and radar backscatter simulations; employing a composite surface approach using a 500 m spatial grid

comprising 120 grid points, and a 150-k wavenumber grid with 24-θ directional grid. Shuchman et al. (1985) considered the effects of underwater bottom topography on surface radar signatures using a first-order wave-current interaction/radar backscatter model (forerunner to the *ERIM* model) computing a two-dimensional grid (of dimensions 25 x 25 km with grid spacing of 20 m) of surface currents arising from topographic variations on the ocean floor. The authors compare the relative change in NRCS across the ocean floor feature with data from *Seasat*, noting favourable comparisons in the observed spatial variation of radar backscatter.

With regards to radar signatures of turbulent ship wakes, studies performed by Lyden et al. (1985) and Lyden et al. (1988) represented first efforts towards uniting simulation results with SAR observation data. These early efforts attempted to understand the complex ship wake system in radar imagery, focussing on aspects of the turbulent, vortical wake and on ship-generated internal waves. In particular, these studies compared cross-wake variations in theoretical and measured radar backscatter values – as demonstrated in Figure 13, from Lyden et al. (1988) – based on surface currents derived from the vortex model of Swanson (1984), showing good comparison between observations and results predicted by the simple theory. Further progress was made in studies by Reed et al., (1990), True et al. (1993), and Milgram et al. (1993) which sought to explain the "dark scar" that was typically observed in a ship's turbulent wake trailing by considering the effect of fine-scale turbulence & velocity fluctuations on surface backscattering waves: such studies were progressed by modifying reference terms in the wave energy balance calculation to account for the effect of fine-scale turbulence on the dissipation of wave energy (discussed in more detail in Appendix D). In particular, such studies attempted to examine the effects of turbulent dissipation on radar backscatter (as shown in Figure 14 from True et al. [1993]) and understanding the role that turbulence plays in suppressing short-wave amplitudes, in the context of other factors such as wind conditions and presence of surface films. Recent studies of ship wake radar signatures have been performed by researchers at Nova Southeastern University and published by Fujimura & Soloviev (2009), and Fujimura et al. (2011). In this work, a Detached Eddy Simulation model using the commercial Computational Fluid Dynamics (CFD) software FLUENT was operated to derive a surface wake behind a 6 m ship model travelling at 10 ms^{-1} and to examine the wind-stress effect on radar backscattering: results are presented for surface currents demonstrating speeds of up to 0.3 ms^{-1}, with a numerical grid of 50 x 50 m used to calculate radar backscatter signatures at grid spacing of 0.5 m (x) and 0.2 m (y). In Fujimura et al. (2010), a 7.5 m ship travelling at 5.14 ms^{-1} was used in conjunction with a pair of counter-rotating vortices (radius 2.5 m and angular velocity 0.08 rads^{-1}).
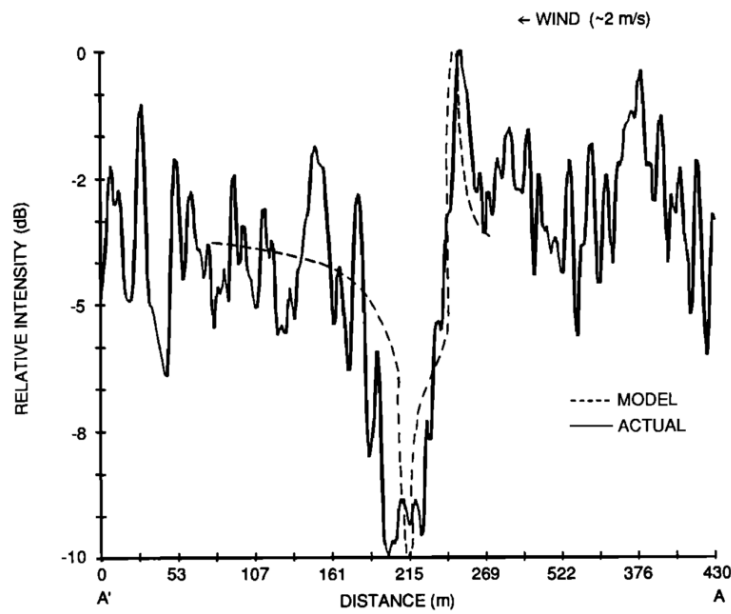
Figure 13. Comparison of predicted radar backscatter variation based on vortex model (dashed line) and actual backscatter measurements (solid line); from Lyden et al. (1988).
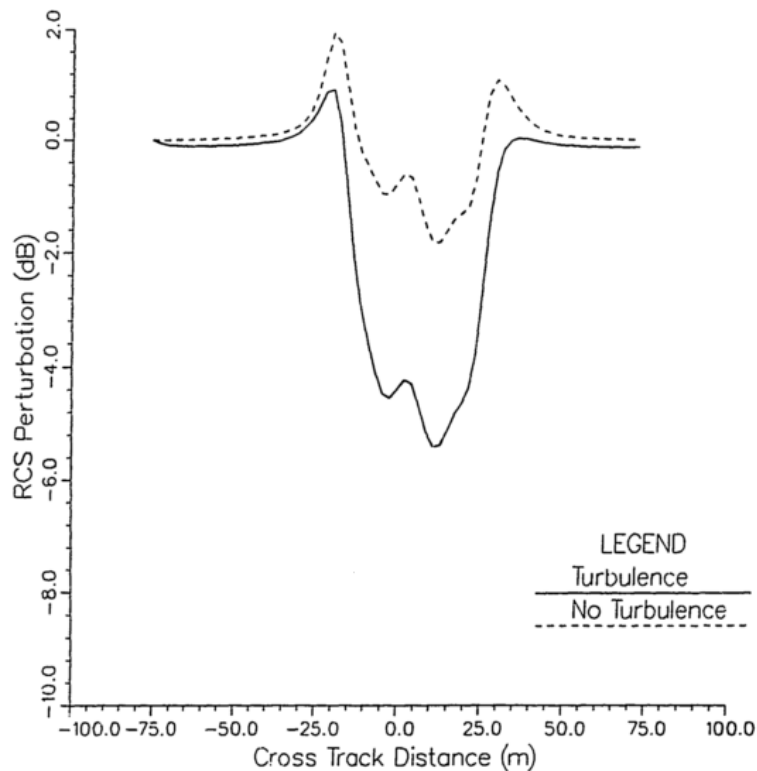
Figure 14. Example of a transect of NRCS profile for a simulated ship wake with (solid line), and without (broken line), turbulent dissipation applied to the wave energy balance; True et al. (1993).

Source	Phenomena/ Process	Applied Radar Model	low Feature Data	Additional Info.
Lyden et al. (1985)	Ship Wake	*ERIM*	Max. current 0.12 ms^{-1}; max. gradient 0.03 s^{-1}	Simulations performed to match measurement campaign from the US Navy tug *Quapaw* of 5 kT military ship and 500 kT supertanker. 800 m horizontal distance, 180 m (cross-wake cut of vortex model); 3 m grid spacing
Lyzenga & Bennett (1988)	Internal Waves	*ERIM*	Max. current 0.42 ms^{-1}	Spatial grid 500 m, 120 grid points; 150-k wavenumber grid, 24-θ directional grid
True et al. (1993)	Ship Wake	*ERIM*		1-D simulations (cross-wale cut); ship velocity 9.26 ms^{-1}. Spatial grid 150 m (1-dimensional); 300 grid points (x), 128 (y); 48-k wavenumber grid (0.01 < λ_w < 50); 12-θ directional grid
Fischer et al. (1999)	Oceanic Convection	*ERIM*		Convection depths 1000 m, 2000 m; surface heat fluxes 200/400 Wm^{-2}; LES model of Garwood et al. (1994), and mesoscale model applied: spatial domain 6 x 6 km (LES), 50 x 50 km (mesoscale); grid spacing 50 m (LES), 98 m (mesoscale)

Table 4. Comparison of (selected) similar simulation strategies extracted from the literature. A full database of similar studies is presented in Appendix C.

Source	Phenomena/ Process	Applied Radar Model	low Feature Data	Additional Info.
Fujimura & Soloviev (2009)	Ship Wake	M4S	Max. current 0.3 ms⁻¹; max. gradient 0.08 s⁻¹	Nominally examining the wind-stress effect. FLUENT non-hydrostatic model Detached Eddy Simulation: 18750000 cells; 10 ms⁻¹ ship (length 6 m), model complete with hull and propeller. Spatial grid 50 x 50 m; 0.5 m grid spacing (x), 0.2 m grid spacing (y)
Fujimura et al. (2010)	Ship Wake	RIM	Uncertain. "Less than 0.1 ms⁻¹"	Nominally examining the wind-stress effect. FLUENT non-hydrostatic model: 240000 cells; 5.14 ms⁻¹ ship (length 7.5 m, beam 10 m). Pair of
Fujimura et al. (2011)	Ship Wake	M4S		<see Fujimura & Soloviev (2009)>

Table 4 (contd). Comparison of (selected) similar simulation strategies extracted from the literature.

A full database of similar studies is presented in Appendix C.

4.3   The Proposed Technique

In this research, an applied simulation strategy was employed to simulate radar surface signatures of ocean turbulent processes. The strategy was initiated to examine the coupling of ocean radar imaging models with numerical turbulence methods; applying integrated hydrodynamic-electromagnetic wave interaction models (hereby referred to as ocean radar imaging models) and fluid simulation techniques to a range of turbulent ocean phenomena. Using CFD software to simulate dynamics of a fluid allows turbulent flows to be generated numerically, and for complete knowledge of all conditions of the flow to be obtained at every point, and at all times within the simulation.

Typical ocean radar imaging models approximate the interaction of the ocean surface with a spatial current generated by some disturbance. Due to concurrent research being pursued within the Aerodynamics & Flight Mechanics Research Group at the University of Southampton regarding (direct) numerical simulation of turbulence, there was opportunity to operate the group's numerical codes for generation of turbulent flows through DNS. In previous simulation studies (which were reviewed in the preceding section), there has been no application of research of this type, using DNS in integration with ocean radar imaging models, to simulate small-scale turbulent flows. Previous investigations considering CFD-derived turbulence and/or vortical motion on wave-current interaction and radar backscattering have operated Large Eddy Simulation (LES)-type model, or commercial CFD models such as FLUENT, to derive the input surface velocity data. In addition, previous work has rarely considered such small-scale phenomena: while there have been studies of the radar signatures ship wake, no study of this type has been pursued with the focus on the measurement capability of resolving turbulence and flow characteristics alone, but have focussed more on considering the whole ship wake system. In this research, attempts were made to isolate the problem of turbulent wave-current interaction to further understand the role that turbulence (and turbulence-derived surface currents) may play on radar backscattering. In this respect, a key novelty of the current research lies in understanding how DNS may be applied to the ocean radar simulation process, and in use of high-resolution numerical flow data in tandem with standard ocean radar imaging models.

The approach adopted in this research took inspiration from the similar study described by Fischer et al. (1999), incorporating computation of numerical fluid turbulence and application of ocean radar imaging modes to develop surface signatures of ocean turbulence and subsequently examine feasibility of observation with SAR. The adopted strategy formed a critical part of a complete end-to-end system to assess the dependency between surface and subsurface turbulence and

configuration of a radar instrument to maximise observation capability. An overview of the simulation process is shown in Figure 15. The strategy is formed of three primary segments: firstly, numerical simulation of small-scale turbulence in the near-surface layer of the ocean and its propagation to the sea surface (and surface signature) [Phase *I*]; secondly, derivation of surface radar signature of the turbulent phenomena in Bragg and composite surface NRCS using ocean radar imaging models [Phase *II*]; and finally, post-processing/analysis of signatures to quantify the NRCS response and the ability to extract information about the surface profile from the character and of the NRCS surface profile [Phase *III*]. This final phase also included expansion from pure NRCS calculations to derive remote-sensing signatures in the context of varying observation conditions, and simulation of theoretical SAR images affected by motion effects and speckle noise.

The strategy comprises integration of a number of numerical models to perform the functions described by Phases *I-III*: in the following subsections, these numerical models are described and developed. Development of this integrated model was also associated with addressing the unique problems/challenges in NRCS simulation, integration of high-resolution (turbulent) current profiles with standard ocean radar imaging and development of simulations links between a number of different modelling/simulation processes. A testing strategy was initiated to identify and address some of these challenges in order to establish candidate phenomena for further study, and this process is discussed in Chapter 5.

The current approach differs from previous studies into ocean radar backscattering signatures, in that the primary goal of the research was to establish how turbulence (and turbulent flow structure) may be revolved in high-resolution SAR images, and to understand the instrument and ambient conditions which may assist in characterising such motions.

PHASE:

Generation of Turbulence
and Propagation to the Ocean Surface

I

Tools: Direct Numerical Simulation

Wave-Current Interaction and Derivation of
Modulated Wave Spectra

Tools: M4S, RIM

II

Normalised Radar Cross-Section Simulations
and Derivation of Radar Surface Signatures

Analysis of Radar Surface Signatures
and Qualitative Evaluation of Resolved
Flow Structure

III

Examination of Effect of Varying Instrument
& Ambient Surface Conditions

Draw Conclusions on Capability of Future
SAR Instruments and Recommendations

Figure 15. End-to-End simulation chain, simplified diagram.

4.3.1 Direct Numerical Simulation of Surface Wake Turbulence

DNS is a technique for computational fluid dynamics which is employed to capture all scales of the turbulent flow without the need for subgrid modelling (for example, as is necessary for a Reynolds-averaged Navier-Stokes closure). In a DNS, all scales are simulated in both space and time, providing complete knowledge of the characteristics of the flow at all times and at all points in the spatial domain. Of course, this places obligations on computation that numerical errors are strictly monitored and controlled. Whilst such simulation has many benefits for awareness of the whole flow, drawbacks of the DNS method lie in computational cost and in limitations on the maximum Reynolds number, Re_{DNS}, which can be calculated numerically by the method. Reynolds number is given by:

$$\text{Re}_{DNS} = \frac{U_{DNS} L_{DNS}}{\nu_{DNS}} \qquad \text{(ix)}$$

where U_{DNS} and L_{DNS} and representative velocity, and length, scales in DNS respectively, and ν_{DNS} represents the kinematic viscosity of the fluid in the DNS. The limitation in Reynolds number arises due to the very fine spatial grids required to satisfy resolution requirements for capturing turbulence down to dissipative scales. Typically, the number of floating-point operations for a single simulation scales with Re_{DNS}^3 (Coleman & Sandberg, 2010), hence computational performance is limited to specific Reynolds number, typically of the order of $\text{Re}_{DNS} = 1000$. The simulation must be progressed in time using an explicit method to maintain stability in the context of the very high memory requirements of the computational process. An introduction to the background, methods and procedures of DNS are presented by Moin & Mahesh (1998).

To perform a DNS computation, one must characterise the Reynolds number and desired time and length scales present in the flow. Initially, U_{DNS} , L_{DNS} and ν_{DNS} are defined, thus deriving a reference Reynolds' number for the simulated flow. Typically, the characteristic velocity scale of the simulation will be selected as the free-stream velocity $(U_{DNS}, 0, 0)$, such that the flow is normalised between 0 and 1, where values of 1 are achieved in the freestream and values < 1 appear in regions of drag and turbulence. All velocity data in the simulation are hence typically normalised by the freestream velocity, whereby:

$$\boldsymbol{u} = \left(\frac{u}{U_{DNS}}, \frac{v}{U_{DNS}}, \frac{w}{U_{DNS}} \right) \qquad \text{(x)}$$

A characteristic length scale, equivalent to the largest scales expected to be present, must also be defined. The DNS numerical algorithm then solves the incompressible Navier-Stokes equations for fluid velocity, $\boldsymbol{u} = (u, v, w)$, which are given in Cartesian tensor notation by

$$\frac{\partial u_i}{\partial t} + u_j \frac{\partial u_i}{\partial x_j} = -\frac{1}{\rho} \frac{\partial p}{\partial x_i} + \nu \frac{\partial^2 u_i}{\partial x_j \partial x_j} + F_i \qquad \text{(xi)}$$

where $i = (x, y, z)$, ρ is the fluid density, ν is the kinematic viscosity, t represents time, F_i represent external forcing terms, p is the fluid pressure and $u_i = (u, v, w)$ represents velocity in the coordinate system given by i.

To represent the solid surfaces of the surface vessel through application of body force terms, immersed boundary methods can employed to introduce characteristics of external bodies into the flow; an introduction to such methods is presented in the review article by Mittal & Iaccarino

(2005). "Body force" terms are introduced to mimic 'real' objects in a flow, though the 'body' of its title does not refer to the physical body of the object, but to a 'body' of gravity which causes the flow to slow down and initiate some turbulent flow. Hence, this technique replicates a distributed force, whereby the numerical code itself defines how the force is distributed in order to describe the shape of the object and the strength with which it obstructs the flow. Body forces enter the Navier-Stokes equation through the F_i term in Equation (xi), representing the contribution of external forces to the fluid system. The drag force imparted by a simple spherical body on the computational grid is described by a three-dimensional Gaussian function of the form (Rojanaratanangkule et al., 2012):

$$F_i = -\frac{J_{IBM}}{\left(\delta_{IBM}{}^2\pi\right)^{3/2}}\exp\left[-\frac{r_{IBM}{}^2}{\delta^2}\right] \tag{xii}$$

where δ_{IBM} is the Gaussian half-width, J_{IBM} is the forcing intensity and the term $r_{IBM}{}^2 = (x - x_0)^2 + (y - y_0)^2 + (z - z_0)^2$ describes a spherical body with centre location at (x_0, y_0, z_0). δ_{IBM} represents the width of Gaussian profile where the level of forcing is one-half of the maximum forcing, typically equivalent to the radius of the sphere. The force acts in the x-direction (upstream) direction only, although the body force itself is three-dimensional to replicate an object embedded in the flow. Integration of the F_i term over the whole volume gives the forcing intensity, J_{IBM}, i.e.

$$J_{IBM} = \int_{dV} F_i dV \tag{xiii}$$

where V represents volume of the domain. Outputs of the non-dimensional simulation are written to disk at specific user-selected time steps, and comprise of three-dimensional velocity (u, v, w) and pressure (p) data at each grid point of the domain. From this data, the surface velocity profile is extracted and converted to dimensional values reflecting real-world comparison. This profile represents the disturbance on the surface caused by surface/subsurface turbulence, which is processed by ocean radar imaging model to simulate the radar backscattering characteristics due to the turbulent flow.

4.3.2 Propagation of Waves in Presence of a Disturbing Current

To calculate the modulation of the ocean surface due to ocean currents, waves and turbulence, current generations of radar imaging models exploit the theory of weak hydrodynamic theory (under the Wentzel-Kramers-Brillouin approximation, hereby 'the WKB approximation'; which

assumes that spatial variations of wavelength are gradual) and Conservation of Wave Action (hereby 'CWA theory') introduced by Whitham (1965), Bretherton (1966) and Phillips (1966). Wave action spectral density, $N(\boldsymbol{k})$, is often used to calculate the evolution of ocean waves since, unlike energy spectral density (which is not conservative), it is a quantity conserved by an ocean wave system which is modulated by the presence of surface currents and is an adiabatic invariant. It therefore represents a useful parameter by which the effects of spatial current changes on the ambient wave spectrum may be calculated. Wave action spectral density is defined by:

$$N(\boldsymbol{k}) = \frac{E(\boldsymbol{k})}{\omega} \tag{xiv}$$

where spatial energy spectral density, $E(\boldsymbol{k})$, divided by intrinsic wave frequency (in a frame of reference moving with the flow), ω. An equation for the transport of wave action may then be written analogously to the Boltzmann transport equation, e.g. Phillips (1977):

$$\frac{\partial N(\boldsymbol{k})}{\partial t} + \left(c_{g,i} + u_i\right)\frac{\partial N(\boldsymbol{k})}{\partial x_i} - k_j \frac{\partial u_j}{\partial x_i}\frac{\partial N(\boldsymbol{k})}{\partial k_i} = S(\boldsymbol{k})\frac{1}{\omega} \tag{xv}$$

where $c_{g,i}$ represents the group velocity of wave component in the ith direction and $\boldsymbol{k}$ is the wavenumber vector of the waves of interest. The right-hand-side of Equation (xv) contains the term $S(\boldsymbol{k})$, which represents the sum of the contributions from external phenomenon which provide energy exchange to, or from, the wave-current system: these include energy input from the wind, energy exchange between different wave scales and energy dissipated (and output of energy from the wave-current system) by breaking waves. $S(\boldsymbol{k})$ are typically referred to as 'source/sink' terms due to their influence as sources and sinks of wave energy. For a complete description of wave action theory and its implementation in ocean radar imaging models, the reader is directed to papers by Jansen et al. (1993), Romeiser & Alpers (1997) and Kudryavtsev et al. (2005). In this respect, interaction of surface turbulence with the waves is addressed indirectly by considering the effect of the current field on the surface waves which the turbulent disturbance is assumed to induce. For calculating the modulation of surface wave spectrum by presence of surface currents and turbulence, a (modulated) directional wave spectrum is derived; that is, the spectrum modulated by wave-current interaction.

Calculation of wave-current interaction within a typical model requires data input of the current profile of the surface current and the ambient wind profile (speed and direction). The current profile, extracted from surface DNS profile, is defined at each point on a surface grid, in either two-dimensional (u and v) or three-dimensional (u, v and w) velocity components, dependent on the

radar imaging model which is being operated. For this study, a MATLAB code was written to extract the surface profile from the DNS results (stored in .bin files) and convert the profile into the file format(s) required to input data into the applied models; .txt (text file) and .mat (MATLAB data file). Wind conditions are defined in a similar manner, with wind velocity components (u_{wind}, v_{wind}) defined at some reference point above the surface, typically 10 m. In this respect a spatially-varying wind may be applied, however for all results presented in this thesis a uniform (spatially-invariant) wind field was assumed.

During calculation, the applied model computes interaction of the surface current with the 'ambient' or 'background' wave spectrum which exists away from the disturbing current; in the process, generating a large data file containing the modulated wave height spectral density at each grid point on the surface, for each wavenumber of the spectrum and in a set number of wave propagation directions. Standard models typically deliver wave height spectral density for around 100 wavenumber bins and 24 propagation directions, delivering 2400 density values per grid point in the simulation. The models operated in this research are described in full in §4.4.

4.3.3   Radar Backscatter Modelling

Scattering of incident radar waves by the Bragg mechanism is the dominant backscattering method during microwave interaction with the sea surface. The Bragg scattering theory developed by Wright (1968) provides:

$$\sigma_{0,Bragg} \cong 8{k_0}^4 \iint \left|G_{pq}(\theta_i, \alpha, \phi)\right|^2 \psi(k_B)P(\alpha, \phi)d\alpha d\phi \qquad \text{(xvi)}$$

$$k_B = 2k_0 \sin\theta_i \qquad \text{(xvii)}$$

where θ_i is the radar's angle of incidence, G_{pq} represents the polarisation scattering coefficient for $p = \text{H, V}$ transmit (horizontal and vertical) waveforms and $q = \text{H, V}$ receive waveforms, and $P(\alpha, \phi)d\alpha d\phi$ represents the probability that two-dimensional surface tilt angles (α and ϕ) lie within specific limits. This theory proposes that the Bragg NRCS, $\sigma_{0,Bragg}$, is proportional to the wave height spectral density, $\psi(k_B)$, of the Bragg-scale waves (of wavenumber k_B; wavelength λ_B) which provide a strong scattering response to radar waves of wavenumber k_0. The wave height spectrum, (k) , can be calculated from the wave action, whereby

$$\psi(\boldsymbol{k}, \boldsymbol{x}, t) = \frac{N(\boldsymbol{k}, \boldsymbol{x}, t)}{\rho\omega(k)}k \tag{xviii}$$

For modelling applications, the wavy ocean profile is approximated as a series of planar facets which are used to calculate model microwave scattering from the surface; a procedure which is described by Romeiser & Alpers (1997) for the *M4S* ocean radar imaging model. For the facet-based geometry, pure Bragg scattering can be simplified to

$$\sigma_{0,Bragg} = 8\pi k_0{}^4\cos^4\theta_i\big|G_{pq}(\theta_i)\big|^2[\psi(\boldsymbol{k_B}) + \psi(-\boldsymbol{k_B})] \tag{xix}$$

whereby only surface waves with the (vector) wavenumber, $\boldsymbol{k_B}$, contribute to the scattering: only waves at the Bragg wavenumber, travelling in the radar look direction (either toward or away from the range direction of the instrument), contribute to the pure Bragg scattering response. Since side-looking radars possess a finite range/elevation beamwidth that allows the instrument to cover a swath of the ocean surface (as shown in Figure 8), θ_i varies from near-range to the far-range, and therefore a variation in the observed Bragg wavenumber in range direction of the derived image.

In reality, the ocean is formed of a variety of wavenumbers which superimpose to generate the ocean wave spectrum: short Bragg-scale waves 'ride' on the motions of longer waves (primarily gravity waves), which can act to 'tilt' the orientation of the Bragg waves and hence modulate the radar response. The composite surface NRCS σ_0 accounts for presence of 'tilt' modulation by including long-wave components of the wave spectrum, expanding the complex scattering coefficient, G_{pq}, to account for surface tilt slopes (α and ϕ) according to Romeiser et al. (1997):

$$\sigma_0 = 8\pi k_0{}^4\cos^4\theta_i\big|G_{pq}(\theta_i, \alpha, \phi)\big|^2[\psi(\boldsymbol{k_B}) + \psi(-\boldsymbol{k_B})] \tag{xx}$$

4.4   Description of Numerical Codes

4.4.1   CgLES

The DNS code operated in the study was a C/C++ fixed boundary code entitled *CgLES* supplied by Dr. T. Glyn Thomas (University of Southampton); further details on the model described by Thomas & Williams (1997). The code solves the incompressible Navier-Stokes equations using an efficient parallel multi-grid technique, and is optimised to run in parallel over large numbers of processors. Based on the specified input and boundary conditions and application of body forces, the code computes the numerical flow for a specified number of time-steps, and outputs the

velocity (in three dimensions) and pressure data (u, v, w, p) at each grid point in the domain. u-velocity is specified in the x-direction (direction of the applied freestream flow), v-velocity in the y-direction (perpendicular to freestream, in the surface plane) and w-velocity in the z-direction (normal to the ocean surface, i.e. depth). The algorithm solves with sufficient numerical accuracy to represent all turbulence scales (Thomas and Williams, 1997; Archer 2008). A projection method based on a second-order explicit Adams-Bashforth scheme is used to advance the solution in time, and a multi-grid method solves for the pressure term. The code advances through time whereby the Poisson equation is solved at the current time step, the velocity updated, and the simulation is then advanced explicitly to the subsequent time step.

The operated code assumes a 'rigid lid' to the surface of the fluid domain to improve computational speed, meaning that the surface will does not deform in the presence of disturbances. Deviations from a flat surface may, however, be approximated by applying the hydrostatic approximation to the pressure data at the surface layer, through

$$\Delta z = \frac{p_z}{\rho g} \qquad \text{(xxi)}$$

where ρ is the density of water, Δz is the deviation in surface height and g is the acceleration due to gravity.

4.4.2   *M4S*

The primary radar imaging algorithm operated in this research, performing combined functions of wave action modelling and radar backscatter simulation, was that of the M4S Toolkit v3.2.0 (hereby *M4S*) supplied by Prof. Roland Romeiser (University of Miami, USA). The model is based upon weak hydrodynamic interaction theory in the "relaxation time" approximation, and is distributed as an executable file, allowing no direct manipulation of the source code. The model is formed of two modules: M4Sw320, which calculates the modulated wave spectrum in the presence of disturbing currents and wind forcing; and M4Sr320, which takes the wave spectrum file from M4Sw320 as input to calculate both the Bragg NRCS and the Composite Surface NRCS based on user input of the radar parameters (frequency, polarisation) and observation geometry (altitude, incident angle, look direction, etc.). Specification of the radar operating frequency f_0 (GHz), incidence angle θ_i (degrees), instrument polarisation (HH/HV/VH/VV), and look direction with respect to the x-axis (defined in degrees) are required in the *M4S* batch file to compute the NRCS backscatter response.

NRCS data is output as a binary data file, and batch files were written to compute multiple executions of M4Sw320 and M4Sr320 and to store the resulting binary files to disk, allowing computations to be processed without user involvement. Further data can be calculated by M4Sr320 to display Doppler information, simulate SAR imagery based on the radar backscattering cross-section or process simulated interferometric images where the relevant input data has been provided. Romeiser & Alpers (1997) and Romeiser et al. (1997) discuss the theory which support the model algorithm. Operation of the M4S tool (and description of the numerical software) is document in the comprehensive user guide of Romeiser (2008).

M4S uses an 'expectation-value'-type model to derive simulated full SAR images based on the calculated backscatter profile and the Doppler characteristics of the antenna platform and ocean surface, accounting for image noise. This procedure yields the ensemble-averaged value of image intensity whereby the Doppler spectrum of the surface reflectivity is computed at each grid cell and used to "map" the NRCS onto the SAR image using the Doppler spectrum to control the mapping. A summary of this procedure can be found in Lyzenga (1986).

4.4.3   Visualisation Tool (*DNSR*)

To visualise the simulated images derived by *M4S*, a MATLAB code was written to display NRCS data on-screen and to generate data and statistics, known informally as *DNSR* (DNS-to-Radar NRCS visualisation tool). The code was modified to allow functionality to be operated by a Graphical User Interface (GUI), shown in Figure 16, permitting the user the view and switch between simulated NRCS images derived using the ocean radar imaging models. For both models, the new tool was required to extract information on the simulated radar configuration, wind and model parameters from *M4S* input data files in order to display both the derived radar signature and the simulated conditions on-screen.

For displaying images derived from *M4S*, the *DNSR* tool extracts NRCS data stored in the *M4S* output binary files, and display it as an intensity image of the simulated scene. The tool maps the NRCS data to the correct grid by extracting the surface grid from input current file, and extracts instrument (and scene) information from the M4S input batch file. The code also allowed 'switching' between various output results (such as Doppler imagery, SAR image intensity), and to visualise the input current fields submitted to the radar model: this allowed wind and wave data to be visualised (as vector plots of u-, v- and w- components of the input current profile) and layered over NRCS results to aid in qualitative observations of flow structure. Additional features were supplemented to the tool to allow qualitative data to be derived about the NRCS signature under

scrutiny: this included quantifying mean NRCS (across a single range line, and over the whole image); contrast with the background NRCS of the ambient water; variation of NRCS across the signature; etc.). The MATLAB code was also written to examine points of interest in the output wave spectrum, to further understand modulated wave spectrum values.
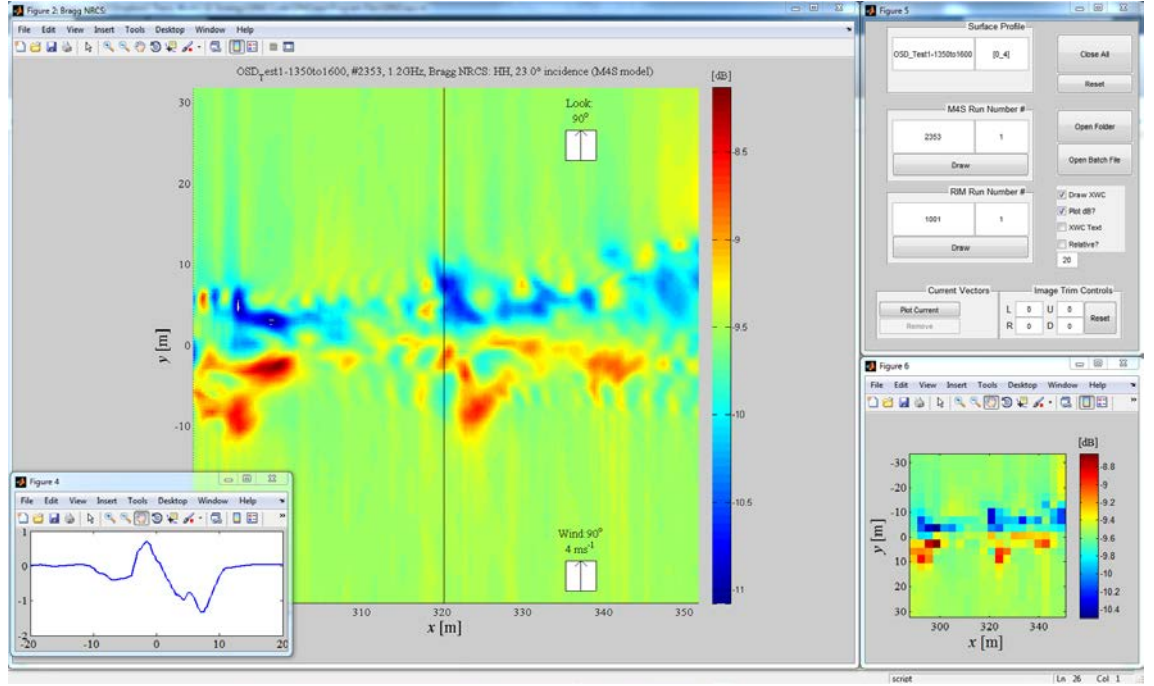
Figure 16. Example screenshot of the MATLAB *M4S* visualisation tool (*DNSR*) and graphical user interface running on Windows 7. The tool allows the user to display calculated NRCS signatures, derive transects of NRCS across the domain and produce images affected by coarse spatial resolution.

4.4.4   Summary

The overall strategy was conceived to form part of an integrated end-to-end simulation tool, beginning with derivation of surface wake velocity profiles using DNS and culminating with analysis of surface signatures under a variety of ambient and observation conditions. The primary simulation models (*CgLES*, *M4S*, *DNSR*) were manipulated to work on combination, deriving an integrated simulation chain to simulate the effect of high-resolution turbulent flow on radar backscattering. An in-depth schematic of the flow of data and information through the system is displayed in Figure 17.

PHASE:
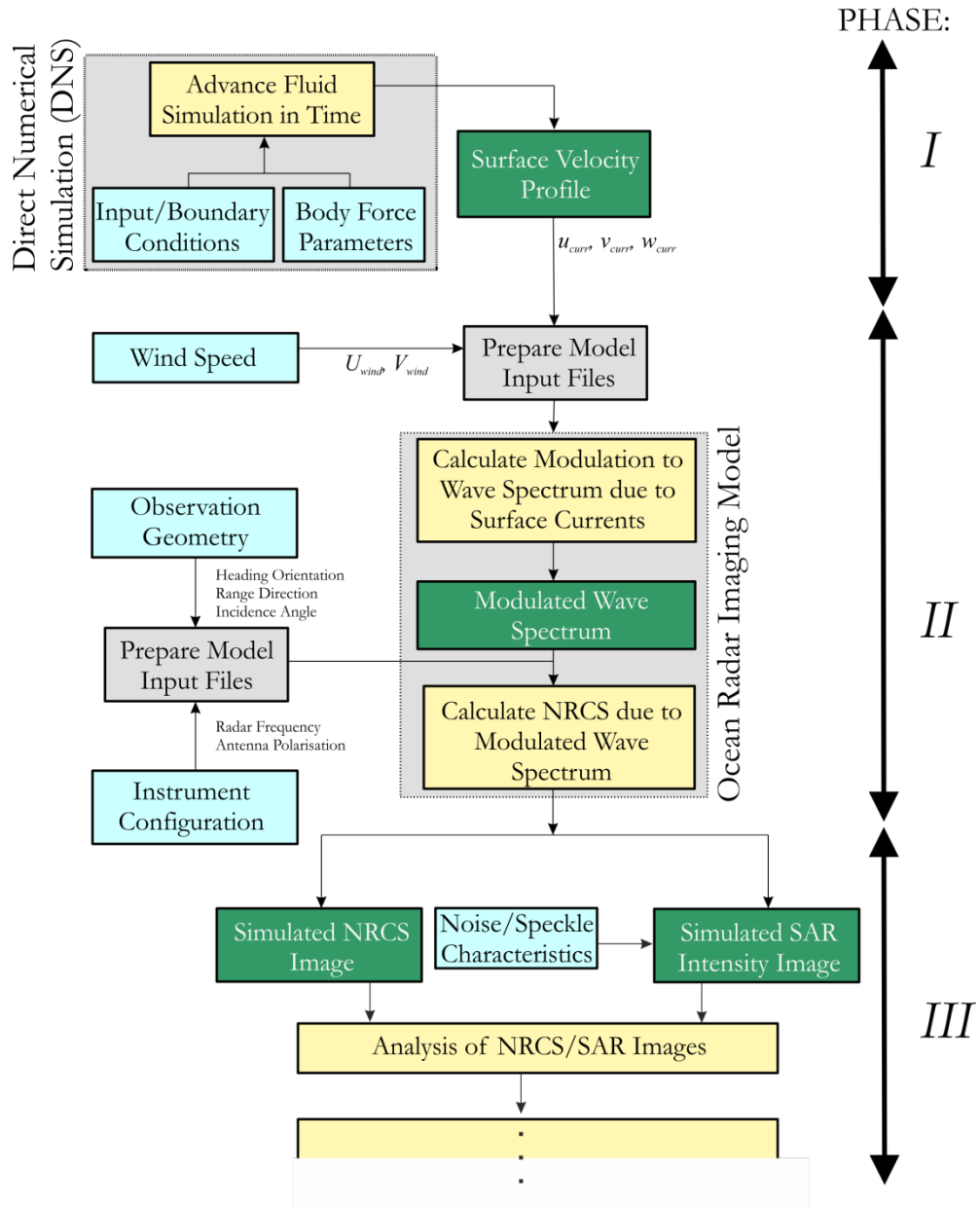
Figure 17. Data flow within the simulation model.

5. NRCS Simulation of Surface Wake Turbulence

5.1   Introduction

Following an exploratory period of testing, the case of turbulent currents embedded in a surface wake was selected as an investigation into a historically well-observed radar phenomena, and one which would provide insight into the response of radar backscatter to (at some points, intense) regions of small-scale turbulence. Ship wakes are common features of the reported literature on small-scale phenomena visible using SAR, and hence there is much supporting discussion on their observation and physics. Henceforth, a study was initiated to consider the effects of such turbulent currents caused by a moving surface vessel on radar backscattering, and to examine the legitimacy of applying existing ocean radar imaging models and techniques to such small-scale, turbulent ocean phenomena. A particularly beneficial case for further study was identified in the form of a surface wake arising from a moving vessel or body: not only are such phenomena common in published SAR imagery (in the form of ship wakes), but there was opportunity to engage in concurrent research into the wakes of underwater manoeuvring bodies (details of which can be found in Rojanaratanangkule et al. [2012]). The surface wake scenario was also beneficial due to the significant heritage of previous ship wake studies, in addition to the presence of representative scales of turbulence relevant to the current application of observing small-scale surface motions. The horizontal currents which are derived from the ship's disturbing effect on the still water give rise to wave modulation which is (potentially) detectable by SAR until after some time, turbulence and surface currents decay such that the surface waves recover to their equilibrium state.

In typical SAR images, the effects of surface wake turbulence are most typically manifest in the turbulent wake extending rearward of a moving surface vessel such as a ship. For reference, a schematic of a typical ship wake is presented in Figure 18. The action of turbulence in the wake on short waves typically causes a region of a smoothed sea surface (often referred to as a 'scar') extending up to 10s of kilometres behind the ship. As a result, the territory where turbulence is present in ship wakes typically appears 'dark' in radar brightness images (due to increased levels of specular reflection in this area); whilst the Kelvin wakes and regions of wave-breaking generate intense radar backscatter and appear 'bright'. This response is demonstrated in the turbulent ship wake resolved by *TerraSAR-X* in Figure 19; reproduced from Soloviev et al. (2010). Examples of turbulent wake features in SAR images, and investigation of the mechanisms responsible for the 'dark' response may be found extensively in the literature, such as Munk et al. (1987), Lyden et al. (1988), True et al. (1993), Milgram et al. (1993), Hennings et al. (1999) and Toporkov et al. (2011).
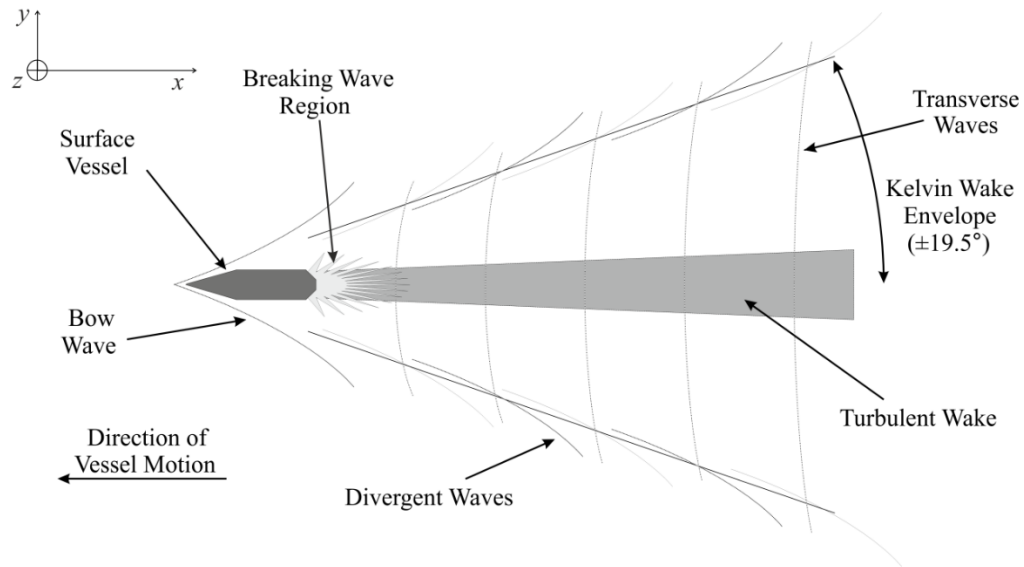
Figure 18. Schematic of typical ship wake.
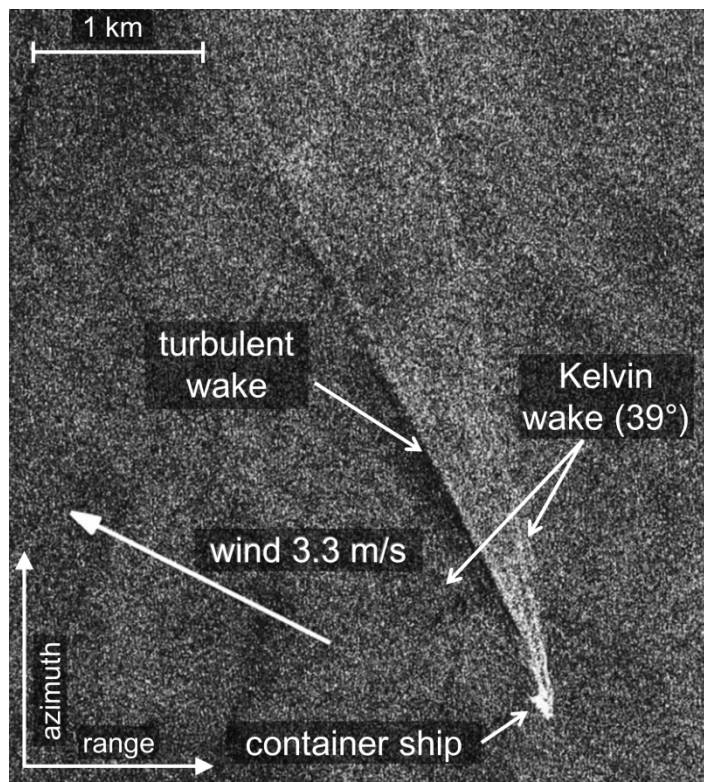
Figure 19. Ship wake in *TerraSAR-X* image, previously shown in Figure 7 without annotation; adapted from Soloviev et al. (2010).

Simulation of a ship-generated turbulence has two primary impacts on calculation of the radar backscattering arising from its effect on short surface waves. Both features require differing methods to incorporate their effects on wave propagation:

1. "Macro-scale" effects: interaction of surface currents (due to the action due to passage of the vessel and action of thrust sources such as propellers) with the surface wave spectrum, as studied by Lyden et al. (1985), True et al. (1993) and Fujimura et al. (2011);

2. "Micro-scale" effects: Redistribution of surface (short) wave energy by fine-scale turbulent fluctuations of velocity in the near-surface layer caused by the wake, as observed and measured by Reed et al. (1990) and Ölmez & Milgram (1992).

The development of high-resolution SARs such as *TerraSAR-X* has reinvigorated the interest in identifying small-scale ocean processes from remote observations, in particular with respect to ship wakes, leading to recent simulation studies of turbulent ship wakes conducted by Soloviev et al. (2010), Fujimura et al. (2011) and Toporkov et al. (2011). These investigations indicate that, with improvement in signal-to-noise capability and spatial resolution of future SAR instrumentation, increased discrimination of low-backscatter features such as patches of near-surface turbulence may be improved. The results obtained here therefore allow further understanding of the relationships between small-scale, ship-wake turbulence and radar backscattering. Examining such hypothetical flow fields will allow comparisons to be drawn with other turbulent phenomena and how they may be rendered visible in remotely-sensed images with improved future instrumentation.

In order to examine the effect of surface currents on radar images, the proposed simulation procedure was examined using a case study of a simple moving surface vessel acting as an initiator for turbulence near the fluid surface: DNS was integrated with ocean radar imaging models to numerically simulate the turbulence at the fluid surface and derive theoretical remote-sensing signatures.

5.2   Fluid Simulation Setup

The *CgLES* numerical code was applied to set up the wake flow, in conjunction with the immersed boundary method. Body-force terms were applied to crudely replicate the hull profile of a ship-sized object at the surface of the fluid domain. A non-dimensional freestream velocity, U, was applied in the *x*-direction to mimic the body moving in a fixed reference frame. The vessel was characterised by a submerged half-sphere of radius δ, where F_i are the external body forces

describing the virtual body surface $\boldsymbol{B} = (B_x, B_y, B_z)$. The submerged half-sphere was modelled using a semi-spherical virtual body surface with no thrust component, leading to a modelled representation of a simple towed surface vessel. A no-slip boundary condition was applied to the embedded surface and a fixed boundary (under the "rigid lid" approximation) was applied to the upper surface of the computational grid. Periodic boundary conditions were applied to the inflow and outflow boundaries. Although the body is three-dimensional, the (drag) force acts in the streamwise (x) direction only, generating a force which opposes the freestream flow. A schematic of the DNS domain and parameterisation of the body is shown in Figure 20, and the parameters employed in the simulation are described in Table 5.
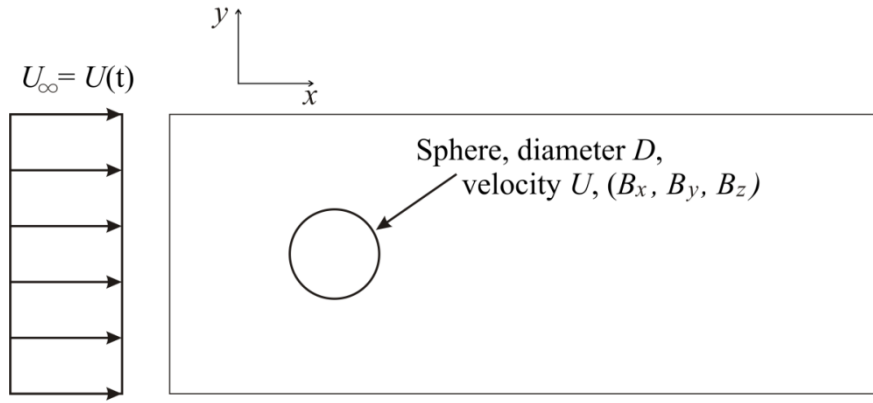
Figure 20. Schematic of body force in DNS according to immersed boundary method.

Sphere Gaussian Half-Width, δ	0.3
Reynolds Number, Re_{DNS}	1000
Forcing Intensity, J	$\frac{-4}{2}e^{-2}$
Time-Step, dt	0.003
Numerical coefficient, b	0.5
Viscosity, ν	1×10^{-4}
Number of Grid Points	x: 2112
	y: 256
	z: 128
Domain Size	$-10 \leq x \leq 40$
	$-10 \leq y \leq 40$
	$-10 \leq z \leq 40$

Table 5. Parameters employed in Direct Numerical Simulation within the case study. All units are non-dimensional unless otherwise indicated.

A Reynolds number of $Re_{DNS} = 1000$ was chosen for the DNS under consideration. A high Reynolds number indicates a greater range of scales; as Re_{DNS} is increased, smaller scales become visible in the flow. Reynolds numbers of a geophysical surface wake in the ocean are typically in the region of Re in excess of 10^4 (Thorpe, 2005); however, the chosen Re_{DNS} is sufficient to derive scale of the largest eddies in the flow, thus to derive the hypothetical flow field operated here. The three-dimensional fluid domain was formed of approximately 70 million grid points: 2112 in the x-direction (direction of vessel motion), 256 in the y-direction (perpendicular to vessel motion in surface plane), and 128 in the z-direction (vertical direction); a schematic of this domain is presented in Figure 21. The numerical flow was processed until the onset of fully-developed turbulence; at desired time steps, pausing the simulation to write to disk the velocity (u, v, w) and pressure (p) data at each grid point in the domain. The three-dimensional velocity data was retrieved, returned to dimensional form and exported to the radar image model to simulate modulation of the surface wave spectrum due to turbulent currents, and subsequently to derive simulated NRCS imagery. The reference frame was adjusted to remain fixed with respect to the fluid (by subtracting the freestream velocity of the flow, U, from the u-velocity data), creating a turbulent wake equivalent to a simulated vessel moving over a stationary water surface.

Preparation for the fluid simulation was conducted by the author, following review of the literature and description of techniques applied by other institutions for deriving ship- and surface-wake flows. The numerical set-up and execution of the *CgLES* code were performed by Mr. Watchapon Rojanaratanangkule (now 'Dr.') with the additional guidance of Dr. Glyn Thomas. Following computation of the DNS procedure, the output data files were delivered to the author for extraction of the surface wake profile, dimensionalisation and translation of the profile into a form acceptable for input to the applied ocean radar imaging models. Fluid simulations were performed using the *IRIDIS3* high-performance computing facility at the University of Southampton.
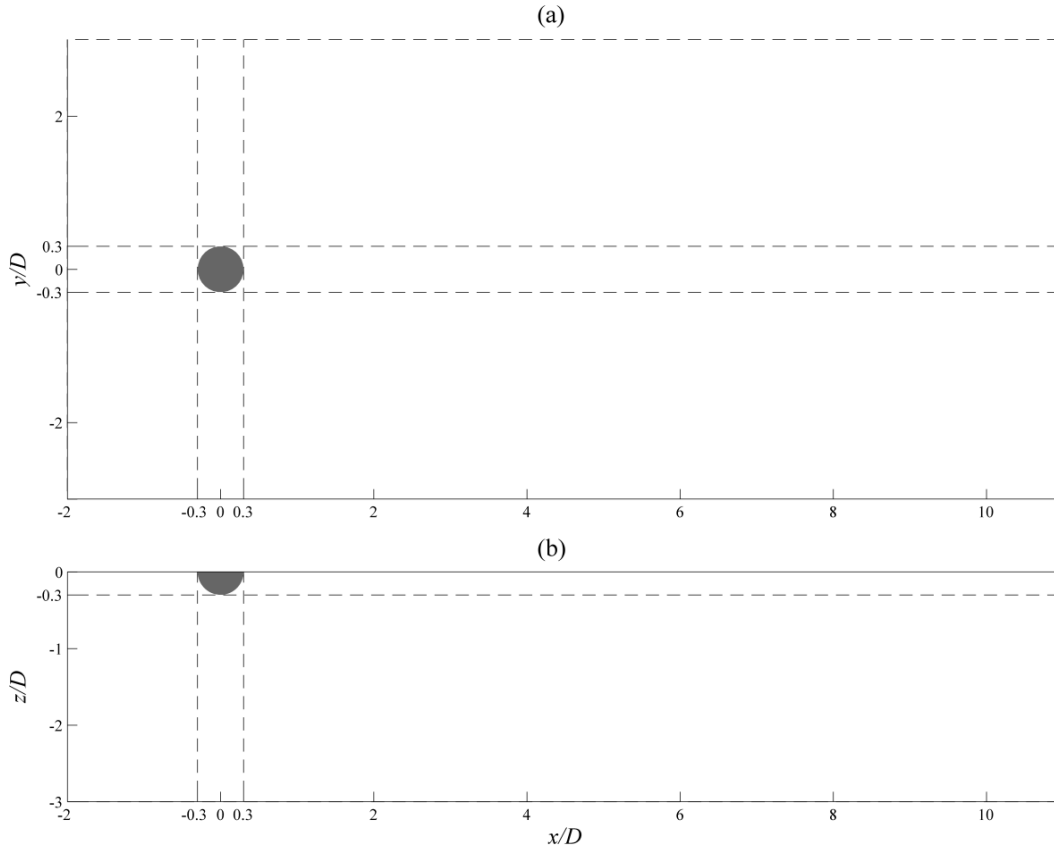
Figure 21. Size and location of half-sphere in the fluid domain.

A representative output from the DNS procedure (in non-dimensional units) is shown in Figure 23 (a) which shows an isosurface of the second invariant of the velocity gradient tensor (Q); a useful visual marker for turbulent structure and vorticity. Immediately aft of the half-sphere (at $x = 0$), the flow remains fairly smooth before giving way to large-scale disturbance at approximately $x = 12$, leading to eddying motion and regions of 'swirling' flow. For the purposes of examining the turbulent wake system of a surface wake, sections of the surface velocity profile beyond $x = 12$ are used to examine radar backscattering. Figure 23 (b) and (c) depict the surface u- and v-velocity profiles at the same time step. The current profiles operated in the wave-current interaction/radar simulation phase were artificially manipulated to produce ("real"-scale) surface wakes suitable for understanding the numerical models, therefore representing hypothetical flow fields which may theoretically be encountered in a geophysical setting. In the current specification of the *M4S* model (Romeiser, 2008), vertical (w-) components of the surface current velocity do not contribute to derivation NRCS signatures (but have effects on derivation of SAR signatures due to their role in calculation of Doppler variations), hence were not applied during the simulation phase.

The applied surface velocity profiles were often divided into multiple, smaller domains to ease computational loads on the ocean radar models and to observe NRCS results at different portions of the wake profile. Designation of the wake current profile(s) which are used to derive surface signatures are shown schematically in Figure 22. These designations will be used in both figures and text in order to describe the wake profiles under scrutiny.
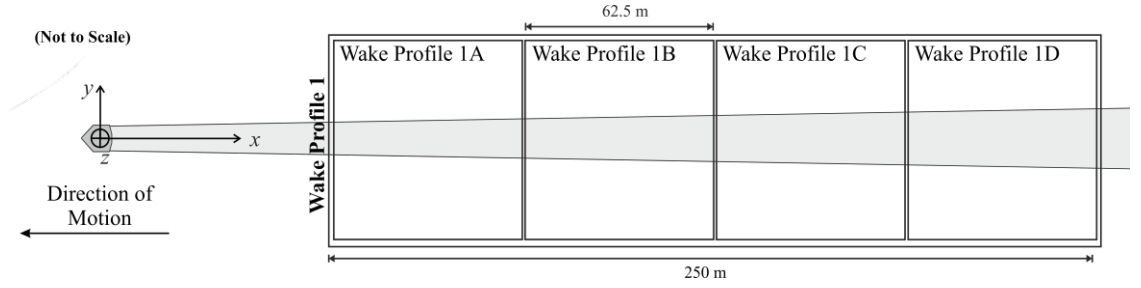
Figure 22. Schematic depicting locations of simulated NRCS images in the turbulent wake.

For the surface wake profiles analysed using the *M4S* ocean radar image modelling algorithm, only the macro- ("integral"-) scale processes (i.e. the primary surface currents at a grid resolution of $O[0.25 \text{ m}]$) were examined. It was not possible to perform investigation of the impact of micro-scale turbulence (for example, dissipation of surface wave energy by turbulent velocity fluctuations, etc.) during the study period, but a review of the relevant literature and a discussion regarding the approach towards implementing micro-scale interactions in future studies are discussed in further depth in Appendix D.
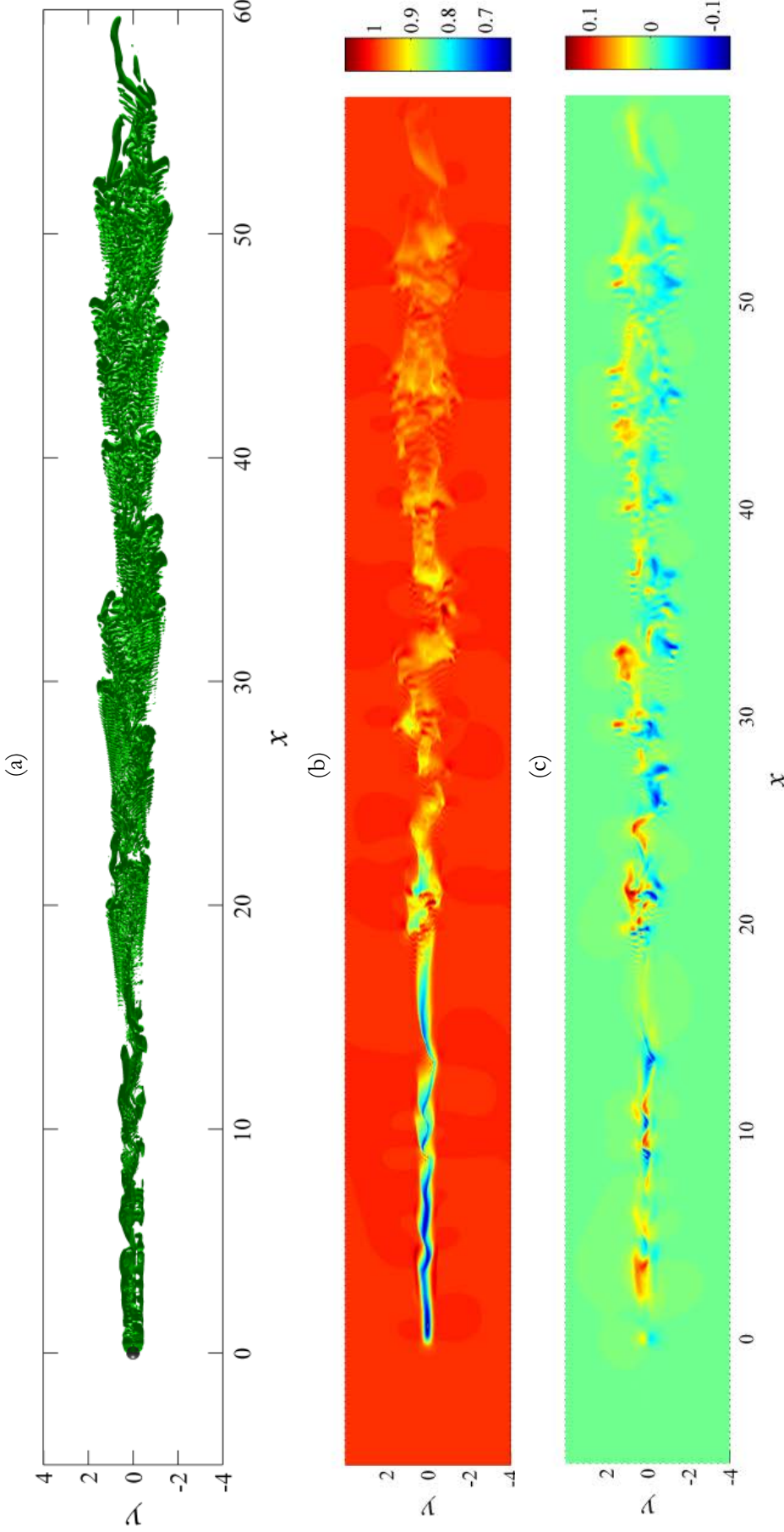
Figure 23. Example plot of the turbulent wake output from the DNS procedure, showing an isosurface of the second invariant of the velocity gradient tensor (**Q = -0.005) at** time step = 60 from (a) top-down views, along with surface (b) u- and (c) v-velocity profiles. The second invariant is a useful visual marker for turbulent structure and vorticity. All length scales are non-dimensionalised using the sphere diameter and freestream velocity, U_{DNS}.

5.3   Discussion of Defined Strategy

This section considers validation of the defined strategy in generating turbulent velocity profiles and for deriving surface signatures of radar backscattering. Since the defined strategy pursues aggressive surface current profiles and approaches the limits of current ocean radar image modelling theories, the implications of applying such theories must be examined.

The research presented in this thesis represents first efforts to unite high-resolution fluid simulation data with standard ocean radar imaging models (using DNS techniques to generate the input surface velocity data) and this has yielded insights toward future directions of this simulation method. Previous studies which have operated ocean radar imaging models have rarely considered small-scale phenomena: while there have been studies of small-scale ship wake radar signatures by other scientists, the high-resolution DNS data operated in the current study is directed at resolving finer spatial scales that have been previously examined. There has also been limited discussion of the implications of considering rapidly-varying current systems using typical ocean radar image modelling methods: the limits of operation of the wave action balance calculation, applicability of the primary assumptions/simplifications of surface wave theory and the use of geometrical optics methods (the WKB approximation) to propagate waves in the presence of a disturbing current. A study/investigation into these issues has been pursued to investigate this problem and to identify alternative methods or possible amendments to the strategy, and these findings are introduced here.

Development of this integrated model also required identifying the unique problems/challenges in radar backscatter simulation and integrating with turbulence models and developing linkages between different modelling processes. Previous work using ocean radar imaging models has been pursued from the point-of-view of trying to understand SAR images, whereas a novel aspect of the current study involved questioning whether ocean imaging modelling techniques may be used to inform the design process for future ocean sensors.

5.3.1   Application of DNS with Ocean Radar Imaging Model

In most previous work (see §4.2 and Appendix C), the fluid models operated to derive the examined surface flow are proprietary research models, large-scale ocean models or Large-Eddy-type models. Such models typically operate at equivalent real-world scales far larger than the application considered here; perhaps with the exception of recent work by Fujimura & Soloviev (2009), which considers the role of a ship wake hydrodynamics on radar visibility. Operation of a DNS-type model in the current research represents a unique application for deriving a set of fluid

surface currents for wave-current interaction modelling. Whilst the reasoning behind use of this technique was previously discussed in §4.2, it is constructive to discuss the suitability of this method in representing a real-world sea surface. Use of DNS as the candidate method for generating the surface flow field is, however, subject to some limitations which cause it to represent a simplified model of a hypothetical surface current.

DNS is a computational process more typically used for academic and industrial research of fluid dynamics; therefore not routinely used to calculate oceanic flows. In this respect, flow phenomena computed using DNS techniques are typically subject to significant constraints in the operable flow geometry and Reynolds number which may be studied. For the DNS scenario operated within this investigation, no efforts to replicate the profile of any existing surface vessel were made, justifying use of a simple half-sphere as the primary vessel generating the surface wake. The wake is hence observed as a region of drag behind the body which causes the freestream flow to decelerate and generate a region of mixing, vorticity and a turbulent wake analogous to that of a surface moving vessel. In this respect, the derived surface velocity profile represents a hypothetical flow field, which may possibly be observed in a geophysical system, but is not explicitly linked to any particularly process. The simulation also neglects other features of a typical vessel wake, such as the Kelvin and transverse wave systems and the presence of breaking waves. The Kelvin wake and its associated system of diverging waves appear, and propagate, away from the turbulent wake and into the ambient water system and therefore have only minor influence on the turbulent wake[12] - omission of these characteristics from the fluid simulation is, hence, a justifiable simplification to the study. In the region immediately aft of a ship in a geophysical ship wake, there is typically an intense region of breaking waves and white water generated by the agitation of a ship's propellers and surface mixing. Such effect is not modelled in the current representation, and the effect of breaking waves are not accounted for in the wave energy balance that is computed by the wave-current interaction model in *M4S*. Furthermore, the presence of natural/manmade surface films and contaminants (which influence both wave action transfer and radar scattering) is not accounted for by the applied model; some of which may have been elevated to the surface by the action of propellers and turbulence itself.

Generation of a (three-dimensional) surface current profile using DNS is made under the assumption that the surface plane is flat (the 'rigid lid' approximation) and that there are no waves, or wave motions present. Therefore, surface currents are assumed to occur on a smooth ("glassy")

---

[12] This influence will likely be restricted to the potential blocking of short-waves propagating into the turbulent wake region; although this will depend on the orientation of the Kelvin wake arms with the wave propagation direction and local wind, and indeed may only be observed in limited cases.

plane and not on a wavy surface; however, this is an acceptable approximation, since the wave-current interaction process adds an (empirical) wave spectrum to the current profile in order to compute the (modulated) wave spectrum which would be observed in a real-world surface current under and wind- and wave-forcing. This process hence accounts for the superposition of multiple wave types in an empirical manner, rather than being processed in the fluid domain. The surface is assumed to have a surface tension of 0.079 Nm^{-1} and seawater density of 1025 kgm^{-3}, and all wave-current interaction is assumed to take place in sufficiently deep water. In computation of wave-current interaction, the relaxation rate of Plant (1982) is assumed, and the source term applied within the wave-current interaction model was that of the "limited" quadratic source function defined in Wensink et al. (1999) [modified from the standard quadratic source function of Thompson & Gasparovic (1986)], which are consistent with parameters used in other simulation studies.

For the purposes of this case study, derivation of a surface flow is not intended to present an accurate representation of a surface wake or of an authentic ocean (surface) process, only to derive a broad representation of surface flow patterns on scales $O(10 \text{ m})$ and with analogy of a surface ship wake. In this respect, strict validation of the DNS case study with a geophysical ocean case was not performed since exact representation with a real-life current was not desired. However, through Reynolds number similarity, the large-scale current patterns of interest are replicated with sufficient clarity in order to retain the macro-scale scale structure. Due to limitations in the Reynolds number that can computationally be performed, translation of the current profile from the DNS domain to the 'real-world' domain in terms of appropriate length and time scales (through Reynolds number similarity) therefore leads to an over-prediction of the viscosity of seawater above what would realistically be observed in the ocean. However, since viscosity primarily affects the smallest scales of turbulence (by converting TKE into heat), the large-scale structure is only minorly affected and therefore largely retains its structure. Therefore, the computed surface current derived from the DNS process translates satisfactorily into representative surface patterns for use in conjunction with wave/current interaction techniques, and can be considered valid from the perspective of this broad study. In terms of confidence in the DNS computation and numerical approach, validation exercises were performed by Mr. Watchapon Rojanaratanangkule (now 'Dr.') and Dr. Glyn Thomas, in conjunction with the parallel work performed on the subject of manoeuvring-body wakes. Description of these exercises can be found in Rojanaratanangkule et al. (2011) and Rojanaratanangkule et al. (2012).

There is only limited consideration of wave energy dissipation in applied source function description presented by the *M4S* wave-current interaction model. The omission of breaking waves

in the wave energy balance will have the effect of dissipating wave energy (short waves lose much of their energy through breaking), but will also directly influence radar scattering. Waves at the onset of breaking will accentuate the effect of surface tilting (by long waves) and may lead to strong radar returns from the steep water face, whereas the presence of a breaking wave and the generation of white water in the surf may lead to more diffuse scattering where there is fine-scale surface roughness. After breaking, the wave will have reduced amplitude due to the dissipation of wave energy and hence lead to a muted scattering response. In the wave energy balance, surfactants will lead to damping of short gravity-capillary waves and surface smoothing, leading to a reduction of Bragg-scale roughness. Where there is the presence of surface film material, this may inhibit interaction of the current profile with the ambient surface waves and obscure the flow patterns of the phenomena of interest. However, in more favourable circumstances, it is possible that the disturbance created by, e.g. the passage of a surface moving object, disturbs the order of a surfactant patch and could render flow patterns visible in a similar manner to that of Figure 4. The effects of wave energy dissipation by fine-scale turbulent velocity fluctuations are also not considered in the current model, but the implications for examining this effect are raised in the literature review presented in Appendix D. The presence of such dissipation effects will likely lead to sea-surface smoothing in the wake region and increased modulation depth of radar signatures of the surface flow in the manner depicted by Figure D1 of Appendix D.

In the main (and for reasons that will be discussed later in this chapter), radar surface signatures are presented for the Bragg wave spectrum $\psi(\mathbf{k_B})$ and only minor comment is made with respect to composite surface NRCS, which accounts for both long- and short-wave contributions to NRCS. In this respect, the derived simulated surface provides a suitable (although heavily simplified) facsimile for a real-world ocean surface comprising short, radar-backscattering waves in the absence of large-scale current motions, surface slopes and gravity waves.

5.3.2   Applicability of Theory of Geometrical Optics in Wave-Current Interaction Computation

A number of challenges were identified during construction and testing of the proposed strategy and operation of the individual numerical tools: these were observed particularly with respect to limitations associated with the operating standard wave-current interaction models and the small-scale ocean surface flows which the strategy attempted to investigate. Questions regarding the consistency of the modelling and simulation techniques used in this research, and also the characteristics of the simulated flows operated with them, must be addressed and some key points discussed. A crucial element of this phase of study was to scrutinise the range of assumptions made that exist in the applied theory of wave-current interaction using geometrical optics, and to further understand the domain of validity of these assumptions such that the credibility of results could be assessed. In particular, two concepts of the current wave-current interaction process (under the regime of geometrical optics) pose significant challenges for adaptation/application of this procedure: namely, the requirement for a "slowly-varying" surface current regime, and the presence of a frozen current. Analysis of these factors is developed in this section.

The accepted method for calculating the effects of spatial currents on ocean waves and wave/current interaction in typical ocean radar imaging models is the theory of Conservation of Wave Action (CWA) under an approximation of geometrical optics; this method was previously discussed in §4.3.2. The evolution of the energy and frequency of a wave system, propagating across a spatial current, is usually approximated using the theory of geometrical optics (the WKB approximation) and a ray-tracing procedure. A limitation is placed on bounds of the spatial and temporal variation of the surface current to satisfy the theoretical method: the exact limit of this validity is unclear and in open debate, hence there are unanswered questions as to the extent to which such theories can be applied to calculate wave-current interaction. This limitation is not well-discussed in the literature or by other authors in previously-published work.

Considering a single wave packet travelling through the current field, its intrinsic wave frequency, ω_0, is Doppler-shifted by motion of the surface, yielding an apparent frequency

$$\omega = \omega_0(\boldsymbol{k}) + \boldsymbol{k} \cdot \boldsymbol{U}(\boldsymbol{x}, t)$$

<div align="right">(xxii)</div>

with respect to a stationary coordinate system. Under the geometrical optics approximation, the ray equations describe a trajectory along which the variations of spatial position, $\boldsymbol{x}$, and wavenumber, $\boldsymbol{k}$, of a wave packet are coupled such that its apparent frequency, ω, (i.e. Doppler-shifted according

by the moving surface) is conserved (LeBlond & Mysak, 1978). Wave frequency, in deep water (i.e. depth larger than half the wavelength), is given by the dispersion relationship which dictates that long waves travel faster than short waves. This relationship connects wave frequency and wavenumber according to

$$\omega = \sqrt{gk}$$

(xxiii)

Under the WKB approach, an assumption is made that a wave packet may be modelled as a collection of idealised beams or 'rays', and that over an infinitesimal increment the ray is approximate to a straight, or 'nearly-plane' wave. This approximation is invoked to calculate the modulation of a wave packet in a current which is "smoothly-varying" (alternatively "slowly-varying"), whereby intensity variation of the wave packet can be computed by tracing the trajectory of the packet along a ray path where ω is conserved. The 'smoothly-varying' assumption is based on the Conservation of Waves (the Kinematic Conservation Equation), discussed by Phillips (1977), whereby wave crests are neither destroyed nor created, and their total number is be conserved. The validity of this assumption breaks down when individual rays intersect or overlap, where caustics appear; hence, ray theory holds under the assumption that the modulating current changes 'slowly' while wave packets travel through it, and that perturbations from equilibrium of different wave packets/wave trains are uncoupled (and there is no transfer of wave action from one wave train to another) – hence the limitations of weak hydrodynamic theory for surface currents are primarily related to the relaxation time of the waves, which defines the ability of perturbations to return to an equilibrium state; leading to the "relaxation time" approximation, discussed in full by Keller & Wright (1975) and Alpers & Hasselmann (1978).

For a current which varies in space and/or time, wave propagation must be approximated based on the theory of geometrical optics; yet under the assumptions defined above, the current must be "slowly-varying" – variations in current (in space and/or time) must be small when compared to a wavelength (λ_w) of the surface wave spectrum being considered. In cases where the current profile does not conform to this assumption, wave propagation may be calculated incorrectly; typically under-predicting the amount of wave modulation which is observed. In this respect, it is primarily the "slowly-varying" requirement that presents the foremost obstacle to considering high-resolution, turbulent surface current profiles using the CWA method. From the perspective of the ocean surface, wave action itself is fully conserved during wave-current interaction (McKee, 1987), even in the case of strong diffraction (Fabrice Ardhuin, personal communication, 12th January 2013). Hence, the primary barrier to computing rapidly-varying current interaction lies in the theoretical

assumptions that are inherent to the accept CWA method for propagation of waves in the presence of the disturbing current.

Under simplifying assumptions, the surface wave field can be adequately described by through linearisation of the wave system about the equilibrium spectrum (Hughes, 1978). For a one-dimensional system with a surface current varying in the x-direction only, Lyzenga & Wackerman (1997) demonstrate linearisation of the one-dimensional wave action equation, rewritten in terms of the spectral perturbation of the wave system, f, where

$$f = \frac{N(k) - N_0(k)}{N_0(k)} \qquad \text{(xxiv)}$$

where $N_0(k)$ is the equilibrium wave action spectral density for an equilibrium wave spectrum; for example, the Phillips spectrum of Phillips (1958a). The linearised (one-dimensional) wave system of Lyzenga & Wackerman (1997) is thus given by:

$$\left(c_g + u\right)\frac{\partial f}{\partial x} - \left[k_x\frac{du}{dx} + k_y\frac{dv}{dx}\right]\frac{\partial f}{\partial k_x} = (\mu - \beta f)(1 + f) \qquad \text{(xxv)}$$

where

$$\mu = \frac{1}{N_0}\left[k_x\frac{du}{dx} + k_y\frac{dv}{dx}\right]\frac{\partial N_0}{\partial k_x} \qquad \text{(xxvi)}$$

and k_x and k_y are components of the ocean wavenumber in the x and y directions respectively, and the β term is a non-dimensional growth rate parameter (also known as 'Miles' parameter') representing wind/wave growth. As μ tends to zero, so does the spectral perturbation; therefore the action balance equation may be linearised by neglecting terms involving f^2 or μf, making the assumption that the current gradients $\frac{du}{dx}$ and $\frac{dv}{dx}$ are small (Lyzenga & Wackerman, 1997). According to studies by Caponi et al. (1988), the linearised calculations display good agreement with the full calculations when current gradients are very weak; however, where modulations are not small (e.g. spectral perturbation $f > 10\%$), the linearised approximation departs considerably from the full equation, and unphysical negative values of spectral density may be observed. Care must hence be taken when utilising the linearised approximation in the presence of strong gradients/modulations in order to avoid unphysical spectral responses being returned by the wave action calculation.

During application of the CWA technique, the wave system is propagated through a region of current flow which, in this case, is a surface velocity profile due to some surface or sub-surface disturbance. While the waves propagate through the current disturbance, the current field is assumed to be 'frozen' and statistically stationary or homogeneous; that is, all mean quantities are invariant under spatial and temporal translations (Hasselmann, 1967). The assumption is made that, if the current is slowly-varying, it can be assumed that, locally, the medium has a uniform velocity, $U(x, t)$, and that a local reference frame may be adopted, in which the current may be assumed to be at rest (Howe, 2007). However, a rapidly-varying current may vary with time such that many wave components feel some current changes (and acceleration) while they propagate through the current field. For strict operation of the WKB approximation, justification must be made of a frozen (in time) current field over the time scale on which waves propagate across the domain.

5.3.3   Challenges

Ocean radar imaging models, in the main, were developed primarily for improving understanding of operational SAR images and to aid in identifying, or discriminating, ocean phenomena. Their operation is therefore more associated with observing phenomena which can currently be resolved in existing SAR images; i.e. internal wave systems, mesoscale eddies, ocean fronts. Therefore, the theoretical basis and typical operation of such models focus on simulation of sub- and mesoscale currents (where current variability is of order of 1-100 km), where there is shown to be satisfactory agreement between the model(s) and observed imagery. The supporting theories were therefore developed to consider cases where the scale of current non-uniformities (e.g. L^*) are significantly larger than the inverse wavenumber of surface waves; i.e. $kL^* \gg 1$. Application of these techniques to smaller-scale phenomena (of total span of the order of 50-100 m) can lead to a number of issues in operation of these models; particularly in the specification of the input surface velocity grid delivered. These issues are related to the characteristics of long waves which in both the wave-current interaction phase (associated with relaxation time) and radar backscattering calculation (associated with surface slopes and specular effects).

The *relaxation time*, τ_w, of a surface wave represents the time taken for the wave to return to an equilibrium state following some disturbance (or deviation from a steady state) and is associated with a *relaxation length*, l_w, (also known as *relaxation scale*) that describes the physical distance that a wave propagates in the time taken to relax to equilibrium state: the variation of relaxation length with wavenumber for a 10 ms⁻¹ wind is presented in Figure 24 (reproduced from Kudryavtsev et al. [2005]). In the wave-current interaction calculation, waves that possess a relaxation length larger

than the size of the computed surface domain may possess artificial modulations since they do not have sufficient distance to relax to equilibrium following a disturbance - At a representative 4 ms^{-1} wind speed, waves with the largest relaxation length are observed at the wind's spectral peak; displaying a wavelength of O(10 m) and k = 0.63 radm^{-1} (Vladimir Kudryavtsev, personal communication, 10th September 2012). Such waves demonstrate a relaxation length in the region of kilometres, compared with a typical size of 50 m of the surface domain: in this respect, it is possible that disturbances to the long-wave spectrum may not be modelled correctly since the entire spatial domain is not sufficient to relax from some disturbance. Bragg-scale waves demonstrate ocean wavenumbers (k) of the order of 20-600 radm^{-1}), therefore possess significantly shorter relaxation lengths of the order of < 1 m, hence relaxation of short waves across the 50 m domain should be calculated without error. For reliable calculation, it is recommended that the variability of wind waves (i.e. the relaxation length) be several times shorter than the variability of the surface current (Vladimir Kudryavtsev, personal communication, 10th September 2012). Hence, whilst Bragg-scale waves are computed correctly with respect to the spatial domain, problems may be introduced in cases where the surface current varies over distances less than 1 m. Therefore, this places limitations on surface velocity to vary with a spatial variability of the order of 10-50 m in order to maintain full applicability of the general theory and to maintain a division of scale between the relaxation length of surface waves, and the scale of current variability. With this result in mind, it is recommended that, when considering spatial domains smaller than 100 m in either (surface) direction, only results arising from the Bragg region of the wave spectrum are considered for absolute levels of wave-current interaction and radar backscattering.
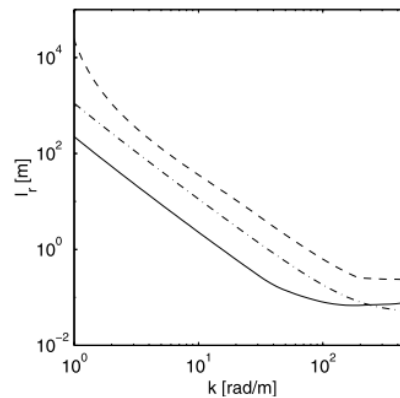
Figure 24. Relaxation length for a 10 ms^{-1} wind against wavenumber for downwind (solid lines), cross-wind (dashed lines) and upwind (dash/dotted lines) directions; from Kudryavtsev et al. (2005).

As discussed previously in Chapter 4, the composite surface method employed by typical ocean radar imaging models uses an approximation of the wavy ocean surface as a series of facets in order

to simplify the radar scattering calculation, and this can present some challenges. Variation in surface slope of the underlying long wave, or current, system can therefore modify the geometry of the facet approximation and Romeiser et al. (1994) describe the assumption that Bragg-scattering facets must be large compared to λ_B, using a facet size of $6\lambda_B$. At operating frequencies of 5-10 GHz (assuming $\theta_i = 23°$), a facet is of the order of 10 cm in length: for C-band (5.3 GHz), a single Bragg-scattering facet is 13 cm length. Applying a grid point separation of, for example, 0.25 m creates a spatial grid resolution of the same order as a typical Bragg-scattering facet at X-/C-band frequencies (and smaller than such a facet with application of an L-band simulated radar, which possesses a single facet of 58 cm in size). Since facet scales may, therefore, be equivalent to the scale of the velocity grid at O(10-20 cm), height variations on the surface at the scale of the velocity grid may then modify mean square surface slopes (MSS), and therefore modify the resulting waveheight spectral density produced by the radar scattering calculation under application of the two-scale model. However, in and of itself, small grid spacing alone with respect to wave-current interaction calculation is not a significant barrier to computation of wave action itself (Vladimir Kudryavtsev, personal communication, 10th September 2012); Jansen et al. (1993) have also previously considered the impact of grid spacing in wave models and how variations in spacing affect convergence of wave models. Typical grid spacing operated in the recent published literature for a variety of ocean phenomena range from 0.2-0.5 m (Fujimura et al. [2011]; ship wake), 40-80 m (Cooper et al. [2005]; submesoscale spiral eddy) and 62.5 m (Romeiser et al. [2004]; oceanic/atmospheric convection). Considering previous work and simulation studies (see Table C1 presented in Appendix C), numerical grids employed by other researchers typically operate grid spacing of the order of 3-20 m.

In addition to the resolution of the surface current grid, consideration must also be made of the resolution of the grid used for computation of wave-current interaction and for propagation of waves across the domain. When calculating spectral modulation, a wave packet's evolution as it is propagated through the disturbing current is modelled with respect to a finite number of prescribed directions with a specific directional resolution. During this process, the behaviour of the wave component at each wavenumber/direction grid point is assumed to be representative of all wave components in the cells around it. By definition, *M4S* operates 24 wavenumber directions with resolution of 15°. In the presence of strong variations in current over a short number of grid points, where there may be significant spectral modulation, the resolution may sometimes be insufficient to provide a smooth variation of the spectra in all directions, potentially leading to mild irregularities in the composite surface NRCS observed in the area outside of the wake. As a wave packet travels across the current field (with strong changes), even a small modification (e.g. 5°) to its direction can

cause it to take a significantly different path, and the assumption of a smooth transition between the (modulated) spectral energy density at adjacent grid points is breached. This results in an under-sampling of the modulated wave spectrum, giving rise to the presence of background fluctuations in composite surface NRCS imagery (Roland Romeiser, personal communication, 29th July 2012). Such fluctuations can be observed in the NRCS profile obtained from *M4S* presented in Figure 25, where these effects are visible in the background area away from the wake. Because of this, the remainder of this thesis focusses primarily on simulated Bragg NRCS signatures, and only minor discussion is made regarding simulated composite surface NRCS signatures: in the Bragg-scattering specification, only waves travelling directly towards (or away from) the radar range direction contribute to the calculated NRCS, therefore issues of the wavenumber computation are somewhat alleviated in the Bragg NRCS-only case.
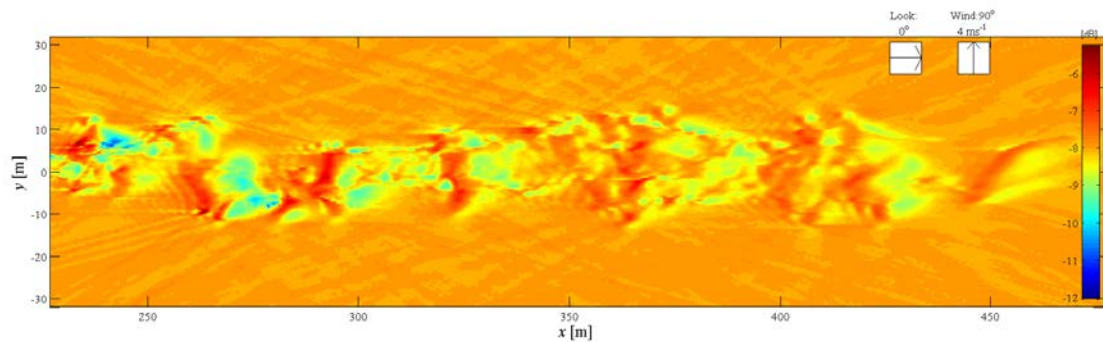
Figure 25. Presence of mild irregularities in the background region of composite surface NRCS plot produced by *M4S*. The displayed colour axis has been manually altered in order to highlight the presence of distortion in the background area of the signature.

Broadly speaking, characteristics of a "slowly-varying" current feature can be described, in both space and time, by the magnitude of gradients in the current which are present at the surface. The strongest current gradients which are observed in the historic literature are in the region of 0.03 s^{-1}, used by Lyden et al. (1985) and Jansen et al. (1993), which were operated successfully to derive radar surface signatures from a ship wake. In more recent work, the data calculated and presented by Fujimura et al. (2011) shows values of gradient up to 0.06-0.08 s^{-1}, which are typically larger than other data observed in the literature. It should be noted, however, that many articles in the literature do not describe or depict the current fields/gradients used in their studies, and so other data cannot be confirmed. In the testing procedure, the effect of current gradients on calculation of wave-current interaction was investigated. The largest gradients were observed primarily in the U-velocity (in the vertical direction; i.e. shear), or the horizontal shear on the v-velocity, and such high gradients occur only over very short distances – with a coarser resolution in the turbulence data, the gradients would be reduced. In the operated current profile, the maximum gradients observed are

in the range of ±0.06 s^{-1} (observed in the variation of u-velocity in the y-direction); these gradients appear "strong" when compared with those operated in other ship wake studies but which will enable investigation of the role of "aggressive" current profiles and the ability to resolve such wake flows.

For the case study examined here, validation of the input surface currents for operation of the designated *M4S* wave-current interaction model was established for the case of the short-wave variation (and therefore for generation of Bragg NRCS profiles), but was not fully validated in the context of larger-scale waves which of wavelength beyond $\lambda_w \sim 1$ m. Such validation was approved according to the definition of acceptable current gradients and variation that maintain broad agreement with the "slowly-varying" assumption in the case of short surface waves. Therefore, whilst Bragg NRCS signatures are validated for the "aggressive" current profiles considered in the hypothetical surface wake data, composite surface signatures (and the impacts of long waves on radar backscattering from the wake) are only discussed sparingly. Furthermore, in the main, derived Bragg NRCS signatures are considered only with regard to relative changes – either within a single image, or in comparison between two equivalent images – and not for absolute measurements; therefore alleviating concerns and/or complications regarding incorrect calculation of wave/current modulation arising from strong variations in current. Therefore, the domain of validity of this technique holds sufficient overlap with the applied current profiles to justify investigation of the wave-current interaction associated with a turbulent surface wake and the resulting effect(s) on modulation of radar backscattering.

5.3.4   Summary

In this selection, definition of a hypothetical (turbulent) flow field was derived which describes a high-resolution current field containing a grid resolution and spatial variation which compares with, and exceeds, specifications which have been studied previously by other authors. The objective of this effort was to understand the role of (potentially) "rapidly-varying" currents on the wave-current/radar backscattering calculation process and to push the boundaries of what can be comfortably accepted under weak hydrodynamic interaction theory, etc. In this respect, there is a somewhat "aggressive" application of surface wake currents which are observed by varying definitions of simulated instrument and ambient/wind conditions, but one which is felt to broadly fall within the domain of validity currently understood regarding the WKB method. Whilst, under more "rapidly-varying" regimes, the WKB method may be suspect and in need of greater validation, it is generally felt that the results are at least qualitatively correct and representative. However, due to the potential concerns regarding the reliability of composite surface NRCS

computations, the results presented in this thesis will focus on radar backscattering signatures comprised from Bragg NRCS. In the main, such signatures are examined for relative variations between two simulated images or cases in order to alleviate concerns over the levels of absolute wave modulation which may be produced in cases where the current profile may (potentially) approach a "rapidly-varying" state in some areas. Whilst there are stronger concerns over reliability of composite surface signatures due to the specified current profile(s) and numerical grid, results, a limited number of composite surface NRCS results have been presented later in this thesis for discussion, along with suitable discussion of their limitations. In general, these have been presented for comparison against simple Bragg NRCS signatures, and to derive some initial results and conclusions regarding long-wave effects.

In summary, the analysis presented in §5.3 has made steps towards establishing a greater understanding of the CWA/WKB method in the context of small-scale regimes and where conditions approach those which may be described as "rapidly-varying". The current research has contributed an initial discussion of this problem, and made progress in establishing a context for considering small-scale turbulence with these methods as well as identifying a range of open questions. The aim of this has been to stimulate a broader discussion of the validity of such methods for similar applications, and it is hoped that experimental and/or theoretical studies in the future will expand on the current base to help to address this challenging topic. Further basis for such discussion is presented in Appendix D, which considers both previous research and future perspectives, as well as providing introduction to potential alternatives approaches to the current technique.

6. NRCS Radar Surface Signatures

6.1   Introduction to Results and Qualitative Observation of Fluid Flow Structure

Following definition of the simulation scenario selected for further study, the *M4S* algorithm was operated to derive a significant body of results through simulation of radar backscatter signatures, arising from surface wake turbulence generated by a simple moving body. Many of the initial tests focussed on analysing the Bragg NRCS response to wave-current interaction, aiming to identify regions of turbulent flow structure and presence of disturbances. For these initial tests, a default wind speed of 4 ms⁻¹ was chosen in order to generate a sufficient distribution of backscattering waves. A range of test configurations were derived to examine the ability of fluid surface conditions to propagate into computed radar surface signatures; a selected number of cases are included here to highlight differences in characteristics such as the tone, texture, character and content contained within the distribution of NRCS. In many cases, the observed characteristics display variation with selected instrument configuration, simulated wind conditions and imaging geometries: a more comprehensive analysis of each of these factors is developed in the remaining sections that make up Chapters 6, 7 and 8. The default instrument & ambient conditions used for deriving the signatures in this section are described in Table 6: a frequency of 5.3 GHz and incidence angle of 23° were selected since they replicate the typical configuration operated by the *ERS-1*, *ERS-2* and *Envisat* spacecraft; whilst an HH-polarisation was chosen since it represents a conservative or 'worst' case for signature extraction (compared with VV-polarisation).

Radar Frequency	5.3 GHz (C-band)
Incidence Angle	23°
Radar Polarisation	HH
Wind Direction	90° to the x-axis (anticlockwise)
Wind Speed	4 ms⁻¹
Range/Look Direction	90° to the x-axis (anticlockwise)

Table 6. Nominal configuration studied in qualitative *M4S* NRCS simulations.

Preliminary results of NRCS simulations were previously presented and published in two conference papers, George & Tatnall (2011) and George & Tatnall (2012); abstracts of these papers may be found in Appendix A. A schematic, showing the order in which the results are presented in the following chapter(s), is depicted in Figure 26.
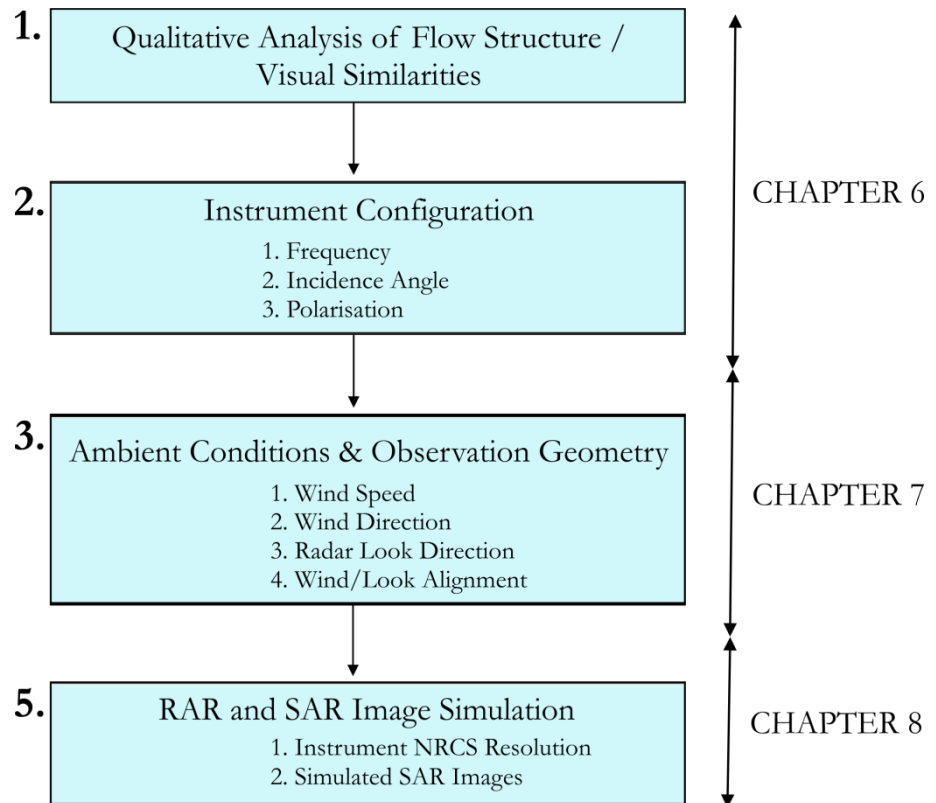
Figure 26. Summary of simulation results presented henceforth.

Through initial testing, it was observed that many of the derived radar backscattering profiles displayed close visual affinity with the input fluid profiles, allowing some qualitative comparisons to be drawn. In particular, visual comparisons can be observed between the original input velocity data and the simulated NRCS profiles, such as the distribution of velocity gradients and comparative texture/flow structure in the NRCS image. The presence of observable flow structure arises purely from the variations in surface velocities that are generated by the wake flow: such structure is revealed because of the effect of wave-current interaction, whereby modulation of ambient waves by the turbulent current pattern is propagated into observable (spatial) changes in radar backscattering. Regions of the surface current profile where velocity gradients and flow structure are present may therefore be qualitatively correlated with areas where there is deviation from the 'background' level of radar backscattering: this is the level of radar backscattering which is present

in the surrounding, (stationary) water in which there is a routine radar backscattering response from the ambient distribution of (unmodulated) short waves generated by the wind. In measuring spatial variations of radar backscattering, a 'negative' modulation is used to refer to areas where the NRCS is lower than in the ambient (stationary) water, whilst 'positive' modulation occurs where radar backscattering is elevated above the background level. The remainder of this document contains a variety of two-dimensional signatures portraying NRCS profiles which are presented on a decibel (dB, $\sigma_{0,dB}$) and linear NRCS (σ_0): it should be noted that such profiles are presented on full-colour and greyscale axes, respectively, and that these values do not provide an absolute measure of NRCS since the value represented by a particular colour or scale may vary between different figures.

As an example, a surface signature of Wake Profile 1-B arising from a simulated 5.3 GHz (C-band) radar is presented in Figure 27, which displays qualitative similarity between (a) the Bragg NRCS and the (b) u- and (c) v- components of the surface velocity profile. Qualitative details of the wake are rendered visible through the spatial variations of Bragg wave energy; resolved in the simulated image through the contrasts of Bragg NRCS which occur across the observed scene. Through the spatial distribution of 'light' and 'dark' areas illuminated by Bragg radar scattering, the texture of a radar backscatter image can hence give indication of the current patterns within the wake arising from the wake flow and permits the presence of flow structure to be observed and identified. In general, a decrease in backscattering is observed along the centreline of the wake when compared with the undisturbed fluid outside of the wake. Furthermore, fluctuations within the wake (and at the edges of the wake where the mixed water meets stationary fluid outside) give rise to increase of Bragg wave amplitude and hence radar (Bragg) backscattering, marked by 'bright' regions in the NRCS profile; indicated in feature [1] of Figure 27. In general, the margin of the wake on the downwind edge (i.e. the lowermost edge of the wake in Figure 27 [a]) appears brighter compared with the upwind side (the uppermost edge), since the convergence of the surface currents in the negative y-direction and ambient wind (in the positive y-direction) cause capillary waves to 'bunch up' and increase in amplitude, elevating the amount of radar backscatter observed in this area.

Close visual similarity may be observed between the flow structure (in terms of the patterns and spatial distribution of current and associated fluctuations in velocity, etc.) which are present in the input surface velocity profiles (which are shown in Figure 27 [b] and [c]), and the observed textures and patterns which are resolved in the simulated NRCS imagery. Such similarity is largely unsurprising, given that the calculated Bragg backscattering profile stems from the distribution of short-wave energy defined from the wave-current interaction calculation; which itself is largely derived from the patterns of current strength and gradient(s) present in the input data. While it is inevitable that the modulated wave spectrum will show similarity to the flow output by DNS

(because the computed wave-current interaction is driven by the flow characteristics derived from the numerical simulation); however, this may still be considered an important result since it demonstrates that, at least theoretically, small-scale wave-current interaction will translate to a radar signature which is resolvable in terms of radar backscattering cross-section. Extrapolating to a real-world scenario, propagation of a geophysical wave system over a current field may then render the structure of the flow field visible in a radar image, and for a discernible surface signature to be realised.
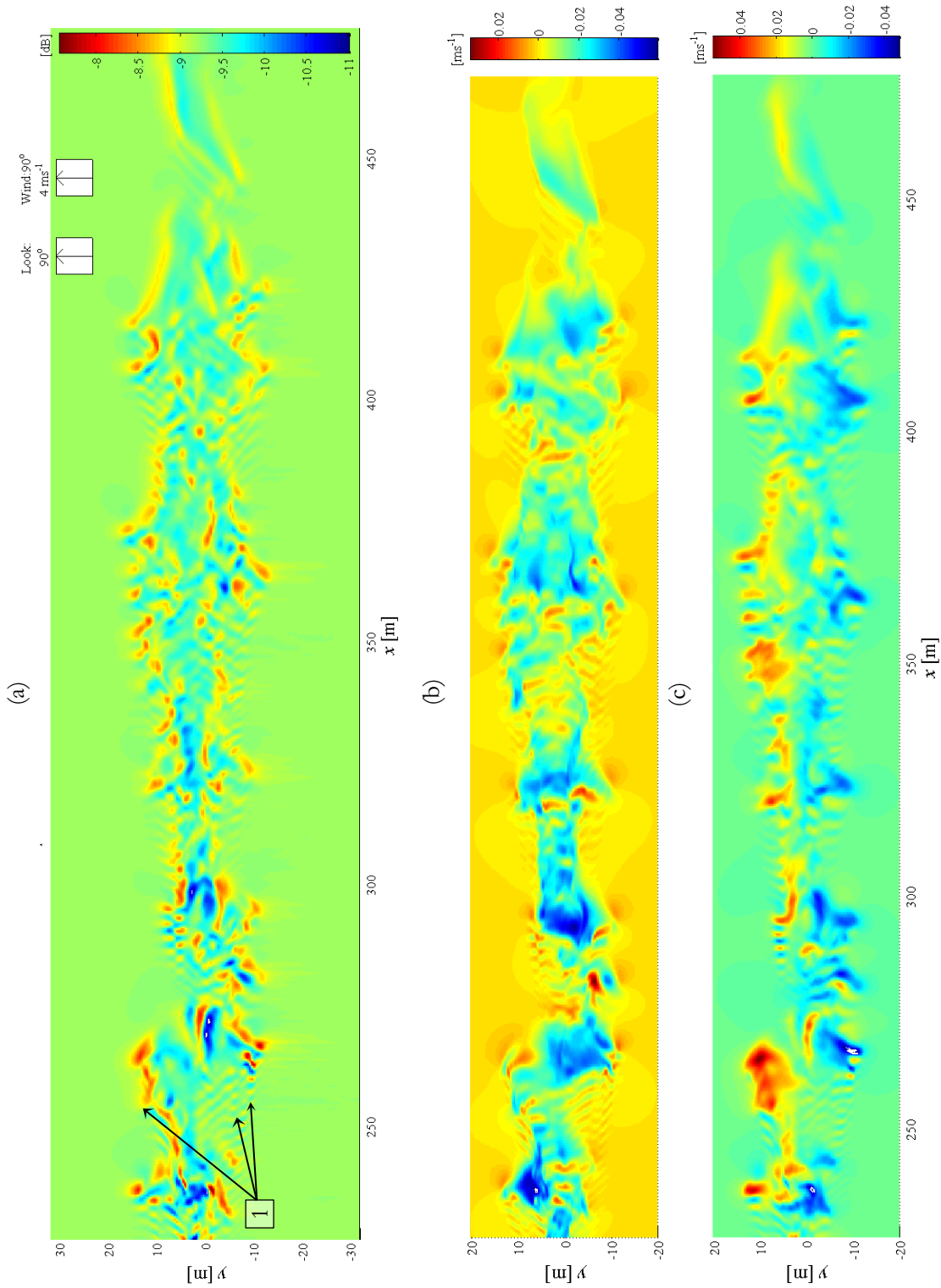
Figure 27. (a) Surface wake rendered in Bragg NRCS, for a C-band (5.3 GHz) instrument operating at 23° incidence angle and HH-polarisation, relative to levels of radar backscatter in the surrounding, stationary, water; (b) streamwise surface velocity profile; (c) spanwise surface velocity profile. The simulated wind profile is a uniform 4 ms^{-1} in the positive y-direction.

Qualitative observations may also be resolved in surface signatures within NRCS profiles which have been derived from composite surface theory. Due to the limitations described in Chapter 5, a significant focus was not made on analysing NRCS surface signatures derived from the two-scale model; however, for examining qualitative criteria, the derived results merit brief discussion such that some initial conclusions may be drawn. In Figure 28, Bragg NRCS (subplot [a]) and composite surface NRCS (subplot [b]) profiles are presented for a 5.3 GHz (C-band) radar operating at 23° incidence angle and HH-polarisation observing Wake Profile 1 in the (positive) y-direction. Where Figure 28 (a) reproduces the same profile that was previously presented in Figure 27 accounting for short waves, the profile of Figure 28 (b) represents both the long- and short-wave contributions to radar backscattering.

In Figure 29, a small section of Wake Profile 1 (denoted by the boxes overlaid on Figure 28) formed of a domain 250 grid points in the x-direction, and 250 points in the y-direction is isolated for more focussed study: sub-plots (a) and (b) depict a C-band (5.3 GHz) profile rendered in Bragg NRCS and composite surface NRCS, respectively, and observed from a look direction in the positive y-axis, and derived at 23° incidence angle and HH-polarisation. These plots demonstrate clear differences in the backscattering profile; in particular, a variation in the observed pattern of peaks/troughs of the spatial scattering signature as well as variation in the intensity levels of the observed NRCS peaks. In the composite surface NRCS profile, it can be observed that the lower side of the wake displays a prominent area of positive backscatter modulation, whilst negative modulation of NRCS can be observed just below the upper extremity of the wake. As a result, the lower side of the wake tends to be more visible in the simulated image and there is a much greater wind effect in the C-band composite surface NRCS profile such that area where the ambient wind opposes (or aligns with) components of the flow, there is surface straining of these components; such that their backscattering details are resolved. In particular, this causes the composite surface NRCS profile to show close qualitative similarity with the v-velocity profile presented in Figure 29 (d). This arises because the long-wave components show greater sensitivity to mean currents, whereas Bragg NRCS response(s) at higher frequencies resolve the structure of velocity gradients present in the flow. With respect to the latter, there is significant qualitative similarity between the (C-band) Bragg NRCS profile displayed in Figure 29 (a) and the arrangement of v-velocity gradients in the y-direction (Figure 29 [c]). The response of high-frequency (C- to X-band) and correlation(s) with gradients in velocity will be revisited again in the following sub-section.
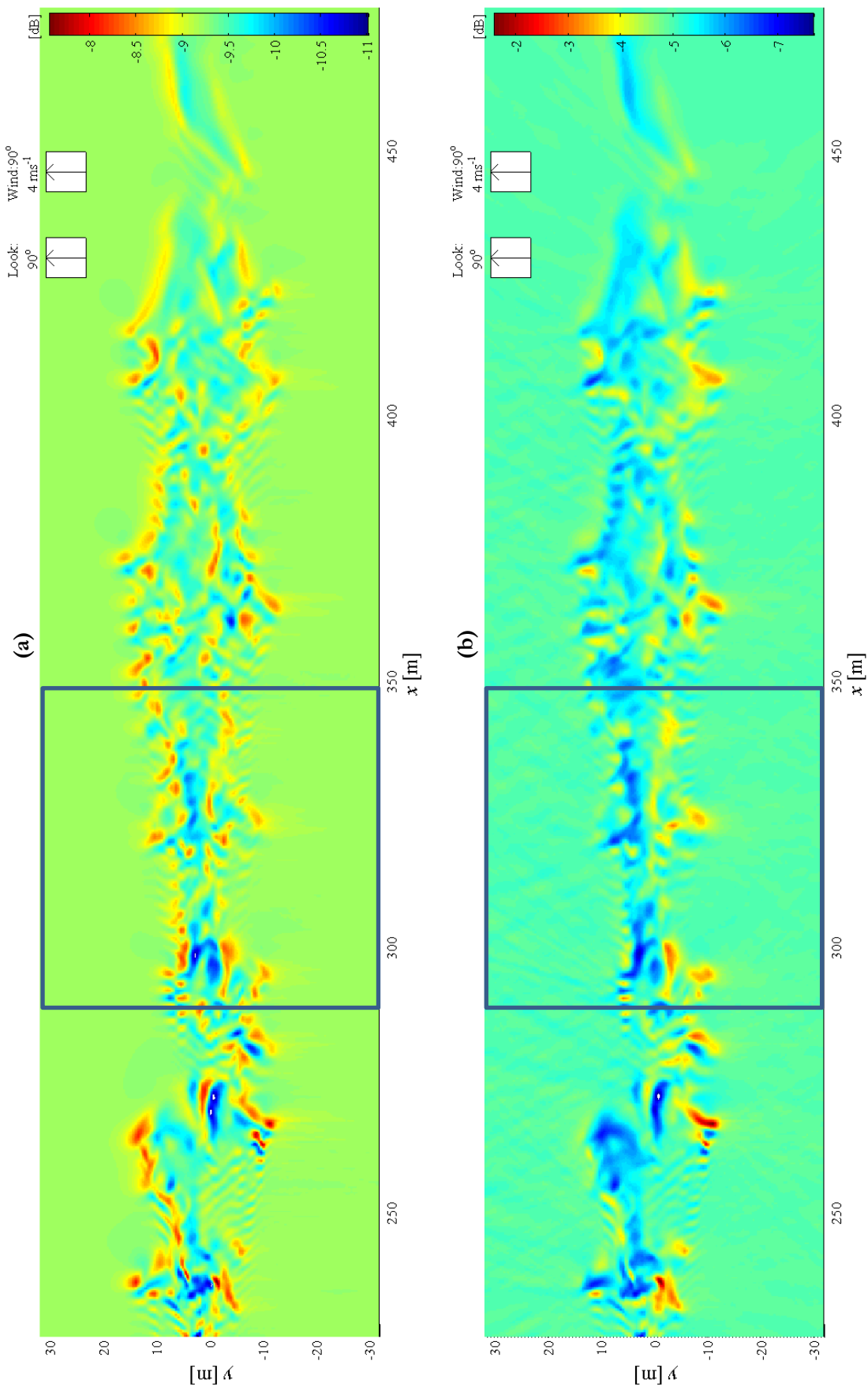
Figure 28 (previous page). Surface wake rendered in (a) Bragg NRCS and (b) composite surface NRCS, for a C-band (5.6 GHz) instrument operating at 23° incidence angle and HH-polarisation. The simulated wind profile is prescribed as a uniform 4 ms⁻¹ aligned with the range (look) direction of the antenna; i.e. the positive y-direction.
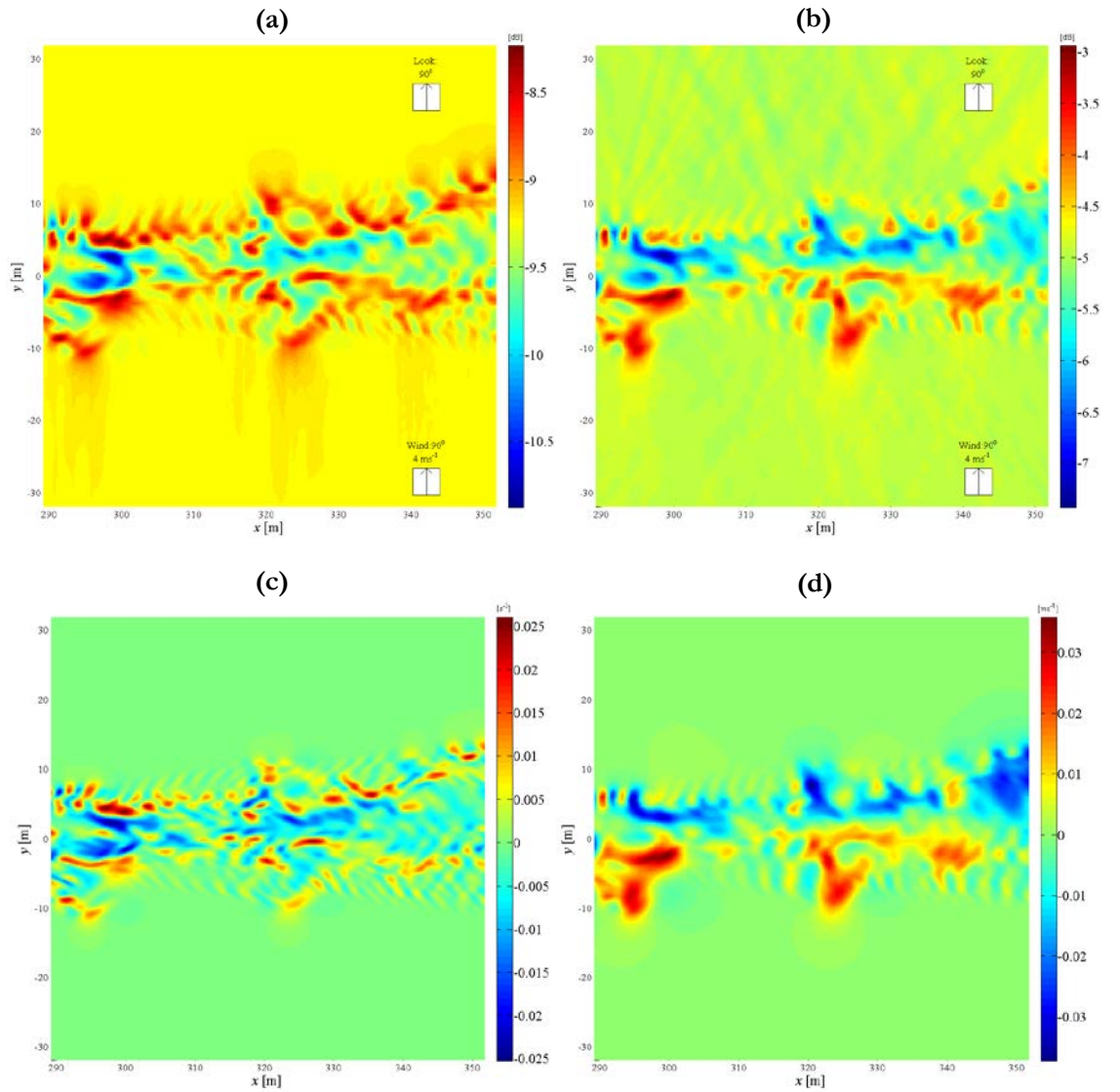
Figure 29. Resolving wake flow structure in simulated NRCS imagery for a 5.3 GHz (C-band) instrument at 23° incidence angle and HH-polarisation for (a) Bragg NRCS and (b) composite surface NRCS. Input profiles for (c) v-velocity (gradient in y-direction); (d) v-velocity (magnitude).

In cases where the radar look direction is aligned parallel with the incident wind, Bragg backscattering (in isolation from long-wave or composite surface effects) can be shown to translate gradients in the component of velocity aligned in the look direction into a resolvable signature. To demonstrate this, Figure 30 (a) depicts a profile over which a 4 ms^{-1} is blowing parallel to the x-axis (that is, aligned with the u-velocity component), being observed in the coincident direction by a (C-band) simulated radar. In parallel with the findings of Figure 29, the Bragg NRCS profile demonstrates a correlation with gradients in the component of velocity aligned in the look direction into resolvable structure (in this case, the gradient of u-velocity in the x-direction). However, as will be discussed in more detail in Chapter 7, the situation is different in cases where there is disparity between the look direction of the radar and that of the primary wind which is responsible for generating the surface profile of backscattering waves.

The texture of the radar backscatter at the wake centre may hence provide indications of internal dynamics within the wake: such texture arises from wave-current interaction between surface motions within the wake and the ambient wave spectrum, and may, in theory, be used to interpret internal flow dynamics. In this respect, the ability to resolve the spatial distribution of wave-current interaction highlights the potential opportunity for high-resolution radar to extract information about surface flow patterns. This ability will, of course, be dependent on the instrument specification (operating frequency, incidence angle and polarisation) as well as the ambient circumstances under which the wake is observed (background wind conditions, alignment of the wake with look direction of the radar, etc.), and these influences are explored more fully in the remainder of this chapter, as well as in Chapter 7.

The results of this chapter have, so far, presented a brief overview of the qualitative similarities between fluid structure of a (hypothetical) surface flow field and the distribution of radar backscattering which may be observed in NRCS images which have been derived under particularly "favourable" conditions. Broadly speaking, the results demonstrate the significant ability of SAR in observing (qualitative) characteristics of flow structures and to understand the source and/or character of a variety of surface flow features. An investigation of the ability of SAR to quantify, or extract information from, radar surface signatures is presented in the following section, whilst the influence of "favourable" and "unfavourable" ambient conditions is considered further in Chapter 7.
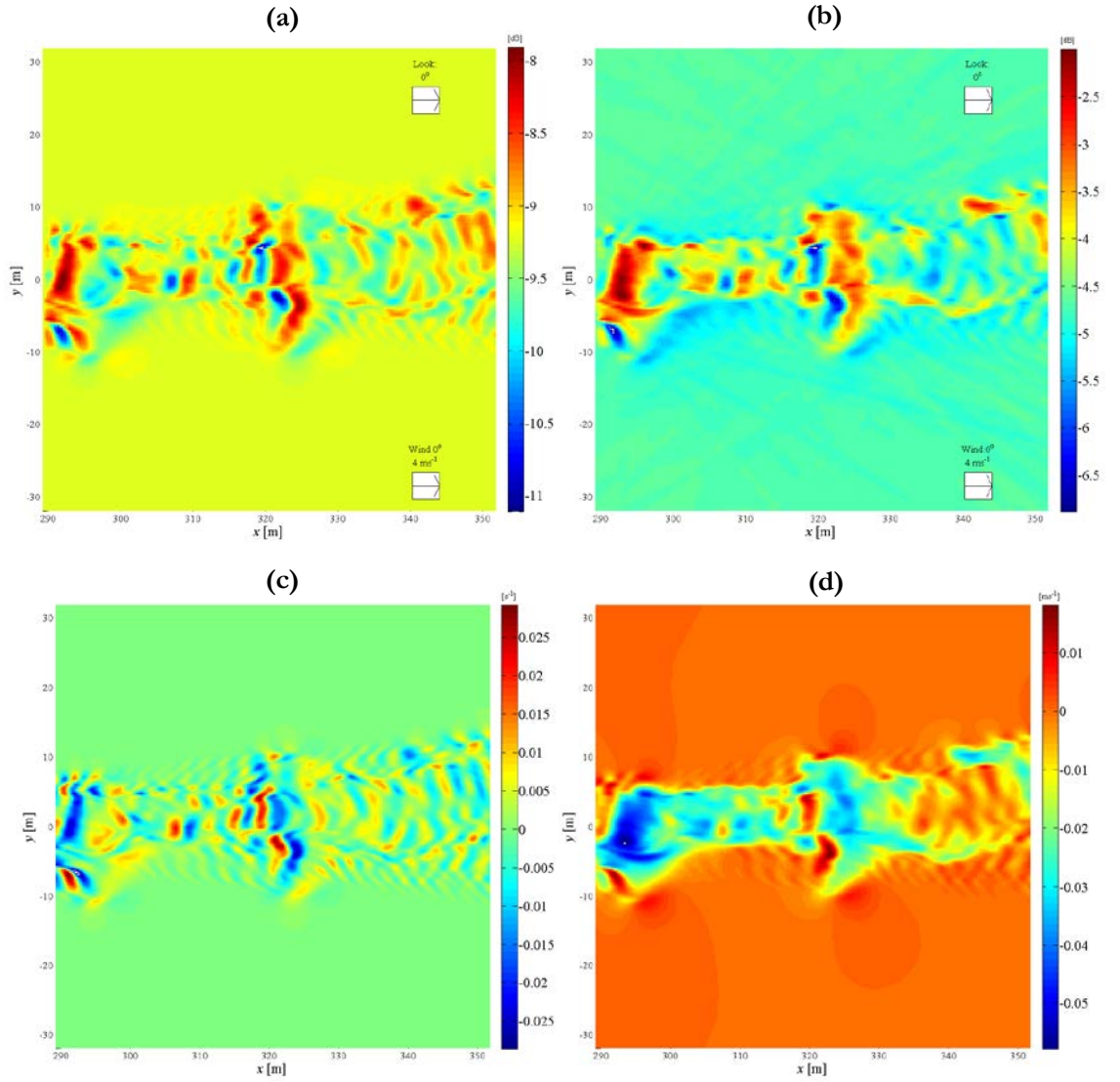
Figure 30. Resolving wake flow structure in simulated NRCS imagery for a 5.3 GHz (C-band) instrument at 23° incidence angle and HH-polarisation observing at a look direction aligned with the x-axis: (a) Bragg NRCS and (b) composite surface NRCS. Input profiles for (c) u-velocity (gradient in x direction); (d) u-velocity (magnitude). 4 ms^{-1} wind is blowing in the x-direction.

6.2 Resolving Radar Signatures and Quantitative Observation of Flow Structure

When considering a radar surface signature, there are two primary "topics" of interest which are relevant to this study; a summary of these topics (and some example questions related to these topics) is listed as follows:

1. Observation of Flow Structure and Current Information {*qualitative*} ~ What features or patterns can be identified or observed within a single image? What information about the surface phenomena can be extracted? What might this information reveal about the source (or character) of the turbulence? Does the radar signature reveal features or components that would not be observed using other remote-sensing means? How 'good' are particular radar/antenna configurations at resolving the structure and observing the flow structure?

2. Visibility of Signature {*quantitative*} ~ How visible is the signature under varying environmental or ambient conditions? What configurations give best performance under a variety of ambient conditions? What improvements in instrument capability are required to improve how they can be resolved? What are the limits under which signatures may be resolved in strong, or weak, ambient conditions?

The discussion presented in §6.1 focussed on qualitative examination of surface wake NRCS profiles and comparison with input flow data, going some way to addressing the questions raised by topic [1]. Topic [2], however, must be addressed by examining the quantitative nature of radar signatures: in the following sub-section, techniques to quantify this structure have been considered in order to extract quantitative data (where possible) about the flow features under scrutiny.

In terms of generating a measurable surface response, there are a number of considerations which govern visibility of a surface signature in a radar image. To resolve the signature against the mean backscattering arising from the surrounding water, sufficient wave-current interaction must drive generation of satisfactory radar modulation such that the radar backscattering pattern deviates from that of the surrounding surface. In addition, there must be a sufficient (mean) value of NRCS such that the (negative modulation from the) radar signature within the wake is observed against the noise floor of the instrument (this is typically -20 to -30 dB). Furthermore, the sensitivity of the instrument to small changes in radar backscattering is important in order to resolve the full range of

variation observed across the signature. Considering the two-dimensional signatures already presented (for example, Figure 30), along with the profile from True et al. (1993) reproduced in Figure 14, the range of positive/negative modulation away from the background response is rarely symmetrical about the background value. In general, the profiles in the current study display larger values of negative modulation than positive; this might indicate a 'stretching' of short waves and/or the obstruction of a wave's passage by the presence of an adverse current. Therefore, whilst signatures may be most visible in terms of negative modulation, it may be harder to resolve such measurements against the noise floor of the instrument. A discussion of the implications for observing low-contrast surface features is raised in the review article by Clemente-Colón & Yan (2000).

In many prominent simulation studies which have considered ship wake surface signatures, a number of characteristic measurements are commonly used to quantify the signature in numerical terms. These have included (but are not limited to) the following measures:

- Ratio of maximum-to-minimum NRCS;
- Modulation depth (max. NRCS - min. NRCS over the entire image; variation of NRCS across signature);
- Radar intensity above minimum intensity level at wake centre;
- Background contrast (NRCS - level of NRCS in ambient region outside of wake);
- Mean NRCS (average across scene, or along a single range line).

The maximum and minimum NRCS values, $NRCS_{max}$ and $NRCS_{min}$, for a radar signature transect and denoted in Figure 31 by features [1] and [2] respectively. The variation between maximum and minimum NRCS observed across the signature is the modulation depth of the image, depicted in Figure 31 by [3] ($NRCS_{max} - NRCS_{min}$).

Since there are some limitations regarding operation of the WKB method for wave-current interaction which have been addressed in Chapter 5, it is most relevant to consider Bragg NRCS modulation (where performance under rapidly-varying currents is more consistent) with respect to the backscattering observed from the stationary ocean surface. Rather than drawing conclusions from 'absolute' values of the NRCS which are referenced on a dB scale, the derived surface signatures are, in the main, examined for relative differences between two signatures, or for their contrast with the 'background' NRCS outside the wake. Where there is only a slender contrast of radar backscattering when displayed on a linear scale or where there is a need to compare

variation(s) between two different images, signatures are presented on dB scale to emphasise such variation. For clarity, decibel images are presented in colour whilst linear NRCS profiles are depicted in greyscale; this is demonstrated, for example, in Figure 31 (a) and (b), which demonstrates a C-band Bragg NRCS profile derived at HH-polarisation and 23° incidence angle presented on dB and linear scales, respectively.

In many of the cases which are presented henceforth, the capability to resolve the turbulent wake has been quantified by characterising the above measures along 'transects' of the NRCS across the wake profile; that is, "slices" of the NRCS in the y-direction of the domain, such as those previously presented in Figures 13 and 14 (from Lyden et al. [1988] and True et al. [1993], respectively). In this respect, measurements along these NRCS transects accompany the two-dimensional surface signatures in the manner shown in Figure 32 (c), which demonstrates the modulation depth observed over the image. It was previously observed, in §6.1, that profiles of Bragg NRCS at, for example, C- and X-band were capable of resolving observed velocity gradients aligned in the radar's look direction: by taking a transect at a position of 324 m in Figure 31 (b) and extracting the (linear-scale) NRCS contrast with the stationary water outside of the wake, a cross-wake transect demonstrates a strong similarity with the distribution of v-velocity gradients in the y-direction shown in Figure 32 (c). In comparison, Figure 33 demonstrates a similar transect, taken from a 1.2 GHz (L-band) Bragg NRCS signatures, and compared with the distribution of v-velocity. As with the previous results, there is correlation with flow characteristics; albeit, in this case, showing similarity with mean current. Such responses further support the findings described qualitatively in the previous sub-section, and reveal how high-resolution radar might be operated to interpret small-scale currents and flow characteristics.

In many profiles derived at low operating frequencies (1.2 GHz L-band and below), some minor artefacts are resolved in the "background" area of the signature; for example, variations which are observed above and below the wake region in Figure 33 (b). Such irregularities are likely to arise from variations in the calculated (modulated) wave spectrum which are most strongly resolved by L-band frequencies and below. While these effects may interfere with the "background" data retrieved by transect plots, a particular effort was made to extract NRCS data from areas where these irregularities cause least disturbance to the signature.

(a)

(b)

(c)
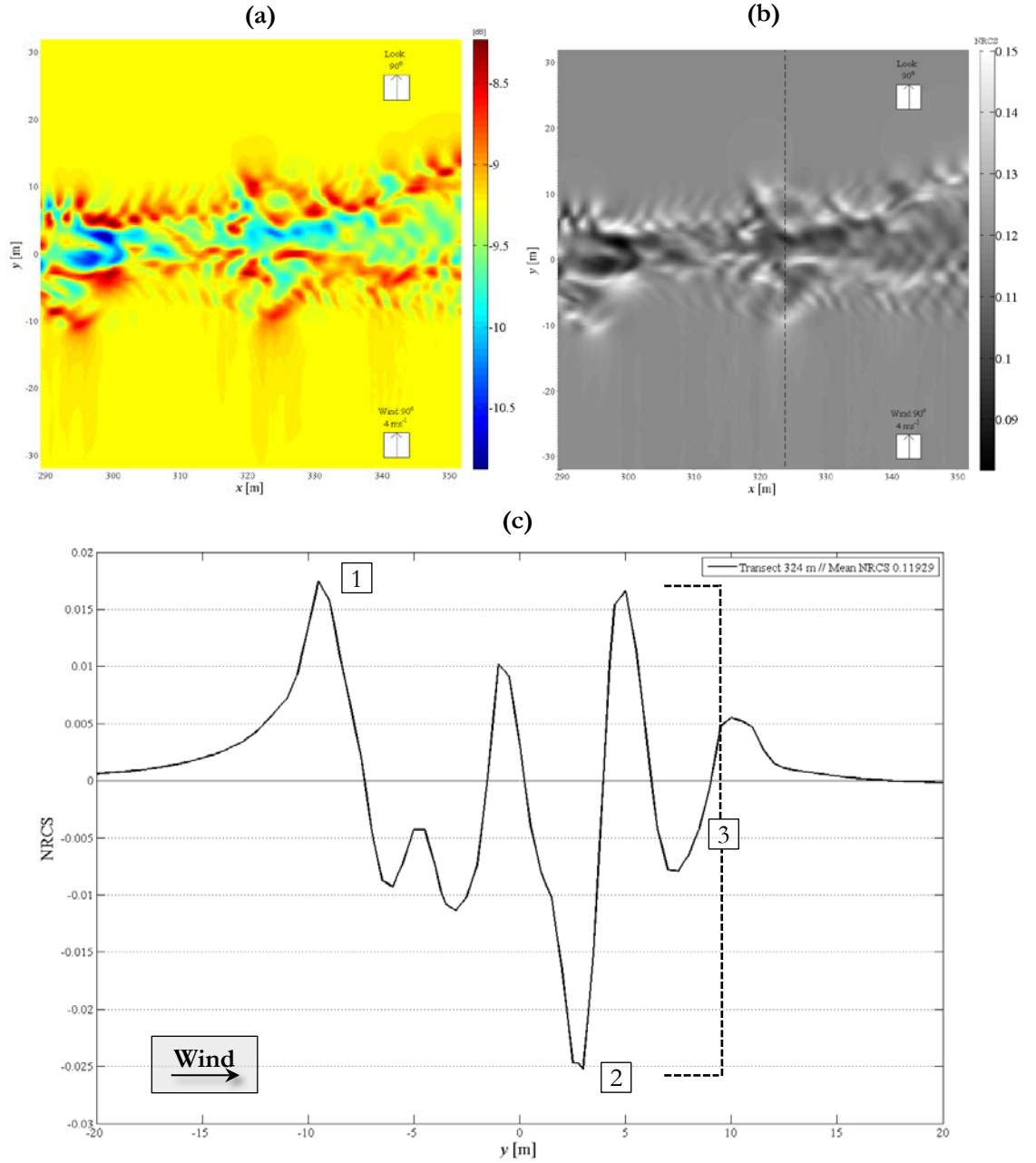
Figure 31. Two-dimensional Bragg NRCS surface signature of a portion of the surface wake (5.3GHz, HH-polarisation, 23° incidence angle) in (a) dB-scale and (b) linear scale; (c) transect of NRCS across the wake, taken at the position marked in plot (b) and referenced to contrast with the 'background' NRCS of the ambient (stationary) water outside the wake. The variation between maximum and minimum NRCS observed across the signature is the *modulation depth* of the image. Key: [1] $NRCS_{max}$; [2] $NRCS_{min}$; [3] Modulation Depth ($NRCS_{max} - NRCS_{min}$).

(a)

(b)

(c)
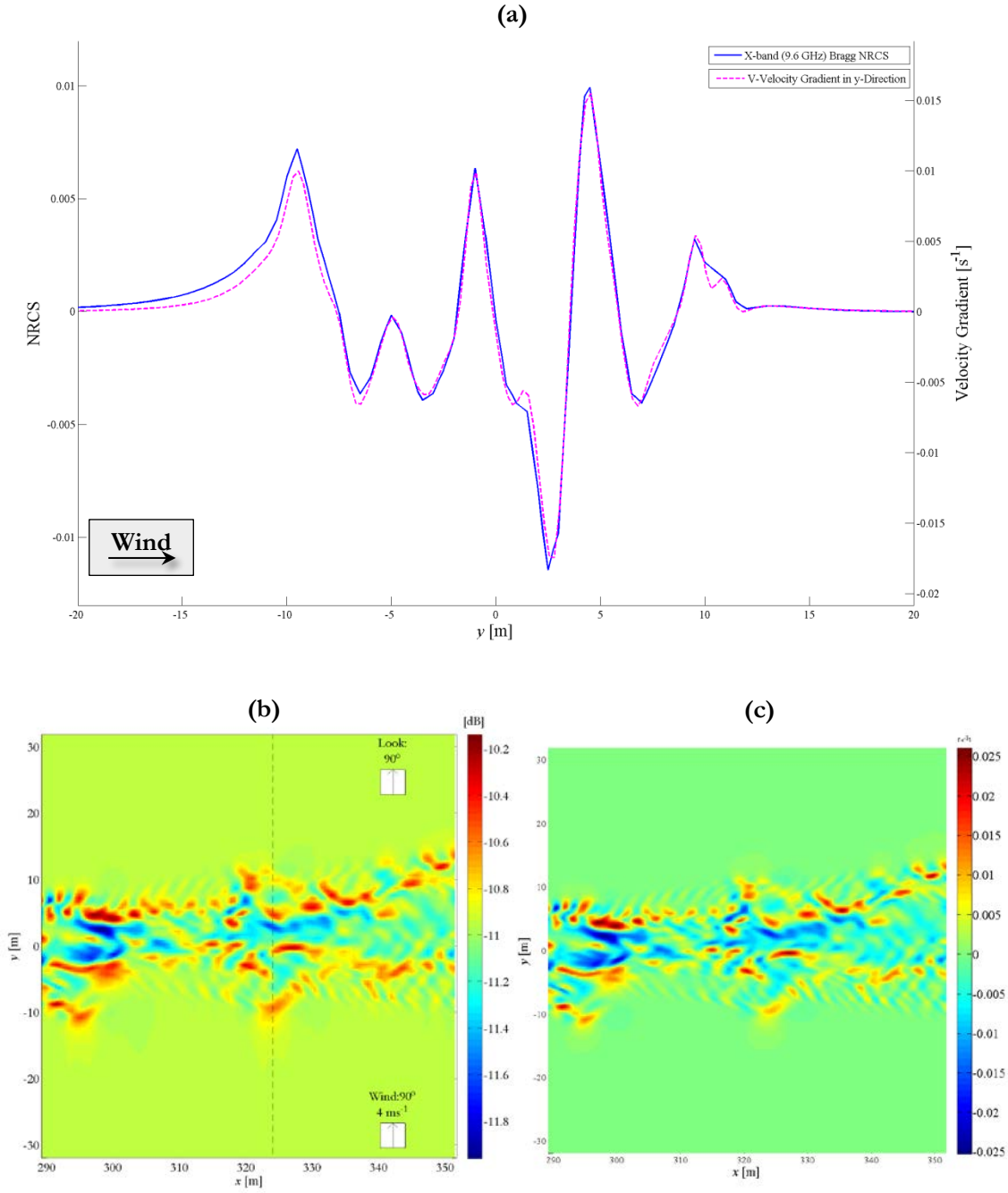
Figure 32. (a) Comparison of transect in the X-band Bragg NRCS profiles [displayed in sub-plot (b)] taken at position $x = 324$ m with transect of the gradient in v-velocity in the y-direction [displayed in sub-plot (c)]. The NRCS transect is scaled relative to the linear Bragg NRCS level of the stationary water outside of the wake region.

(a)

(b)

(c)
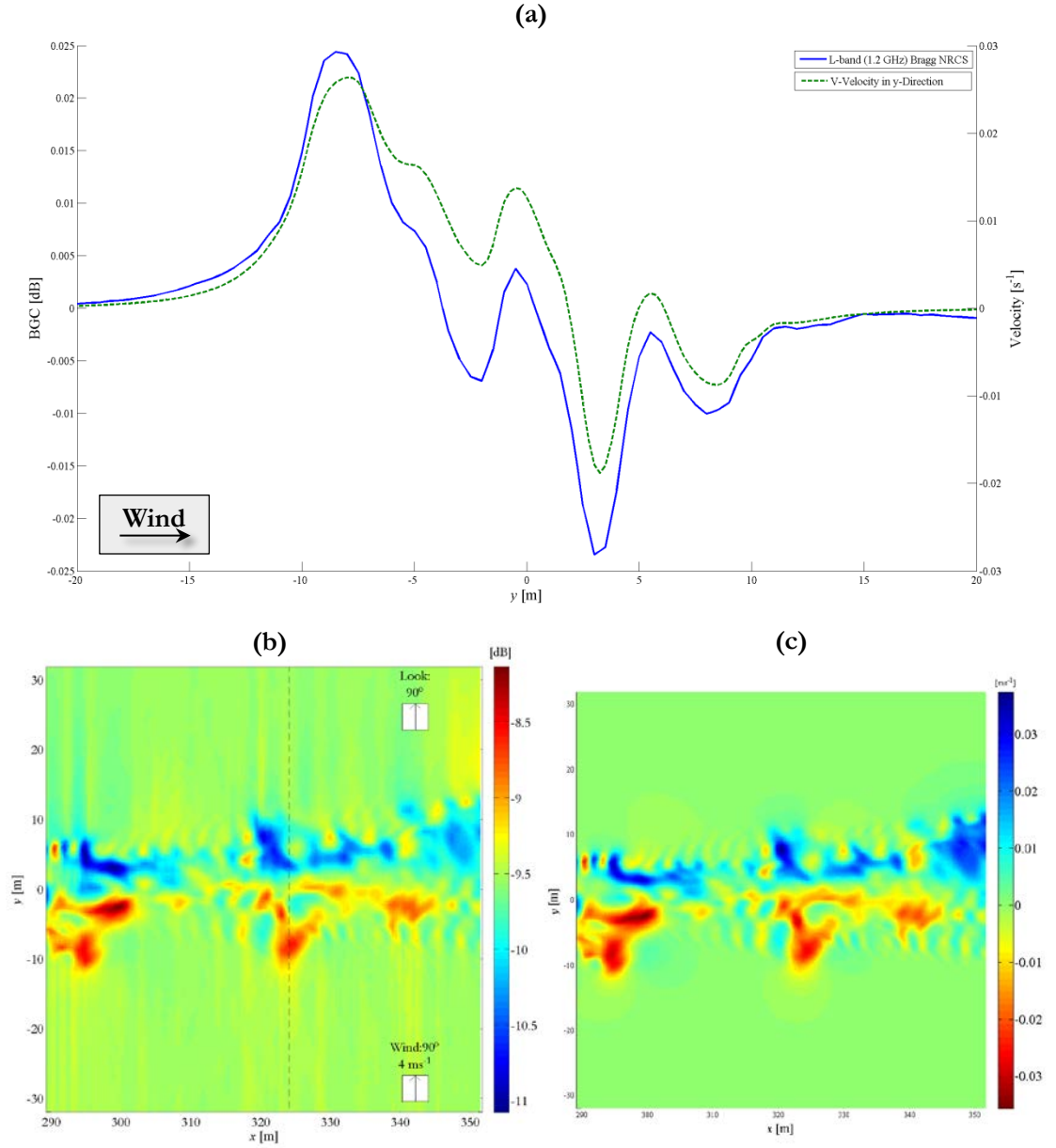
Figure 33. (a) Comparison of transect in the L-band Bragg NRCS profiles [displayed in sub-plot (b)] taken at position x = 324 m with transect of v-velocity in the y-direction [displayed in sub-plot (c); in this case, the colour scale of the velocity plot has been reversed]. The NRCS transect is scaled relative to the linear Bragg NRCS level of the stationary water outside of the wake region.

The remainder of this chapter, along with the one that follows, investigates the effects of varying instrument conditions which affect visibility of the surface wake, and the relative ability to resolve the observed flow structure under distinct wind conditions. The purpose of this process was to explore the "data space" that exists in in the context of the multiple, interacting parameters that govern derivation of theoretical radar surface signatures of Bragg NRCS. In particular, a focus was placed on understanding how different parameters affect the observed response, and what effects they have on the ability to resolve the radar signature of a hypothetical flow field. Presentation of the results of this investigation begins with the variation in observed structure that is resolved when considering different instrument configurations or parameters, such as operating frequency, polarisation and incidence angle.

6.3 Role of Instrument Configuration

Aside from the state of the ocean surface itself (such as the presence of a surface current; the role of the ambient wind field; presence of surfactant materials atop the ocean surface, etc.), the observed radar backscattering profile is predominantly defined by specification of the radar instrument which is used to observe it. From the perspective of simple Bragg backscattering, three primary instrument parameters contribute to Equation (xx), and are as follows:

- Instrument operating frequency (f_0), which contributes to the Bragg wavelength λ_B, but also defines the radar wavenumber, k_0, in Equation (xviii) [§6.3.1].
- Antenna polarisation (HH/HV/VH/VV, etc.), which affects the complex scattering function $G_{pq}(\theta_i, \alpha, \phi)$ [§6.3.2].
- Incidence angle (θ_i), which contributes directly to $\sigma_{0,Bragg}$ through the $\cos^4\theta_i$ term, but also contributes to the observed Bragg wavelength, λ_B [§6.3.3].

The effect of surface tilting on the pure Bragg NRCS varies with both incidence angle and antenna polarisation. The presence of long waves O(1-10 m) at the ocean surface adds further complexity to the effect of instrument configuration on composite surface NRCS: the large-scale wave system causes 'tilting' of the Bragg-scattering surface and modification to the complex scattering function $G_{pq}(\theta_i, \alpha, \phi)$. The ambient conditions which may affect the backscattering response (such as the present wind profile and observation geometry and look direction of the instrument with respect to the wake centreline) are also examined in Chapter 7, whilst the effect of spatial resolution limitations is considered in Chapter 8.

In this current chapter, only parameters associated with the instrument (and affecting direct radar backscatter) have been examined. For all of the cases simulated here, a uniform 4 ms^{-1} wind, blowing parallel to the y-direction, has been assumed and the simulated radar observes the scene in a direction parallel to the wind: this was chosen to provide sufficient wind to derive simulated wave-current interaction effects and to maximise the ability of the radar to detect the subsequent variations of radar backscattering cross-section. The role of instrument configuration on resolving surface wake structure of two-dimensional radar Bragg NRCS signatures is first examined with respect to the effect of radar operating frequency. A comprehensive listing of the examined instrument parameters is presented in Table 7. Notation for the orientation of the incident wind and look directions are made with respect to the x-axis in a counter-clockwise fashion as presented diagrammatically in Figure 34.

Radar Frequency (primary remote-sensing frequencies)	0.4 GHz (P-band)	1.2 GHz (L-band)
	3.2 GHz (S-band)	5.3 GHz (C-band)
	9.6 GHz (X-band)	15 GHz (Ku-band)
	35 GHz (Ka-band)	
Radar Frequency (additional frequencies)	1.4 / 1.6 / 1.8 / 2.0 / 2.6 / 2.9 / 3.0 / 3.1 / 3.3 3.4 / 3.5 / 3.6 / 3.7 / 3.8 / 4.4 / 5.0 / 18.0 21.0 / 24.0 / 27.0 / 30.0 / 33.0 (GHz)	
Incidence Angle	20° / 22° / 24° / 26° / 28° / 30° / 40° / 50° / 60°	
Radar Polarisation	HH / VV / HV	
Wind Direction	90° (to x-direction)	
Wind Speed	4 ms⁻¹	
Look Direction	90° (to x-direction)	

Table 7. Comprehensive description of instrument configurations studied using the *M4S* tool.
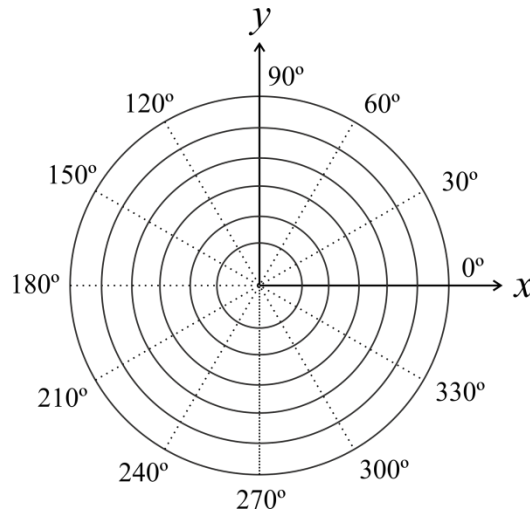
Figure 34. Definition of angle terminology used to describe wind and radar range/look direction(s) used in the remainder of this thesis.

According to Equation (xx), Bragg NRCS is proportional to the wave height spectral density of waves at Bragg wavenumber, k_B; which itself is defined by the operating frequency and incidence angle of the instrument as described by Equation (xviii). As interaction of surface waves and wake-generated turbulent/flow currents may have different effects at different wavelengths (since there may be differing effects on wave energy exchange at different scales), observing the surface at a different Bragg wavenumber therefore provides a different measure of the Bragg-scale wave energy in the presence of the turbulent wake structure. Variation of the observed Bragg wavenumber may be investigated by modifying the instrument operating frequency, f_0, while keeping the prescribed incidence angle of the instrument fixed; or, alternatively, by using the same operating frequency but shifting the operated incidence angle (although this can have additional impacts on radar backscattering, since $\sigma_{0,Bragg}$ is also influenced by a $\cos^4\theta_i$ term). The pure Bragg backscattering

regime is also affected by the polarisation characteristics of the operated instrument; modifying the observed radar response through modification of the complex scattering coefficient, $G_{pq}(\theta_i, \alpha, \phi)$, based on the p, q combination of horizontal- and vertical-polarisation of transmitted and received waves. For simple Bragg scattering, co-polarised (i.e. HH and VV) antennas possess the following functions for the complex scattering coefficient (from Romeiser et al. [1997]):

$$G_{HH} = \frac{\varepsilon}{\left(\cos\theta_i + \sqrt{\varepsilon}\right)^2} \tag{xxvii}$$

$$G_{VV} = \frac{\varepsilon^2(1 + \sin^2\theta_i)}{\left(\varepsilon\cos\theta_i + \sqrt{\varepsilon}\right)^2} \tag{xxviii}$$

Considering the Bragg scattering regime only[13], there is no cross-polarised (i.e. HV or VH) radar return, therefore $G_{HV} = G_{VH} = 0$.

6.3.1 Role of Instrument Configuration I: Operating Frequency

In essence, varying the operating frequency of the simulated instrument has the effect of shifting the wavelength of the surface waves which are responsible for backscattering of radar energy. Different radar frequencies will therefore resolve differing levels of contrast and modulation depth in the wake region (because different wave frequencies experience different characteristics of wave-current interactions), and thus may observe different characteristics or regions of the turbulent wake and its flow structure. Varying the instrument operating frequency will vary the observed spatial backscattering profile (in both pattern and in magnitude of NRCS), therefore there is a potential wealth of "new" information which can be extracted from alternative configurations which are used to analyse the flow; this may include non-canonical frequencies, or multi-frequency instruments which observe the scene at more than one frequency. In previous studies (discussed in §4.2), research has typically focussed on replicating conditions present in real SAR imagery, and hence have largely considered historical spaceborne instrument configurations; namely L-/C-/X-band instruments at 20-30° nominal angle of incidence (or, in a more limited number of cases, airborne configurations with generally higher angles of incidence). There is a grand heritage of ocean SAR instruments at C-band (*ERS-1/2*, *Envisat* ASAR, *RADARSAT-1/2*, forthcoming *Sentinel-1*), and to a lesser extent L- and X-band (*Seasat*, *ALOS* PALSAR; *TerraSAR-X*, *Cosmo-*

---

[13] In the context of the composite surface regime, the form of $G_{pq}(\theta_i, \alpha, \phi)$ is more complex, taking into account the tilting of the ocean surface through tilt angles α and ϕ in the surface plane. With the addition of long waves creating tilting of the surface, the ocean typically generates a cross-polarised radar response under the two-scale regime such that $G_{HV/VH} \neq 0$.

SkyMed); however, operation of other frequencies from space are more sparse. To date, there has thus far been only limited operation of S-band SARs; for example, the Russian *ALMAZ-1* (1991-2) and the forthcoming SSTL *NovaSAR-S* spacecraft (2015). Other frequencies (P-band [~ 0.4 GHz], Ka-band [~15 GHz], Ku-band [~35 GHz]) have seen limited study from airborne platforms such as the SARSEX (1984, Ka-/Ku-band) campaign and multiple campaigns of the NASA AIRSAR and DLR E-/F-SAR platforms (P-band, among other frequencies). New missions are typically designed to provide continuation of data at existing radar frequencies such as L-, C- and X-band. Therefore, analysis of the simulation surface signatures presented here was performed from the perspective of understanding whether alternative configurations could offer benefits for ocean study.

Considering the four primary radar frequencies used in airborne/spaceborne SAR (1.2 GHz L-band, 3.2 GHz S-band, 5.3 GHz C-band, 9.6 GHz X-band), Figure 35 depicts the effect of observing a region of Wake Profile 1-B on Bragg NRCS (dB scale) by shifting the defined frequency at a fixed incidence angle of 23° and HH-polarisation. The qualitative pattern of NRCS modulation within the four sub-plots of Figure 35 demonstrates that the distribution of Bragg wave energy (and thus levels of radar backscatter) varies with k_B, in addition to the levels of modulation which are observed[14]. The L-band (1.2 GHz) plot of Figure 35 (a) shows a relationship of positive/negative on the upwind/downwind edges of the wake which qualitatively resembles the C-band (5.3 GHz) composite surface NRCS profile which was previously presented in Figure 29 (b); although there are minor differences in the spatial distribution and also in the observed levels of modulation. In this respect, the L-band signature also closely matches the observed v-velocity profile, suggesting that the spanwise velocity component (which, in this case, is aligned with the incident wind direction) may be resolved with respect to the components of the wave spectrum at L-band or larger (i.e. those contributing to composite surface response). In comparison, profiles of Bragg NRCS derived at higher frequencies (particularly C- and X-band) more clearly resolve the interior structure of the wake as well as distinguishing backscattering peaks at the edges of the wake region with some clarity: in these profiles, of the internal flow structure and dynamics is visible in the distribution of positive/negative (NRCS) modulation which is present in the centreline area of the wake. As was established in §6.1, Bragg NRCS profiles at C- and X-band show resemblance to the distribution of velocity gradients aligned with the wind and/or look direction of the radar: this is most prevalent in revealing the wake edges (where there a gradients with the stationary water, and in revealing some of the internal dynamics and structure of the interior of the wake.

---

[14] The reader is advised to take note of the differing colour values which are used for each image, which demonstrates the variation in NRCS modulation observed at varying frequency.
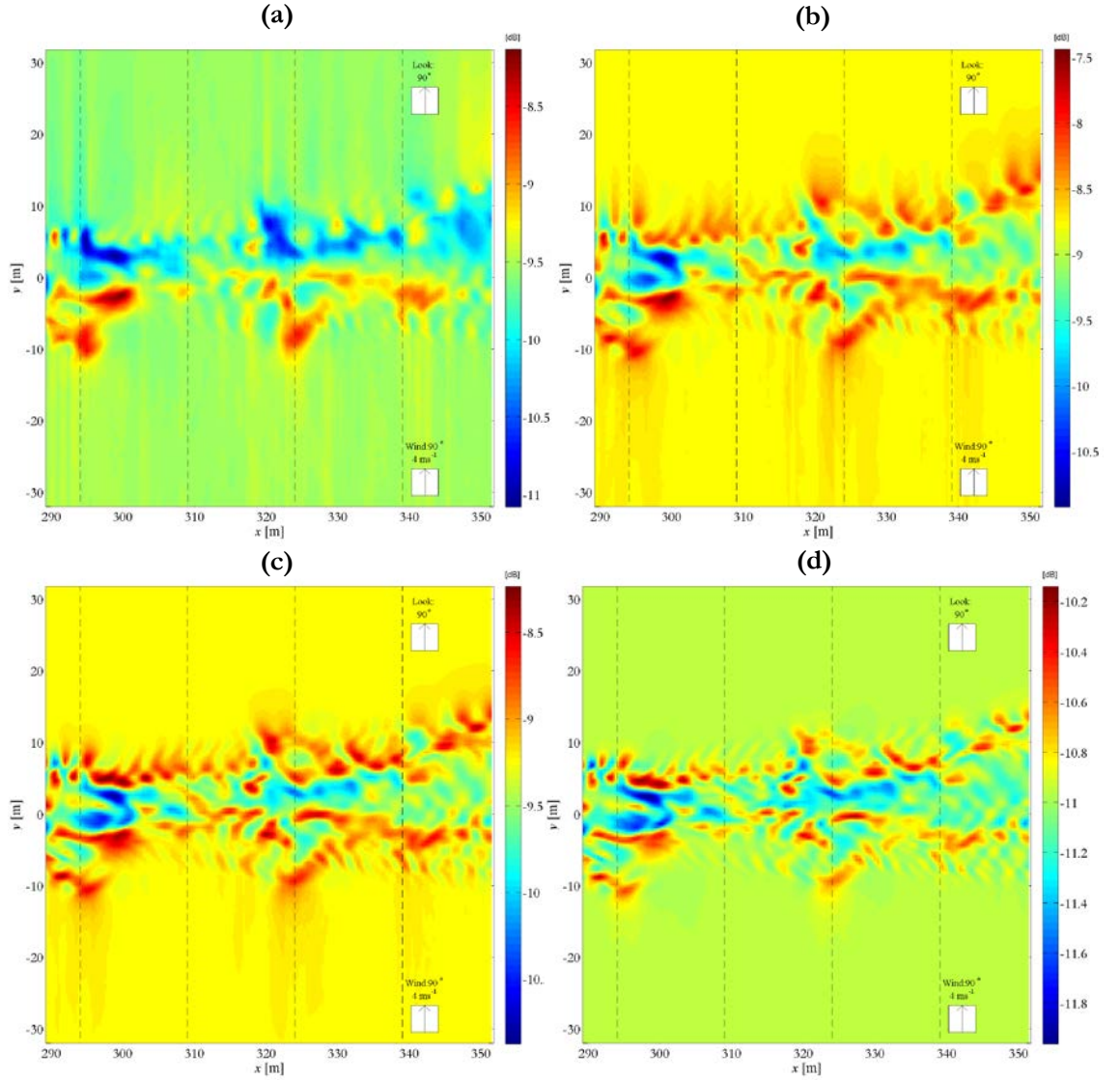
Figure 35. Effect of radar frequency on visibility of flow structure in Bragg NRCS profile: (a) L-band [1.2 GHz]; (b) S-band [3.2 GHz]; (c) C-band [5.3 GHz]; (d) X-band [9.6 GHz]. For all plots shown, the simulated instrument is HH-polarised and with an incidence angle of 23°. The NRCS values in all figures are presented in decibel (dB) form.

From Figure 35, transects of Bragg NRCS were extracted at four different positions along the x-axis and presented in Figure 36 for simulated L-, S-, C- and X-band frequencies. In the derived transect data, the performance of various radar frequencies in resolving structure across the wake

flow may be assessed by presenting the contrast of each profile against the background NRCS of the stationary water outside of the wake. The mean NRCS value of each frequency along the transect is displayed in the figure legend, whilst statistics of the measured modulation depth along each transect, and the mean NRCS and modulation depth observed across the whole image, are tabulated in Table 8. The variation in shape of the extracted Bragg NRCS transects is evidence that the presence of flow structure (and subsequent wave-current interaction arising from interaction with the ambient ocean spectrum) has differing effects at different wavenumbers or regions of the ocean wave spectrum; not just in the magnitude of modulation (i.e. height of the peaks), but in the 'shape' of the observed transect profile.

Considering the transects of Bragg NRCS presented in Figure 36, it can be observed that 3.2 GHz (S-band) profiles typically present a strong depth of modulation; this depth shows a decrease with increasing (C-, X-band) or decreasing (L-band) frequency. Where L-band profiles display increased backscatter in areas of strong positive modulation (e.g. feature [4] of Figure 36 [d]), in areas of reduced backscattering responses, L-band signatures often do not display such negative modulation as for S-band (e.g. feature [5]). Similar trends are observed for increasing frequency from S-band to C- and X-band. However, there is some inconsistency towards the response and location(s) of peaks at different radar frequencies, arising from differing wave-current interaction occurring at varying ocean wavenumbers (and hence k_B).

Figure 36 (following pages). Effect of radar frequency (L-, S-, C- and X-bands) on visibility of flow structure, across four transects in the Bragg NRCS profiles displayed in Figure 35. Transects of NRCS are taken at (a) x = 294 m; (b) x = 309 m; (c) x = 324 m; (d) x = 339 m. For all plots shown, the simulated instrument is HH-polarised and with an incidence angle of 23°. Each frequency transect is scaled relative to the linear Bragg NRCS level of the stationary water outside of the wake region.

(a)

(b)

(c)

(d)
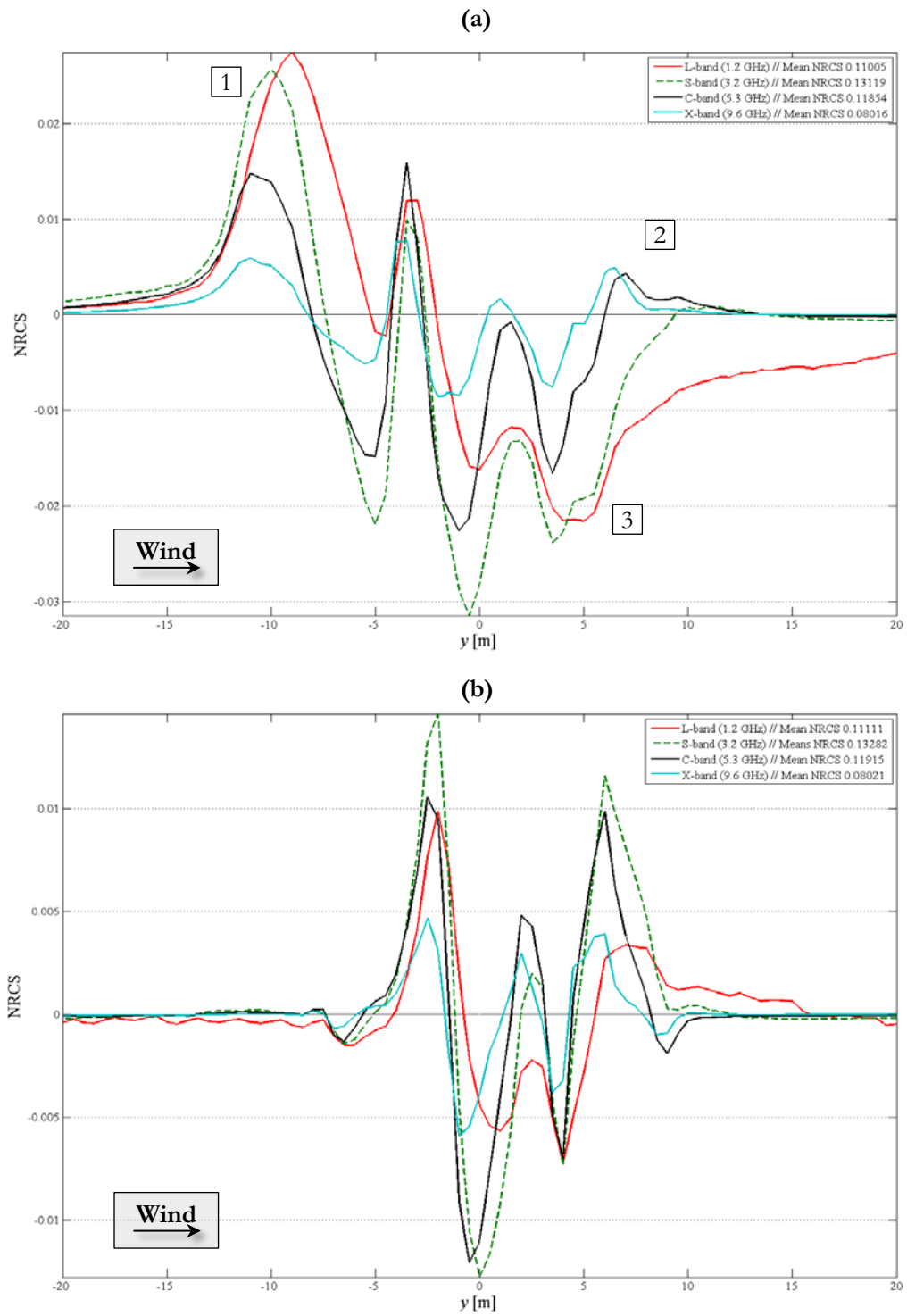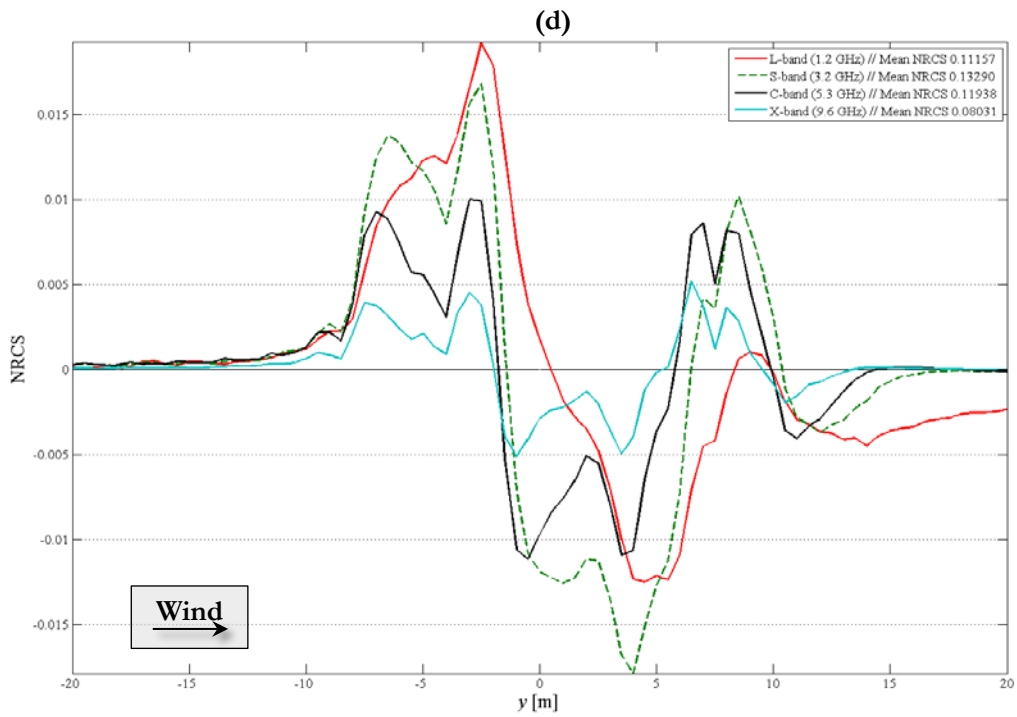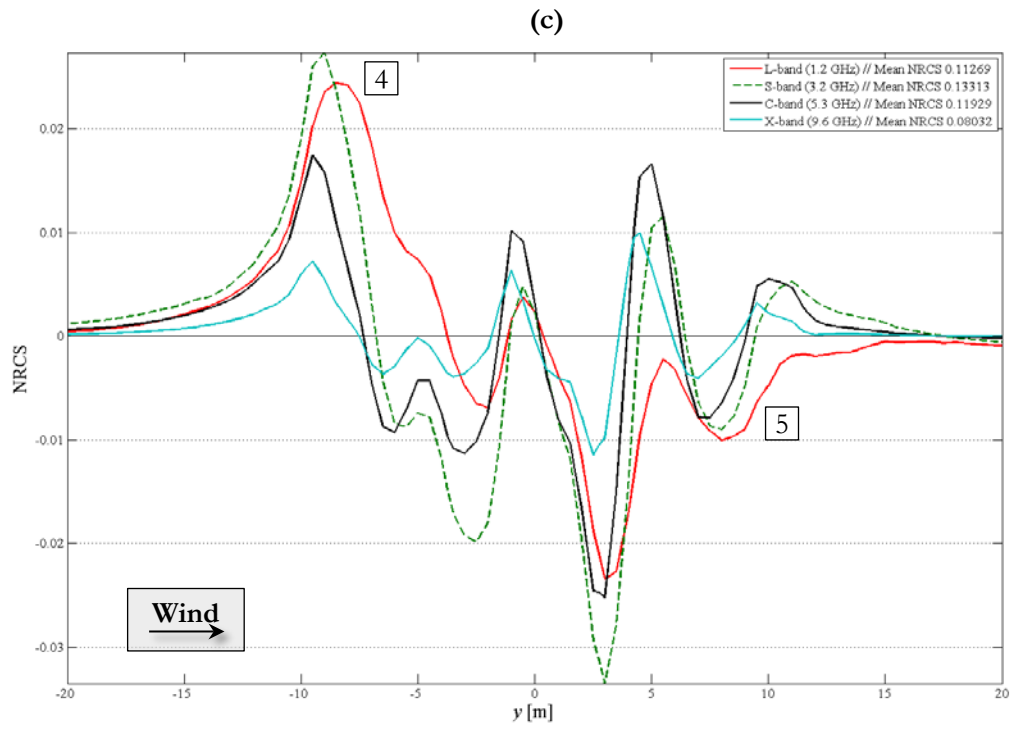
In addition to coverage of canonical operating frequencies such as L-, S-, C- and X-band, it is relevant to discuss also the role of other, more non-canonical frequencies which may be employed for radar observation of turbulence surface signatures; primarily those below 1 GHz (P-band) and beyond 10 GHz (Ku-, Ka-bands). Figure 37 depicts Bragg NRCS profiles for these frequencies, derived for a simulated HH-polarised instrument at a 23° incidence angle, with the resulting surface signatures displayed in a decibel scale with differing colour axes. For these cases, signatures for P- (0.4 GHz), Ku- (15 GHz) and Ka- (35 GHz) bands are depicted alongside a typical 5.3 GHz (C-band) signature for comparison (depicted by a solid black line). Transects of Bragg NRCS, taken at four positions in the x-axis from the profiles of Figure 37, are also presented in Figure 38; statistics for these cases can be found in Table 8. Results from these frequencies generally show a continuation of the trends revealed for L- to X-band frequencies. For example, decreasing to a 400 MHz (P-band) frequency (k_B = 29.3 cm) demonstrates a further reduction in modulation depth from that observed at L-band; whilst increasing to Ku-/Ka-band presents reduction in modulation depth beyond that measured for the X-band profile. It can be seen that Ku-/Ka-band signatures demonstrate very slender depths of modulation but high levels of mean NRCS. At frequencies beyond ~12 GHz, the Bragg wavenumbers associated with a 23° incidence angle are in excess of ~643 s^{-1} (λ_B < 2.5 cm), therefore derive primary Bragg backscattering from surface waves shorter than 1 cm. Such waves are very short, and with short-lived timescales, therefore do not respond to modulation (since they are very sensitive to changes in the wind and/or currents) in the same manner as capillary-scale waves at longer wavelengths; such that their surface signatures are resolved only modestly.

As operating frequency is increased, the Bragg NRCS signature is sensitive to gradients in velocity: on the transect plot(s) of Figure 38, the Ka-band profile (blue line) shows modest variation when compared to, for example, the P- or C-band profiles (dashed green and solid black lines, respectively). However, by plotting the C-band and Ka-band Bragg NRCS on separate vertical axes, as is shown in Figure 39, it is possible to see that each profile retains the same relative structure (as would be expected from the general theory). Therefore, whilst a C-band instrument will likely observe greater variation of NRCS values based on modulation depth at this frequency, this demonstrates that satisfactory extraction of surface flow structure(s) could be achieved with a high-frequency instrument, should the antenna be very sensitive to small variations of NRCS. Of course, this statement does not address the implications of resolving components of Bragg backscattering in the context of a composite surface profile, where there may be greater difficulty in extracted (Bragg) NRCS modulation over contributions from other regions of the surface wave spectrum.
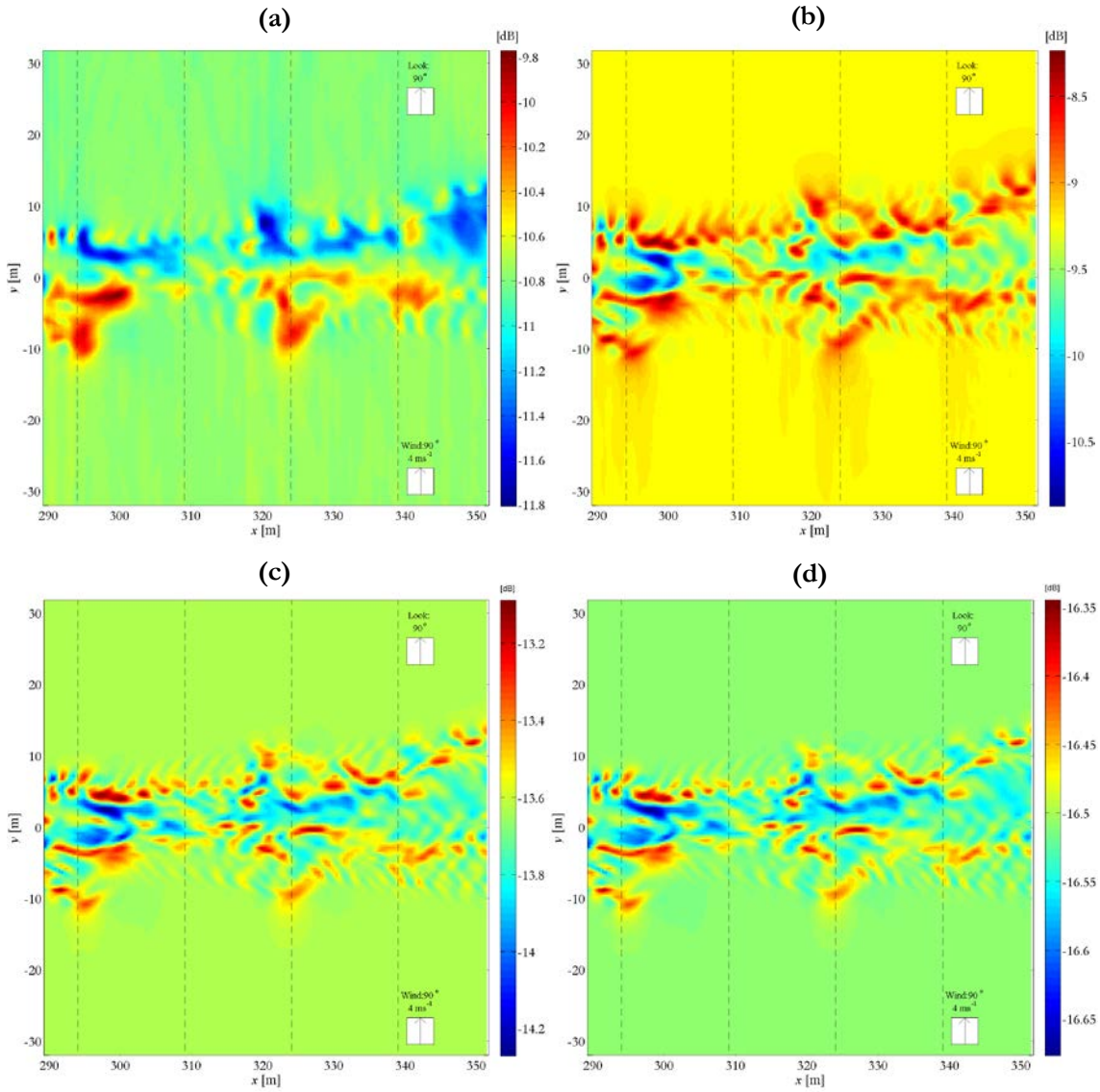
Figure 37. Effect of radar frequency on visibility of flow structure in Bragg NRCS profile: (a) P-band [0.4 GHz]; (b) C-band [5.3 GHz]; (c) Ku-band [15 GHz]; (d) Ka-band [35 GHz]. For all plots shown, the simulated instrument is HH-polarised and with an incidence angle of 23°. The NRCS values in all figures are presented in decibel (dB) form.

Figure 38 (following pages). Effect of radar frequency (P-, C-, Ku- and Ka-bands) on visibility of flow structure, across four transects in the Bragg NRCS profiles displayed in Figure 37. Transects of NRCS are taken at (a) $x = 294$ m; (b) $x = 309$ m; (c) $x = 324$ m; (d) $x = 339$ m. Each frequency transect is scaled relative to the linear Bragg NRCS level of the stationary water outside of the wake region.

(a)

(b)

(c)

(d)
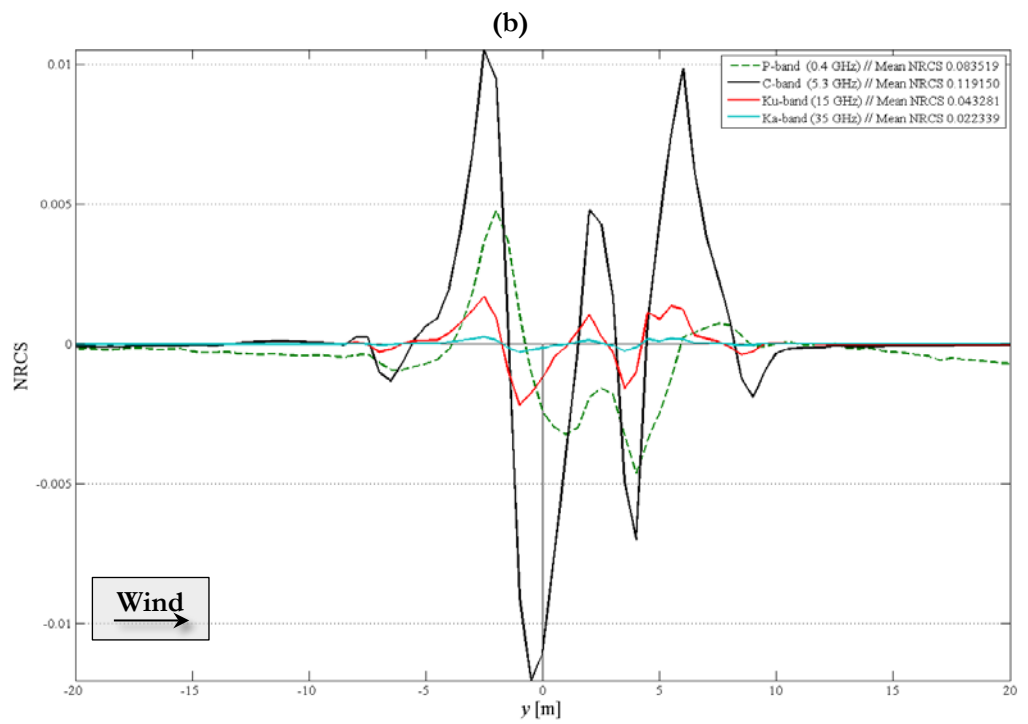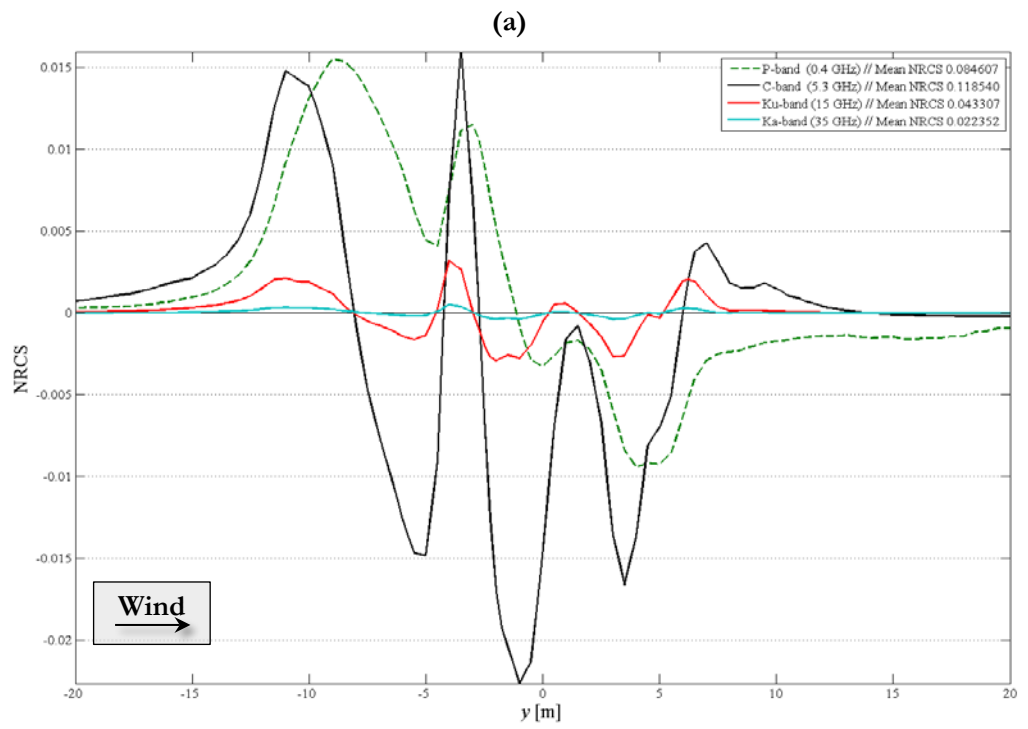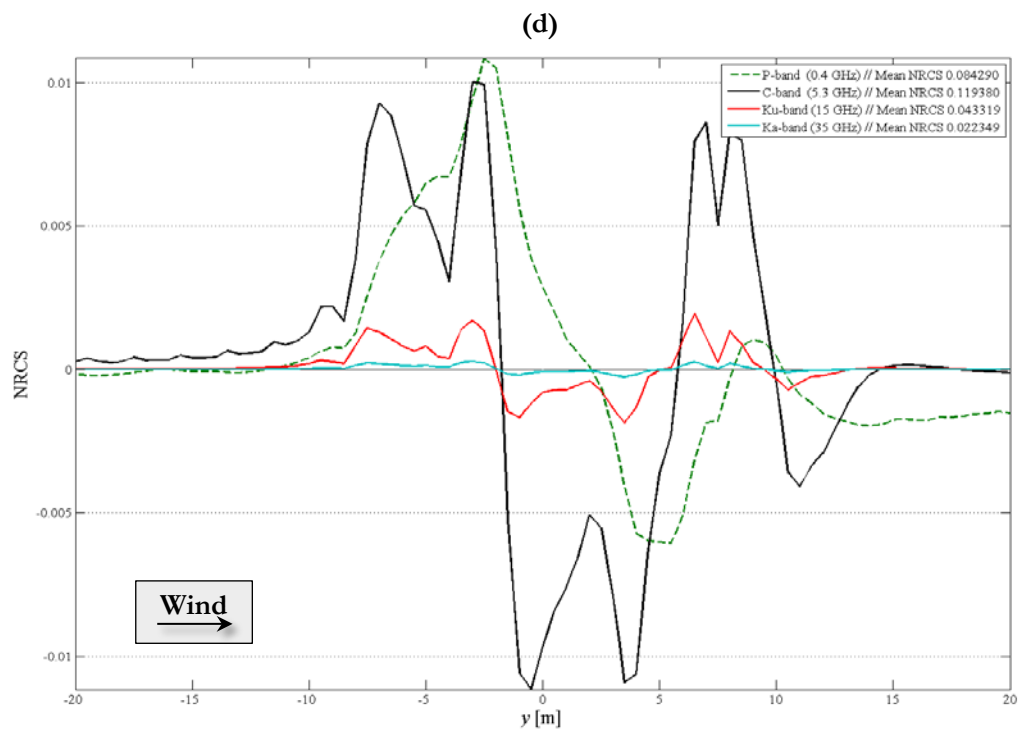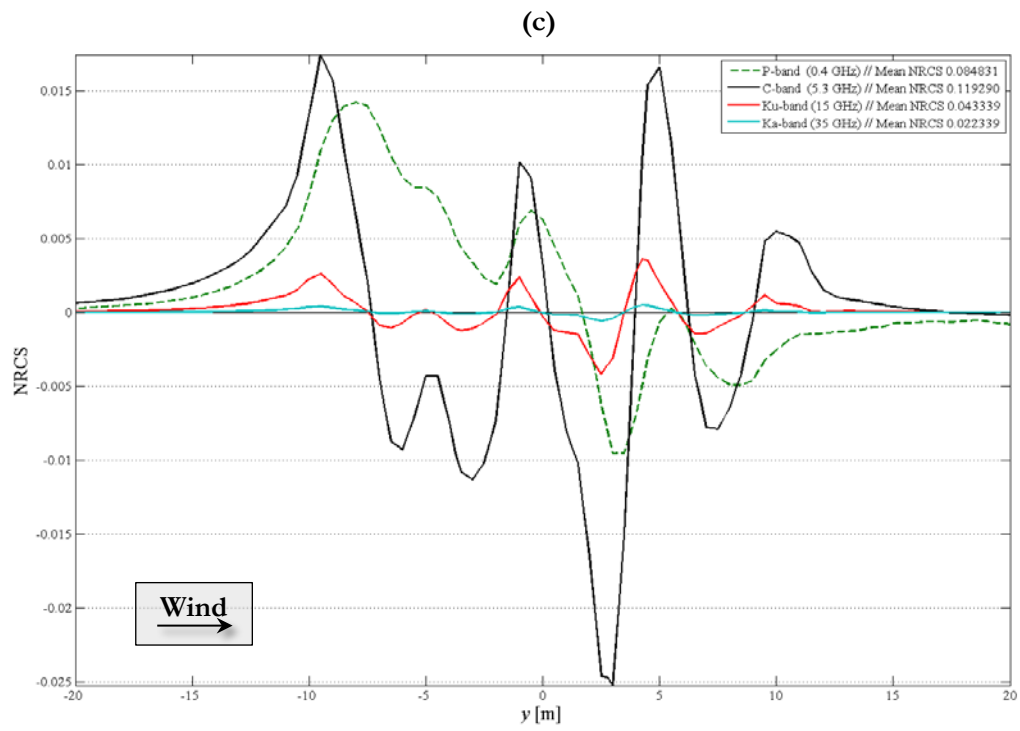
Radar Frequency	Position of Transect				Across Whole Image	
	294 m	309 m	324 m	339 m	Mean NRCS	Mod. Depth
P-band (0.4 GHz)	0.024939	0.009408	0.023786	0.016896	0.0837	0.0394
L-band (1.2 GHz)	0.049057	0.017149	0.047883	0.031764	0.1110	0.0756
S-band (3.2 GHz)	0.057196	0.027353	0.060867	0.034722	0.1326	0.0993
C-band (5.3 GHz)	0.038564	0.022577	0.042724	0.021192	0.1191	0.0684
X-band (9.6 GHz)	0.016322	0.010588	0.021400	0.010330	0.0802	0.0332
Ku-band (15 GHz)	0.006120	0.003894	0.007791	0.003822	0.0433	0.0117
Ka-band (35 GHz)	0.000891	0.000538	0.001086	0.000544	0.0223	0.0017

Table 8. Modulation depths (in linear NRCS form) taken along individual range lines from Figure 37 at various positions in the x-axis; variation with operated radar frequency.
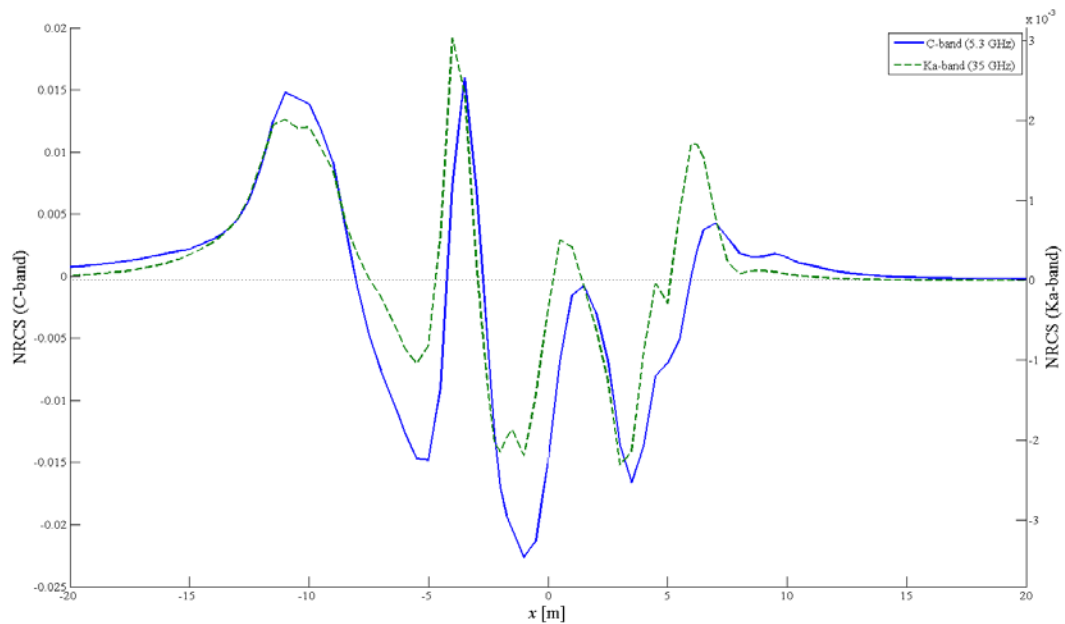
Figure 39. Comparison of Ku- and C-band backscattering along transect of Bragg NRCS profiles taken at $x = 294$ m of Figure 37 (a). For both profiles, the simulated instrument is HH-polarised and with an incidence angle of 23°. Each frequency transect is scaled relative to the linear Bragg NRCS level of the stationary water outside of the wake region.

In terms of trends observed in the profiles (of background contrast) presented thus far, the greatest range of modulation depth of Bragg NRCS along a single transect is consistently displayed by a simulated radar at S-band (3.2 GHz) frequency the S-band profile (showing a Bragg wavenumber k_B = 9.37 cm for 23° incidence angle) displays a positive NRCS modulation typically on the order of (or greater) than L-band, and negative modulation in excess of other frequency profiles, thus deriving a larger total modulation depth. Feature [1] of Figure 36 demonstrates the effect of varying frequency on a single peak of Bragg NRCS: with increasing radar frequency (and hence k_B), the location at which the first peak of modulation (from the left-hand side of Figure 36 [a]) moves increasingly leftwards. Differing textures & patterns are observed with different k_B: L-band profiles, in general, display a substantial modulation depth of NRCS values observed over a single transect or the whole image (which may aid discrimination of the signature within a particular scene), but demonstrate more difficulty in resolving internal structure of the wake. In this respect, where the upwind NRCS peak depicted in feature [2] of Figure 36 is discriminated in all frequency profiles, the peak depicted in feature [3] in the wake interior is not resolved at L-band (although it has been established that this is due to different frequencies responding to differing aspects of the current field). Where S-, C- and X-band profiles show similar themes in the observed variation in NRCS along a single transect (although different values of background contrast), the structure observed at L-band demonstrates a marked change in the observed pattern.

In Figure 40, the NRCS contrast observed along the four transects of Wake Profile 1-B (studied for varying radar operating frequency in Figures 36 and 38) is presented against frequency. The total modulation depth (across the whole image) is also presented for its variation with operating frequency. It is clearly visible that the same trend is not observed at each transect, therefore there are changes in the 'shape' of the frequency-contrast profile at different transects in addition to differences in the relative magnitudes of contrast displayed between different transects. If (maximum) NRCS contrast is to be used as a goal for selecting a desirable operating frequency for study of surface flow features, it is relevant to consider the location of maximum contrast over both y-axis transects and over the entire image[15]: x = 294 m (2.6 GHz), x = 309 m (3.2 GHz), x = 324 m (2.6 GHz), x = 339 m (2.0 GHz); total modulation depth (2.6 GHz). Peak ability to observe a large modulation depth, over the hypothetical flow feature and limited ambient conditions considered here, therefore occurs in an S-band configuration in the region of 2.0-3.2 GHz. For reference, the maximum level of mean (and background) image NRCS observed across all of the studied frequencies is observed at 3.2 GHz.

---

[15] Of course, this discussion is made without consideration of frequency (band) designations stipulated by the ITU and IEEE which SAR operators must adhere.
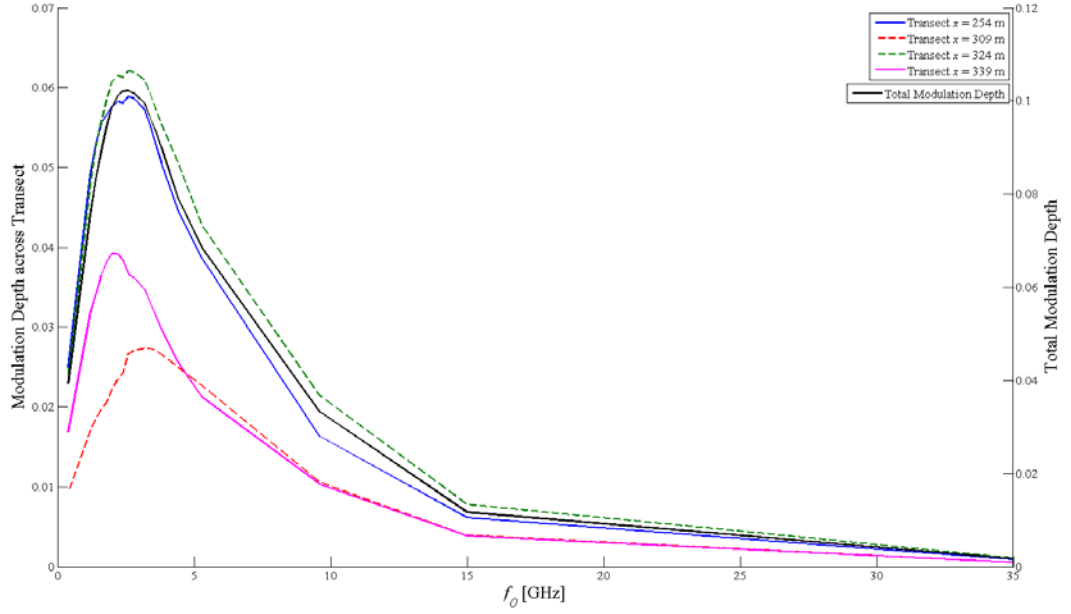
Figure 40. Variation of modulation depth with radar frequency for transects of Wake Profile 1-B presented in Figures 36 and 38. For all cases, the profile was subject to 4 ms^{-1} blowing in a direction parallel to y-direction and observed with a simulated HH-polarised antenna at 23° incidence angle and look direction in the y-axis.

6.3.2   Role of Instrument Configuration II: Antenna Polarisation

From Equation (xx), the observed Bragg backscattering response of the ocean surface has a dependency on $G_{pq}(\theta_i, \alpha, \phi)$; a function describing the complex scattering of the surface at different radar polarisation and surface tilting effects. Observing the ocean surface at differing antenna polarisation hence yields a modified scattering response in both Bragg and composite surface NRCS profiles. For Bragg backscattering only, there is no cross-polarisation of incident radar waves since direct Bragg backscattering causes reflection of incident radar waves at the same polarisation (i.e. no cross-polarisation of radar waves, therefore), G_{HV} and G_{VH} are zero. Under the two-scale model, tilting of the Bragg backscattering surface may cause some incident waves to change polarisation, therefore G_{HV} and G_{VH} are non-zero; to simplify radar scattering calculations, G_{HV} and G_{VH} are assumed to be equal, leading to identical responses in composite surface NRCS at HV- and VH-polarisation. Modifying the simulated radar polarisation therefore

alters the observed scattering signature, and the effects of differing polarisation can be observed for the simulated Bragg NRCS signatures presented in Figure 41.

In Figure 41 (a) and (b) (for HH- and VV-polarised responses presented on decibel scale), the Bragg NRCS profiles have been depicted on differing colour axes demonstrating no change in the observed spatial pattern of the signatures or in modulation depth (although there is increase in the mean NRCS). In terms of relative contrasts on a linear NRCS scale, the HH- and VV- Bragg NRCS transect profiles shown in Figure 41 (c) demonstrates the deviation of the profile from the 'background' Bragg NRCS of the surrounding, stationary water and variation in radar backscattering at different polarisation: there is an increase in modulation depth and mean NRCS in the VV-polarised case (0.1128 and 0.2058, respectively) over the HH-polarised cases (0.0653 and 0.1191, respectively). Considering signatures derived using the two-scale model, modulation depth (on a σ_0 linear NRCS scale) is larger at VV-polarisation although greater difference between maximum and minimum dB values (on $\sigma_{0,dB}$ NRCS scale) is observed at HH- than for VV-polarisation. Statistics from the examined range of polarisation cases are presented in Table 9.

Polarisation	Position of Transect				Mean NRCS	
	356.5 m	371.5 m	386.5 m	401.5 m	Linear Scale	dB Scale
HH	0.038564 1.4594 dB	0.022577 0.8316 dB	0.042724 1.6269 dB	0.021192 0.7775 dB	0.1191	-9.25 dB
VV	0.066607 1.4594 dB	0.038994 0.8316 dB	0.073792 1.6269 dB	0.036602 0.7775 dB	0.2057	-6.87 dB
HH	0.20564 2.6362 dB	0.091496 1.2133 dB	0.21709 2.9035 dB	0.145120 1.8674 dB	0.3206	-4.95 dB
HV / VH	0.000261 1.4967 dB	0.000166 1.0009 dB	0.000332 2.0078 dB	0.000163 0.9420 dB	0.0007	-31.29 dB
VV	0.236110 2.3907 dB	0.106870 1.0965 dB	0.25606 2.6801 dB	0.167670 1.6861 dB	0.4143	-3.84 dB

Table 9. Modulation depths (in linear Bragg NRCS form) taken along individual range lines from Figure 41 at various positions in the x-axis; variation with operated radar polarisation. Rows which are highlighted in a light blue tone present results from Bragg NRCS profiles; in light green represent composite surface NRCS results.
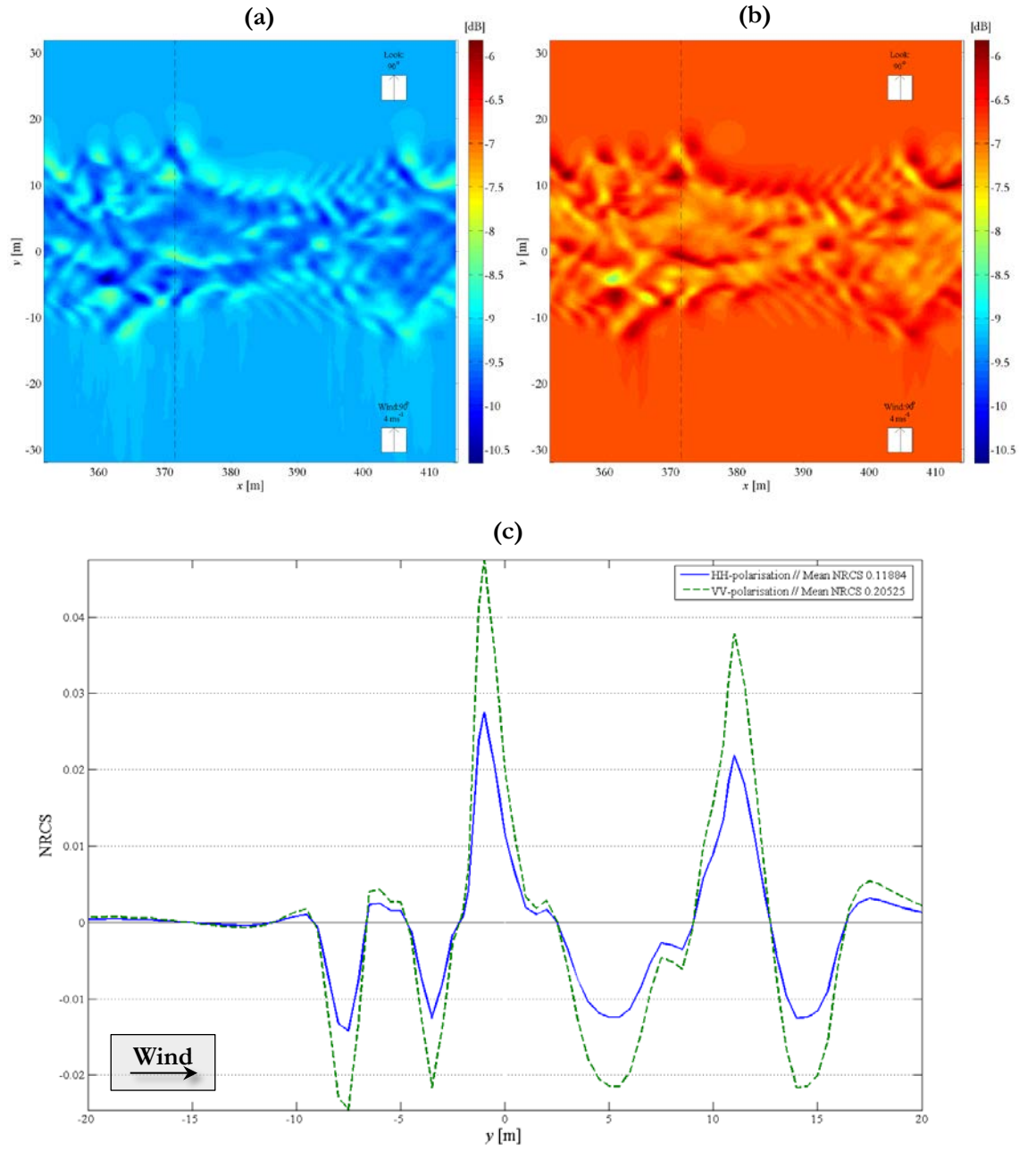
Figure 41. Effect of radar polarisation on Bragg NRCS signature from Wake Profile 1-C observed at (a) HH-polarisation and (b) VV-polarisation and presented in dB scale, matched to the same colour scale; (c) transects of Bragg NRCS at x = 371.5 m, relative to background Bragg NRCS on a linear scale for the HH- and VV-polarised profiles presented in (a) and (b). All profiles were generated for a C-band (5.3 GHz) antenna at θ_i = 23.

6.3.3 Role of Instrument Configuration III: Incidence Angle

The Bragg scattering response of the surface can also be altered by varying the angle of incidence of the instrument, which modifies not only the Bragg wavenumber observed by the instrument (k_B) but also the effective area of a surface facet which is directed towards the antenna[16]. Typical (mean) incidence angles for air- and spaceborne SARs are 20-45° (depending on the desired swath width and desired application), with 20-26° being a typical configuration, and the minimum incidence angle that may be investigated using the M4S tool is 20°. The performance of radar backscattering with incidence angle and surface roughness is depicted in Figure 42, which is based on a similar figure published by Robinson (2004).

The effect of varying incidence angle (in a subset of θ_i most commonly applied aboard spaceborne SARs) is presented in Figure 43, where transects of NRCS contrast (against background) are extracted from C-band (5.3 GHz), HH-polarised profiles of Bragg NRCS at incidence angles between 20° and 30° (in 2° increments). Examples of two-dimensional surface signatures derived at 20° and 30° are presented in Figure 43 (b) and (c) respectively. Visually, there is little difference in the pattern/distribution of modulation observed at difference incidence angle, although there is some variation observed in the magnitude of linear NRCS values. The effect of increasing incidence angle serves to maintain the general pattern of NRCS modulation, but to constrain the range of values that are encountered: to first order, higher incidence angle causes the background contrast encountered at e.g. 'peaks' of the NRCS profile to be adjusted to the same scale; although there are local variations in the magnitude of some peaks (e.g. Feature [1] in Figure 43 [a]). Since (in general) the shape of Bragg NRCS transects remains fairly constant, such effects arise from variations in backscattering calculation arising from the $\cos^4\theta_i$ term in Equation (xx) rather than variations in the observed Bragg wave spectrum[17].

---

[16] In this respect, incidence angle enters the Bragg backscattering calculation of Equation (xx) in three ways: through the observed Bragg wave spectrum $[\psi(k_B) + \psi(-k_B)]$, contributing to the complex scattering function $G_{pq}(\theta_i, \alpha, \phi)$ and through the $\cos^4\theta_i$ term.

[17] This is because variation of k_B between incidence angles at 20° and 30° at C-band is very small; a more significant variation in the Bragg wave spectrum is achieved by shifting frequency (at, say, constant 20° incidence angle) to S- or L-band. The impact of varying Bragg wavenumber is likely the source of variation in the profile observed in Feature [2] of Figure 42 (a).

The effect of higher incidence angle (beyond 30°) on visibility of the wake signature is depicted in Figure 44, where further characteristics for modulation depth (both over the whole image, and average across transects in the y-axis) and mean image NRCS are investigated for θ_i = 20°, 30°, 40°, 50° and 60° under the conditions described by Figure 43. A tabulation of statistics from the range of the expanded range of incidence angles is also presented in Tables 10 and 11. It can be seen that variation in incidence angle beyond 30° will lead to a continuation of the trend in reduction in modulation depth and mean NRCS whilst, beyond 40°, levels of radar backscattering from the surface fall considerably and the ability to resolve the surface signature may be reduced.
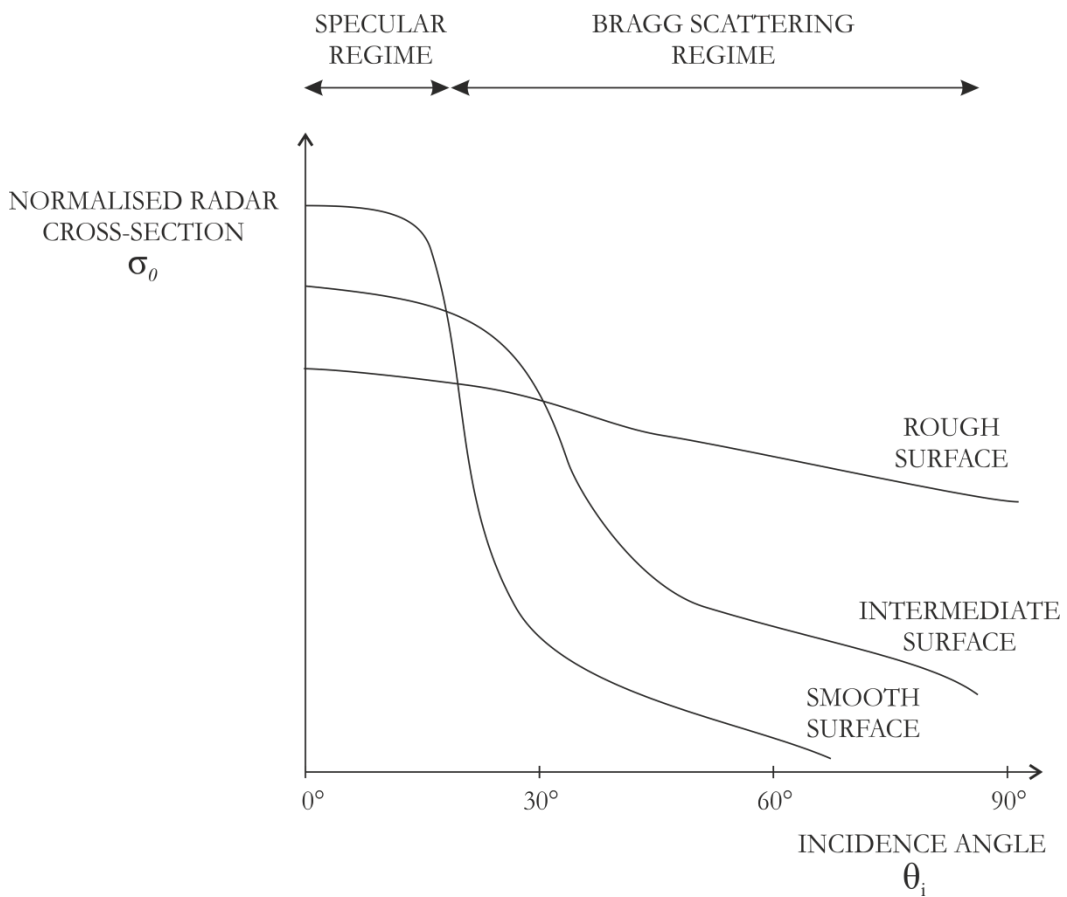
Figure 42. Effect of radar backscattering with surface roughness and incidence angle; adapted from Robinson (2004).

(a)

(b)

(c)
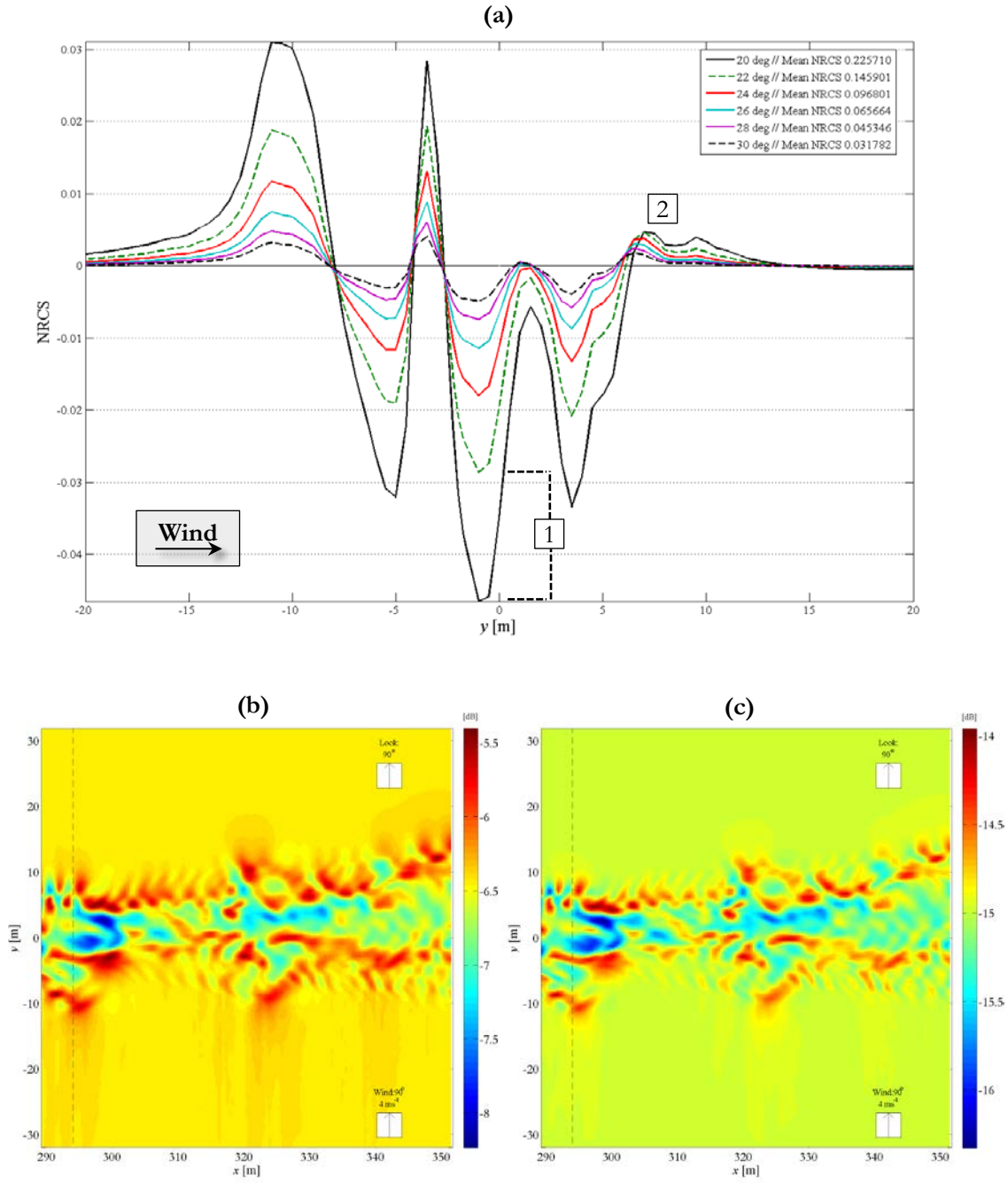
Figure 43. (a) Effect of incidence angle on Bragg NRCS signature from Wake Profile 1-B observed between $\theta_i = 20°$ and $30°$ in $2°$ increments: transects of Bragg NRCS (scaled relative to the linear Bragg NRCS level of the stationary water outside of the wake region) taken at $x = 294$ m, for a 5.3 GHz (C-band) antenna with HH-polarisation. Associated two-dimensional surface signatures of Bragg NRCS derived at (b) $\theta_i = 20°$ and (c) $\theta_i = 30°$.

Incidence Angle	Position of Transect				Mean NRCS	
	294 m	309 m	324 m	339 m	Linear Scale	dB Scale
20º	0.077420	0.044263	0.088027	0.043839	0.2271	-6.44 dB
22º	0.047961	0.028131	0.054018	0.026665	0.1467	-8.34 dB
24º	0.031053	0.018183	0.033927	0.016912	0.0972	-10.12 dB
26º	0.020288	0.011946	0.022309	0.010966	0.0659	-11.81 dB
28º	0.013413	0.007959	0.015257	0.007325	0.0455	-13.42 dB
30º	0.008965	0.005366	0.010500	0.004997	0.0319	-14.96 dB
40º	0.001396	0.000879	0.001794	0.000862	0.0063	-22.01 dB
50º	0.000263	0.000171	0.000344	0.000166	0.0014	-28.53 dB
60º	0.000050	0.000032	0.000064	0.000031	0.0003	-35.27 dB

Table 10. Modulation depths of Bragg NRCS (in linear form) taken along individual range lines of Wake Profile 1-B from Figure 43 at various positions in the x-axis; variation with incidence angle. Rows shaded in light blue represent those most relevant for spaceborne SAR operation.

Incidence Angle			Modulation Depth (Linear)		Background NRCS		Mean NRCS	
θ_i (º)	λ_B (cm)	$\cos^4\theta_i$	Average Across Transect	Total Across Image	Linear Scale	dB Scale	Linear Scale	dB Scale
20º	1.94	0.7797	0.0722	0.1378	0.2274	-6.43 dB	0.2271	-6.44 dB
22º	2.12	0.7390	0.0452	0.0858	0.1468	-8.33 dB	0.1467	-8.36 dB
24º	2.30	0.6965	0.0290	0.0553	0.0973	-10.12 dB	0.0972	-10.12 dB
26º	2.48	0.6526	0.0190	0.0368	0.0659	-11.81 dB	0.0659	-11.81 dB
28º	2.66	0.6078	0.0127	0.0248	0.0455	-13.42 dB	0.0455	-13.42 dB
30º	2.83	0.5625	0.0086	0.0169	0.0319	-14.96 dB	0.0319	-14.96 dB
40º	3.64	0.3444	0.0014	0.0028	0.0063	-22.07 dB	0.0063	-22.07 dB
50º	4.34	0.1707	0.0002 (7434…)	0.0005 (3034…)	0.0014	-28.54 dB	0.0014	-28.54 dB
60º	4.90	0.0625	0.0000 (5105…)	0.0000 (9745…)	0.0002 (7976…)	-35.53 dB	0.0002 (7974…)	-35.53 dB

Table 11. Statistics extracted from Bragg NRCS profiles of Wake Profile 1-B for varying incidence angle under a uniform 4 ms⁻¹ wind blowing parallel to the y-axis. Frequency and polarisation of the simulated antenna are 5.3 GHz (C-band) and HH-polarised for all tested cases, for look direction at 90º to the x-axis. Rows shaded in light blue represent those most relevant for spaceborne SAR operation.

6.4   Discussion

Over the course of this chapter, various instrument configurations have been examined for their ability to resolve qualitative and quantitative observations of surface wake turbulence, based on simulation of a hypothetical surface flow field using an integrated wave-current interaction/radar backscattering calculation process. The final section of this chapter will be used to discuss of these results and to draw some conclusions about the findings of this study.

The results presented have given strong indications that, where present, qualitative characteristics of the wake flow structure at the surface propagate through calculation of wave-current interaction to affect the distribution of wave amplitudes of short, backscattering waves and hence may be rendered visible in simulated NRCS profiles. As a result, this has allowed visual comparison(s) to be drawn between characteristics of the wake flow in velocity profiles and the simulated radar signature derived from operation of ocean radar imaging models. Encouraging results stem from observations that characteristics of the internal flow structure – that is, the velocity fluctuations along the centre line of the wake axis – can produce modulation of the surface wave spectrum such that they can be resolved in the NRCS response of imaging radar. This is encouraging for the operation of future (high-resolution) SAR sensors for ocean study since it indicates that, at least under the simplified conditions which have been tested here, a reasonable assessment of turbulent wake structure can be drawn from a radar backscattering image and that this could, theoretically, be used to obtain further information about the character or source of that turbulence. The potential for instruments to observe low-backscatter (or low-contrast) wake profiles due to the presence of a moving object at, or below, the surface through measurable variations in surface current may be beneficial for a number of additional applications, such as maritime tracking and surveillance.

The presence of a drop in NRCS which is observed in the simulated profiles at the centre of the wake is broadly consistent with characteristics that are observed in many typical SAR ship wake observations (such as the schematic previously shown in Figure 18), where the presence of surface currents lead to a dark 'scar' in the radar backscattering images and observation of complex surface patterns trailing behind the vessel. Remote-sensing studies by Reed et al. (1990), Milgram et al. (1993) and True et al. (1993) postulated that the presence of fine-scale turbulence (acting to extract wave energy from short waves) was a significant source of this response, although there may be other contributions to the effect of a dark 'scar' behind the ship; for example, arising from the effect of other influences such as surfactant materials which are elevated to the surface by action of the ship's propellers and its motion through the water. Where some previous studies of ship wake surface signatures (in particular, Reed et al. [1990], Milgram et al. [1993] and True et al. [1993]) have

considered the effects of both macro-scale surface currents and fine-scale dissipation of wave energy by turbulent velocity fluctuations, the results presented here have considered only the effects of the macro-scale currents present in the wake; the implications for considering dissipation of wave energy by turbulence are covered in a literature review presented in Appendix D. In addition, there are components of a moving vessel's wake which are not represented in the current case: most notably, the bow wave and Kelvin wake envelope arising from the front of the vessel and the transverse & divergent waves which extend from the rear. Presence of these wake components will produce additional currents and velocity interactions in the ambient water outside of the turbulent wake region, which is assumed to be stationary in the present scenario.

The discussion presented in §6.3.1 considered the effect of instrument operating frequency to observe qualitative flow structure, examining both canonical (L-, S-, C- and X-band) SAR frequencies along with frequencies operated more infrequently (P-band, Ku-band and Ka-band). Variation of operating frequency offers the benefit of observing different effects of surface straining (due to the presence of surface currents) at different parts of the ocean wave spectrum. The results demonstrated the ability of differing Bragg wavenumber (k_B) to observe different components of the surface flow structure and extract different spatial patterns (and levels) of modulated radar backscatter. Since observation of a simple Bragg (-only) backscattering profile at differing frequencies can hence provide a different estimate of (Bragg-) wave energy at different ocean wavenumbers, this could theoretically be exploited to help understand the effects of wave-current interaction and to derive a 'picture' of the flow field based on its effect on wave modulation.

In Figure 35, it was shown that different frequencies can resolve different details of surface flow structure: in particular, L-band frequencies demonstrated correlations with mean currents aligned in the wind/look direction; whilst S-band (and higher) frequencies displayed correspondence with velocity gradients and fine structure. Through qualitative examination of two-dimensional Bragg NRCS signatures in the interval (1.2 - 3.5 GHz), a "crossover point" was identified at, or near, (1.6 to 2.6 GHz) where the character of such signatures undergoes a transition in general pattern. This transition is depicted in the series of surface signatures presented in Figure 44, cataloguing the variation in character between 1.2, 1.6, 2.6 and 3.2 GHz. The ability to extract different levels of backscattered energy from different regions of the (perturbed) surface wave spectrum, and/or observe different characteristics of the surface current structure may promote the use of multi-frequency instruments: SAR sensors which operate in a 'multi-frequency' capacity have the ability to transmit/receive multiple radar frequencies quasi-simultaneously (typically at the same incidence angle), therefore obtaining images of the same scene at different Bragg wavenumber(s). From the results presented in this chapter, there is evidence that collecting radar backscatter at multiple

frequencies (and at multiple polarisations) could aid in discrimination of flow structure and extraction of flow patterns. Quasi-simultaneous observation of surface flow field at a variety of Bragg wavenumber (k_B) specifications could be used to provide additional, independent sources of information which aid in constructing a multi-dimensional survey of the scene, aiding interpretation of turbulent ocean processes in terms of detailed flow mechanics. In the context of Figure 44, it may mean that it is relevant to observe multi-frequency signatures at both L-band and S-/C-/X-band frequencies in order to maximise the ability to capture distinct flow characteristics. Multi-frequency instruments have, so far, seen operation on airborne platforms (with the possible exception of the SIC-C/X-SAR mission of the Space Shuttle *Endeavour*), and some details of their operation is described in Table 19 of Chapter 7, along with research papers which publish data from various measurement campaigns. However, a key conclusion which may be drawn from the current results regards the ability of the simulated backscatter images to resolve variations in backscattering (at the spatial resolution of the input velocity grid), and therefore the potential for existing, or future, radar instruments to observe such flow structures in cases where there may be no other visible profile of other surface parameters (such as temperature or surface height). Where modulated energy spectra in the simulated profiles can be modelled accurately, there is good comparison between the surface flow structure and the derived Bragg NRCS profile. There is indication that the diverging (in this case, those in the y-direction) currents produced by the wake oppose the propagation of waves (within the wave-current interaction calculation) into the area at the centreline of the wake, resulting in a deficit in (the amplitude of) short waves propagating into this region of the wake flow. While the results presented here demonstrate a drop in radar backscattering arising solely due to the action of macro-scale wake currents (and the effect of adverse currents on reducing the energy/amplitude of short waves propagating into the centre of the wake), the phenomena of turbulent dissipation of wave energy has also been shown to contribute to such responses (e.g. Reed et al. [1990] and True et al. [1993]). Appendix D draws some perspectives on expanding these results and for incorporating turbulent dissipation of wave energy into future simulations.

With respect to image characteristics observed over various frequencies, the variation of mean image NRCS, average modulation depth across transects (in the y-direction) and total modulation depth (over the whole image) with radar operating frequency is presented in Figure 45. Relevant data for the range of studied cases (for various frequencies between 0.4 GHz and 35 GHz) is tabulated in Table 12. Considering radar frequencies which have seen principal operation by airborne & spaceborne SARs, there is evidence in Figures 44 and 45, along with signatures previously discussed, that S-band SAR (2 - 4 GHz) could play a more active role in observation of the ocean. Profiles extracted from a simulated S-band instrument demonstrate a good balance

between mean NRCS, contrast with background NRCS and observed modulation depth. Such results provide encouraging prospects for the forthcoming *NovaSAR-S* spacecraft (2015), which operates a 3.1 - 3.3 GHz S-band antenna at HH/HV/VH/VV polarisation at 23-25° nominal incidence angle. However, whilst these conclusions suggest beneficial opportunities for observing the ocean from space with frequencies which have seen limited study (such as S-band), operation of more non-canonical frequencies (away from L-, C- and X-bands, for which there has been a significant amount of validation of the agreed backscatter theory) may demonstrate a deviation from the theoretical backscattering response[18]; additional testing may be required at these unconventional frequencies. Before alternative SAR frequencies are routinely accommodated on spaceborne instruments, further development of airborne campaigns is recommended in order to reinforce understanding of radar backscattering theory at these frequencies.

---

[18] For example, in an airborne campaign observing ship-generated internal waves, Hogan et al. (1996) encountered disagreement between measured and theoretical modulations of Ka-band NRCS, and it is likely that a movement towards unconventional SAR frequencies will encounter similar differences in prediction until the mechanisms are fully understood. Even in the range of frequencies which have seen greater study, the accepted theory may sometimes deviate from observed values; for example, Romeiser et al. (1997) observe an overestimate of NRCS values at X-band.
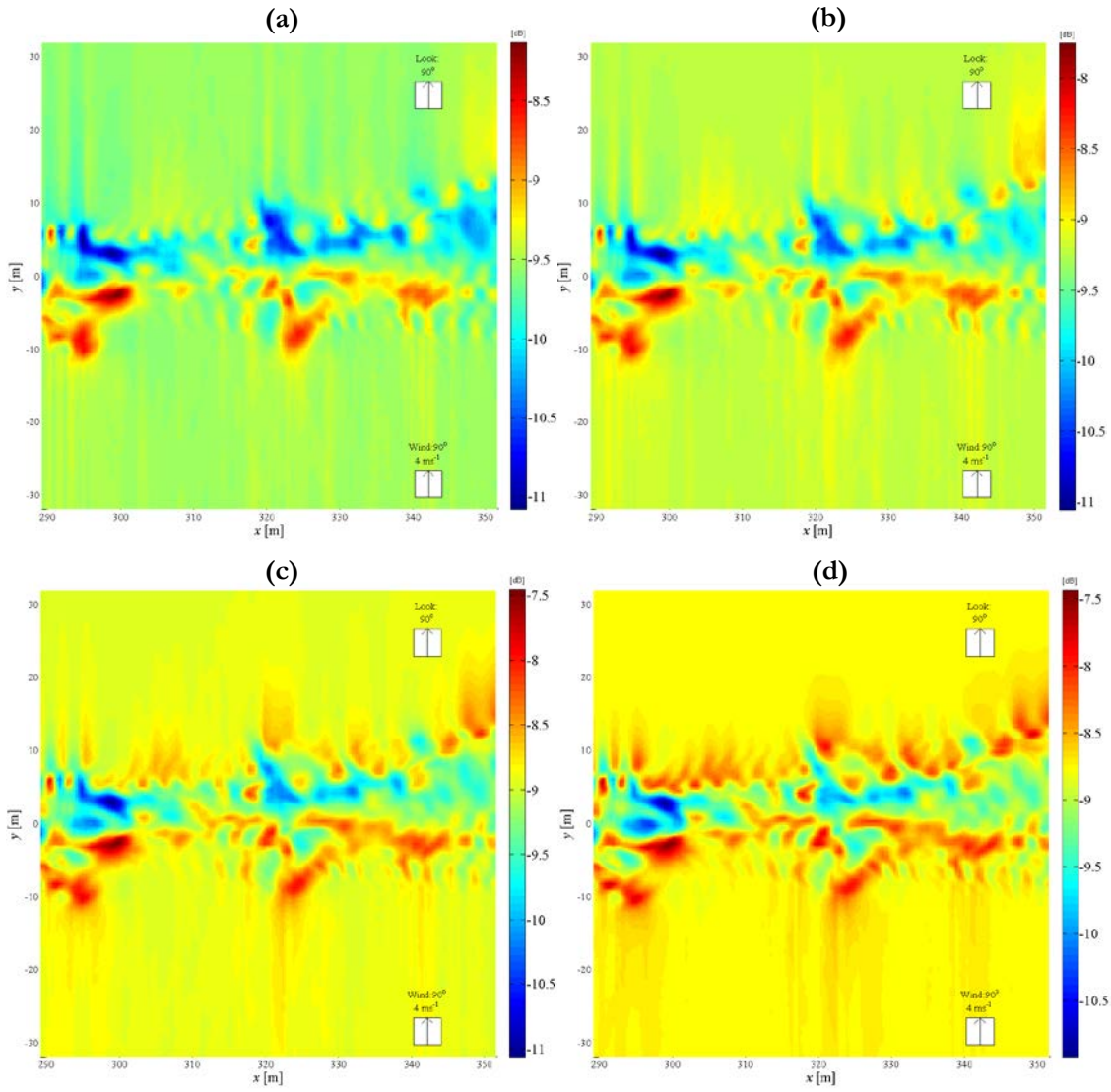
Figure 44. Study of the evolution of Bragg NRCS surface signatures in the interval between L- and S-band. (a) 1.2 GHz (allocated ITU frequency for L-band SAR); (b) 1.6 GHz (high L-band); (c) 2.2 GHz (low S-band); (d) 3.2 GHz (allocated ITU frequency for S-band SAR). For all profiles, HH-polarisation and a 23° incidence angle is assumed, with a look direction aligned with the wind direction at 90° to the x-axis.
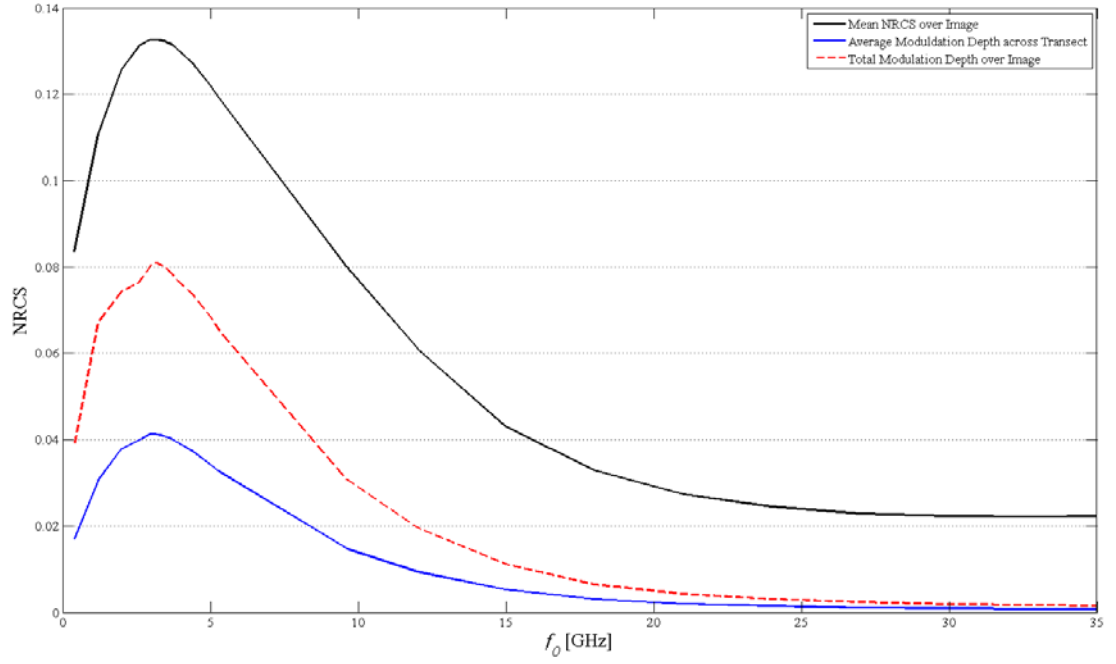
Figure 45. Variation of mean image NRCS, average modulation depth across transects in the y-direction and total image modulation depth with radar operating frequency. The data used to construct this diagram, and other statistics from the radar frequency investigation, are presented in Table 12.

Radar Frequency			Modulation Depth (Linear)		Background NRCS		Mean NRCS	
Freq. (GHz)	λ_B (cm)	k_B (rad^{-1})	Average Across Transect	Total Across Image	Linear Scale	dB Scale	Linear Scale	dB Scale
0.4	29.30	21.4	0.0171	0.0386	0.0844	-10.737	0.0837	-10.773
1.2	9.77	64.3	0.0306	0.0671	0.1124	-9.492	0.1109	-9.551
2.0	5.86	107.2	0.0379	0.0743	0.1277	-8.938	0.1257	-9.007
2.6	4.51	139.4	0.0399	0.0766	0.1324	-8.781	0.1312	-8.821
2.9	4.04	155.4	0.0411	0.0795	0.1333	-8.752	0.1324	-8.781

Table 12. Statistics extracted from Bragg NRCS profiles of Wake Profile 1-C for varying radar frequencies under a uniform 4 ms^{-1} wind blowing parallel to the y-axis. Incidence angle and polarisation of the simulated antenna are 23° and HH-polarised for all tested cases, for a look direction at 90° to the x-axis.

Radar Frequency			Modulation Depth (Linear)		Background NRCS		Mean NRCS	
Freq. (GHz)	λ_B (cm)	k_B (rad^{-1})	Average Across Transect	Total Across Image	Linear Scale	dB Scale	Linear Scale	dB Scale
3.0	3.91	16.08	0.0413	0.0804	0.1334	-8.748	0.1326	-8.775
3.1	3.78	166.2	0.0413	0.0808	0.1334	-8.748	0.1326	-8.775
3.2	3.66	171.5	0.0412	0.0808	0.1333	-8.752	0.1326	-8.775
3.3	3.55	176.9	0.0411	0.0806	0.1332	-8.755	0.1325	-8.778
3.4	3.45	182.2	0.0409	0.0802	0.1329	-8.765	0.1323	-8.784
3.5	3.35	187.6	0.0406	0.0797	0.1326	-8.775	0.1321	-8.791
3.6	3.26	193.0	0.0404	0.0791	0.1323	-8.784	0.1318	-8.801
3.7	3.17	198.3	0.0401	0.0783	0.1318	-8.801	0.1314	-8.814
3.8	3.08	203.7	0.0397	0.0774	0.1313	-8.817	0.1309	-8.831
4.4	2.66	235.8	0.0373	0.0735	0.1274	-8.948	0.1271	-8.959
5.0	2.34	268.0	0.0342	0.0685	0.1221	-9.133	0.1220	-9.136
5.3	2.21	284.1	0.0326	0.0653	0.1193	-9.234	0.1191	-9.241
9.6	1.22	514.6	0.0148	0.0309	0.0802	-10.958	0.0802	-10.958
12	0.98	643.2	0.0094	0.0197	0.0610	-12.147	0.0611	-12.140
15	0.78	804.0	0.0053	0.0112	0.0433	-13.635	0.0433	-13.635
18	0.65	964.8	0.0031	0.0065	0.0329	-14.828	0.0329	-14.828
21	0.56	1125.6	0.0020	0.0043	0.0274	-15.622	0.0274	-15.622
24	0.49	1286.4	0.0015	0.0031	0.0245	-16.108	0.0245	-16.108
27	0.43	1447.3	0.0011	0.0024	0.0229	-16.402	0.0229	-16.402
30	0.39	1608.1	0.0009	0.0019	0.0223	-16.517	0.0223	-16.517
33	0.36	1768.9	0.0008	0.0017	0.0222	-16.536	0.0222	-16.536
35	0.33	1876.1	0.0007	0.0015	0.0223	-16.517	0.0223	-16.517

Table 12 (contd). Statistics extracted from Bragg NRCS profiles of Wake Profile 1-C for varying radar frequencies under a uniform 4 ms^{-1} wind blowing parallel to the y-axis.

The results presented in §6.3.2 and §6.3.3 were associated with the effect on radar backscattering of antenna polarisation and incidence angle, respectively. The findings of this investigation have demonstrated a consistency with the results of similar investigations published by other researchers, along with those which are implied by the general theory. According to Equations (xix) and (xx), radar scattering theory dictates that a higher 'mean' value of Bragg NRCS will be observed under VV-polarised conditions whilst there is no effect on the observed modulation depth on a log/decibel scale, and this is confirmed by the signature observed in Figure 41. While this is may not appear to be a substantial finding since it is expected based on the general theory, it does reinforce (and, indeed, highlight) the selection of vertical co-polarisation for ocean study since it may improve the ability to resolve contrast(s) in derived images, along with the potential to improve ability to resolve low-backscatter processes. Furthermore, through an initial investigation of two-scale signatures and the role of polarisation, larger modulation depth ($\sigma_{0,dB\ (Max)}$ - $\sigma_{0,dB\ (Max)}$) in dB images is observed at HH- rather than VV-polarisation; although, it must be noted that mean NRCS is lower at HH-polarisation. Such results are consistent with observations by Fischer et al. (1999), who note NRCS values for HH-polarisation below those for VV-polarisation, but also higher contrast. For implementation of future instruments for ocean study, it is still recommended that antennas with full, quad-polarisation (HH/VV/VH/HV) are employed, although the findings presented here indicate that there may be significant value in considering HH-polarised signatures in analysis of radar backscattering modulation.

With respect to the impact of incidence angle on observed radar surface signatures, the current study has revealed findings which are in alignment with those of previous research (for example, True et al. [1993] and Fischer et al. [1999]), and those predicted by the general theory: the variation of θ_i contributes both in modifying the observed Bragg wavenumber, k_B, through Equation (xviii), in addition to affecting the $\cos^4\theta_i$ term in the Bragg NRCS radar backscatter equation (Equation [xx]). The radar scattering response observed at varying incidence angle is therefore a factor of both observing a different region of the wave (energy) spectrum, but also to the geometrical variation of observing a (roughened) surface at a different angle to the local normal. From the point of view of $\cos^4\theta_i$ in isolation, it is desirable to reduce incidence angle in order to maximise $\sigma_{0,Bragg}$; however, from the perspective of examining the effect on the observed portion of the Bragg wave spectrum, the case of incidence angle is more complex: variation of θ_i (at fixed frequency) over the range of useful remote-sensing configurations has a lesser impact on k_B than variation of f_0 (at fixed incidence angle) between 1-10 GHz. The observed trend in incidence angle demonstrates that θ_i in the interval of 20° to 24° resolve the highest (mean) values of Bragg NRCS across the image, along with modulation depth. Therefore, to maximise the radar scattering characteristics of

surface signatures (such as the hypothetical flow field considered here), incidence angles should be confined to this interval.

In Figure 46, mean NRCS and total modulation depth (over the whole image), and average modulation depth (across transects taken in the y-direction) are plotted against incidence angle: the trend, displaying an increase in these quantities as the incidence angle of the instrument is reduced, can be clearly observed and supports the findings discussed in this sub-section. Due to limitations of the radar scattering theory used by *M4S*, only incidence angles beyond 20° were considered in this current study; it is likely that a peak response in modulation depth and mean NRCS lies in the interval of 18-20° (since levels of Bragg backscattering will once again decrease as the incidence angle approaches the nadir angle of the instrument), however this remains untested at this time. At more considerable incidence angles (larger than 40°), less radar energy is returned to the antenna under these conditions and hence observing modulation of the surface by the hypothetical flow feature, in the context of image noise, is likely to become challenge. Modulation depth of (linear NRCS) σ_0 falls with increasing incidence angle, however there is only a minimal reduction in modulation depth of ($10\log_{10}$ NRCS) $\sigma_{0,dB}$ as incidence angle is increased.
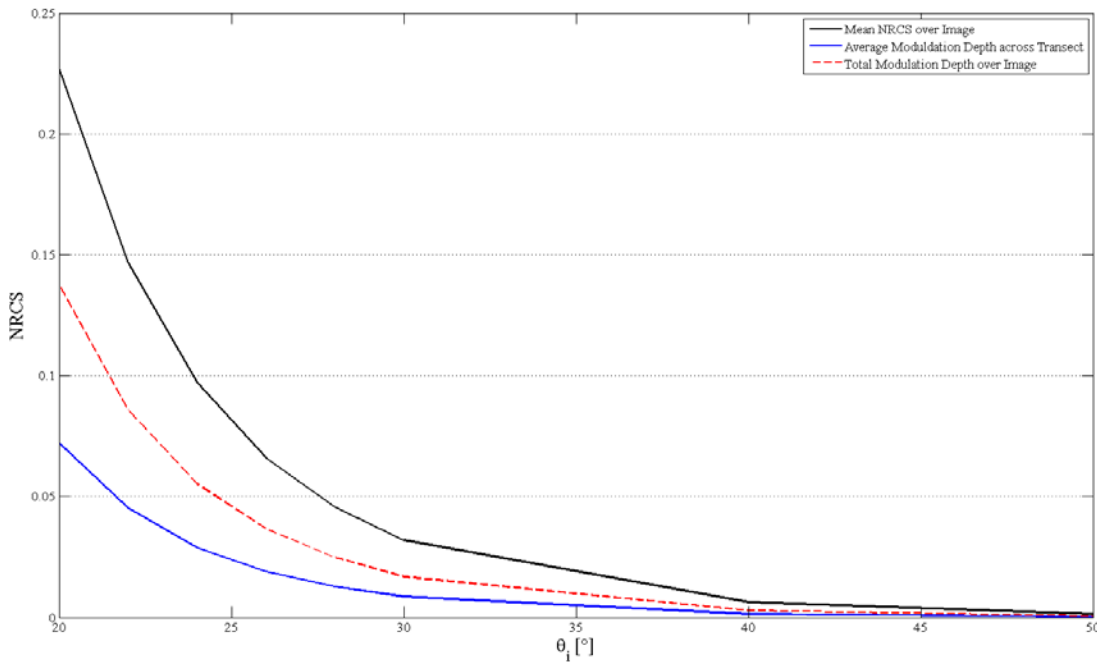
Figure 46. Variation of mean NRCS and modulation (over whole image) with incidence angle, along with variation of average modulation depth observed across transects of Bragg NRCS, for the cases studied in Figure 43. For all cases, the profile was subject to 4 ms^{-1} blowing in a direction parallel to y-direction and observed with a simulated C-band (5.3 GHz), HH-polarised antenna with look direction in the y-axis.

Of course, in the simulation cases pursued in this investigation, a number of simplifications have been made which place some limitations on the raw conclusions which may be drawn, and these have been introduced and discussed previously. In particular, a uniform wind speed/direction of 4 ms^{-1} blowing perpendicular to the x-axis, and a co-incident radar look direction in parallel has been assumed; as will be addressed in Chapter 7, the visibility of surface signatures under differing wind/look directions is a more complex issue. Furthermore, there has been limited consideration of full NRCS signatures derived from composite surface theory: the simulation results in this thesis focus primarily on surface signatures derived in Bragg NRCS, however drawing some initial conclusions about composite surface NRCS signatures is crucial, since radar operating over the ocean cannot consider Bragg backscattering alone (in isolation from surface tilting effects).

According to the two-scale model, the observed Bragg wave spectrum (for the Bragg wavenumber viewed by the simulated radar) is assumed to sit atop a long-wave spectrum which causes modification to the radar backscattering response according to local tilting effects from large-scale waves. In this respect, the short-wave response may be obscured by long-wave effects, as is the case in Figure 29 (b) where tilting effects cause the pure Bragg response to be obscured[19]: the addition of long-wave components to the backscattering wave spectrum will generally contribute to a more complex system, perhaps obscuring the structure and trends observed at single Bragg-only frequencies of the surface wave spectrum. At high incidence angles, observation may also be susceptible to phenomena such as specular reflection, shadowing by steep waves, etc. which may also obscure the visible surface signature (Romeiser et al., 2003). Furthermore, where Bragg and composite surface NRCS signatures show difference in texture or pattern, this may indicate a change in the primary mechanisms causing radar backscattering (i.e. between resonant Bragg-scattering and reflection from longer waves), or difference(s) in the effect of the flow structure at different oceanic wavelengths. Where this is observed, such instance could potentially reveal further understanding about how turbulence and surface currents interact with the ocean surface.

The findings of Chapter 6 have been progressed by considering the effects of instrument configuration in isolation; neglecting the effects of look orientation and ambient wind conditions which will affect the character and context of the observed image. These factors will now be examined in the following chapter, which also covers the effect of other limitations such as spatial resolution and image sensitivity in RAR and SAR images.

---

[19] In this respect, the Bragg NRCS signature presented in Figure 31 (a) represents the radar signature that would be observed if the surface current was interacting with a perfectly glassy surface upon which only waves of wavelength 2.21 cm (Bragg wavenumber $k_B = 284$ s[-1]) are propagated.

6.5   Radar Frequency and Ability to Resolve Surface Flow Structure

As was first discussed in §6.2 (e.g. Figures 32 and 33), transects taken across NRCS signatures are found to bear strong resemblance to the distribution of surface velocity components (and their gradients) that are aligned in the radar look direction. Expanding on this discussion, the capacity for differing radar frequencies to resolve differing aspects of the surface velocity structure is examined in greater detail in this section, by qualitatively comparing the similarity of velocity profiles with the structure contained within radar surface signatures.

To permit comparison of pattern similarity of these profiles, the distributions of velocity, gradients in velocity and background contrast of Bragg NRCS along a single surface transect were normalised to the range $(-1,1)$ in the manner demonstrated in Figures 47 and 48. For this investigation, all Bragg NRCS signatures/transects were derived for an instrument at $23°$ incidence angle and HH-polarisation, with both wind direction and look direction aligned at $90°$ to the x-axis. Using the normalised data, it was therefore appropriate to consider the similarity of the profiles to ascertain the ability of different radar frequencies to resolve different characteristics of surface flow structure.

As a first step, a measure of this correlation was obtained by simple subtraction of the two normalised profiles, yielding a one-dimensional variation of the discrepancy in structure observed between the two profiles. Figure 49 (a) and (b) show the results of one such exercise, performed for the transects displayed in Figures 47 and 48 for six radar frequency profiles (L-, S-, C-, X-, Ku- and Ka-bands) and for V-velocity, and V-velocity gradients, respectively. The deviation of the derived discrepancy curve from the zero plane (i.e. $y = 0$) indicates a greater dissimilarity between the (normalised) NRCS profile and the (normalised) velocity/gradient profile, and hence a poorer ability to resolve the characteristics – a 'perfect' match between the two profiles would yield a solid flat line of value '0'.

As was previously observed in §6.2 with respect to qualitative measurement, it is once again found that the L-band (1.2 GHz) profile in Figure 49 (a) [blue line] displays a relatively good match for resolving the V-velocity profile, but a poorer capacity to record variation in gradients of the surface **(a)** current. In contrast, the X-band (9.6 GHz) [red line] performs poorly when compared with V-velocity but more closely extracts content of velocity gradient variations, as was the case when drawing qualitative conclusions during the discussion presented earlier in this chapter. However, analysis should now be discussed regarding a quantitative examination of the ability of differing radar frequencies to extract details of surface currents and flow structure.
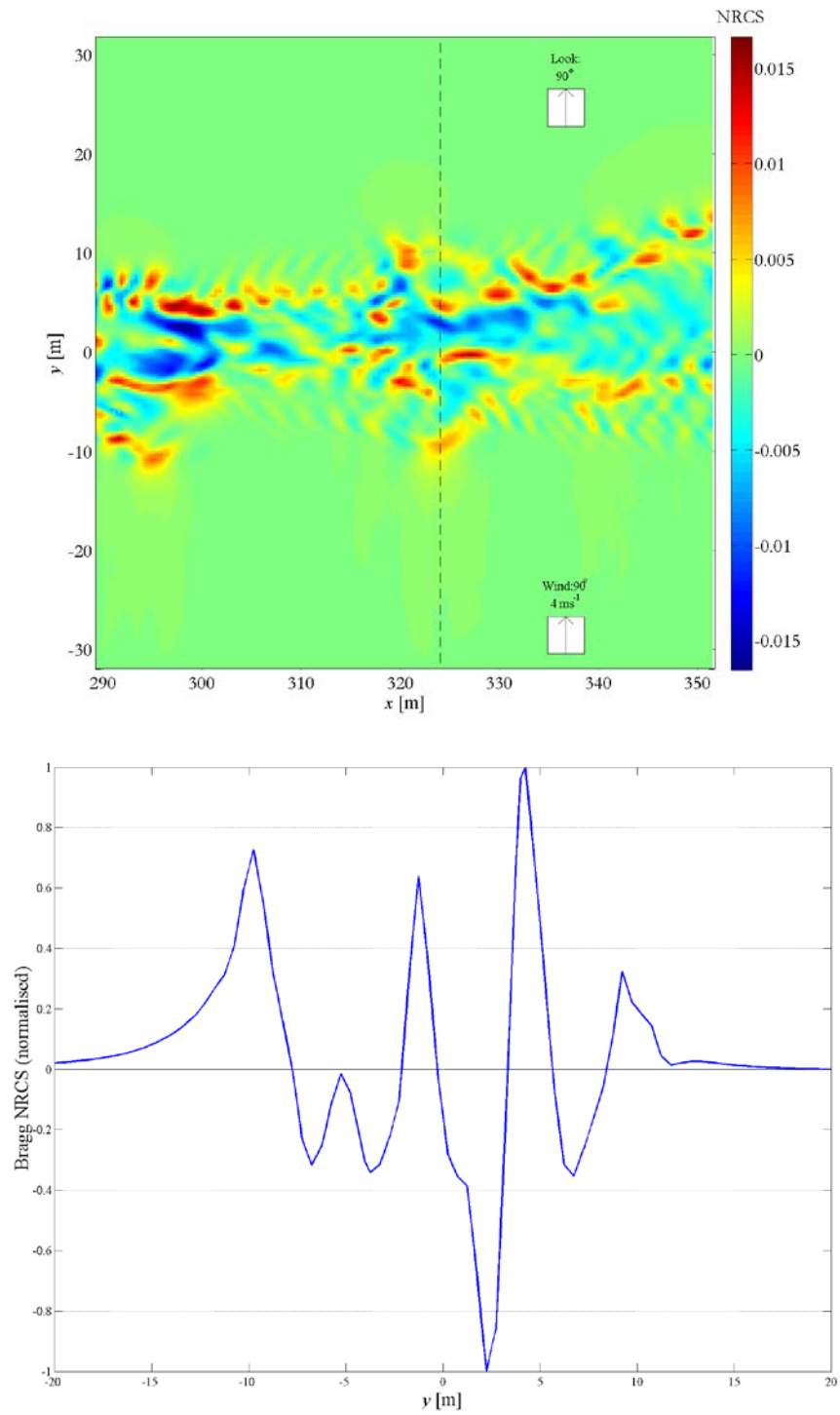
Figure 47. (a) Bragg NRCS derived for a section of the wake and resolved in X-band (9.6 GHz) at 23° incidence angle, HH-polarisation and a look direction aligned with the wind direction at 90° to the x-axis; (b) transect of Bragg NRCS extracted at position $x = 324$ m.

(a)
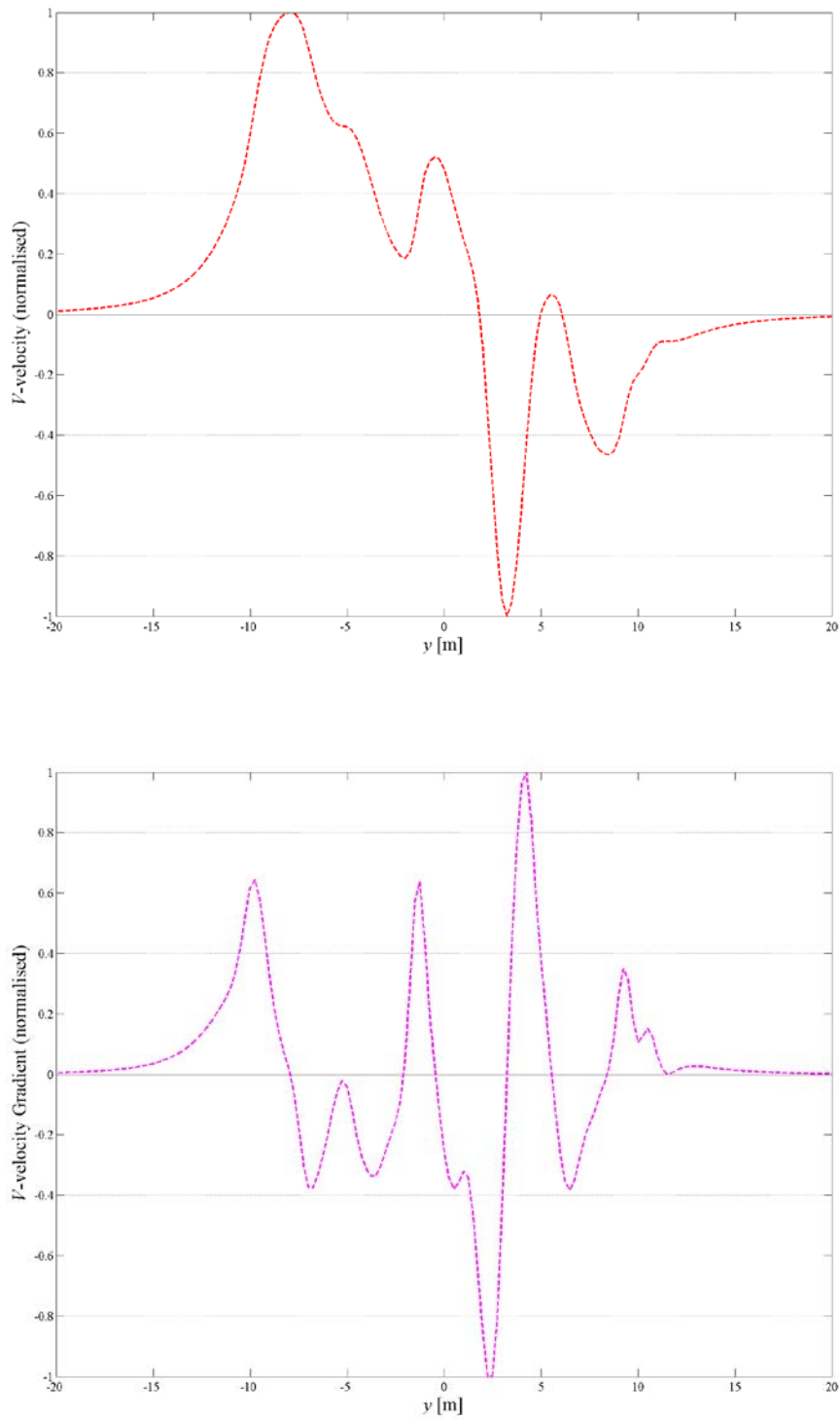
Figure 48. Normalised plots of (a) V-velocity and (b) gradients of V-velocity in the y-direction, taken at the equivalent marked transect position (shown in Figure 47 [a]) of the surface V-velocity profile.

(a)

(b)
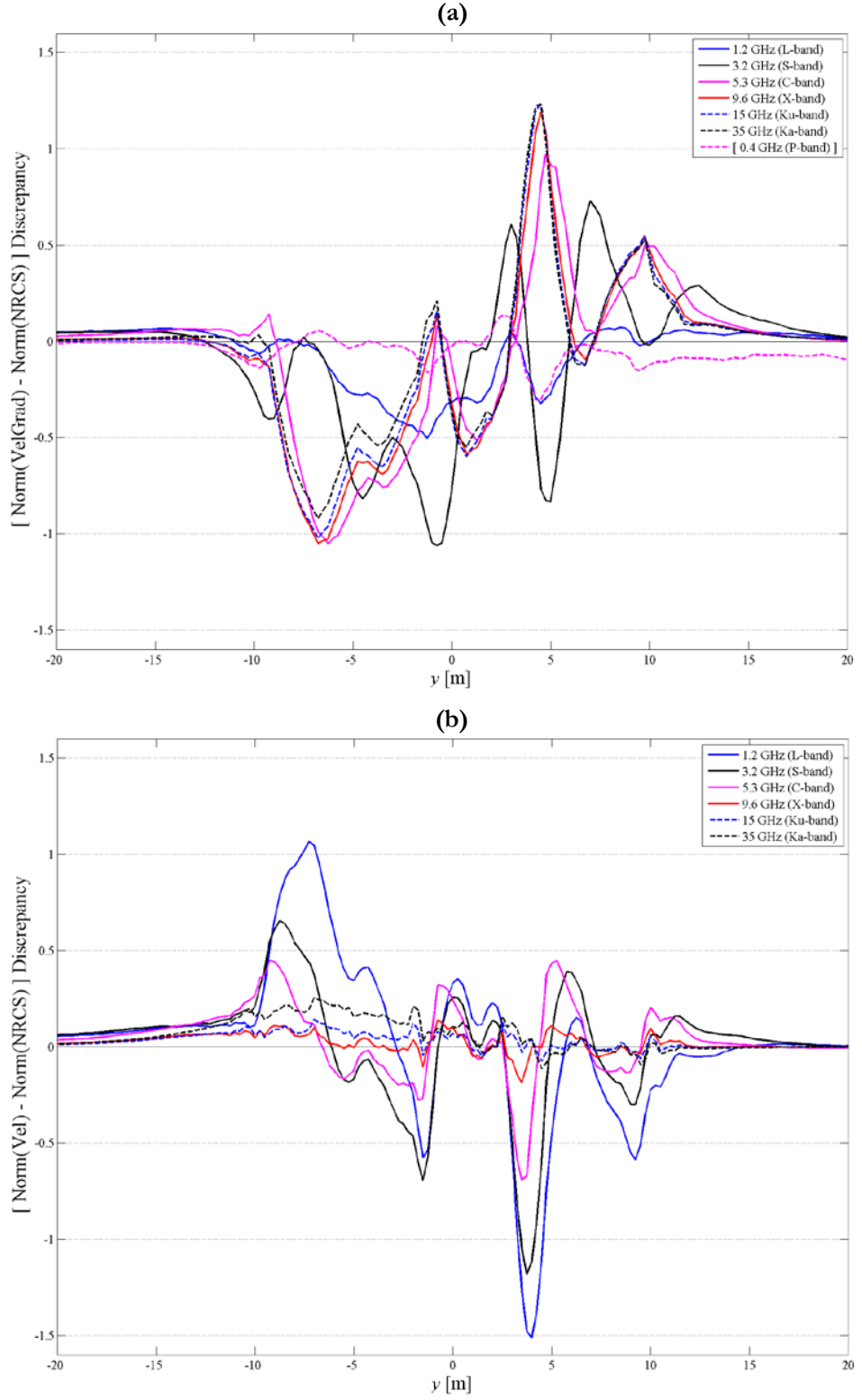
Figure 49. Discrepancy profiles of normalised Bragg NRCS at varying radar frequency, with respect to normalised profiles of (a) V-velocity and (b) gradient of V-velocity in the y-direction.

To obtain quantitative information regarding the similarity of equivalent profiles, the derived discrepancy curves (between normalised Bragg NRCS and normalised velocity transect data) were integrated, using a trapezium rule, to estimate the extent to which Bragg NRCS surface signature resolve the underlying velocity structures aligned with the radar's look direction. This process yielded a single value (denoted 'Discrepancy Area Measure' [DM]), evaluated along the designated transect, which characterises the similarity between the radar surface signature profile and that of patterns observed in surface velocity and the gradients therein. In this manner, a higher value of DM represents greater deviation of the (normalised) NRCS profile from that of the (normalised) velocity profile under inspection, with the ideal DM value of zero indicated a perfect "match" between the two profiles.

Each of the frequency transects presented Figure 49 (a) and (b) was used to calculate their relative similarity to the input velocity/gradient profiles (where a smaller value represents closer similarity to the velocity profile), and to outline the variation with radar frequency. Figure 50 (a) shows the results of this process for the case of similarity with a V-velocity profile, for varying radar frequency between 1.2 GHz (L-band) and 35 GHz (Ka-band). As was found in the earlier discussion in §6.2, simulated instruments in the range of P- and L-band (0.4-1.2 GHz) show a close resemblance to the flow structure of velocity components aligned in the look direction of the radar, but there is great disparity between such profiles and the NRCS signatures derived at frequencies beyond L-band. The minimum DM value (greatest similarity between the normalised NRCS and V-velocity profiles) is observed at 1 GHz, although it is clear that a narrow band of characteristic operating frequencies in the range of P-/L-band which are most successful in resolving the underlying surface velocity patterns. With respect to the ability of differing radar frequencies to resolve gradients in V-velocity across transects of radar backscattering cross-section, results are presented in Figure 50 (b). These findings indicate that the minimum DM value (greatest capability to extract details of surface velocity gradient structure from radar backscatter data) is observed in the range of X-/Ku-band (8-18 GHz); consistent with the qualitative findings which were presented in §6.2. Strictly speaking, the minimum response was observed at a frequency of 12 GHz; however, good performance is observed at high-X-band (10-12 GHz) and low Ku-band (12-15 GHz) in resolving characteristics of surface velocity (gradient) structure through extraction of transect data. Again, these results support the qualitative conclusions which have been drawn and discussed earlier in this chapter, and may now pave the way for further examination of two-dimensional surface profiles and the observed discrepancy.

(a)

(b)
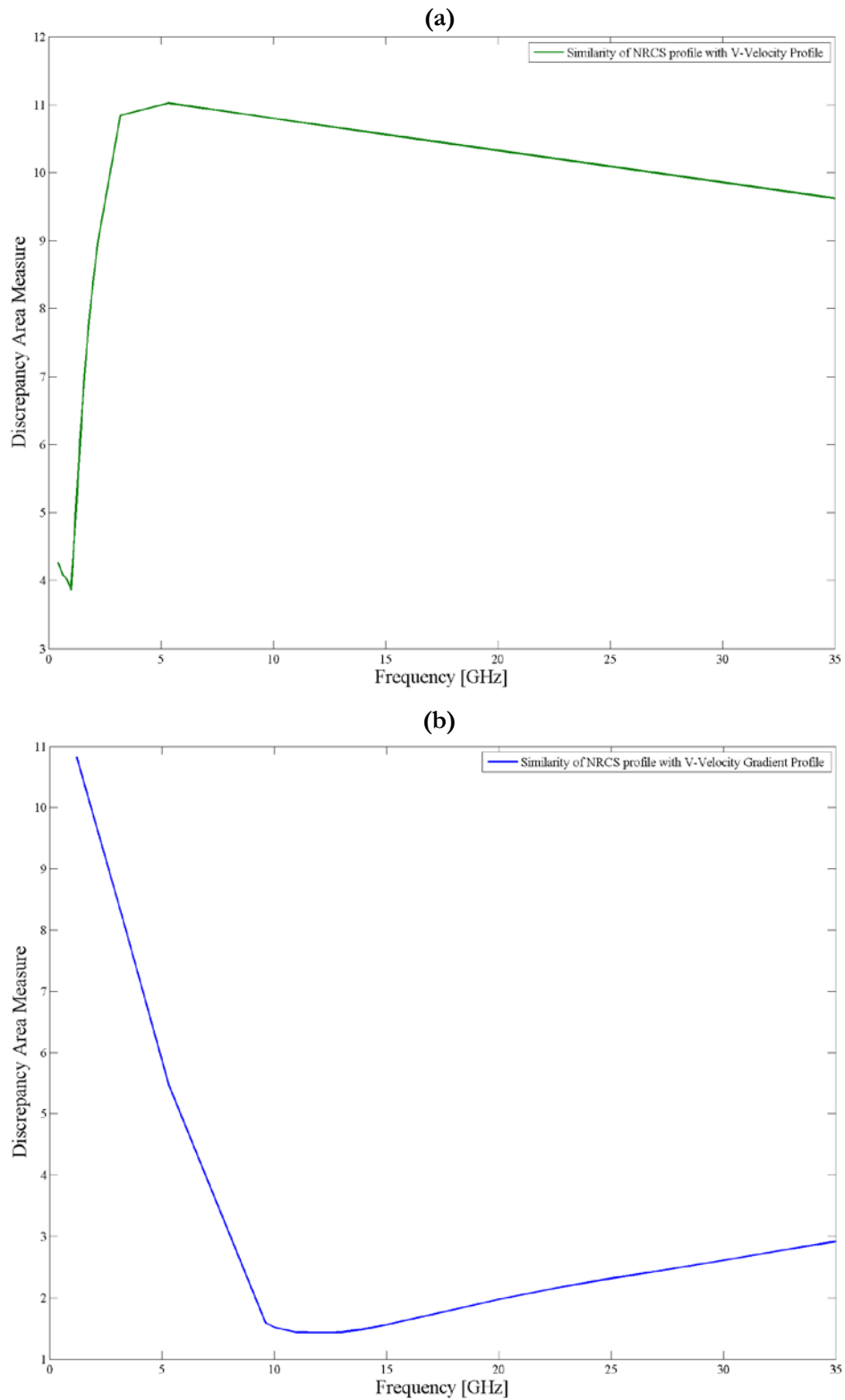
Figure 50. Averaged discrepancy values for normalised Bragg NRCS at varying radar frequency against one-dimensional transect profiles of normalised (a) V-velocity and (b) V-velocity gradients in the y-direction.

With respect to surface profiles, a similar procedure was performed whereby the normalised velocity/velocity gradient profile was deducted from normalised Bragg NRCS profiles on a pixel-by-pixel basis, yielding a two-dimensional profile of (normalised) discrepancy present across the extent of a single Bragg NRCS image. Using this measure, 2-D profiles of discrepancy between normalised Bragg NRCS (at varying frequencies between 0.4 and 35.0 GHz) were calculated with respect to 2-D profiles of V-velocity/gradients; and averaged across all pixels to derive a single value of the correlation observed between the two profiles.

When plotted against varying radar frequency (as in Figure 51 [a] and [b]), the resulting discrepancy value acts as a valuable measure with which to identify regions of the frequency spectrum which yield the greatest opportunity for extracting details of surface structures through NRCS imagery. In the main, these curves demonstrate similar relationships between radar frequency and discrepancy as those observed for simple, one-dimensional transects in Figure 50 (a) and (b). The greatest ability for the surface structure of velocity components aligned in the radar look direction is clearly most favourable at low frequencies (P- and L-band), whereas the greatest opportunity to resolve structures of velocity gradients occurs in the range of 5-15 GHz.

Of course, the analysis that has been pursued in this section does not account for the effect of modulation depth, and operates under the assumption that the (normalised) NRCS profiles at frequencies above e.g. 15 GHz can be adequately resolved. As was previously encountered in §6.3.1, and demonstrated in graphs such as Figure 45, surface signatures derived at radar frequencies at Ku-band and above (12 GHz +) produce only slim contrasts against the stationary water outside the wake region. Hence, whilst frequencies in this region can produce proficient impressions of the underlying velocity gradient structure, there may be a significant challenge in observing such slim variations of NRCS using contemporary SAR equipment. Furthermore, this simple analysis neglects consideration of such approaches as pattern/texture analysis, and in delineating particular features or coherent structures, and a recommendation for future study would focus attention on extracting quantitative information of surface structure and patterns embedded within velocity profiles, and the ability to translate these explicit structures into quantitative measures of surface variation via observation of radar surface scattering, perhaps in the context of other de-stabilising characteristics such as additional (background) surface currents, wind interactions and disturbances, etc.

(a)

(b)
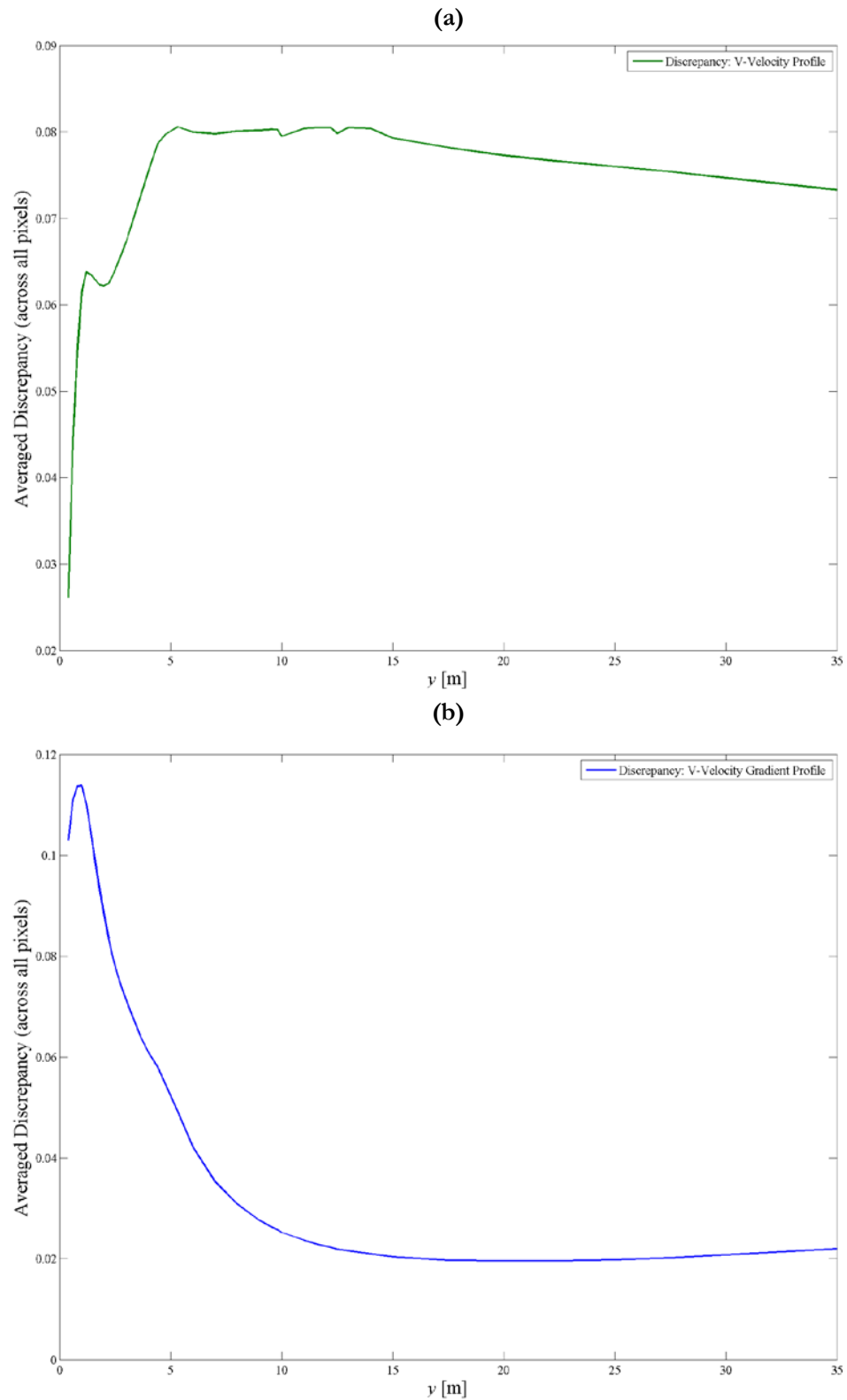
Figure 51. Averaged discrepancy values for normalised Bragg NRCS at varying radar frequency against two-dimensional profiles of normalised (a) V-velocity and (b) V-velocity gradient in the y-direction.

Overall, the findings presented in this sub-section have established a qualitative basis for examining the performance of differing radar operating frequencies in extracting details of surface velocity and velocity gradient structure. In general, these have supported the qualitative presentations discussed in §6.2, and reveal positive benefits of operating particular frequency regimes (P-/L-band, X-/Ku-band) to observe characteristics of the surface flow profile.

In the context of the findings of the rest of this chapter and identification of S-band as an under-exploited radar frequency that may offer potential benefits for increased ocean study, there is strong argument for increased use of multi-frequency instrumentation to probe ocean current profiles to improve understanding of small-scale ocean surface flows. In this respect, a sensor capable of operating at L-, S- and X-/Ku-band frequencies could improve measurement of surface current patterns and visibility of flow structure; balancing the ability to theoretically resolve characteristics of surface velocity profile at L- and X-/Ku-bands with the good 'all-round' performance of S-band.

7. Remote-Sensing Signatures of Wake Turbulence

7.1 Introduction

Whilst simulation of radar backscattering signatures arising from wave-current interaction (observed under 'perfect' NRCS conditions) are of general benefit in understanding the scattering process and visibility of such signatures, of greater significance is the ability to extract such information under adverse ambient conditions or in limited visibility. To this effect, the study was expanded to examine the feasibility of obtaining high-resolution data on surface backscattering under observation by a physical antenna under variable or unpredictable wind conditions.

The simulations performed in this phase were most interested in examining the limiting conditions which hinder observation of small-scale, turbulent surface flow phenomena and whether these limitations influence definition of beneficial instrument configuration for observing such flows. Two primary influences were investigated regarding their role on visibility of the surface signature in the context of particular limitations, namely:

    (i)   The effect of the ambient wind conditions on visibility of the wake system in a range of wind speeds and directions [§7.2.1].

    (ii)   The effect of observation conditions and unknown circumstances of alignment of the radar range/look direction with both the surface current profile and the prevailing (uniform) wind [§7.2.2]

The present chapter begins by considering those circumstances which are unpredictable when observing the ocean surface with a physical SAR antenna; that is, the prevailing wind profile and alignment of the range range/look direction with the surface signature. The full range of characteristics which were examined in this phase of study are presented in tabular form in Table 13.

Radar Frequency	5.3 GHz (C-band)
Incidence Angle	23°
Radar Polarisation	HH
Wind Speed	0 / 2 / 4 / 8 / 10 / 12 / 20 / 28 ms^{-1}
Wind Direction	0° to 330° (30° increments)
Look Direction	0° to 330° (30° increments)
Azimuth Direction	0° to 330° (30° increments) [always 90° to look direction]

Table 13. Comprehensive list of ambient conditions studied in *M4S*
NRCS simulation.

7.2   Ambient Conditions and Observation Geometry

In terms of rendering surface (or sub-surface) current disturbances visible to imaging radar, the primary agent in creating an adequate distribution of surface backscattering waves (and thus derivation of a single radar backscattering signature) is the prevailing wind field blowing over the surface. Air motion, causing shearing of the surface, is the primary mechanism for generating a background wave spectrum containing both long- and short-wave components with which the turbulent/current profile will interact. With respect to the wind response, it is the relative motion of the air over the surface (not the absolute wind speed) that drives formation of short waves and swell, through shearing of the water surface. A typical 'rule-of-thumb' states that surface winds of 2-8 ms^{-1} are necessary to generate favourable conditions for surface signatures to be resolved through modulation of the ocean wave spectrum. Below these speeds, waves may not possess sufficient energy to resolve wave-current interaction: a minimum of 2 ms^{-1} is typically required to generate sufficient shearing of the water surface to yield adequate distribution of short (backscattering) waves on the surface (Holt, 2004); beyond 10-12 ms^{-1}, the wind interaction may generate significant energy in the short wave spectrum such that waves are not appreciably modulated by surface currents, causing flow structures to be unresolved. In high winds, the shearing may be sufficiently strong to cause breaking of waves, and the energy of short waves to be destroyed, inhibiting the ability for wave-current interaction to resolve components of the underlying current/flow field in modulated radar backscatter.

In this "window" of favourable ambient wind speeds, an increase in wind speed typically displays a rise in mean image NRCS (and in addition to a rise in the background NRCS of the ambient water away from the wake region) and a reduction in the modulation depth observed across the derived

signature; although very strong winds may, in some cases, generate a very high dynamic range of modulation. The direction of the prevailing wind significantly affects the primary direction in which (short) waves are propagated: in ocean radar imaging models, the background wave spectrum (which is propagated across the current field during the wave/current interaction procedure) is typically generated according to some empirical (equilibrium) wind-wave spectrum, such as those prescribed by Phillips (1985), Romeiser et al. (1997) or Elfouhaily et al. (1997). The energy spectrum of the wave system (distributed in both wavenumber and direction of propagation) is derived from this equilibrium spectrum, therefore the primary orientation of the propagated wave system with components of the flow field will be a strong influence on the observed wave-current interactions. For all of cases the studied here, the default spectrum of Romeiser et al. (1997) was used as the equilibrium reference.

In previous studies, the role of ambient conditions on visibility of simulated radar backscatter signatures has not been subject to a thorough examination. This shortfall arises primarily because such studies have been performed in order to replicate in-situ measurements or conditions which were present during a dedicated measurement campaign (i.e. those measured at the time that a comparison image was generated). Hence, such studies have endeavoured to reproduce ambient parameters (wind speed and direction) to match the observed conditions. There has been some previous investigation into simulated surface signatures under varying wind speed (at fixed wind direction), such as the studies by Lyden et al. (1985), Fischer & Shuchman (1996) and Fujimura et al. (2011), however there has been only limited study as to the effect of wind direction (or the range/look direction of the radar; with respect to the either the surface feature, or the wind direction, or both) on backscattering signatures. Such studies are limited to those by True et al. (1993) [which considers varying wind and heading directions], and Hennings & Lurin (1999) [which examines the effect of 8 differing heading directions on radar surface signatures of ocean bottom topography]. With the broad aim of this research in identifying the feasibility of observing turbulent processes, the role of (perhaps unpredictable) ambient conditions must be established. With this in mind, the limitations on observation due to the specified wind profile are identified and expanded in the rest of §7.2.

7.2.1 Effect of Wind Speed

Understanding the role of wind speed & direction on visibility of the wake signature (in a range of radar images and for a small number of varying radar configurations) was first investigated by assuming a uniform wind field of varying strength, blowing in a fixed direction. Wind speeds were considered in increments of 2 ms⁻¹ for a wind directions at 0° and 90° to the x-axis of the surface

velocity profile, and operated to consider the effect on visibility of flow components in the wake in Bragg NRCS. An example suite of profiles, demonstrating C-band images derived at HH-polarisation and 23° incidence angle for a wind direction at 90° to the x-axis, are shown in Figure 52 (a)-(f) for a 2 ms^{-1}, 4 ms^{-1}, 8 ms^{-1}, 12 ms^{-1}, 20 ms^{-1} and 28 ms^{-1} wind speeds. From these representative profiles, it is possible to conclude that there is a considerable role played by wind speed on the ability to resolve signature against the background ocean. In particular, there is an observable decrease in image modulation depth observed over the whole wake signature, as well as an increase in the mean image NRCS (and the NRCS of the 'background' water), with increasing wind speed; a predictable result based on the expected response of short waves to wind forcing. From a qualitative perspective, there is a definite difference in the general pattern(s) which are observed at low (2 ms^{-1}; sub-plot [a] of Figure 52) and very high (28 ms^{-1}; shown in sub-plot [f]) wind speeds when plotted on a default colour scale. The reader's attention should, however, be alerted to the varying colour values which are used in each sub-plot, depicting the true range of Bragg NRCS which are observed.

Image statistics for the wind speed cases examined in Figure 52 are tabulated in Table 14, and the variation of modulation depth with wind speed is plotted in Figure 53 with respect to total modulation depth (across the whole image) and average modulation depth (along transects in the y-direction). From Figure 53, it can be seen that peak modulation depth is observed at wind speeds between 2 and 8 ms^{-1}, supporting previous research and the general "rule of thumb" that this interval represents the subset of conditions most likely to derive an observable signature. With respect to the mean Bragg NRCS (and the NRCS of the ambient, stationary water under wind forcing), a linear relationship was observed with increasing wind speed, although these results are not published here: a doubling of wind speed demonstrates a linear increase in mean NRCS, as expected from the general theory.

Figure 52 (following page). Effect of wind speed on Bragg NRCS (dB scale) signature for wind direction aligned in the y-direction , for u_{wind} = (a) 2 ms^{-1}; (b) 4 ms^{-1}; (c) 8 ms^{-1}; (d) 12 ms^{-1}; (e) 20 ms^{-1}; (f) 28 ms^{-1}. For all plots shown, the simulated instrument is a C-band, HH-polarised antenna at 23° incidence angle with a range/look direction aligned in the y-direction.

(a)　　　　　　　　　　　　(b)

(c)　　　　　　　　　　　　(d)

(e)　　　　　　　　　　　　(f)
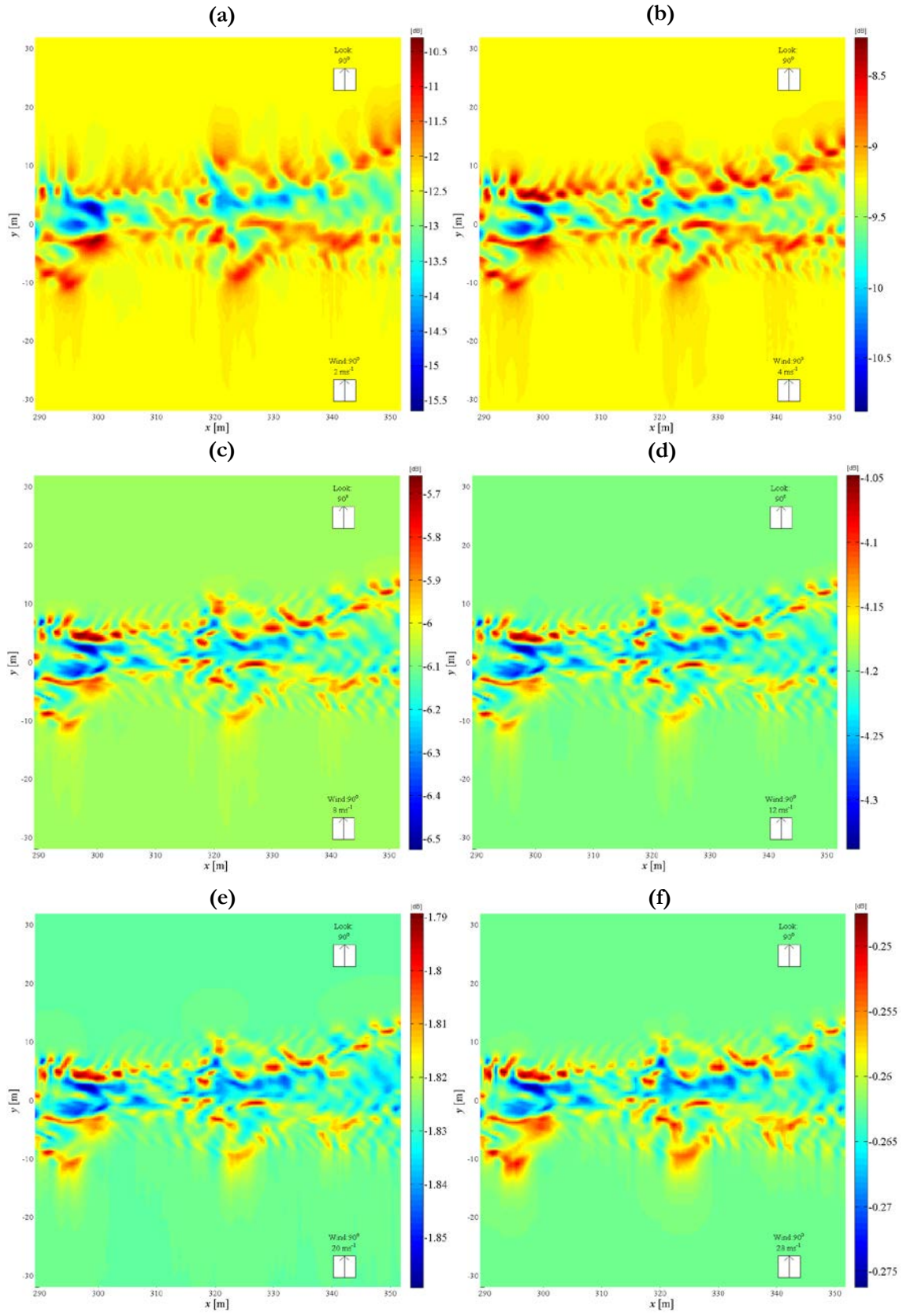
In order to resolve a viable surface signature, a sufficient wind speed is required to propagate surface wave energy such that adequate wave-current interaction can occur through wave modulation, yet it should be observed that the total image modulation depths drops quite significantly below 8 ms^{-1}. The effect of wind speed on modulation depth, from the point of resolving decibel levels in a radar image, is most clear in Figure 54: in sub-plot (b), it can be observed that positive and negative modulation does not exceed 1 dB beyond ~ 6 ms^{-1}, therefore demonstrating that favourable wind speeds are crucial for the ability to discriminate details of the surface structure from a simulated image.
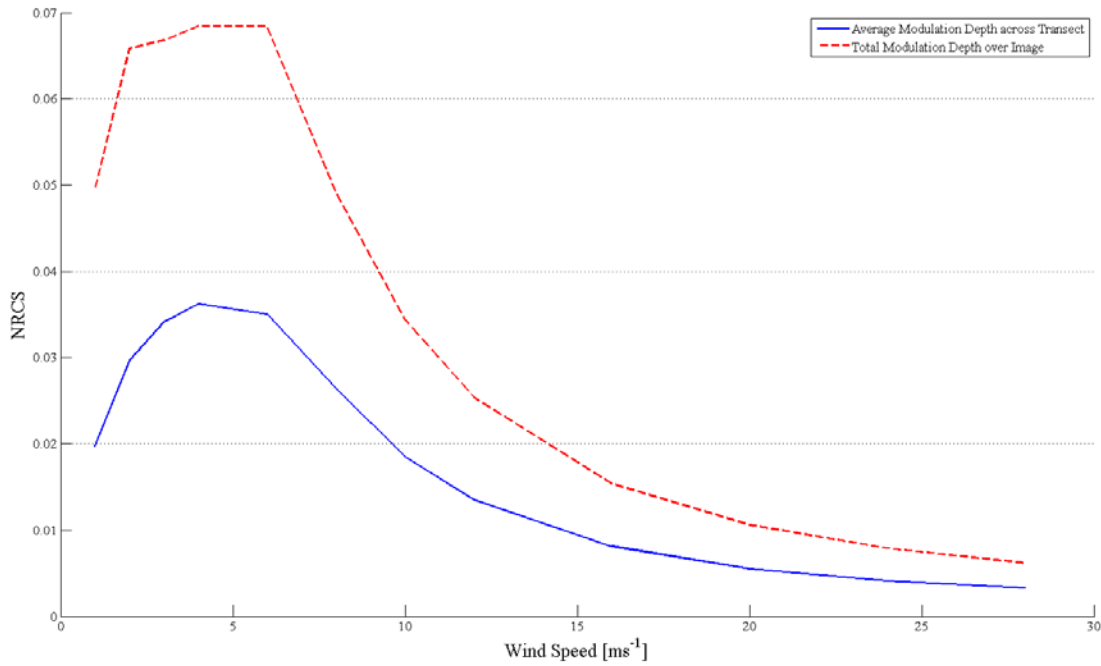
Figure 53. Variation of average modulation depth across transects in the y-direction and total image modulation depth with radar operating frequency. The data used to construct this diagram, and other statistics from the radar frequency investigation, are presented in Table 14.

(a)

(b)
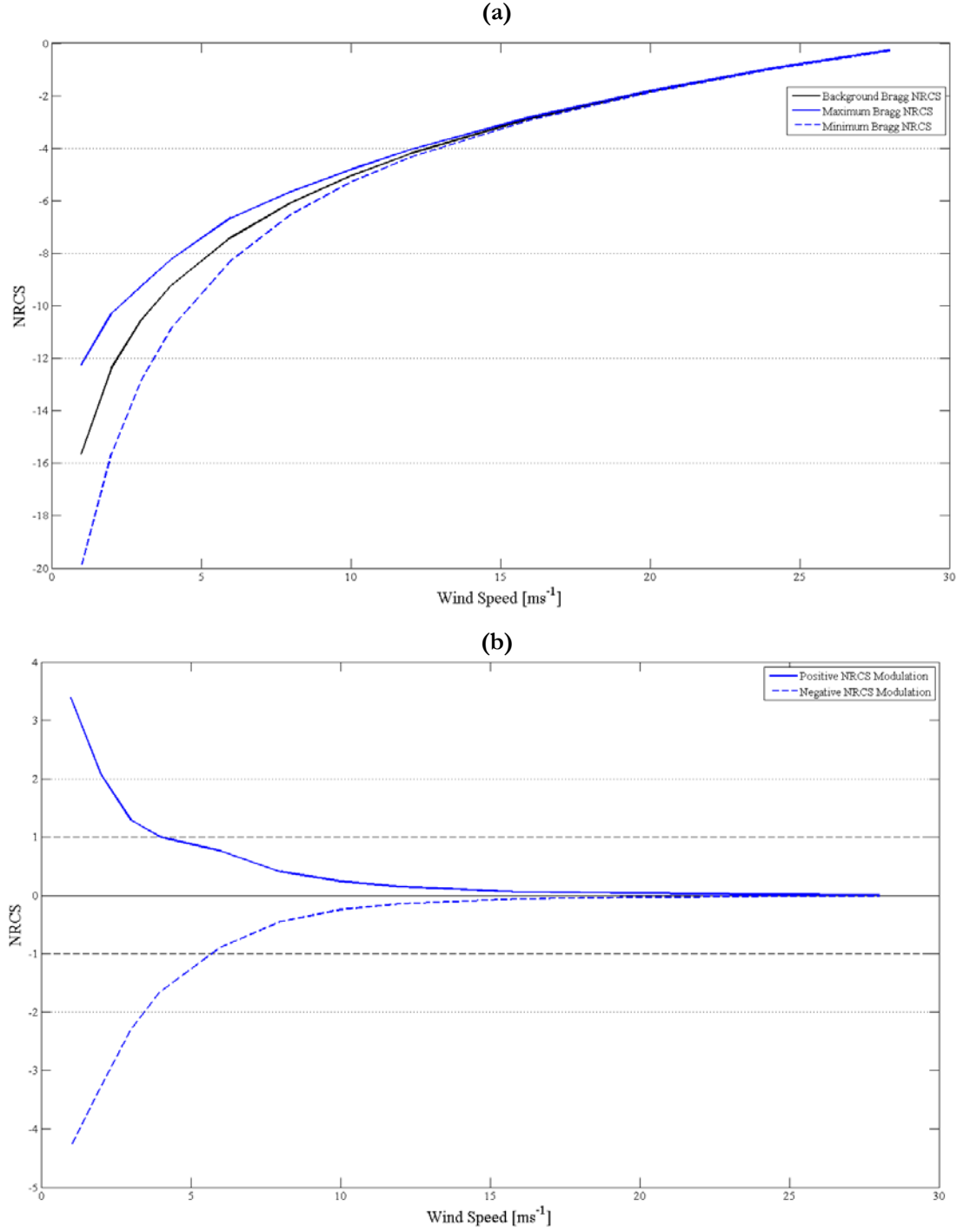
Figure 54. (a) Variation in image modulation depth observed over Bragg NRCS signatures from Wake Profile 1-B observed by a simulated 5.3 GHz (C-band) antenna at HH-polarisation and 23º incidence angle for varying wind speed in the positive y-direction; (b) variation in (positive and negative) background contrast with wind speed. Background NRCS is plotted alongside minimum/maximum NRCS envelope.

	Max./Min. Values (Across Image) [dB]		Modulation Depth (Linear)		Background NRCS		Mean NRCS	
Wind Speed	Positive	Negative	**Average Across Transect**	**Total Across Image**	**Linear Scale**	**dB Scale**	**Linear Scale**	**dB Scale**
1 ms⁻¹	-12.26 dB	-19.95 dB	0.0197	0.0494	0.0275	-15.65 dB	0.0272	-15.65 dB
2 ms⁻¹	-10.31 dB	-15.65 dB	0.0297	0.0658	0.0581	-12.38 dB	0.0577	-12.39 dB
3 ms⁻¹	-9.25 dB	-12.84 dB	0.0341	0.0668	0.0884	-10.54 dB	0.0882	-10.55 dB
4 ms⁻¹	-8.24 dB	-10.88 dB	0.0362	0.0684	0.1192	-9.24 dB	0.1191	-9.24 dB
6 ms⁻¹	-7.40 dB	-6.64 dB	0.0350	0.0684	0.1823	-7.40 dB	0.1823	-7.39 dB
8 ms⁻¹	-5.66 dB	-6.52 dB	0.0264	0.0491	0.2471	-6.07 dB	0.2472	-6.07 dB
10 ms⁻¹	-5.04 dB	-4.80 dB	0.0185	0.0344	0.3133	-5.04 dB	0.3134	-5.04 dB
12 ms⁻¹	-4.05 dB	-4.34 dB	0.0135	0.0254	0.3805	-4.20 dB	0.3806	-4.20 dB
16 ms⁻¹	-2.86 dB	-2.92 dB	0.0081	0.0154	0.5173	-2.86 dB	0.5174	-2.86 dB
20 ms⁻¹	-1.79 dB	-1.86 dB	0.0055	0.0106	0.6567	-1.83 dB	0.6568	-1.83 dB
24 ms⁻¹	-0.98 dB	-0.96 dB	0.0041	0.0079	0.7980	-0.98 dB	0.7981	-0.98 dB
28 ms⁻¹	-0.25 dB	-0.28 dB	0.0033	0.0062	0.9413	-0.26 dB	0.9414	-0.26 dB

Table 14. Statistics extracted from Bragg NRCS profiles of Wake Profile 1-B for varying wind speed blowing parallel to the y-axis in the positive y-direction. Frequency and polarisation of the simulated antenna are 5.3 GHz (C-band) and HH-polarised for all tested cases, for a look direction at 90° to the x-axis and a 23° incidence angle. Rows shaded in light blue represent wind speeds typically considered necessary for satisfactory observation of ocean surface signatures.

With respect to linear σ_0 modulation, Bragg NRCS signatures for a wind aligned in the y-direction with strength (a) 2 ms⁻¹ and (b) 4 ms⁻¹ are depicted in Figure 55, and data from transects of Bragg NRCS (taken at four positions along the x-axis of the Figure 55 profiles, as well as for similar profiles under higher wind strengths), are presented in Table 15. For reference, results from the transect at x = 294 m (where Bragg NRCS variation is presented in linear scale and have been referenced to the NRCS level of the ambient water outside of the wake) are presented alongside the equivalent transect arising from the analogous Bragg NRCS signatures observed under a reversal of wind direction (i.e. wind blowing in the negative y-direction). In the observed transect data of Figure 56, the "upwind" peak (for example, feature [1a] of sub-plot [a]; feature [1b] of sub-plot [b] for opposing wind direction) of Bragg NRCS under 2 ms⁻¹ wind conditions consistently resolves a strong background contrast, yet demonstrates a significantly greater level of negative modulation than is observed at other wind speeds. However, in contrast, the "downwind" peak (for example,

feature [2] of sub-plot [a]) is not resolved as a region of positive modulation, unlike the structure detected at higher wind speeds. Considering the location of the transect ($x = 294$ m) taken on the 2 ms^{-1} Bragg NRCS signature of Figure 55 (a), this demonstrates that the "downwind" edge of the wake is not resolved at low wind speeds; likely due to the effect of adverse currents inhibiting passage of waves. In this respect, the application or presence of only a modest wind speed may not resolve much of the small-scale structure which appears near the centreline of the wake. Application of higher wind speed creates more viable conditions for resolving more of smaller-scale features embedded within the wake's current profile.
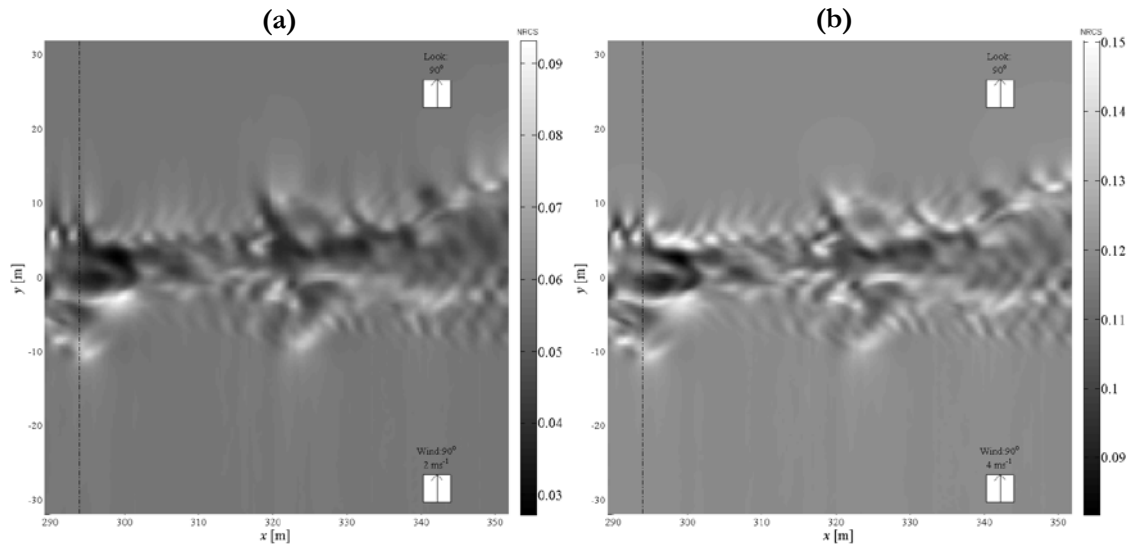
Figure 55. Effect of wind speed on Bragg NRCS (linear scale) signature for wind direction aligned in the y-direction , for $u_{wind} =$ (a) 2 ms^{-1} and (b) 4 ms^{-1}. For all plots shown, the simulated instrument is a C-band, HH-polarised antenna at 23° incidence angle with a range/look direction aligned in the y-direction. A transect of NRCS are denoted at $x = 294$.

In all of the investigated wind speed cases, the Bragg NRCS signature observed within the centre of the wake region consistently exhibits a more negative deviation from the background/ambient scattering level: this may emanate from the presence of adverse currents (that is, those opposing the wind direction and hence primary direction of surface waves) which may be responsible for obstructing the passage of short waves into the 'centre' of the wake, therefore leading to lower levels of (Bragg) wave energy in this area. In comparison, profiles extracted at higher wind speeds (4 ms^{-1} and beyond) show a greater facility to resolve the internal structure(s) of the flow field since the energy of Bragg-scale waves is more significant at higher wind speeds; however, strong winds (12 ms^{-1} and beyond) demonstrate only a modest modulation depth across the signature, which may hinder observation of fine spatial variations.

Wind Speed	Position of Transect				Mean NRCS	
	294 m	309 m	324 m	339 m	Linear Scale	dB Scale
2 ms⁻¹	0.037924	0.017774	0.040092	0.024227	0.0577	-12.40 dB
4 ms⁻¹	0.038564	0.022577	0.042724	0.021192	0.1191	-9.25 dB
8 ms⁻¹	0.026057	0.016114	0.033395	0.016249	0.2472	-6.07 dB
12 ms⁻¹	0.013372	0.007866	0.016447	0.008039	0.3806	-4.20 dB
20 ms⁻¹	0.005571	0.003205	0.006466	0.003196	0.6568	-1.83 dB
28 ms⁻¹	0.003415	0.003300	0.003749	0.001962	0.9414	-0.39 dB
-2 ms⁻¹	0.03488	0.019413	0.03264	0.023968	0.0577	-12.39 dB
-4 ms⁻¹	0.037544	0.022737	0.042802	0.025512	0.1191	-9.24 dB
-8 ms⁻¹	0.025035	0.016073	0.031921	0.016606	0.2472	-6.07 dB
-12 ms⁻¹	0.013082	0.008081	0.015962	0.0087423	0.3806	-4.20 dB
-20 ms⁻¹	0.0061703	0.0034517	0.0064455	0.0044421	0.6568	-1.83 dB
-28 ms⁻¹	0.004397	0.0021011	0.0037353	0.0031701	0.9414	-0.39 dB

Table 15. Modulation depths (in linear NRCS form) taken along individual range lines from Figure 55 (and profiles derived at higher wind speeds) at various positions along the x-axis; variation with wind speed in the (positive) y-direction. Rows shaded in light green represent winds propagated in the (negative) y-direction.

(a)

(b)
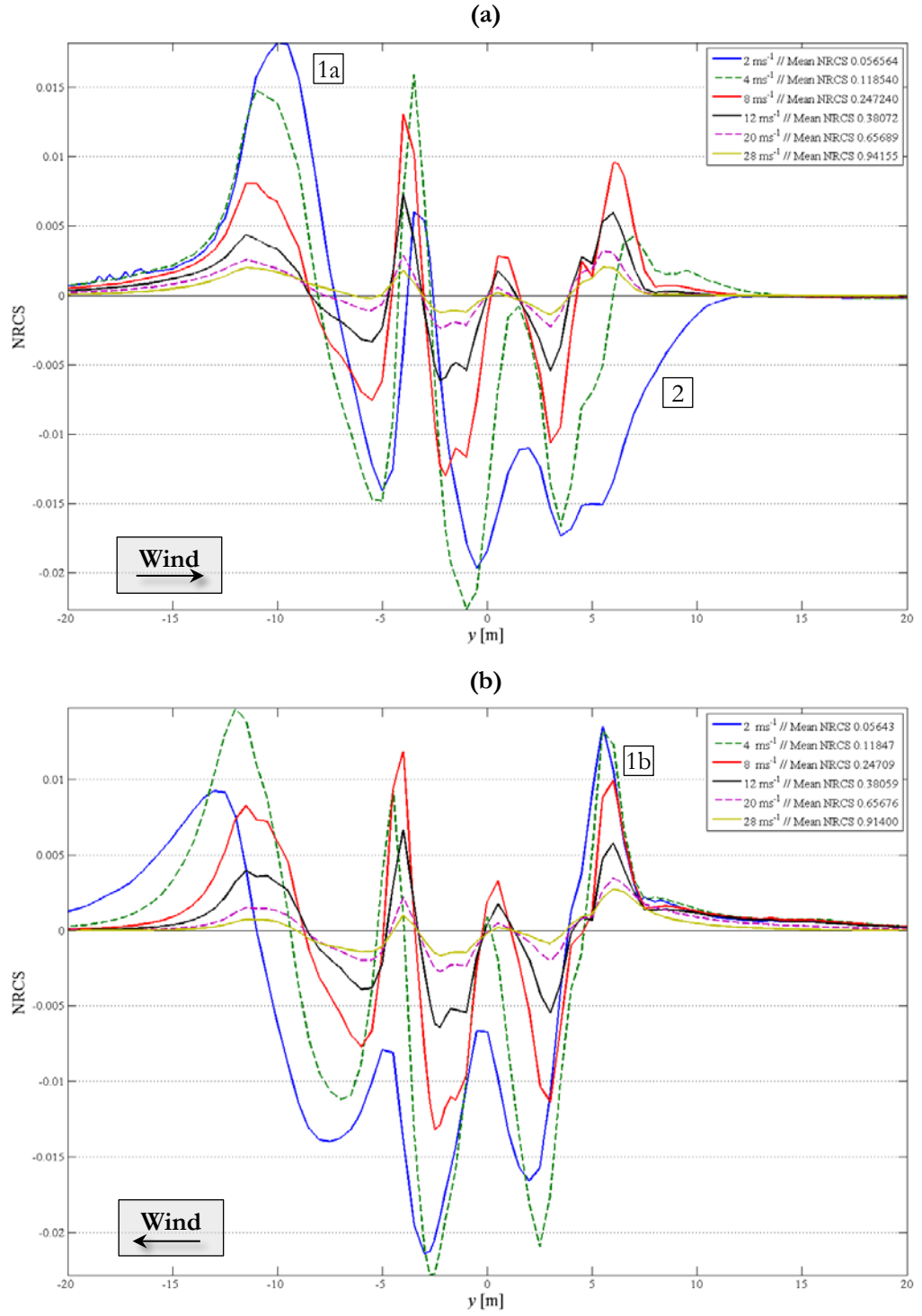
Figure 56. Effect of wind speed on Bragg NRCS signature for wind direction aligned in the **y**-direction: comparison of NRCS transects taken across the data of Figure 34 at positions: (a) 294 m [wind in positive y-direction] and (b) [wind in negative y-direction]. For all plots shown, the simulated instrument is a C-band, HH-polarised antenna at 23° incidence angle.

The derived results are consistent with the findings of True et al. (1993), which also found that increasing wind speed leads to a reduction in NRCS perturbation from background levels; although the maximum wind speed presented by their results was 20 knots (10.3 ms^{-1}). Their study also measured maximum modulation depth (across transects of a turbulent ship wake) at wind speeds of 10 knots (5.14 ms^{-1}), aligning with the statistics observed in the current findings. Naturally, definition of the ambient wind speed (and likewise direction) are not under the control of the radar designer or turbulent ocean scientist, and therefore observations of turbulent surface signatures are, to some extent, at the mercy of the "favourability" of the incidental wind conditions. However, where wind speeds in the vicinity of 4-6 ms^{-1} demonstrate greatest potential for resolving signatures in terms of positive/negative modulation, this may agree favourably with the average (measured at 10 m height) oceanic wind speed of 6.64 ms^{-1} found by Archer & Jacobson (2005). Where this discussion has focussed on varying wind speeds blowing in direction(s) parallel to the y-axis, it must also be noted that wind direction also plays a crucial role on resolving surface signatures; the details of which will be examined in the following sub-section.

7.2.2 Role of Wind Direction

Alignment of the wind profile (which is the agent that drives generation of short waves across the ocean surface) with the primary axes of the investigated current profile is a crucial component in the ability to discriminate details of surface wave-current interaction within a radar image. A test study examined the impact of specification of the initial wind state on simulated imagery, allowing some conclusions to be drawn regarding the ability of a simulated instrument to discriminate the surface flow in a range of potential scenarios. Presentation of results from this investigation begin by considering the effect of varying wind direction on scenes observed from a fixed look direction (at 90° to the y-direction). For reasons which will be discussed in more detail later in this section, the effect of wind direction on visibility is not driven solely by the wind itself, and there is an associated effect which arises based on the alignment between the wind vector and radar look direction.

A suite of results for a C-band, HH-polarised radar at 23° incidence angle is presented in Figure 57, showing two-dimensional signatures of Bragg NRCS for Wake Profile 1-B under forcing from a 4 ms^{-1} wind rotated in increments of 30° with respect to the x-axis. The observed NRCS signature varies in both the observed pattern/structure and in magnitude of NRCS modulation and all of the examined signatures share a common theme of a reduced NRCS response within the interior of the wake, and an elevated response at the wake edges where there are higher gradients of (spanwise)

velocity. The general structure of the wake remains qualitatively consistent under all observed conditions; although minor variations in structure can be observed between different images: such variations reflect variations in wave-current interaction that occur due to wave-current interaction of the primary wind-generated waves with differing components of the flow structure. In some of the derived profiles, some minor distortion is observed on the 'upwind' side of the wake, causing the appearance of "streaming" which propagates along the look direction: such effects likely arise from the finite (wavenumber and/or directional) resolution of the wave propagation model, yielding some minor aberrations in the smooth background spectrum. For the purposes of this investigation, these artefacts are not considered. Statistics extracted from the signatures in Figure 57 are presented in Table 16.

Figure 57 (following pages). Effect of wind direction (alignment with x-direction, ϕ_{wind}) on Bragg NRCS signature: (a) $\phi_{wind} = 0°$; (b) $\phi_{wind} = 30°$; (c) $\phi_{wind} = 60°$; (d) $\phi_{wind} = 90$; (e) $\phi_{wind} = 120°$; (f) $\phi_{wind} = 150°$; (g) $\phi_{wind} = 180°$; (h) $\phi_{wind} = 210°$; (i) $\phi_{wind} = 240°$; (j) $\phi_{wind} = 270$; (k) $\phi_{wind} = 300°$; (l) $\phi_{wind} = 330°$. For all plots shown, the simulated instrument is a C-band, HH-polarised antenna, with range/look direction aligned in the y-direction.

Wind Direction	Look Direction (± 180º)	Look/ Wind Diff.	Modulation Depth (Linear)		Transect at x = 324 m		Mean NRCS	
			Average Across Transect	Total Across Image	Contrast	Mean	Linear Scale	dB Scale
0º	90º	90º	0.0249	0.0482	0.026782	0.080371	0.0803	-10.95 dB
30º	90º	60º	0.0282	0.0537	0.028037	0.090229	0.0902	-10.48 dB
60º	90º	30º	0.0334	0.0614	0.036079	0.1099	0.1098	-9.59 dB
90º	90º	0º	0.0362	0.0684	0.042724	0.11929	0.1191	-9.24 dB
120º	90º	30º	0.0345	0.0628	0.042908	0.11008	0.1099	-9.59 dB
150º	90º	60º	0.0295	0.0547	0.035534	0.090285	0.0901	-10.45 dB
180º	90º	90º	0.0263	0.0553	0.030409	0.080409	0.0802	-10.96 dB
210º	90º	60º	0.0306	0.0593	0.036347	0.090553	0.0901	-10.45 dB
240º	90º	30º	0.0360	0.0703	0.038632	0.1102	0.1098	-9.59 dB
270º	90º	0º	0.0383	0.0761	0.042802	0.1191	0.1191	-9.24 dB
300º	90º	30º	0.0360	0.0741	0.040845	0.10992	0.1099	-9.59 dB
330º	90º	60º	0.0302	0.0642	0.033676	0.09031	0.0902	-10.48 dB

Table 16. Statistics extracted from Bragg NRCS profiles of Wake Profile 1-B (Figure 57) for a uniform 4 ms^{-1} wind blowing at varying directions with respect to the x-axis. Frequency and polarisation of the simulated antenna are 5.3 GHz (C-band) and HH-polarised for all tested cases, observed at a 23º incidence angle and from a look direction in the positive y-axis.

When the wind is fully aligned at 90° to the primary direction of the wake, short surface waves are propagated primarily in the spanwise direction of the surface current, creating maximum wave-current interaction where peak gradients in v-velocity act to modulate the surface wave spectrum. Under these conditions, there is a peak in the (linear) modulation depth observed over the image as well as in the observed mean image NRCS, producing the strongest signature that may be resolved over the background NRCS of the (stationary) water. Conversely, for a wind blowing in a direction at 0° (or equivalently at 180°) to the x-axis, the modulation depth observed across the NRCS transect is weak because current variations in u- velocity are typically very small: there may not be significant modulation of the waves by the current in order to derive a modulated backscattering response. Furthermore, when the wind is perpendicular to the radar look direction, there is typically a minimal backscattering signature, since such an alignment will result minimal (wave) energy of surface waves travelled toward/away from the radar look direction; this is responsible for the profile observed in background NRCS where look direction differs from that of the wind; this may

be observed by considering the solid black line in Figure 58. Where winds possess a component which blows in the look direction, modulation depth increases and structure of the surface currents becomes visible. In these cases, there is a minimum of mean image NRCS (and the background NRCS) along with a minimum of modulation depth, meaning that there is likely to be greater difficulty in observing a signature under such conditions. Therefore, where observed signatures (like those of subplots [c] and [i] from Figure 57) demonstrate qualitative similarity with input surface velocity profiles, it is likely that there will be greater difficulty in correlating the radar backscattering profile with surface structure(s) when the wind and look directions are not fully aligned. Transects extracted from the profiles presented in Figure 57 at position $x = 324$ m for varying wind direction (0° to 330° in 30° increments) under fixed 90° look direction are presented in Figure 59, demonstrating the varying structure that observed when the incident winds at, or close, to orientations perpendicular to the radar look direction.
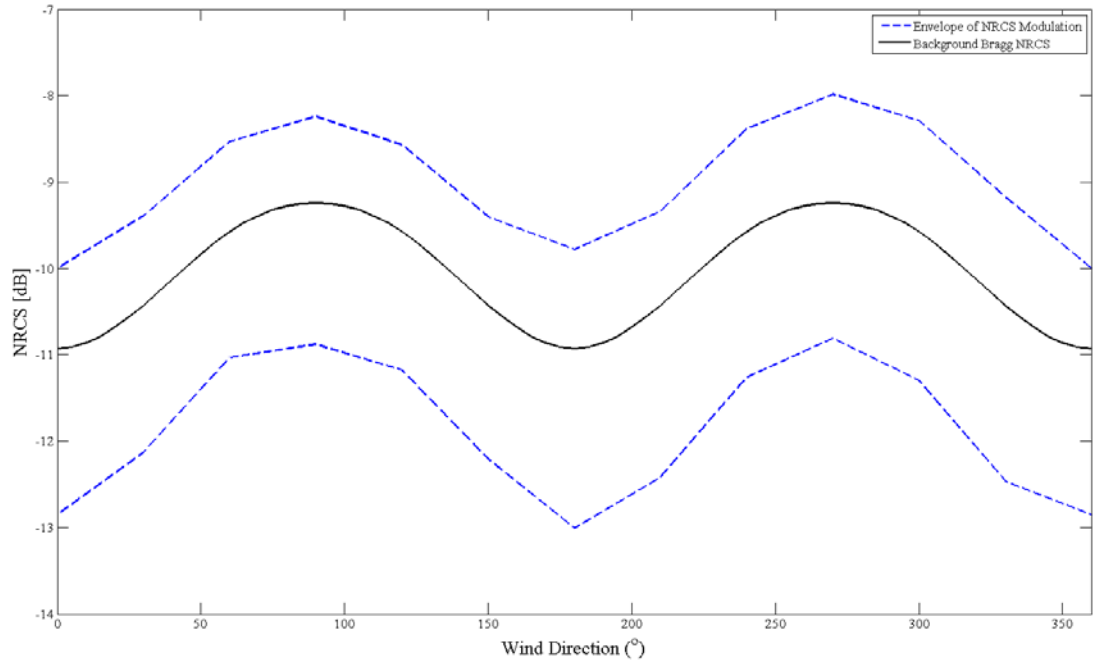
Figure 58. Variation of background Bragg NRCS and positive/negative Bragg NRCS modulation for wind direction (0° to 330° in 30° increments) profiles presented in Figures 58 and 59. For all cases, look direction is fixed at 90°; the simulated antenna is a 5.3 GHz (C-band) instrument with HH-polarisation and 23 incidence angle.

(a)

(b)
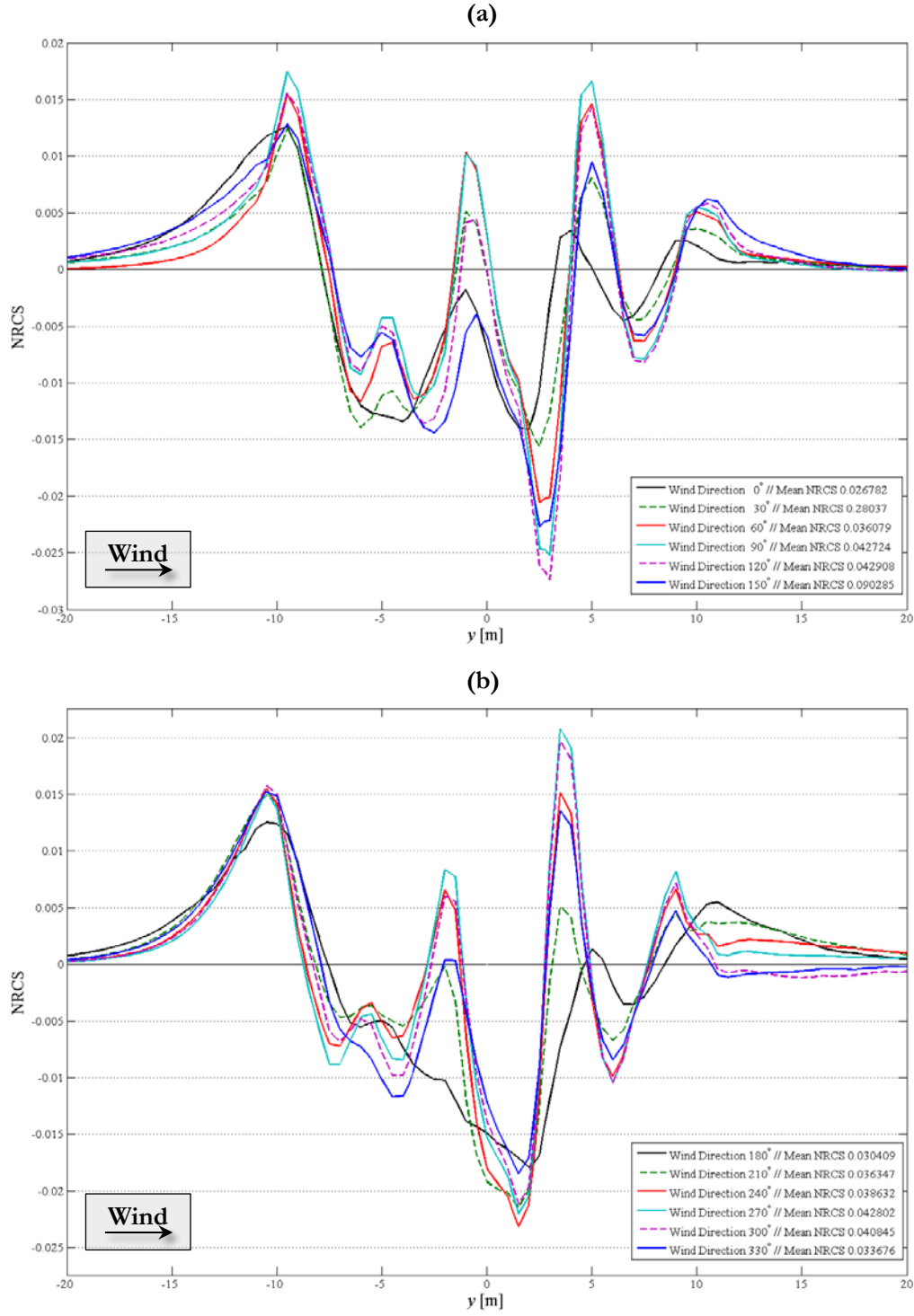
Figure 59. Effect of wind direction on Bragg NRCS signature for a fixed look direction aligned in the y-direction: comparison of NRCS transects taken across the data of Figure 57 at $x = 324$ m for (a) 0° to 150 ° in 30° increments and (b) 180° to 330 ° in 30° increments. For all plots shown, the simulated instrument is a C-band, HH-polarised antenna at 23° incidence angle.

A variety of statistics taken from Figure 57 are presented in Figure 60 on a polar grid, which demonstrate the variation of modulation depth (average across transects taken in the y-direction; total across whole image) and mean NRCS. These results indicate that, in the main, there is an expected pseudo-symmetry of the observed statistics aligned about the axes of maximum (0°, 180° wind direction) and minimum (90°, 270° wind direction) difference between the wind and look directions. However, these profiles also indicate that there exist certain, preferential directions (or favourable alignments of the observed wind and/or look vectors) for observation, owing to the anisotropy of the current profile; this is particularly noticeable in Figure 60 (b), where there is a clear asymmetry in (total) image modulation depth where the unique, varying flow structure interacts with wave energy propagating from different directions.

(a)

(b)

(c)
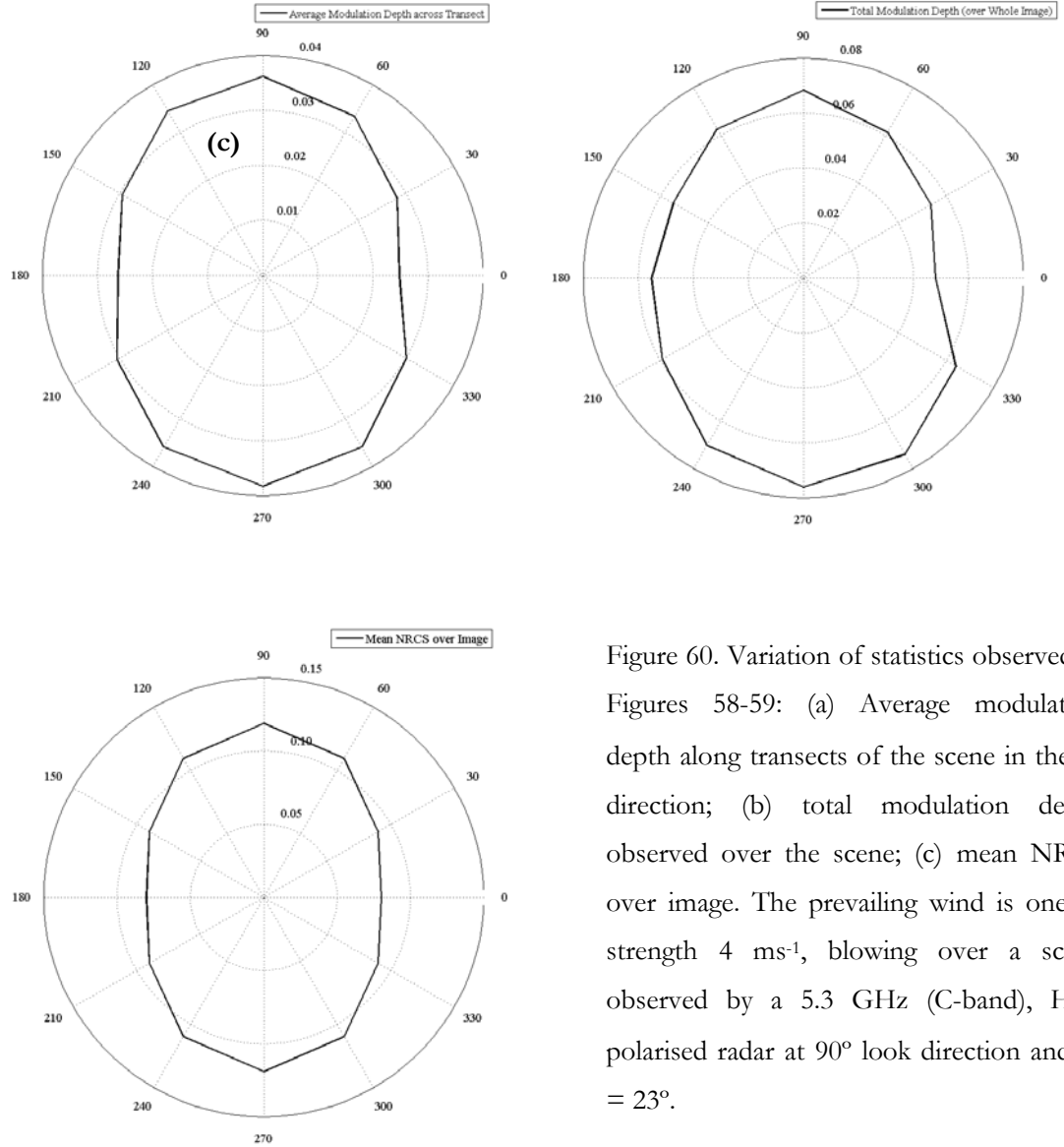
Figure 60. Variation of statistics observed in Figures 58-59: (a) Average modulation depth along transects of the scene in the y-direction; (b) total modulation depth observed over the scene; (c) mean NRCS over image. The prevailing wind is one of strength 4 ms⁻¹, blowing over a scene observed by a 5.3 GHz (C-band), HH-polarised radar at 90° look direction and θ_i = 23°.

Where the findings discussed in §7.2.2 have thus far examined differences in the radar signature which may be observed when considering scenes of radar backscatter viewed from a fixed look orientation under varying wind direction, in reality, the effect of wind direction is explicitly coupled to the associated direction in which the simulated radar observes the scene. Specification of a wind speed and direction in a radar backscatter simulation principally defines the background (equilibrium) wave spectrum and distribution of energy (in wavenumber and direction) of the backscattering waves. In the case of *M4S* and this study, a spectrum based on that of Romeiser et al. (1997) was used. It is not possible, therefore, to isolate the effects of wind direction (or, equally, look direction) alone in order to understand their influence on the ability to resolve flow structure due to the coupling effects that are observed when one or other is manipulated. Therefore, the results presented in in this section regarding alignment of wind and look directions must be tempered by a consideration of these coupling effects. The investigation into the role of wind direction hereby continues by considering the effect of varying wind direction with a coincident look direction aligned in the same direction as the wind.

The backscattering response observed in a Bragg NRCS profile is dependent on two mechanisms. Firstly, the wave-current interaction and the resulting modulation of the (equilibrium) wave spectrum: both will vary based on directional distribution (as well as distribution in wavenumber) of short-wave energy with respect to the surface current components; secondly, the alignment of the radar look direction with the Bragg wave(height) spectrum which governs the $[\psi(\boldsymbol{k_B}), \psi(-\boldsymbol{k_B})]$ contribution to the observed radar backscattering signature and hence defines the observed amplitude of short waves travelling explicitly toward/from the radar look direction. Under ideal circumstances, the distribution of short, backscattering waves would be isotropic in direction, such that there is no directional variation in the (wave) energy of the background wave spectrum, and therefore there is no prerequisite for particularly "advantageous" wind/look alignment. However, in reality, there is some directionality with which the wind direction drives the swell and short wave energy; although there will be waves propagating in all directions, albeit with minimal wave energy. In this respect, observing in a look direction in which there is likely to be minimal wave energy (and hence minimal modulation through wave-current interaction) will create significant change in the surface signature when compared with observing in a direction aligned with the local wind. A further complication occurs since the hypothetical flow field is also not isotropic, and therefore the alignment of both the wind and the look direction with the primary axes of the surface wake must also enter consideration: there are more favourable directions to observe the wake, i.e. where wave-current interaction effects are more strongly discerned.

Some discussion of the role of varying wind direction (with co-incident look direction) was previously raised during consideration of qualitative structure in §6.3 and, as established previously, the strongest response was most clearly observed when the incident wind direction was aligned at 90° to the x-axis along with the radar look direction. The effects of rotating both the wind direction and radar look direction on visibility of surface flow patterns in Bragg NRCS signature are further demonstrated in Figure 61: in these cases, the radar look direction is rotated between 0° and 330° (in 30°) increments, where a 4 ms^{-1} wind is also manipulated to align with look direction. Statistics from the profiles presented in Figure 61 are tabulated in Table 17. Considering the observed surface signatures, a clear effect on the resolved structure can be observed as the wind/look direction is rotated: at 0° and 90° wind/look directions (Figure 61 [a] and [d], respectively), the observed signatures are the same as those previously shown in Figures 29 (a) and 30 (a), demonstrating an affinity with input current data as was discussed in Chapter 6. As the wind/look direction is rotated, the surface signature resolves components of velocity (along with gradients of velocity) which are aligned in the look direction of the instrument. This is intuitive, since the Bragg backscattering equation (Equation [xx]) considers only (modulated) waves of frequency k_B which propagate toward/away from the look direction: such waves are likely to be modulated only by components of the surface current which are aligned in the same direction, therefore the capacity to resolve these components in the simulated NRCS image should come as no surprise. The challenge in considering visibility of radar surface signatures, therefore, lies in deriving a robustness to 'favourable' and 'unfavourable' ambient/observation conditions and a capability to observe surface signatures under a variety of unpredictable conditions.

Figure 61 (following pages). Dependence of wind/look direction alignment on visibility of wake structure with wind and look directions at (a) 0°, (b) 30°, (c) 60°, (d) 90°, (e) 120°, (f) 150°, (g) 180°, (h) 210°, (i) 240°, (j) 270°, (k) 300° and (l) 330° to the x-axis. Bragg NRCS signature has been resolved in from a simulated C-band (5.3 GHz) at HH-polarisation and 23° incidence angle.

| Wind Direction | Look Direction (± 180º) | Look/ Wind Diff. | Modulation Depth (Linear) | | Transect at x = 324 m | | Mean NRCS | |
			Average Across Transect	Total Across Image	Contrast	Mean	Linear Scale	dB Scale
0º	0º	0º	0.0330	0.0841	0.043462	0.1223	0.1190	-9.24 dB
30º	30º	0º	0.0374	0.0879	0.038672	0.12202	0.1191	-9.24 dB
60º	60º	0º	0.0383	0.0760	0.043817	0.12021	0.1190	-9.24 dB
90º	90º	0º	0.0362	0.0684	0.042724	0.11929	0.1191	-9.24 dB
120º	120º	0º	0.0404	0.0995	0.037688	0.1193	0.1191	-9.24 dB
150º	150º	0º	0.0402	0.1105	0.040765	0.11974	0.1190	-9.24 dB
180º	180º	0º	0.0316	0.0847	0.048846	0.1195	0.1188	-9.25 dB
210º	210º	0º	0.0371	0.1063	0.040734	0.11971	0.1189	-9.25 dB
240º	240º	0º	0.0369	0.0828	0.036966	0.11965	0.1190	-9.24 dB
270º	270º	0º	0.0383	0.0761	0.042802	0.1191	0.1191	-9.24 dB
300º	300º	0º	0.0422	0.0853	0.035959	0.11966	0.1192	-9.24 dB
330º	330º	0º	0.0408	0.1016	0.042772	0.12114	0.1193	-9.23 dB

Table 17. Statistics extracted from Bragg NRCS profiles of Wake Profile 1-B (Figure 61) for varying wind directions for a uniform 4 ms^{-1} wind blowing at angles with respect to the x-axis. Frequency and polarisation of the simulated antenna are 5.3 GHz (C-band) and HH-polarised for all tested cases, observed at a 23º incidence angle and from a look direction in the positive y-axis.

As previously mentioned, it is not possible to isolate the role of wind direction (alone) in order to understand the influence on the ability to resolve flow structure: the investigation into the role of wind direction will now be expanded by considering the effect of varying look direction at fixed wind direction. Such investigation is, perhaps, the most relevant study with respect to real SAR operation since, depending on the passage of the antenna platform over the scene, there may an element of pseudo-randomness as to the instantaneous look direction. As has been established, there is a significant advantage in observing a surface flow feature from a perspective where the radar look direction is aligned with the wind in order to maximise visibility of surface flow structure characteristics. In reality, this is unlikely to be quite so fundamental since physical wind fields are rarely entirely uniform and therefore will create more local variation and fluctuations in speed and/or direction such that there is less reliance on favourable wind direction for wave-current interaction[20].

The case of a fixed-direction uniform wind field, observed under a variety of radar look orientations, is explored in Figure 62. Since the $[\psi(k_B), \psi(-k_B)]$ term in Equation (xx), Bragg NRCS for a 0° look direction is identical to that for 180°, only results between 0° and 150° (in 30° increments of look direction) have been presented here. As discussed previously, there is a minimum of mean NRCS and modulation depth observed when invoking a look direction that is perpendicular to the local wind direction; for example, in the profile depicted in Figure 62 (a). Despite this, the Bragg NRCS signature shown in sub-plot (a) shows qualitative comparison with the structure of the u-velocity current profile, although the structures appear distorted. Such distortion likely appears due to reduced wave modulation arising from wave-current interaction since waves propagating in the look direction will have smaller amplitudes than those propagating in the wind direction, and therefore the current flow structures resolved by such interaction are less well-defined. Where sub-plot (d) demonstrates good resemblance to the distribution of gradients of v-velocity in the y-direction, sub-plots (b), (c), (e) and (f) [i.e. where the look direction has some component in both the x- and y-directions and therefore alignment with some component(s) of both the u- and v-velocity characteristics] resolve varying characteristics of the velocity structure associated with these different directions: for instance, sub-plot (e) [depicting a look direction at 120° to the positive x-direction] resolves aspects of the u-velocity gradients aligned in the x-axis, but also characteristics of the v-current structure.

---

[20] As discussed in the description of the current study, a uniform wind (with no spatial variation) is assumed for all simulations. It is perhaps worth noting that variable wind field(s) could act to obscure some details of surface structure due to local variations in wind speed/direction and therefore the local propagation of surface waves. In addition, the presence of breaking waves and/or whitecapping could severely hamper wave propagation and/or the local backscattering response.

The conclusions of this investigation, therefore, remain qualitative rather than quantitative: the general theme that emerges is that the surface signature will resolve the components of surface velocity which are aligned in look direction of the observing instrument. Furthermore, there is some robustness as to the capability to resolve such signature under varying wind direction, but a natural preference for maximising the signature arises where the look direction and primary wave direction are parallel. Whilst this finding is not a surprise (indeed, it is intuitive based on the Bragg backscattering theory), it is one which merits such investigation regarding the influence of "favourability" of the ambient or wind conditions. In cases where there is a "favourable" wind (which is blowing parallel to the radar look direction), the surface signature will resolve small-scale structures with greater clarity, whilst even "unfavourable" alignments of the wind and look directions may still resolve some broad details of the surface flow signature.

Figure 62 (following page). Dependence of look direction on visibility of wake structure with look direction at (a) 0°, (b) 30° (c) 60°, (d) 90°, (e) 120° and (f) 150° to the x-axis. The radar signature has been resolved in Bragg NRCS from a simulated C-band (5.3 GHz) at HH-polarisation and 23° incidence angle. In all cases, the wind is 4 ms^{-1} aligned in the y-direction.
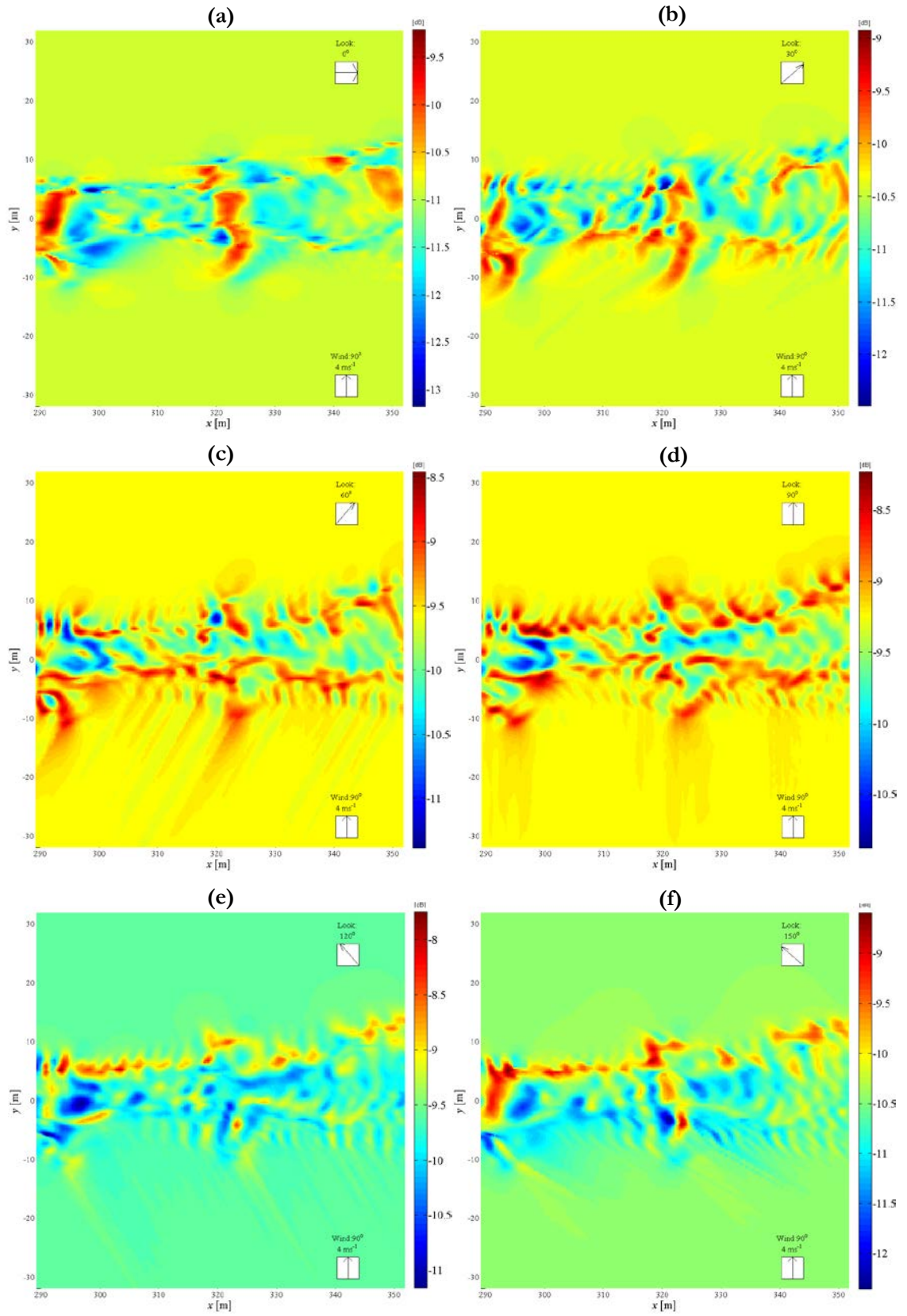
7.2.3 Summary

As has been discussed, the unpredictability of the ambient, surface conditions poses particular challenges for resolving some surface signatures and in interpreting surface flow conditions. Of course, it is not possible for a remote-sensing instrument to ensure that favourable ambient/wind conditions are present over the surface when obtaining a radar image of the scene; it is important, however, to understand how a surface signature may vary with differing (local) wind conditions and how this could help in interpretation of real flow fields observed by imaging radar. In general strong wind conditions (speeds beyond 8-10 ms^{-1}) will cause the signature to deteriorate significantly such that flow structure resolved in NRCS modulation may not be detected, except by highly-sensitive instruments. At wind speeds beyond 6 ms^{-1}, it was observed that positive/negative NRCS modulation does not exceed ~1 dB, whereas under more modest wind and sea states (2-5 ms^{-1}) the turbulent wake structure may be more easily resolved and comparisons with characteristics of the input current profile may be drawn. The obtained results were qualitatively consistent with results from previous studies, such as those presented by True et al. (1993) for a turbulent ship wake and Fischer et al. (1999) in the case of open-ocean convection. The role of the wind also governs the passage of short- (and long-) waves across the flow feature under scrutiny, which will influence local wave-current interaction and the observed surface signature.

Wind direction also plays a crucial role in governing the observed surface signature. In particular, the alignment of the wind direction with both the radar look direction and the orientation of the flow structure is, potentially, a source of considerable variation. Where the wind and look direction are aligned, there are typically satisfactory conditions with which to make qualitative comparison and correlation with characteristics of the input current profile; where they differ, extracting details of the signature becomes more challenging. The most unfavourable conditions are present when the wind and look vectors are perpendicular. In this respect, the case of wind/look alignment (at least for the Bragg NRCS case) can be very influential in defining how well some surface flow feature is resolved through its radar surface signature. According to the theory of a linear modulation transfer function (Alpers & Hennings [1984]), hydrodynamic modulation (of waves) is at its maximum when the prevailing wind opposes the primary surface flow currents, supporting the conclusions drawn here: with the advancement of high-resolution instrumentation capable of observing fine radar surface features, there will be an increasing role in surface (ambient) characteristics in governing how fine, surface details can be made visible and how this may affect interpretation of such signatures. Extracting details of flow structure in the context of (potentially unknown or uncooperative) ambient conditions (i.e. wind/look alignment) is a complex issue; one that cannot be fully addressed in this exploratory study.

In the previous chapter, investigation of instrument configuration yielded encouraging results indicating that increased observation of surface flow features using S-band frequencies could offer potential benefits. To investigate the role of S-band instruments in the context of unpredictable arrangement of wind and look vectors with the centreline of the wake flow, Figure 63 presents a comparison of (5.3 GHz) C-band and (3.2 GHz) S-band responses to the profiles observed in Figure 62 for a varying look aspect under a fixed wind direction. A particular objective for this brief study was to examine the robustness of S-band observations to application of varying wind & look orientations (compared with more practised frequencies such as C-band), and to understand the resilience of derived signatures to (potentially) unpredictably ambient conditions. In this very simple investigation, only a single wind speed (4 ms⁻¹) and look direction (90° to the x-axis) was considered, but with application of wind directions between 0° and 330°, separated by 30° increments. The results agree with the findings of §6.3.1 (which were derived for a fixed look direction at 90°; parallel with the applied wind), indicating a similar trend in mean NRCS and modulation depth for S-band profiles over a reference C-band case. Statistics for the tested cases are tabulated in Table 18.

Look Direction (± 180°)	Frequency	Modulation Depth (Linear)		Mean NRCS	
		Average Across Transect	Total Across Image	Linear Scale	dB Scale
0°	3.2 GHz	0.0357	0.0803	0.1062	-9.74 dB
	5.3 GHz	0.0280	0.0715	0.0799	-10.97 dB
30°	3.2 GHz	0.0401	0.0842	0.1134	-9.45 dB
	5.3 GHz	0.0302	0.0715	0.0900	-10.46 dB
60°	3.2 GHz	0.0424	0.0855	0.1271	-8.96 dB
	5.3 GHz	0.0344	0.0698	0.1098	-9.59 dB
90°	3.2 GHz	0.0457	0.0993	0.1326	-8.77 dB
	5.3 GHz	0.0362	0.0684	0.1191	-9.24 dB
120°	3.2 GHz	0.0417	0.0961	0.1275	-8.94 dB
	5.3 GHz	0.0368	0.0912	0.1099	-9.59 dB
150°	3.2 GHz	0.0415	0.0840	0.1137	-9.44 dB
	5.3 GHz	0.0339	0.0800	0.0901	-10.45 dB

Table 18. Statistics extracted from Bragg NRCS profiles of Wake Profile 1-B for varying look directions for a uniform 4 ms⁻¹ wind blowing at a 90° angle with respect to the x-axis and under inspection by simulated (3.2 GHz) S- and (5.3 GHz) C-band antennas. For all cases, a HH-polarisation antenna and a 23° incidence angle are assumed.

(a)

(b)

(c)
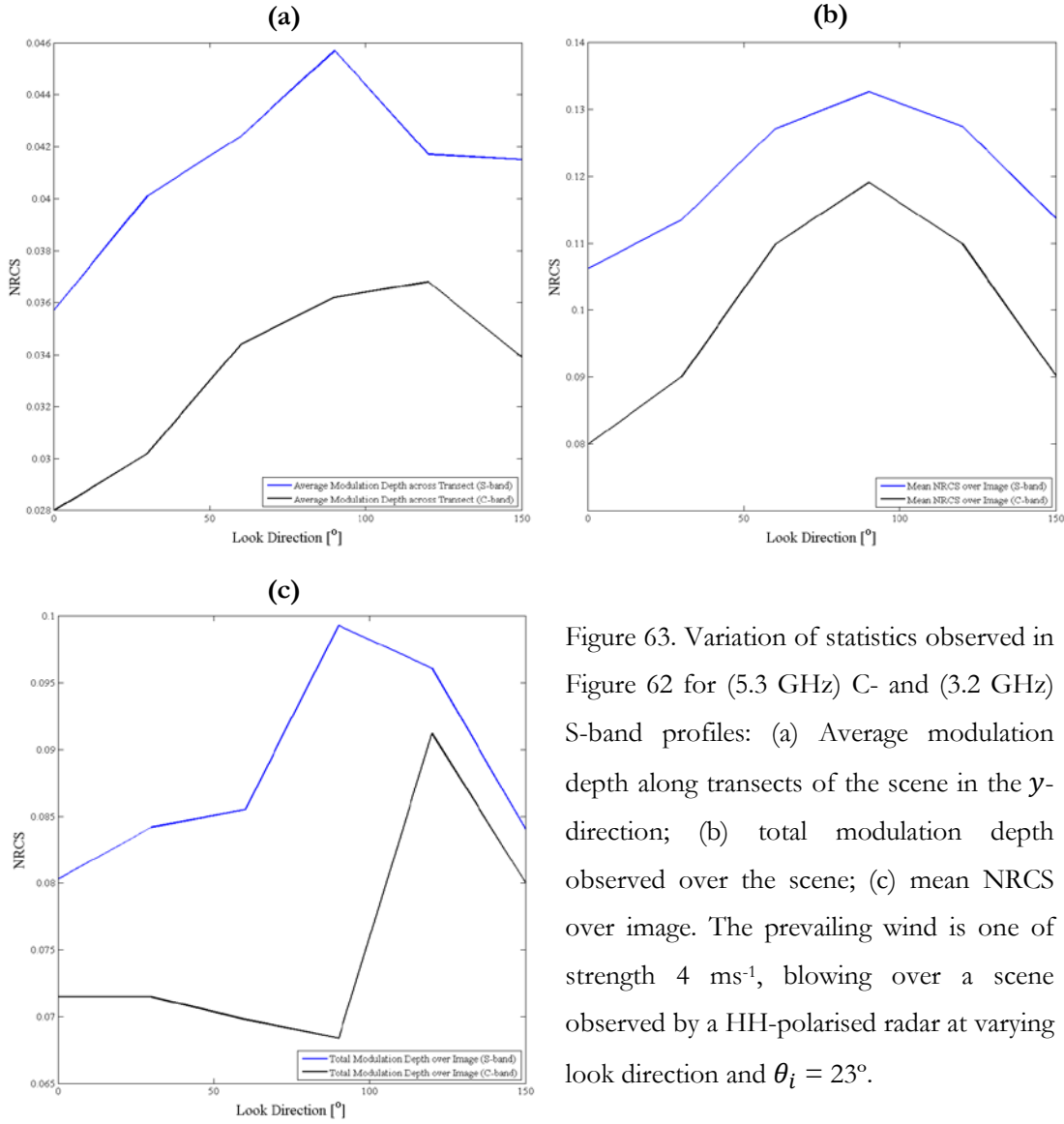
Figure 63. Variation of statistics observed in Figure 62 for (5.3 GHz) C- and (3.2 GHz) S-band profiles: (a) Average modulation depth along transects of the scene in the y-direction; (b) total modulation depth observed over the scene; (c) mean NRCS over image. The prevailing wind is one of strength 4 ms^{-1}, blowing over a scene observed by a HH-polarised radar at varying look direction and $\theta_i = 23°$.

The results which have been presented and discussed have focussed, in the main, on radar backscattering profiles derived in terms of Bragg NRCS: appropriate comments must be made regarding the limitations posed by omission of composite surface NRCS signatures in this study. Particularly at high wind speeds, tilting of long waves will be significant and therefore cause significant modification to the observed backscattering profile. Furthermore, the effects of background currents and sea state have not been considered in the current study, but will supplement a more complex system; both for wave-current interaction characteristics as well as surface radar backscattering. With respect to design or selection of a suitable SAR instrument, a crucial task may lie in identifying a configuration which offers satisfactory performance in all circumstances/a range of likely ambient scenarios.

8. RAR/SAR Simulation and Perspectives

8.1 Instrument NRCS Resolution

Consideration of radar scattering profiles in Chapter 6 and 7 was confined only to profiles of pure Bragg backscattering (and a selection of composite surface NRCS profiles), presented with a pixel resolution defined by the spatial grid of the input current field. For such profiles, spatial resolution of simulated images is 25 cm, whereas most current spaceborne SAR instrumentation is not capable of obtaining profiles of surface backscatter at such fine resolution. At present, *TerraSAR-X* presents the finest nominal resolution of (3-5 m; up to 1 m in SpotLight mode) achievable for a civilian spacecraft; although, it is estimated that sub-metre resolution is achievable with the military X-band SAR constellation, *SAR-Lupe*. Details of currently-operating and future spaceborne SAR missions are presented in Table 19, whilst Table 20 provides a selection notable airborne campaigns and/or instruments which are documented in the literature. Finer spatial resolution (perhaps below 1 m) may typically be achieved by airborne platforms compared with spaceborne instruments due to reduced slant range distance from the antenna to the surface, therefore consideration of such campaigns is important. Table 19 does not contain a comprehensive list of all airborne SAR campaigns, but aims to provide a representative subset of historical airborne/spaceborne campaigns to provide context for simulated cases.

To examine the effect that spatial resolution has on the ability to resolve an ocean process from the observed surface signature, a new algorithm was derived for re-sampling radar signatures at typical spaceborne spatial resolution from the idealised backscatter profiles. A computational procedure to artificially degrade spatial resolution was applied to NRCS data using a block-averaging algorithm: adapting the Matlab code written for block-averaging by Simon (2010)[21], the new algorithm combines multiple pixels (at original resolution) into a single, coarser pixel, having the effect of artificially "degrading" the spatial resolution of the NRCS signatures such that they can be observed at coarser resolution. A similar technique was employed in the generation of simulated images presented by Fujimura et al. (2011), although it is not known how such signatures were derived.

---

[21] Jan Simon, University of Heidelberg (*blockmean.m*, 2010) MATLAB code available at:
http://www.mathworks.co.uk/matlabcentral/fileexchange/24812-blockmean (last accessed 15/02/2013)

Instrument	Launch	Orbital Details	Frequency	Spatial Resolution
SAR-Lupe[22]	2006-2008	500 km	X-band	1-2 m (estimated) 0.5 m (Spotlight, estimated)
RADARSAT-2[23]	2007	798 km	C-band	25 x 28 m (4 looks) 10 x 9 m (1 look)
TerraSAR-X[24]	2007	514 km	X-band	3 x 3 m nominal 1 m (SpotLight mode)
Cosmo-SkyMed[25]	2007-2010	619 km		
PAZ[26]	2014 (expected)	505 km		
ALOS-2[27] (PALSAR-2)	2014 (expected)	628 km	L-band	10 m 1-3 m (SpotLight mode)
Sentinel-1[28]	2014 (expected)	693 km	C-band	25 x 25 m (multi-look) 5 m (1 look)
NovaSAR[29]	2015 (expected)	580 km	S-band	20-30 m (ScanSAR) 6 m (Stripmap; 4 looks)

Table 19. Current spaceborne SAR missions and their spatial resolution, sorted in order of launch date. All spacecraft operate in a circular, polar Earth orbit.

In this respect, the derived results represent simulated radar images at highly idealised spatial resolution and unaffected by Doppler/motion effects or other limitations of the SAR technique. Operation of this procedure is, in itself, analogous to the method of multi-look image generation, whereby "smoothed" signatures (with reduced speckle interference) are constructed from a high-resolution single-look image by averaging over several pixels. All simulated images presented in this section are retained in decibel form, for immediate comparison with published SAR imagery: such profiles represents simple radar cross-section images which are affected by instrument resolution, but which do not account for the (motion/Doppler) effects arising from motion of the antenna or surface, nor for the effects of instrument noise or speckle. In this respect, these results represent simulated "ideal" RAR images, albeit presented to a spatial resolution significantly finer than would be achievable using the RAR technique from Earth orbit. To maintain consistency with results presented earlier in this thesis, simulation images have been derived using profiles of Bragg NRCS as a baseline; in reality, images derived by airborne or spaceborne platforms will observe the full surface wave spectrum (not just the Bragg frequency of waves) and therefore observe images more comparable with surface signatures derived in composite surface NRCS.

---

[22] Information from: http://www.swp-berlin.org/fileadmin/contents/products/fachpublikationen/ SAR_Lupe_ks.pdf (last accessed 15/02/2013)
[23] Information from: http://www.asc-csa.gc.ca/eng/satellites/radarsat2/radarsat-tableau.asp (25/07/2013)
[24] Information from: http://www.astrium-geo.com/terrasar-x/ (15/02/2013)
[25] Information from: http://www.telespazio-vega.com/PDF/2811Cosmov2%20-%20Axel.pdf (15/02/2013)
[26] Information from: http://www.astrium.eads.net/en/programme2/paz-odb.html (25/07/2013)
[27] Information from: http://www.jaxa.jp/projects/sat/alos2/index_e.html (25/07/2013)
[28] Information from: http://esamultimedia.esa.int/multimedia/publications/SP-1322_1/ (15/02/2013)
[29] Information from: http://www.sstl.co.uk/Downloads/SSTL-Brochure-pdfs/ 1904-SSTL-NovaSAR-Brochure (02/03/2013)

Instrument	Flight & Instrument Details	Frequencies	Relevant Studies/Campaigns
Dual-Beam Interferometer	Nominal altitude 590 m Nominal velocity 102 ms^{-1} Resolution: 6 m (range, azimuth) 60-82° incidence angle	C-band; ATI-SAR	Toporkov et al. (2011)
DLR AeS-1	Nominal altitude 3200 m Nominal velocity 83 ms^{-1} 45° incidence angle	X-band; ATI-SAR XTI-SAR	Siegmund et al. (2001) Siegmund et al. (2004)
NASA/JPL UAVSAR [30]	Nominal altitude 12 km Resolution: 5 m x 7.2 m	L-band	Jones et al. (2011)
Pi-SAR [31]	Nominal altitude 8-9 km Nominal velocity 214 ms^{-1} Resolution: 1.5 m (4 looks) 40° incidence angle	X-band[**] L-band	Nadai et al. (2011)
NORCSEX experiment	Nominal altitude 7 km Nominal velocity 120 ms^{-1} Resolution: 7.5 m (azimuth), 15 m (range); 45-85° incidence angle	C-band X-band	Johannessen et al. (1991)
SARSEX experiment	Nominal altitude 7 km Nominal velocity 125 ms^{-1} Resolution: 0.3-6 m (azimuth), 0.6-16.7 m (range) 21-30° incidence angle	P-band L-band C-band X-band Ku-band Ka-band	Hogan et al. (1996)
ERIM-CCRS SAR	Nominal altitude 6.7 km (also 0.9 km, 1.5 km, 3.4 km) Resolution: 3 m (az., slant range) 58.5 ° incidence angle	L-band[**] C-band X-band	Gasparovic et al. (1988)
NASA/JPL AIRSAR[32]	Nominal altitude 8 km Nominal velocity 230 ms^{-1} Resolution: 1 m (az.), 5-10 (range) 20-65° incidence angle; NESZ: -35 dB	P-band[**] L-band C-band	Thompson & Jensen (1993) Ouchi et al. (1997) Lee et al. (1998) Johnson (2003)

Table 20. Sample of historical airborne instruments/campaigns and studies published in the literature. Attempts have been made to cover the breadth of airborne experiments, without presenting an exhaustive list. The superscript (**) denotes simultaneous collection of radar backscatter at multiple radar frequencies.

---

[30] Information from: http://uavsar.jpl.nasa.gov/: http://www.asf.alaska.edu/news_notes/7-1/jpl_uavsar
[31] Information from: https://directory.eoportal.org/web/eoportal/airborne-sensors/pi-sar2
[32] Information from: http://airsar.jpl.nasa.gov/documents/genairsar/airsar_paper1.pdf
(all webpages last accessed 26/07/2013)

Instrument	Flight & Instrument Details	Frequencies	Relevant Studies/Campaigns
DLR E-SAR[33]	Nominal altitude 6 km Nominal velocity 100 ms^{-1} Resolution: 0.25-1.5 m (azimuth), 2-4 m (range) 27-55° incidence angle	P-band** L-band C-band X-band	Hennings et al. (2001)
DLR F-SAR [34]	Nominal altitude 6 km Nominal velocity 100 ms^{-1} Resolution: 0.2-1.5 m (azimuth), 0.3-2.25 m (range) 25-55° incidence angle	P-band** L-band S-band C-band X-band	Rogers et al. (2008)
Sandia Twin-Otter SAR Testbed [35]	Nominal range 1-16 km Nominal velocity 35-70 ms^{-1} Resolution: 0.3-3 m; 2-10 m (VHF/UHF) 2-90° incidence angle	Ka-band** Ku-band X-band VHF/UHF	Walker et al. (1996)
SIR-C/X-SAR	Nominal altitude 224 km Nominal velocity 7900 ms^{-1} Resolution: 25 x 25 m (multi-look) **45° incidence angle**	L-band** C-band X-band	Melsheimer et al. (1998b) Chubb et al. (1999)

Table 20 (contd). Sample of historical airborne instruments/campaigns and studies published in the literature. Attempts have been made to cover the breadth of airborne experiments, without presenting an exhaustive list. The superscript (**) denotes simultaneous collection of radar backscatter at multiple radar frequencies

Figure 64 (a) represents a simulated (Bragg-only) backscatter scene for Wake Profile 1-C at the original NRCS pixel resolution output by *M4S*, whilst sub-plots (b) [1 x 1 m], (c) [5 x 5 m] and (d) [10 x 10 m] depict the same data which has been resampled at different pixel resolution. At a coarse resolution of 10 x 10 m (Figure 64 [d]), very little of the wake signature is visible and there is only a very slender modulation depth (0.26 dB) that is observed; the original Bragg backscattering signature demonstrates a much larger modulation depth (2.5 dB). As pixel resolution is improved, the depth of modulation increases and more of the surface structure is resolved across the signature: this can be observed in Figure 65, which depicts the positive/negative Bragg NRCS modulation for images sampled at different pixel resolution. The dashed blue line represents the 'envelope' of modulation observed across the image (i.e. variation of $NRCS_{min}$ and $NRCS_{max}$), displaying how positive and negative NRCS modulation varies as pixel resolution is made coarser. In particular, this

---

[33] Information from: http://www.dlr.de/hr/en/desktopdefault.aspx/tabid-2326/3776_read-5679/ (last accessed 26/07/2013)

[34] Information from: http://www.dlr.de/hr/en/desktopdefault.aspx/tabid-2326/3776_read-5691/ (last accessed 26/07/2013)

[35] Information from: http://www.sandia.gov/radar/datacoll.html (last accessed 11/09/2013)

demonstrates that, as would be expected, negative modulation of the signature is more visible than that of positive modulation: along the x-axis, the positions are marked at which the (positive/negative) modulation falls below 1 dB above/below the background NRCS, which may indicate that capability to resolve significant variations of NRCS across the signature may be difficult beyond 1-2 m resolution.

For all resolution cases, the mean NRCS observed across the image remains the same, since this will be a natural feature of the block-averaging process. The effect of pixel resolution on modulation depth (in positive/negative deviation from the background value) can be observed both over the whole image, and over transects of the NRCS signature: the results depicted graphically in Figures 66 and 67 demonstrate how the ability to resolve small-scale structure naturally declines when resolution capability is deteriorated. Details of transect data (as well as further statistics extracted from Wake Profile 1-C processed at different pixel resolution) are tabulated in Table 21.
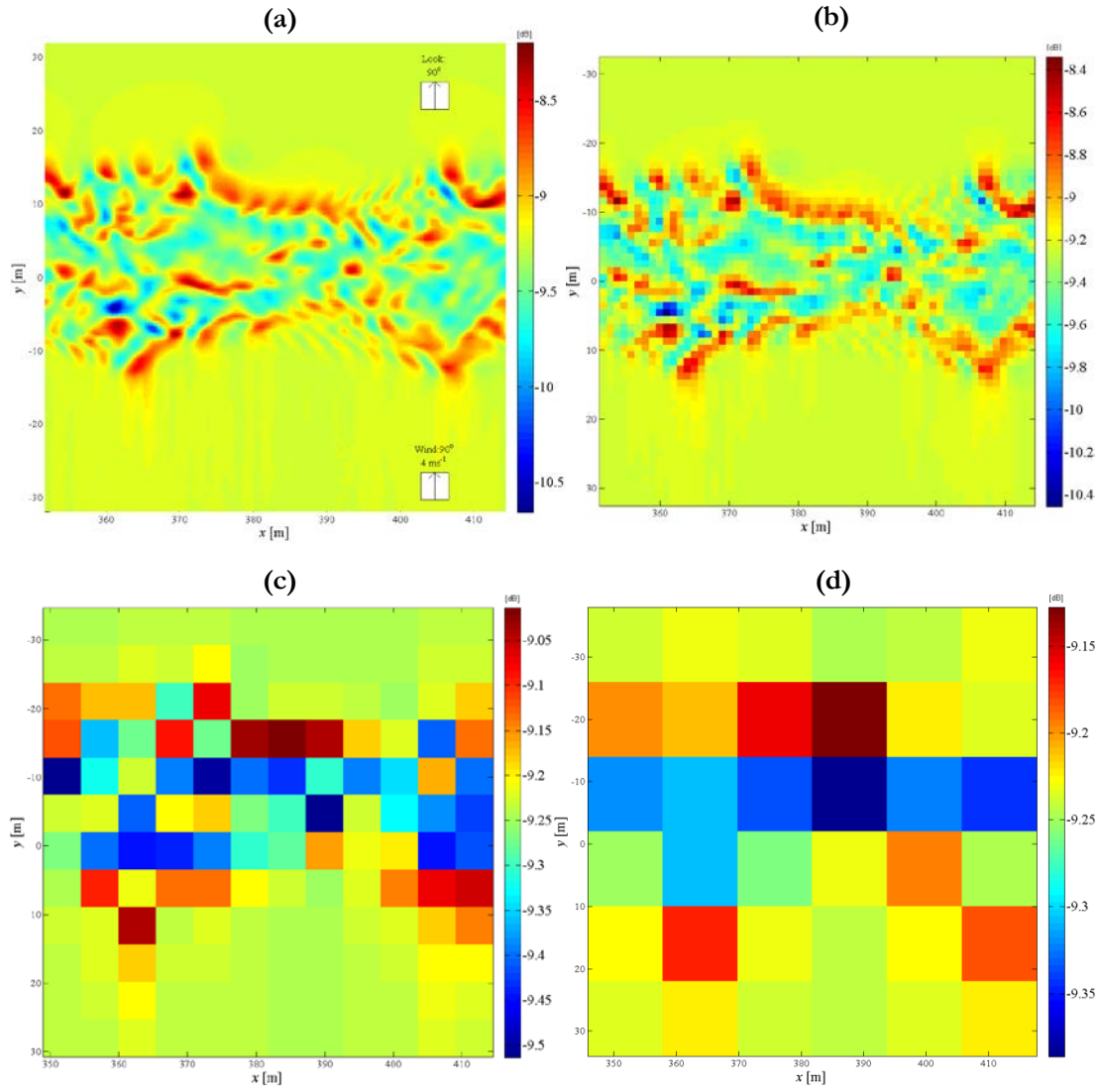
Figure 64. Comparison of block averaging on 5.3 GHz (C-band) Bragg NRCS radar signature for Wake Profile 1-C: (a) original NRCS resolution; resolution down-sampled to (b) 1 x 1 m, (c) 5 x 5 m, (d) 10 x 10 m. Polarisation is HH and incidence angle is 23º; ; look and wind (4 ms^{-1}) directions are both in the positive y-direction.

A transect of Bragg NRCS, taken at $x = 324$ m, is presented in Figure 66. Where the solid black line indicates the original backscattering profile (at 0.25 m resolution), the solid blue line marks a re-sampled transect at 1 m resolution, and the influence that coarsened pixel resolution has on "approximating" the structure is very clear, since there is an obvious effect of truncating the ability to resolve peaks of NRCS fine structure and the full range of modulation, but keeping the relative (spatial) distribution intact. Such response is observed because the scale of the variation (primarily the width of the peaks/troughs observed in the y-direction) is larger than the 1 m resolution; in profiles sampled at more coarse pixel resolution (for example, the solid red line [10 m resolution]), the backscattering signature loses clarity in both range of modulation and ability to resolve surface features of small spatial scale.
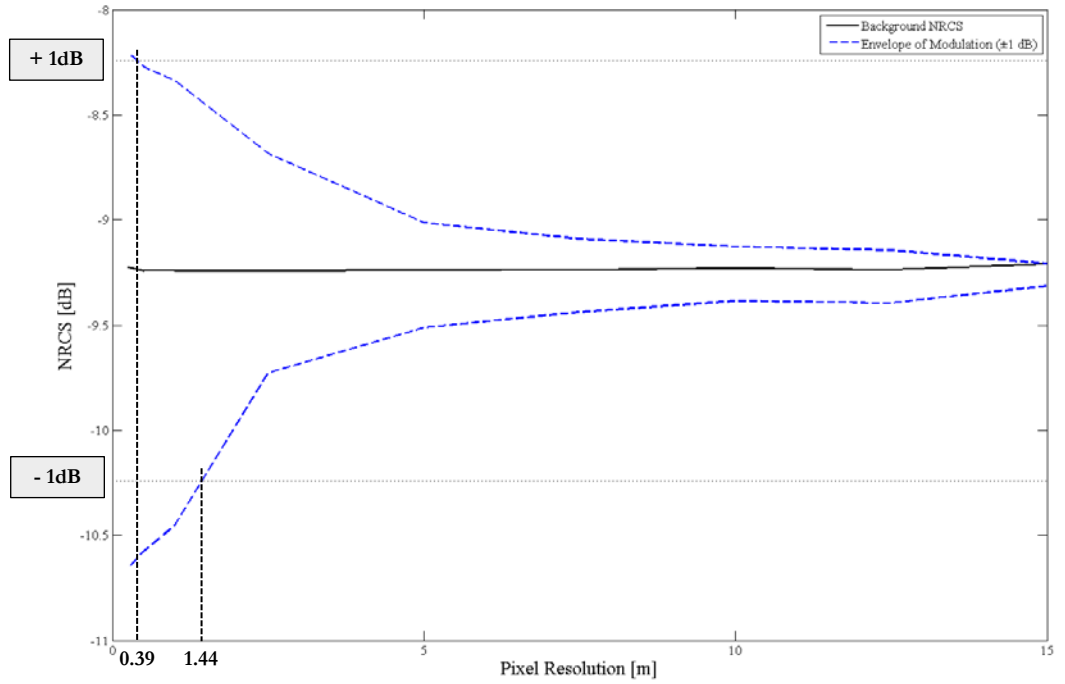
Figure 65. Variation of background Bragg NRCS and positive/negative Bragg NRCS modulation for profiles presented in Figure 64/Table 21 with varying pixel resolution. Data points for re-sampled signatures are mapped the centre point of the coarsened pixels. For all cases, look direction is fixed at 90°; the simulated antenna is a 5.3 GHz (C-band) instrument with HH-polarisation and 23 incidence angle. A 4 ms⁻¹ wind is blowing in the positive y-direction.

The unexpected profile which is marked by the dashed green line (5 x 5 m resolution) on Figure 66 differs from other profiles due to the method by which individual pixels are "grouped" by the block-averaging method. Depending on how the block grid falls onto the original NRCS signature (equivalent in real life to the location of individual scatterers fall within the Doppler frequency history and how they are binned into a single pixel), the observed response can differ. Figure 67 reproduces the Bragg NRCS signatures of Wake Profile 1-C previously depicted in Figure 64, whereby sub-plot (a) has been overlaid with a grid demonstrating how pixels are grouped into the 5 x 5 m re-sampled signature shown in sub-plot (b). Table 21 presents a range of statistics for the investigated cases: rows shaded in light red represent those cases which were presented in Figure 64.
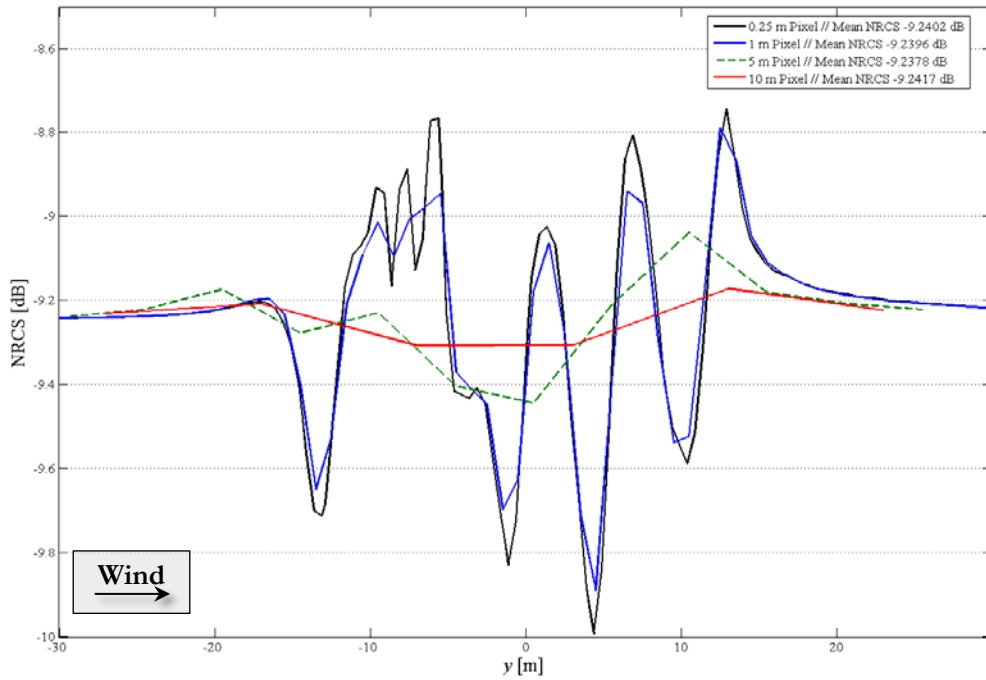
Figure 66. Transect taken at position $x = 362.75$ m from the Bragg NRCS profiles presented in Figure 64. For all plots shown, the simulated instrument is a C-band, HH-polarised antenna at 23° incidence angle with (4 ms^{-1}) wind and look direction in the positive y-direction.

Pixel Resolution	Max./Min. Values (Across Image) [dB]		Modulation Depth		Transect at $x = 324$ m		Background NRCS
	Positive	Negative	Average Across Transect	Total Across Image	Contrast	Mean NRCS	
Original (0.25 m)	-8.20 dB	-10.66 dB	1.18 dB	2.46 dB	1.34 dB	-9.2402 dB	-9.2258 dB
0.5 m	-8.27 dB	-10.58 dB	1.23 dB	2.31 dB	1.23 dB	-9.2396 dB	-9.2422 dB
1.0 m	-8.34 dB	-10.45 dB	1.10 dB	2.12 dB	1.10 dB	-9.2396 dB	-9.2422 dB
2.5 m	-8.68 dB	-9.73 dB	0.71 dB	1.04 dB	0.71 dB	-9.2421 dB	-9.2415 dB
5.0 m	-9.01 dB	-9.51 dB	0.41 dB	0.50 dB	0.41 dB	-9.2378 dB	-9.2386 dB
7.5 m	-9.09 dB	-9.44 dB	0.24 dB	0.35 dB	0.24 dB	-9.2419 dB	-9.2370 dB
10.0 m	-9.13 dB	-9.39 dB	0.14 dB	0.26 dB	0.14 dB	-9.2417 dB	-9.2310 dB
12.5 m	-9.14 dB	-9.40 dB	0.14 dB	0.25 dB	0.14 dB	-9.2441 dB	-9.2374 dB
15.0 m	-9.21 dB	-9.31 dB	0.09 dB	0.11 dB	0.09 dB	-9.2424 dB	-9.2105 dB

Table 21. Statistics extracted from Bragg NRCS profiles of Wake Profile 1-C for varying pixel resolution. Frequency and polarisation of the simulated antenna are 5.3 GHz (C-band) and HH-polarised for all tested cases, observed at a 23º incidence angle and from a look direction in the positive y-axis. The incident wind is of strength 4 ms⁻¹ blowing in the positive y-direction.
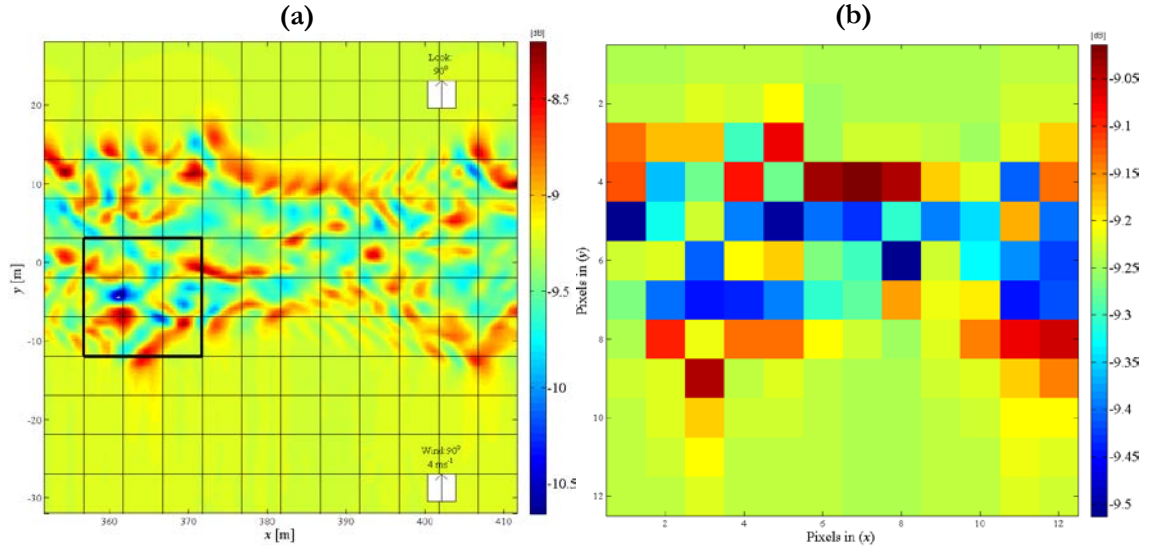
Figure 67. Location of pixel bins in the block-averaging procedure applied to a 5.3 GHz (C-band) Bragg NRCS radar signature for Wake Profile 1-C: (a) original NRCS resolution; (b) resolution down-sampled to 5 x 5 m. Polarisation is HH and incidence angle is 23º; look and wind (4 ms⁻¹) directions are both in the positive y-direction.

To demonstrate the effect that location of the grid can have on the observed signature, Figures 70, 71 and 72 depict a portion of the signature under the Bragg NRCS grid and the observed (re-sampled) 5 x 5 m signature. The profile depicted in Figure 68 is a portion of the grid as highlighted in the black box overlaid on Figure 67 (a), whereas the profile depicted in Figures 71 and 72 demonstrates where the location of the grid has been translated by 5 pixels (Fig. 71; equivalent to +1.25 m), and -2 pixels (Fig. 72; equivalent to -0.5 m) in the x- and y-directions, respectively. In all cases, the relevant colour axes have been manipulated to match the equivalent scale(s) used in Figure 67.

From these figures, it is clear to see how translating the location of the grid has particular effects on the magnitude of NRCS observed in the re-sampled profile. For example, where the peak of Bragg NRCS (denoted by an asterisk [*] in Figure 69) falls in the bottom-left grid box, the re-sampled pixel shows a strong NRCS response; however, where it falls in the centre grid box (denoted by an asterisk [*] in Figure 70), it is joined by a region of low-NRCS which causes the re-sampled pixel to depict a (comparatively) poor NRCS response. This demonstrates that, for the 5 m pixel size considered here, there is a potential source of sensitivity in how the "fine structure" of the surface backscattering is mapped to coarse pixels: where the spatial resolution of the instrument is on the same order as the variation in surface structure (e.g. separation of a peak or trough of NRCS), the location to where individual (Bragg NRCS) pixel are grouped can visibly change the observed (re-sampled) response. In real operation, where single bright scatterers (or areas of strong backscattering; for example, "double-bounce"-like reflection between a smooth sea surface and a vertical surface such as a ship's hull) can "swamp" the response at a single pixel, this may be even more problematic. In cases where spatial resolution is larger than the scale of the fine structure, Bragg NRCS will be averaged into large pixels, and there is unlikely to be a major influence arising from the grid location; however, where spatial resolution is fine, there will be greater flexibility for resolving the fine structure, as demonstrated by Figure 64. In this respect, drawing conclusions from re-sampled profiles (or, equivalently, from true SAR imagery of small-scale surface flows) can introduce particular challenges associated with understanding a range of potential scenarios arising from the erratic manner in which sub-resolution backscattering is averaged to derive intensity of a single pixel, and the resulting effects on discrimination of surface features.
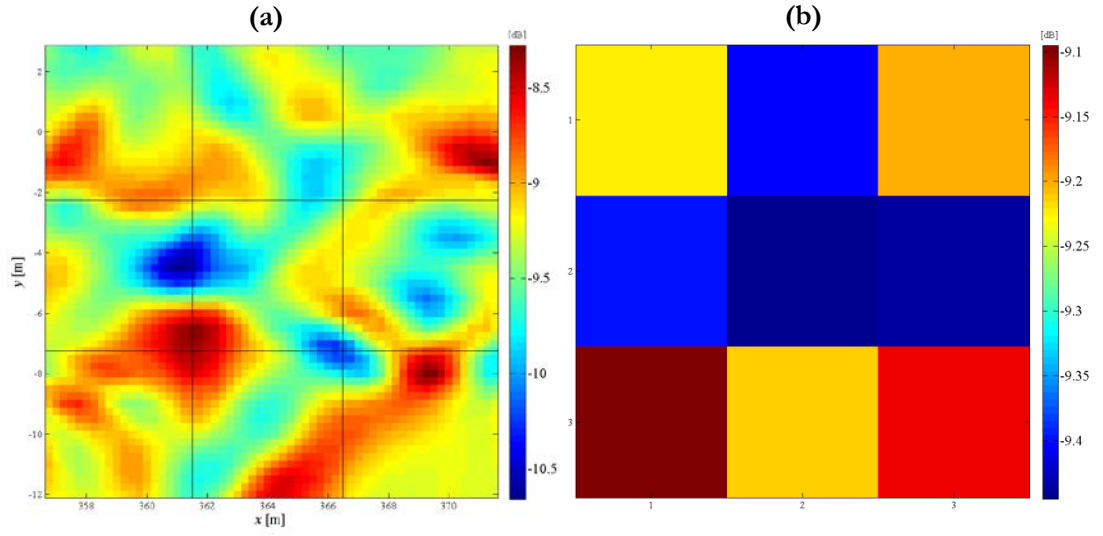
Figure 68. 3 x 3 pixel portion of a 5.3 GHz (C-band) Bragg NRCS radar signature for Wake Profile 1-C of (a) Bragg NRCS and (b) re-sampled Bragg NRCS at 5 x 5 m [0, 0]. Pixel location is designated by the highlighted area in Figure 70. Polarisation is HH and incidence angle is 23°; look and wind (4 ms⁻¹) directions are both in the positive y-direction.
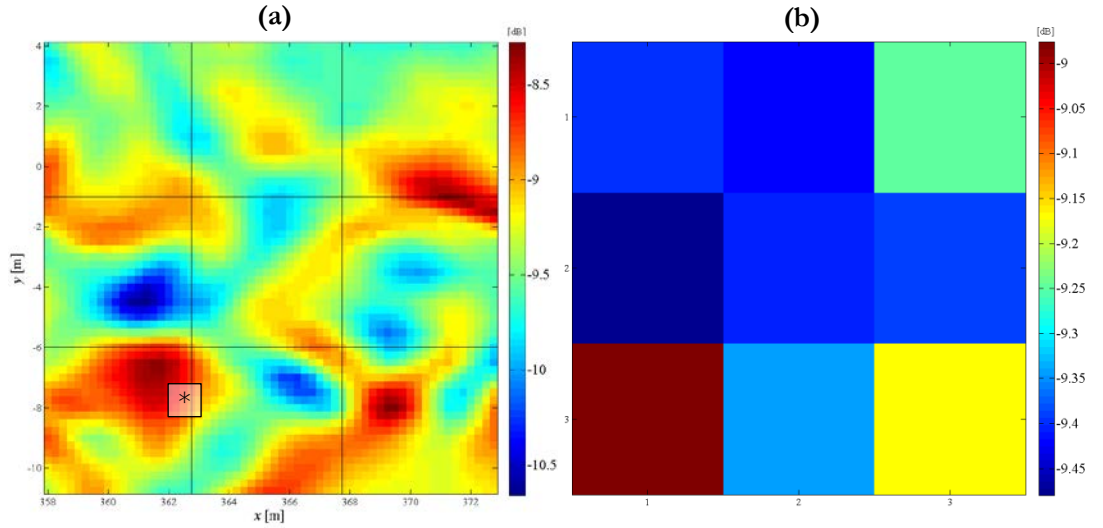
Figure 69. 3 x 3 pixel portion of a 5.3 GHz (C-band) Bragg NRCS radar signature for Wake Profile 1-C of (a) Bragg NRCS and (b) re-sampled Bragg NRCS at 5 x 5 m [+1.25 m, +1.25 m]. Pixel location is designated by the highlighted area in Figure 70, translated by +1.25 m in both x- and y-directions. Polarisation is HH and incidence angle is 23°; look and wind (4 ms⁻¹) directions are both in the positive y-direction.
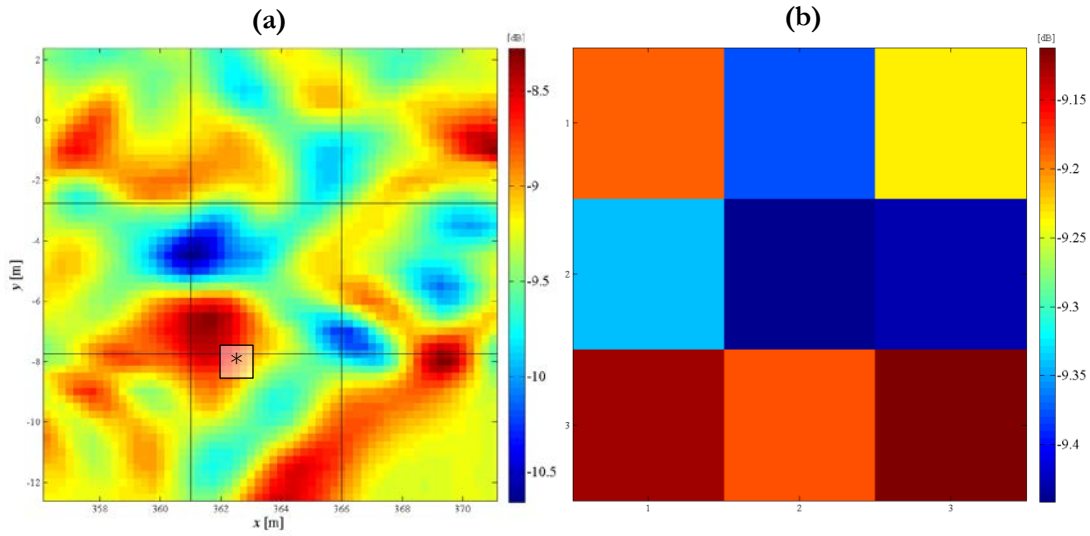
Figure 70. 3 x 3 pixel portion of a 5.3 GHz (C-band) Bragg NRCS radar signature for Wake Profile 1-C of (a) Bragg NRCS and (b) re-sampled Bragg NRCS at 5 x 5 m [-0.5 m, -0.5 m]. Pixel location is designated by the highlighted area in Figure 70, translated by -0.50 m in both x- and y-directions. Polarisation is HH and incidence angle is 23°; look and wind (4 ms^{-1}) directions are both in the positive y-direction.

To provide a context in which a wake profile may be observed in a real image, simulated surface signatures from Wake Profile 1 are presented in Figures 73 and 74 to the spatial resolution of current, and future, high-resolution SAR sensors. The C-band Bragg NRCS signature presented in Figure 71 (a) is resampled to a 5 x 5 m (single-look) pixel resolution in sub-plot (b) to replicate capability of the forthcoming *Sentinel-1* mission; whilst the X-band Bragg NRCS signature presented in Figure 72 (a) is resampled to a 3 x 3 m (single-look) pixel resolution in sub-plot (b) to reflect performance of the *TerraSAR-X* spacecraft. To aid in visual comparison, the equivalent re-sampled signatures have been presented on the same colour axis as the original backscattering profiles. All profiles are observed under the same wind and incidence angle/polarisation conditions.

Firstly, due to differences in the observed frequency, there are variations in the observed modulation depth which are resolved in the original C- and X-band Bragg NRCS profiles; where the Bragg NRCS display 3.46 dB and 2.41 dB (for C- and X-band profiles, respectively) variation between maximum and minimum NRCS over the image, the re-sampled profiles display modulation depths of 1.19 dB and 0.72 dB. In this respect, the 5 m (C-band) profile exhibits the greatest variation in maximum/minimum backscattering, but at such spatial resolution there is little in the way of qualitative (or quantitative) information that can be extracted from the wake signature

aside from, perhaps, an estimate of the width of the turbulent wake. In the X-band (3 m resolution) signature, the structure is resolved with a minor improvement in visibility, owing to finer spatial resolution. In particular, there is an improved ability to resolve some regions of positive modulation primarily at the 'edge' of the wake where the flow structure is adjacent to the ambient water; this may aid discrimination of the wake within a procedural image. However, due to the block-averaging process, the range of modulation in the re-sampled signatures of subplot (b) from Figures 73 and 74 still tends towards the 'lower' range of modulation of the original Bragg NRCS signatures; therefore, in general, negative modulation is resolved better than positive modulation.
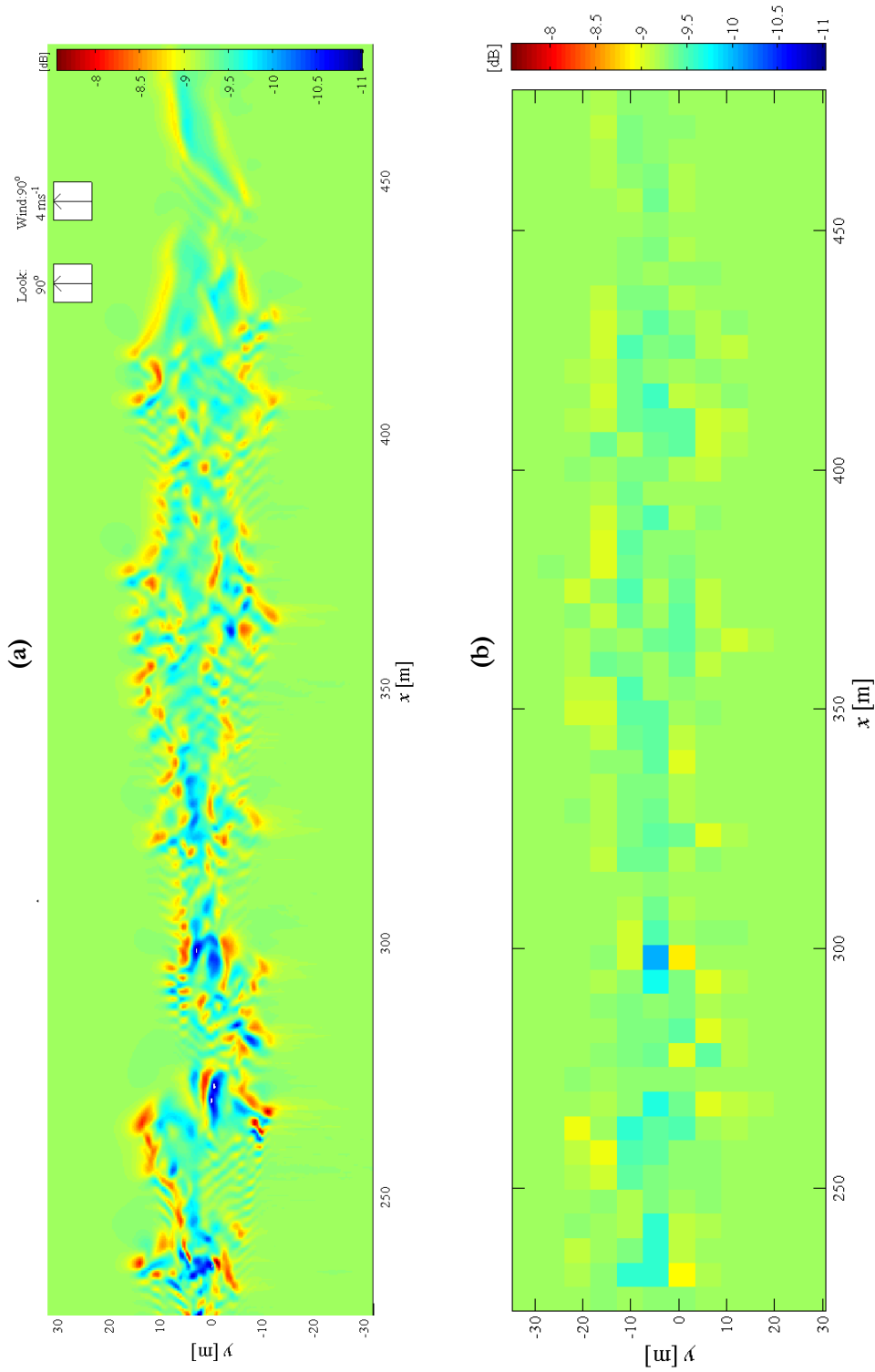
Figure 71. NRCS backscatter profiles resampled to pixel resolution of present SAR capabilities. (a) (5.3 GHz) C-band Bragg NRCS, (b) (5.3 GHz) C-band Bragg NRCS resampled to 5 x 5 m pixel resolution. In all cases, the simulated antenna is operated at HH-polarisation and a 23° incidence angle.
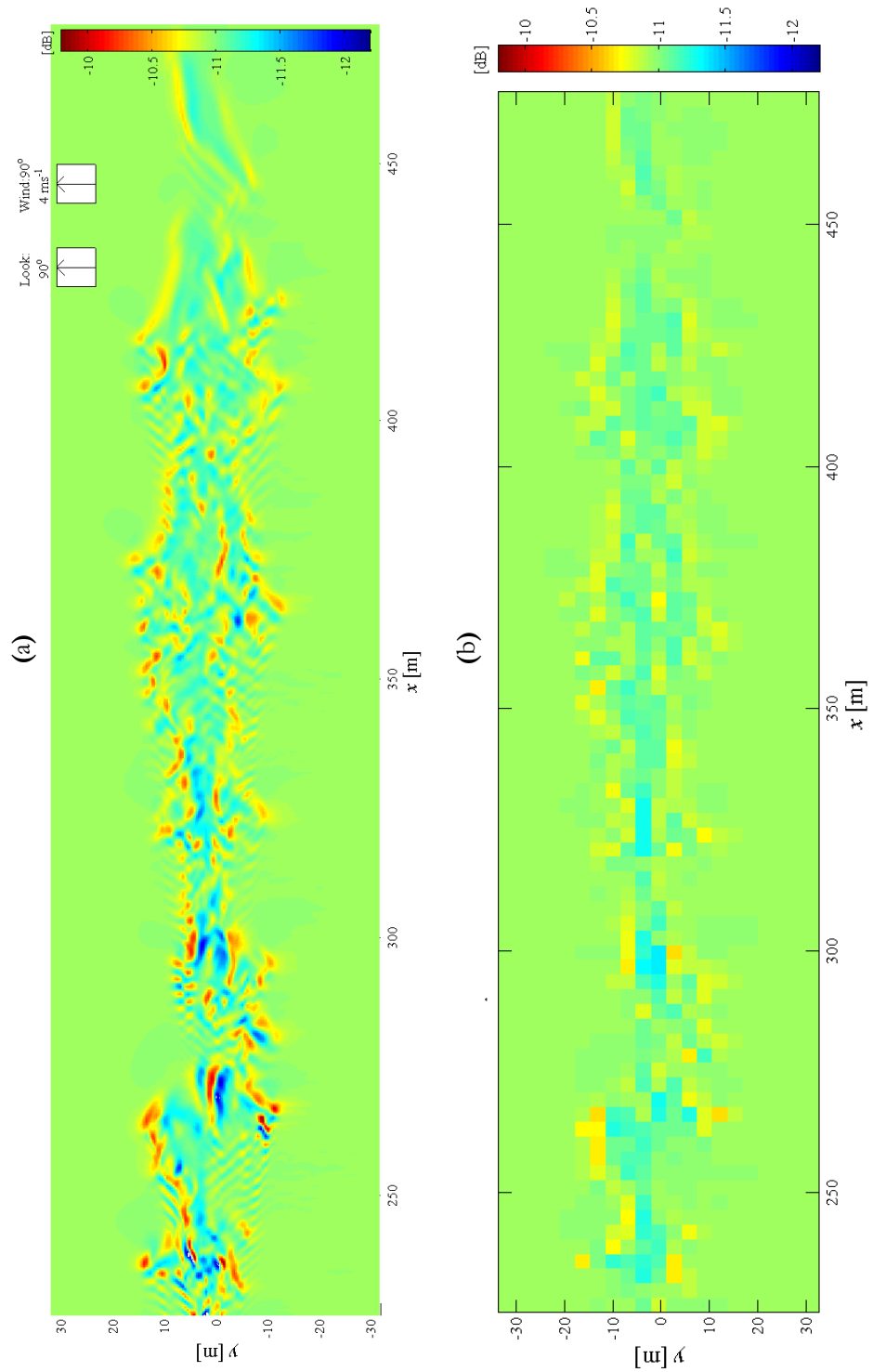
Figure 72. NRCS backscatter profiles resampled to pixel resolution of present SAR capabilities.(a) (9.6 GHz) X-band Bragg NRCS, (b) (9.6 GHz) X-band Bragg NRCS resampled to 3 x 3 m pixel resolution. In all cases, the simulated antenna is operated at HH-polarisation and 23º incidence angle.

8.2   Comments on Physical SAR Operation

Whereas the backscattering profiles analysed thus far have focussed on pure radar backscattering only (Bragg NRCS and composite surface NRCS signatures; along with those which have been artificially coarsened in spatial resolution), an instrument performing the SAR technique also accounts for motion-related effects. As discussed in §4.1, for operation of side-looking radar techniques, the antenna must be placed on a moving platform, whilst for SAR the Doppler characteristics of echoes backscattered to the antenna are also collected and used in processing to construct the final image. As a result, a SAR instrument exploits the Doppler frequency of backscattered echoes in order to construct a phase history of the observed scene and to derive an equivalent synthetic aperture to that of a much larger RAR antenna. Motion of the instrument platform (aircraft or spacecraft), as well as motion of the ocean surface itself, will cause the Doppler frequency of reflected echoes to be "shifted" such that the echo returns (received by the antenna system) are mapped to an incorrect location in the derived SAR intensity image. In addition, real-world SAR instruments are also subject to limitations of radiometric resolution (sensitivity of NRCS measurement), and the disturbing effect of noise (both of the thermal operation of the instrument and statistical-type interference arising from the effect of speckle) which serve to deviate the observed measurement away from the theoretical backscattering profile.

Because they do not exploit the Doppler history of the received radar echoes, pure backscattering (NRCS) and simulated RAR signatures are not subject to displacement or distortion of pixels or of the distribution of backscattered energy. In such images, scattering pixels are registered to the grid scale of the input surface velocity profile (or, in the case of simulated RAR images, to a defined instrument resolution). However, full SAR intensity signatures are subject to Doppler-related effects, where large (range-velocity) R_0/v_s ratios cause "blurring" and "smearing" of the surface motions in the resultant SAR image: the coherent summation of radar echoes reflected from a surface (which is moving towards or away from the radar's line-of-sight) leads to a "blurring" of adjacent pixels in the final image, since radar echoes are mapped to a spread of pixels in the azimuth direction ("smearing") and there is movement of point scatterers (that is, surface waves) during motion of the antenna along the synthetic aperture (Holt, 2004).

The effects of azimuth smearing will be likely be problematic for SAR observation (at large R_0/v_s ratio, e.g. spaceborne platforms)[36] of turbulent ocean surface profiles such as the one investigated in the current study; particularly where is presence of large variation of currents and current

---

[36] Typically, Range-velocity ratio (R_0/v_s) for a spaceborne SAR is O(100), whilst for aircraft it is typically smaller due to the reduced slant range, of O(40-80).

gradients. in the SAR image, the distance over which the point scatterers within a single resolution cell will be smeared in the azimuth direction, δx, is given by Lyzenga (1986):

$$\delta x = 2(R_0/v_s)\sigma_v$$

<div align="right">(xxix)</div>

$$v_r = u_y \sin\theta_i$$

<div align="right">(xxx)</div>

where v_r is the radial velocity of the scatterer (i.e. the patch of ocean being imaged) in a line-of-sight towards the radar and σ_v is the standard deviation of radial velocities (v_r) within the cell. An example of this occurring in an operational SAR image is presented in Figure 73, adapted from Soloviev et al. (2010); this effect is also demonstrated graphically in Figure 74; adapted from Lyzenga (1986). Therefore, a higher R_0/v_s ratio hence leads to a higher misregistration distance and thus larger regions of smearing; which will act to 'mask' the surface signatures arising from surface turbulence and wave-current interaction alone. Typically, Range-velocity ratio (R_0/v_s) for a spaceborne SAR is $O(100)$, whilst for aircraft it is typically smaller due to the reduced slant range, of $O(40\text{-}80)$. For a comparison of various R_0/v_s ratios for current air and space SAR instruments, details are tabulated in Table 22.
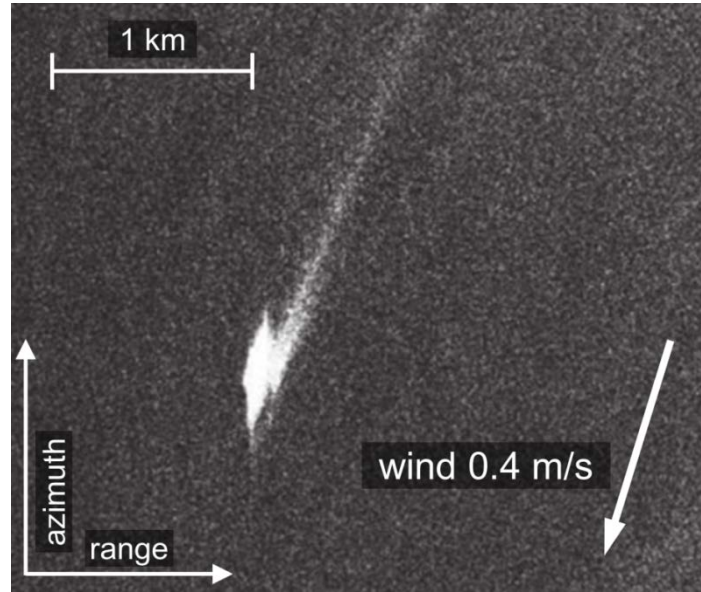
Figure 73. *TerraSAR-X* image of a ship showing the effect of azimuthal displacement due to the boat's radial velocity in the line-of-sight of the radar © DLR; from Soloviev et al. (2010).
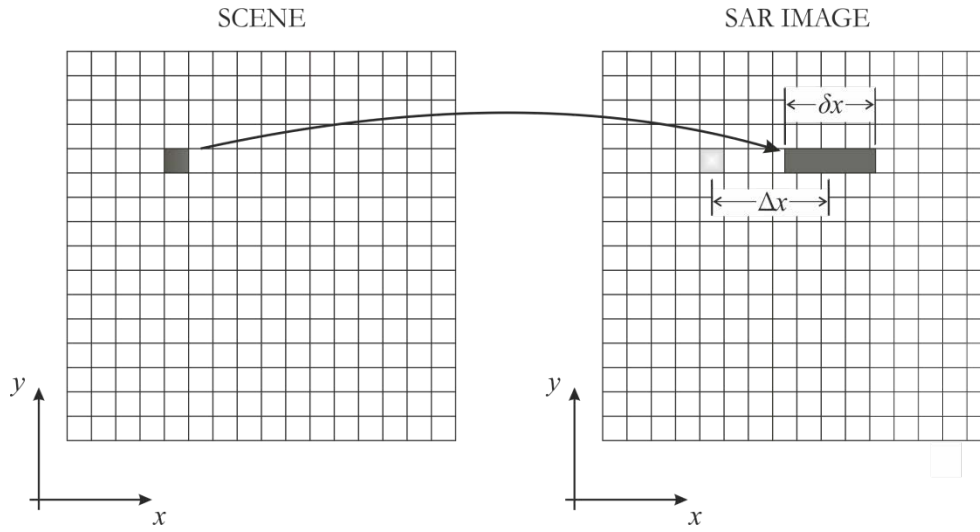
Figure 74. Illustration of azimuthal shifting and smearing effects due to surface motions, where

$$\Delta x = (R_0/v_s)v_r \text{ and } \delta x = 2(R_0/v_s)\sigma_v; \text{ adapted from Lyzenga (1986)}.$$

Instrument	Flight & Instrument Details	R_0 (avg.)	R_0/v_S
Dual-Beam Interferometer	Nominal altitude 590 m, velocity 102 ms^{-1} 71° mean incidence angle	1812 m	17.8
NASA/JPL AIRSAR	Nominal altitude 8 km, velocity 230 ms^{-1} 42.5° mean incidence angle	10850 m	47.2
DLR AeS-1	Nominal altitude 3200 m, velocity 83 ms^{-1} 45° incidence angle	4525 m	54.5
SARSEX experiment	Nominal altitude 7 km, velocity 125 ms^{-1} 26° mean incidence angle	7788 m	62.3
DLR F-SAR	Nominal altitude 6 km, velocity 100 ms^{-1} 40° mean incidence angle	7832 m	78.3
DLR E-SAR	Nominal altitude 6 km, velocity 100 ms^{-1} 41° mean incidence angle	7985 m	79.9
NORCSEX experiment	Nominal altitude 7 km, velocity 120 ms^{-1} 65° mean incidence angle	13397 m	111.6
SIR-C/X-SAR	Nominal altitude 224 km, velocity 7.9 kms^{-1} 45° incidence angle	316.8 km	40.1
SAR-Lupe	Orbital altitude 500 km, velocity 7.6 kms^{-1} 35° mean incidence angle	610 km	80.3
RADARSAT-2	Orbital altitude 798 km, velocity 7.45 kms^{-1} 32.5° mean incidence angle	946 km	127.0

    Airborne Instruments   Spaceborne Instruments

Table 22. Comparison of R_0/v_S ratio for air & spaceborne instruments previously introduced in Tables 19 and 20. 'Perfect' SAR visibility, with no losses due to platform motion, is acquired when the range-velocity ratio is equal to 1.

In sub-plot (a) of Figure 75, a simple Bragg NRCS backscattering profile is presented, whilst sub-plots (b) and (c) demonstrate the effect of range/velocity ratio on signatures derived from airborne ($R_0/v_s = 40$) and spaceborne ($R_0/v_s = 100$) geometry. These profiles assume a 'perfect' SAR instrument which is unaffected by limitations of spatial resolution or speckle/noise derived by the instrument: such influences would be further additive to the effects of R_0/v_s interference. In the case where the range-velocity ratio is unity, the observed response is equivalent to the σ_0 signature, and there is no presence of range-velocity blurring. For comparison, sub-plot (d) of Figure 75 depicts a "perfect" SAR image which has been derived at a R_0/v_s ratio of unity (1), which is statistically equivalent to an explicit composite surface NRCS profile. Therefore for typical spaceborne cases ($R_0/v_s \sim 100$), this indicates that there is likely to be a significant challenge in observing turbulent ocean surface profiles (with large variation of currents and current gradients) at high resolution since, in general, the distance that a single scatterer (pixel) is displaced/smeared is larger than the pixel resolution; meaning that the content of the pixel [image] is likely to be obscured. Furthermore, the action of speckle (introduced in §4.1) and instrument noise at such high resolution will reduce both the observed modulation depth and measured distribution of fine spatial structure; averaging multiple images of the same scene ('multi-looking') will reduce the effect of speckle interference but at the expense of spatial resolution, which may limit the ability to resolve fine structures. With the addition of noise and resolution constraints, resolving the turbulent wake and its structure may become increasingly demanding and difficult. In the context of other fluid motions at the ocean surface and wind variability, resolving the radar surface signature of wake flow structure alone is likely to be challenging. In particular, the limitations posed by R_0/v_s ratio may require novel techniques or concepts in order to reduce the effect of "smearing" and/or "blurring" of signatures.

In summary, the current research has demonstrated that, at least theoretically, the radar backscattering arising from (wave-current interaction) modulation of waves by surface wake turbulence is sufficient to generate observable, and potentially resolvable, variations in Bragg backscattering cross-section. However, the possible complications regarding distortions by scene and motion and speckle noise may mean that observation of such signatures from space is ultimately unattainable with current techniques; although there may be opportunities to observe such features using high-resolution airborne imaging radar.

(a)

(b)

(c)

(d)
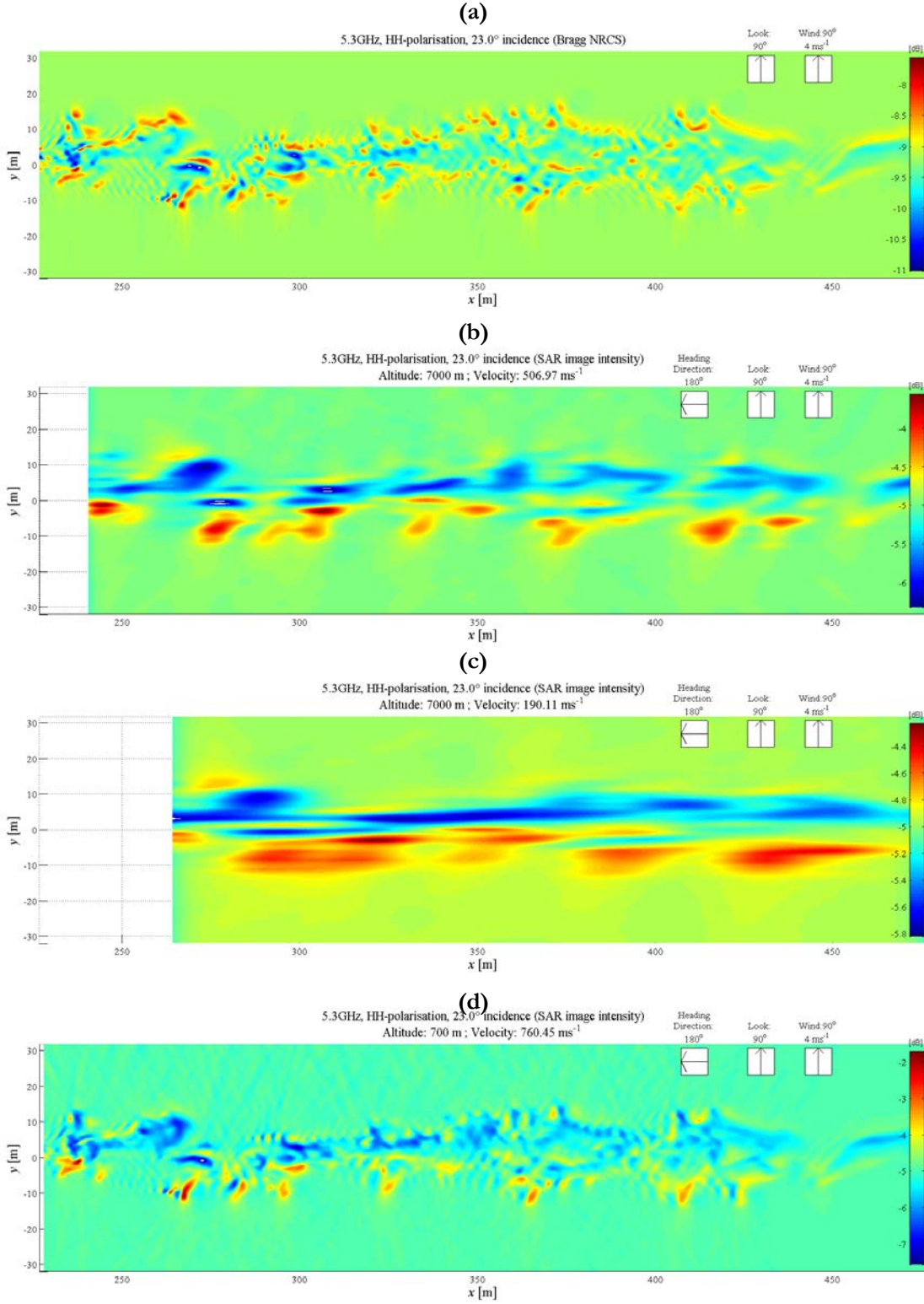
Figure 75. Effect of R_0/v_s ratio on clarity of simulated image: (a) Bragg NRCS for a 5.3 GHz (C-band) radar and equivalent SAR signatures for (b) $R_0/v_s = 15$; (c) $R_0/v_s = 40$; (d) $R_0/v_s = 1$ (equivalent to composite surface NRCS profile). Details of flight conditions for simulated SAR images are annotated, and all images were derived at HH-polarisation and a 23° incidence angle.

9. Conclusions

9.1 Thesis Summary

In the research presented in the preceding eight chapters, first efforts have been made to draw perspectives on how developments in remote-sensing instrumentation may have a valuable application in the study of ocean turbulence (especially at small- to intermediate-scales where there is a current shortfall in the capability of remote-sensing instruments specifically designed for ocean study) and to postulate what role future sensors could play in satellite oceanography and measurement of ocean turbulence. The study was characterised by the development of an integrated remote-sensing simulation strategy, uniting aspects of "remote-sensing" and "ocean turbulence" within a single end-to-end simulation procedure. This resulted in a proof-of-concept investigation into using numerical turbulence simulation with ocean radar imaging models; constructed to consider the role of remote-sensing in characterising turbulence in the ocean, to appreciate current capability, and to speculate potential future instrumentation for improved ocean study. Development of this strategy, with respect to the application of oceanic turbulence, represented a novel feasibility study towards the capabilities of current, and future, remote instrumentation to observe the ocean. This study considered radar backscattering simulation with a focus on the resolving "turbulence" and flow characteristics in the ocean, as opposed to previous studies which have been initiated with a focus on particular processes or phenomenon. As such, a concentration was made on examining the visibility of turbulent surface signatures under a range of instrument, and ambient or atmospheric, conditions to understand the limits of visibility of such processes and the influence on instrument configuration.

As a first step, an examination study was performed in order to analyse the measurement needs for observation of a variety of ocean processes and identify a candidate instrument for further study of potential, future capabilities. A significant 'gap' was identified in the spatial scales which separate traditional remote-sensing (intermediate- to large-scale process) and in-situ (fine- to small-scale processes) observations, and the ability of Synthetic Aperture Radar to observe turbulent phenomena such as ship wakes, large- and small-scale eddies and open-ocean convection offers the potential to fill this "gap", highlighting its suitability for this remote-sensing simulation study. Following this, a simulation case study was performed to understand the role that future SAR capabilities may play in observation of small-scale ocean processes and turbulence, and a simulation strategy was developed to process numerical turbulence and derive high-resolution simulated surface signatures using established ocean radar imaging models. In particular, this led to a novel

application of applying current profiles (derived through Direct Numerical Simulation) to ocean radar imaging models and identifying the primary barriers in deriving high-resolution (simulated) radar backscatter images. The obtained simulation results represent an idealised case of a turbulent wake produced by a simulated surface vessel moving across a smooth surface of fluid, over which a spectrum of waves (based on specification of a spatially-invariant wind field) was propagated to understand the effects of turbulent wave-current interaction on radar backscatter. From this perspective, the simulation procedure was performed to understand whether potential improvements in instrument capability could reveal additional information about turbulent currents, as well as conducting unique investigation into the capability of resolving surface signatures in a range of ambient and instrument conditions.

The gathering of initial results led to examination of the suitability of existing SAR simulation techniques (using the theory of Conservation of Wave Action under the WKB approximation), and use of such methods to aid in understanding the role(s) of instrument configuration and ambient condition in resolving flow structure(s) embedded in surface wake profiles. In simulation of new current fields derived from DNS of a surface wake arising from a partially-submerged sphere, high-resolution current profiles were used to derive a hypothetical flow field for study using the ocean radar imaging model, *M4S*. These current profiles were designed to expand the realm of what flow conditions are studied using standard ocean radar imaging models, particularly with respect to small-scale phenomena and turbulent flow currents. In pursuit of this simulation strategy, the obtained results have provided a substantial insight into the opportunities to observe and resolve small-scale ocean turbulence and surface flows by remote means, in addition to establishing an improved understanding of the CWA/WKB method in the context of such regimes. The general picture that emerges is that, where wave-current interaction involved turbulent flow structure is present, such interactions have the potential to be observed using SAR. The primary finding of the simulation case study is that relatively small spatial surface current variations (in the turbulent wake of a surface moving vessel) can cause substantial radar signatures (i.e. positive/negative deviations of the NRCS from mean value), according to the operated models. A smaller dynamic range of surface currents present within the flow structure generally makes it harder to distinguish individual flow patterns due to reduced wave-current modulation.

The study of turbulence and its effect on simulated radar imagery has shown that details of the turbulent structure can be adequately resolved in NRCS data due to modulation of the surface wave spectrum by disturbing currents and turbulence. In particular, it has been shown that, where "interesting" structure is embedded in the flow, it can be translated into observable changes in NRCS which may potentially be detected by spaceborne radar. Surface currents (and their

associated gradients) associated with small-scale wake turbulence can be seen to propagate through the ocean/radar wave interaction process into simulated NRCS images, observed as qualitative flow characteristics and the presence of coherent fluid structures. As a consequence, the derived results have led to an improved understanding of the relationship between turbulence and flow structure in the upper ocean, and its influence on radar backscattering. The ability of SAR to respond to small variations of surface roughness at high resolution allows significant characteristics of phenomena to be resolved that modulate the surface wave pattern and hence qualitatively flow characteristics. A range of encouraging results processed from a turbulent wake has indicated that (surface wake) turbulence can be resolved by modelling of NRCS and that the observed patterns and structures compare favourably with the input flow conditions provided by DNS. The generated data is consistent with published SAR ship wake images, displaying a deficit of NRCS inside the wake region due to presence of turbulent surface currents. The results indicate that turbulent structure embedded in turbulent ship wakes can be translated to and resolved by changes in radar backscatter. Where fluid structure is propagated through to Bragg or composite surface NRCS, there is promise for these features to be observed in the associated simulated SAR data.

Study of the effect of perturbing the parameters of the radar instrument has yielded encouraging results regarding the turbulent structure that can be detected. The results obtained from examining the effect of changing frequency and polarisation of the simulated SAR instrument suggest that different structure within the turbulent wake can be discriminated and resolved. This, and future efforts in this vein, will aid in deriving desirable instrument characteristics and for developing the remote-sensing instrument, platform and overall strategy which may be employed to measure ocean turbulence from space. For the case of the hypothetical flow field operated in the current study, it was found that S-band in particular could offer benefits for further ocean study: the improved capability for resolving surface flow structure through positive/negative (Bragg) NRCS modulation highlights the need for increased operation of S-band frequencies in study of the ocean. There is also compelling evidence for the operation of multiple-frequency instruments observing the surface quasi-simultaneously to improve understanding of surface flow structure and the spatial distribution of the wave energy of short, surface waves where (turbulent) ocean currents are present. In addition, the effect of varying ambient conditions was studied to examine the impacts of wind speed and direction on the resolved Bragg NRCS image: prevailing winds blowing perpendicularly improve the discrimination characteristics of the wake due to the spanwise flows from the ship's propellers that oppose the wind and create 'bunching' of Bragg-scale capillary waves. Strong winds can generate large modulation depths and improve detection capabilities, but wind speeds too strong can suppress short-wave amplitudes and decrease visibility of the underlying phenomena and

turbulence. However, even for lighter and more typical wind speeds between 2 and 8 ms^{-1}, there may be challenges associated with observing low-backscatter signatures in the presence of ambient wind conditions and sea current/states which may hinder turbulence wake signatures being resolved. Furthermore, the spatial resolution offered by current SAR systems present further challenges towards resolving the fine details of surface wake turbulence such as the flow structures contained within the hypothetical flow field considered here: when block-averaged to similar resolutions, the NRCS signatures arising from the examined surface current profiles show significant deterioration and a reduction in the capability to observe small-scale structure. These findings indicate that sub-metre pixel resolution is desired for extraction of turbulence surface signatures in (Normalised) Radar Cross-Section, although there could be significant challenges associated with range-velocity (R/V) "smearing" distortions which are introduced during the imaging of dynamic ocean waves.

In execution of the research and operation of the defined simulation strategy, a number of challenges were encountered which highlighted limitations in the current suite of ocean radar imaging models for study of small-scale ocean processes. In particular, a significant challenge continues to lie in considering surface currents– particularly on length scales of $O(10 \text{ m})$ or so – which vary beyond the "slowly-varying" restriction, and a discussion of alternative techniques or modifications is presented in Appendix D. In addition, with respect to the construction of rigorous source terminology modelling the influences on surface wave energy, there is scope for further development of the relationship of near-surface oceanic turbulence on dissipation of wave energy of capillary waves, also discussed in Appendix D. However, in spite of such challenges, the current research has demonstrated a robust attempt to tackle radar backscattering simulation of small-scale wake turbulence. Further work in this field is actively encouraged, and it is hoped that the discussion presented in §9.2 may stimulate such future endeavours.

9.2   Summary of Findings

The results presented in the preceding two chapters have made steps towards establishing an optimum range of instrument configuration(s) for observing surface turbulent wakes such as the hypothetical flow examined in this thesis. The key results are condensed into Table 23, which report the major findings and recommendations for design of a theoretical SAR instrument for observing ocean turbulence. These details act as the primary outcomes of this overall study, and summarise the overall conclusions of the radar backscatter simulations computed during this research.

However, it is also important to discuss, in summary, the details of the simulation study under which the results were derived, and to review the constraints and limitations which may act as caveats to the reported findings. These constraints – along with details of the applied method – are re-examined here in brief, and listed in tabular form in Table 24. The case of a true, real-world ocean surface is, fundamentally, more complex and variable than the simplified model considered in this study. First and foremost, a variety of background currents and water motions will complicate the simple surface current pattern, in addition to a more unruly spectrum of long- and short-surface waves; this will likely obscure the clear patterns and radar signatures that have been presented in Chapters 6, 7 and 8. The deriving surface flow is a hypothetical current profile which is broadly analogous to the turbulent wake behind a moving surface vessel. Although not considered in this simple simulation, other features of a typical vessel wake, such as the Kelvin and transverse wave systems and the presence of breaking waves, may also tend to obscure the signature arising from the turbulent wake alone; although may, themselves, be highly-visible features of the wake's radar signature which are detected by an active radar instrument.

Therefore, whilst this study has yielded valuable results and positive recommendations regarding observation of small-scale ocean turbulence and surface flows (particularly with respect to potential configuration of a suitable instrument and favourable ambient conditions for extraction of surface signatures), it remains a highly-simplified case that establishes a basis for future study incorporating a range of additional complexity. Recommendations for expansion of the simulation study, and for examination of other considerations, are discussed in the following sub-section.

Parameter	Optimum Characteristic	Comments
Instrument Parameters		
Instrument Frequency	3.1-3.2 GHz	S-band in the vicinity of 2.9-3.2 GHz demonstrates good performance in terms of mean NRCS observed over the image and modulation depth/contrast with the stationary water away from the current profile. Low frequencies (e.g. L-band) tend to demonstrate an ability to resolve velocity components aligned in the radar look direction, whereas higher frequencies (e.g. C-, X-bands) tend to resolve gradients in surface velocity. In this respect, a multi-frequency instrument combining L-, S- and C-/X-bands may provide unique insight into small-scale current flow features.
Polarisation	VV-polarisation	For Bragg NRCS signatures, equivalent levels of modulation depth are observed for both HH- and VV-polarised antennas, although VV-polarisation demonstrates higher mean NRCS, thus likelihood of observing a visible signature. For the limited composite surface NRCS cases examined, HH-polarised signatures demonstrate a minor improvement in the resolved modulation depth, but still (in general) resolve a lower level of NRCS when compared to VV-polarised equivalent.
Incidence Angle	20° off nadir	The minimum tested incidence angle displays the strongest radar signatures, with maximum observed deviation of NRCS away from the ambient radar scattering away from the current profile. However, these conclusions drawn from Bragg NRCS signatures only; the relationship of signature visibility with varying incidence angle will be less explicit in the context of additional surface/wave slope effects.
Other Characteristics		
Wind Speed	2-6 ms⁻¹	Peak signature modulation depth is observed between 2 ms^{-1} and 6 ms^{-1} wind speed; largest positive/negative deviation from background NRCS visible at minimum wind speed.
Wind Direction	Dependent on flow component of interest	NRCS response resolves velocity components in radar look direction: under most favourable conditions, wind direction aligns with flow component of interest (in this case, transverse currents in the y-direction).
Radar Look Direction	Coincident with wind direction	Peak response observed when radar look direction is aligned with the local wind direction. Ability to resolve fine details of the signature is significantly impaired when the radar observes at a perpendicular angle to the wind; however, alignment of less than 45° typically provides adequate clarity of signature.

Table 23. Summary of key findings from radar backscatter simulations presented in Chapters 6, 7 and 8.

Characteristic	Comments
Definition of Moving Surface Vessel	Simple sphere, half-submerged beneath the surface; vessel assumed to be towed (no independent thrust; no hull profile or propeller/propulsion characteristics. No additional (background currents) applied to the domain: a uniform flow is propagated past the sphere. Non-deformable fluid assumed ('rigid lid' approximation) – motion of the vessel through the flow does not cause deformation of the fluid surface or generation of waves.
Definition of Sea Surface, etc.	Surface currents (arising from the surface wake) assumed to occur on a smooth ("glassy") plane, over which an empirical ocean wave spectrum is propagated. The sea surface is assumed to be clean and free of surfactant material. No background currents applied to the sea surface domain (water outside of the wake is assumed stationary). The presence of additional surface features typically observed in a real-world vessel wake (bow waves, Kelvin wake pattern, transverse waves, etc.) are not included in the representation. The intense region of wave-breaking and white water observed immediately aft of a ship is not represented. Equilibrium wave spectrum of Romeiser et al. (1997) is applied, based on input wind speed. Spatially-invariant wind speed, referenced at 10 m above the sea surface, is assumed for all cases. The surface is assumed to have a surface tension of 0.079 Nm^{-1} and seawater density of 1025 kgm^{-3}.
Calculation of Wave-Current Interaction	The default wave-current interaction model within *M4S* was operated (theoretical basis: Romeiser et al. [1997], Romeiser and Alpers [1997]). All wave-current interaction is assumed to take place in deep water. Source term within the wave-current interaction model was that of the "limited" quadratic source function defined in Wensink et al. (1999); modified from the standard quadratic source function of Thompson & Gasparovic (1986). The relaxation rate of Plant (1982) is assumed. Wave-current interaction between two-dimensional surface "macro-scale" currents (arising from the surface moving object) with the background sea surface spectrum is computed. The effects of breaking waves, and excitation of short waves by longer breaking waves, are not accounted for in calculation of wave energy. "Micro-scale" effects (redistribution of short-wave energy by fine-scale turbulent fluctuations of velocity in the near-surface layer) are not accounted for in the wave-current interaction process. No feedback/roughness mechanism is assumed between the modulated wave spectrum and a revised wind field.

Table 24. Summary of conditions under which radar backscatter simulations were performed, and from which results were derived.

Characteristic	Comments

Calculation of Wave-Current Interaction (contd.)	The operated wave-current interaction model operates using the principle of Conservation of Wave Action (CWA) under the Wentzel-Kramers-Brillouin (WKB) approximation. It is assumed that the operated fluid profile adheres to the "slowly-varying" assumption legitimising operation of the CWA/WKB method.
Derivation of Radar Backscatter Signatures	Radar surface signatures derived under a range of instrument and ambient conditions (see Tables 7 and 13). Signatures primarily derived for Bragg NRCS, with passing comment made with respect to composite surface NRCS profiles. For all quantitative data, only radar backscattering arising from short waves (under the Bragg scattering regime) is used to derive radar surface signatures. The effect of long waves, tilting and surface slopes are not represented in the published results. The spatial resolution at which NRCS signatures are derived is extremely optimistic (0.25 m) and beyond the capabilities of current spaceborne SAR sensors. Furthermore, NRCS signatures are not processed in the context of motion, speckle and noise effects.

Table 24 (contd). Summary of conditions under which radar backscatter simulations were performed, and from which results were derived.

9.3 Modifications to Technique & Future Perspectives

A principal finding of the current study is that, whilst the presented results demonstrate the effects of applying a radar simulation strategy for deriving high-resolution numerical ocean surface flows using imaging radar, additional study should be performed in this area to further understand the implications for the design of future SAR ocean instrumentation.

From the basis provided by the current research, there is significant scope for applying the current techniques to process a broad range of further radar conditions which have so far seen only limited study. At present, most study (both presented here and in similar research published elsewhere) has examined the impact of surface currents on the Bragg wave response and on the resulting NRCS imagery: however, the available tools (such as *M4S* and *ERIM*) also accommodate numerical models which permit simulation of SAR image intensity and interferometric measurements, which may be used to simulate images which may be acquired from real SAR instrumentation. It is recommended that future simulation studies consider these aspects such that they might be better understood. Regarding generation of NRCS backscattering signatures and expanding the results

presented in the current study, the logical extension of the present research lies in investigating a broader range of test flow fields and examining their radar backscatter signatures. These could involve the following aspects:

- Operation of more complex wind profiles, or spatially-variant wind conditions;

- Further study of full simulated SAR signatures for comparison with heritage SAR imagery;

- Further understanding of correlation between flow structure and observed radar surface signatures (comparison of flow input characteristics and observed backscattering distribution for extraction of flow quantities from the measured NRCS profiles);

- Increased understanding of detection analysis and requirements for extracting NRCS data;

- Understanding of the role of temporal disturbance of (two or more) radar images of an evolving wake, and ability to infer surface (or subsurface) flow dynamics;

- Further development of instrument configuration study under alternative current regimes and across a broader range of ambient conditions;

- Generation of further techniques to display or observe surface signatures (for example, false-colour images comparing three operating frequencies;

With respect to understanding the implications of the observed flow structure, simulation of a wide array of surface flow features (both geophysical and canonical) and their resulting influence on radar backscattering could broaden the current range of obtained surface signatures and permit derivation of a 'gallery' of flow features which may be used to interpret real-life signatures: this may assist in pattern recognition and/or identification purposes for surface flows observed in high-resolution radar images. This could apply such as features as shearing flows, current jets, "turning flows", etc. and allow the observed radar surface signatures to be interpreted in greater detail. Furthermore, regarding observations of surface turbulence which have been made by SAR in the open ocean, there are indications that turbulence can be resolved according to HH-VV coherence, which is also known as the Co-Polarised Phase Difference: polarimetric observations by Lee et al. (1998) and Migliaccio et al. (2009) have indicated that surface roughness influences the coherence between polarimetric components, and that regions of surface wave decay (due to surfactant or turbulence damping) can be measured using multi-polarisation instruments. Further investigation of the effects of turbulence on SAR polarimetry (particularly from an experimental perspective) could yield improved insights into the process of wave-current interaction.

Regarding simulation of numerical turbulence, the DNS surface velocity profiles derived in the current study were computed using a 'rigid lid' description of the fluid surface, as described in §4.3.1. The ability to expand the DNS procedure to accommodate a deformable surface (perhaps to directly measure or account for vertical motions causing deflection of the ocean/atmosphere boundary) would greatly improve robustness of this phase of simulation – a more accurate elevation profile of the surface, for input into radar backscatter models, would likely show significant improvement in signatures derived from composite surface NRCS. Expanding the applied strategy of using DNS in conjunction with ocean radar imaging models, further study may be beneficial to expand simulation of surface wake(s). This may involve the following considerations:

- Increased complexity of the shape of the disturbing body (hull profile, etc.) through modification to the applied body forces;
- Further testing of the role of the vessel's speed (role of forcing intensity, drag characteristics, etc.);
- Application of thrust to model a self-propelled body;
- Size and location of the disturbing body (for example, examining the wake surface signatures of underwater moving bodies, etc.);
- Addition of background (longitudinal or transverse) currents in which the vessel is travelling;
- Computation using a deformable ocean surface;
- Addition of surface (wind) stress and/or thermal characteristics (for example, as performed by Fujimura et al. [2011]);
- Extraction of time signature of wake and its evolution;
- Addition of more complex body characteristics (e.g. propellers, etc.);
- Understanding interaction of current with ocean bottom topography, other surface disturbances, etc.;

A further optimistic goal would be to directly simulate the "wavy" ocean surface [complete with gravity waves down to Bragg-scattering $O(1 \text{ cm})$ waves] in order to accurately understand the effect of a numerical turbulence regime on the capillary wave system and hence radar backscattering. This still remains a highly ambitious goal for current computational systems, due to the difficulties in capturing a broad set of scales [from a domain size on $O(40 \text{ m})$ to the necessary resolution to simulate short surface waves]. While it is currently not computationally feasible to propagate a turbulent flow in DNS which includes a deformable surface where both large-scale currents and

Bragg-scale waves are present, this role is currently performed empirically in the current work through the wave-current interaction theory.

The current technique of calculating wave-current interaction – i.e. applying high-resolution surface current flows to a surface wave spectrum using the principle of conservation of wave action – holds some limitations and concerns regarding the presence of 'rapidly-varying' currents; these grounds were previously discussed in Chapter 5. To rectify the issues surrounding rapidly-varying currents and to derive wave-current interaction, analysis of alternative wave propagation models should be investigated. To this effect, a review of alternative models for wave propagation, and regarding the previous research towards including the effects of turbulent dissipation on short surface waves, is presented in Appendix D to act as stimulus to such an investigation. Meanwhile, in the simulations pursued in the current study, the characteristics of the equilibrium wave spectrum (which is propagated over the simulated wake velocity profile) are defined based on the applied wind profile; which, in this case, was assumed to be uniform across the domain. In reality, there is likely to be more significant spatial variation in wind speed and direction, leading to spatial variation of the waves responsible for backscatter and a departure from the idealised wave-current interaction statistics computed here. There is also scope for expanding the description of the ocean surface to incorporate further fidelity: for example, characteristics of surface wind shear and thermal variation at the ocean surface as were pursued in the study by Fujimura et al. (2011).

9.4 Final Comments

In essence, the substance of this research has been to develop, and put to scrutiny, a complete remote-sensing "chain" showing a direct relationship between the generation and occurrence of turbulence and evaluating the ability for remote-sensing instrument to yield satisfactory measurements of the phenomena. Considering the role of SAR observing a surface wake produced by a ship or moving vessels, the research presented here has fulfilled the aim of linking the diverse fields of fluid dynamics, remote-sensing and oceanography. In this respect, this thesis represents a body of work which seeks to address the role that remote-sensing can play in studying oceanic turbulence, extracting details of fluid structure and flow, and in providing insight into small- and submesoscale ocean processes. In particular, the simulation strategy presented a 'proof-of-concept' on how selection of beneficial instrument configuration(s) may be examined using existing SAR simulation tools. In addition, this strategy has formed part of a novel research study to analyse the implications for using surface current data derived from DNS in radar backscatter simulation and the barriers towards deriving high-resolution (simulated) radar images.

The results obtained from case study allow perspectives to be drawn regarding the ability of wake turbulence to influence small-scale surface currents and, subsequently, simulated radar backscatter signatures. In particular, that surface flow structure is translated through the wave-current interaction process to be resolved in NRCS profiles and that resolving capability can show significant variation with the applied (simulated) instrument configuration, ambient conditions and observation geometry. It is hoped that, with future application of research in this area, further steps may be made towards some of the challenges posed by the applied simulation technique and that future endeavours may go some way towards "bridging" the limitations held by current capabilities.

Bibliography

Agrawal, Y. C., Terray, E. A., Donelan, M. A., Hwang, P. A., Williams III, A. J., Drennan, W. M., Kahma, K. K., & Kitaigorodskii, S. A. (1992). Enhanced Dissipation of Kinetic Energy beneath Surface Waves. *Nature*, *359*.

Allen, J. T., Smeed, D. A., & Chadwick, A. L. (1994). Eddies and Mixing at the Iceland-Faeroes Front. *Deep Sea Research I*, *41*(1), 51–79.

Alpers, W. R., & Hasselmann, K. (1978). The Two-Frequency Microwave Technique for Measuring Ocean-Wave Spectra from an Airplane or Satellite. *Boundary-Layer Meteorology*, *13*(1972), 215–230.

Alpers, W. R., & Hennings, I. (1984). A Theory of the Imaging Mechanism of Underwater Bottom Topography. *Journal of Geophysical Research*, *89*(C6), 10–529.

Alpers, W. R., & Vlasenko, V. (2002). Study of Secondary Internal Wave Generation by the Interaction of an Internal Solitary Wave with an Underwater Bank by using ERS SAR Imagery and a Numerical Model. *Pan Ocean Remote Sensing Conference* (pp. 1–5). Bali, Indonesia.

Alpers, W. R., Campbell, G., Wensink, H., & Zhang, Q. (2004). Underwater Topography. *SAR Marine User's Manual* (pp. 245–262). Available online: http://www.sarusersmanual.com

Androsov, A., Rubino, A., Romeiser, R., & Sein, D. V. (2005). Open-Ocean Convection in the Greenland Sea: Preconditioning Through a Mesoscale Chimney and Detectability in SAR Imagery Studied with a Hierarchy of Nested Numerical Models. *Meteorologische Zeitschrift*, *14*(6), 693–702.

Anis, A., & Moum, J. . N. (1995). Surface Wave-Turbulence Interactions: Scaling E(z) near the Sea Surface. *Journal of Physical Oceanography*, *25(9)*.

Apel, J. R. (1994). An Improved Model of the Ocean Surface Wave Vector and its Effects on Radar Backscatter. *Journal of Geophysical Research*, *99*(1).

Apel, J. R. (2004). Oceanic Internal Waves and Solitons. *SAR Marine User's Manual* (pp. 189–206). Available online: http://www.sarusersmanual.com

Archer, C. L., & Jacobson, M. Z. (2005). Evaluation of Global Wind Power. *Journal of Geophysical Research*, *110*(D12).

Archer, P. J. (2008). *A Numerical Study of Laminar to Turbulent Evolution and Free-Surface Interaction of a Vortex Ring*. University of Southampton: PhD thesis.

Ardhuin, F., & Jenkins, A. D. (2006). On the Interaction of Surface Waves and Upper Ocean Turbulence. *Journal of Physical Oceanography*, *36*(3), 551–557.

Askari, F., Geernaeft, G. L., Keller, W. C., & Raman, S. (1993). Radar Imaging of Thermal Fronts. *International Journal of Remote Sensing*, *14*(2), 275–294.

Barale, V., Aberotanza, L., & Gower, J. (Eds.). (2010). *Oceanography from Space: Revisited*. Springer.

Baumert, H. Z., Simpson, J. H., & Sundermann, J. (Eds.). (2005). *Marine Turbulence - Theories, Observations and Models*. Cambridge, UK: Cambridge University Press.

Blume, H.-C., Kendall, B. M., & Fedors, J. C. (1978). Measurement of Ocean Temperature and Salinity via Microwave Radiometry. *Boundary-Layer Meteorology*, *13*(1-4), 295–308.

Borue, V., Oszag, S. A., & Staroselsky, I. (1995). Interaction of Surface Waves with Turbulence: Direct Numerical Simulations of Turbulent Open-Channel Flow. *Journal of Fluid Mechanics*, *286*, 1–23.

Bourassa, M. A., Gille, S. T., Jackson, D. L., Roberts, J. B., & Wick, G. A. (2010). Ocean Winds and Turbulent Air-Sea Fluxes Inferred from Remote Sensing. *Oceanography*, *23*(4).

Boyev, A. G. (1971). The Damping of Surface Waves by Intense Turbulence. *Izvestiya, Atmospheric and Oceanic Physics*, *7*, 31–36.

Bretherton, F. P. (1966). The Propagation of Groups of Internal Gravity Waves in a Shear Flow. *Quarterly Journal of the Royal Meteorological Society*, *92*(394), 466–480.

Buranapratheprat, A., Laongmanee, P., Sukramongkol, N., Prommas, R., Promijinda, S., & Yanagi, T. (2010). Upwelling Induced by Meso-Scale Cyclonic Eddies in the Andaman Sea. *Coastal Marine Science*, *34*(1), 68–73.

Burrage, D. M. (2003). Structure and Influence of Tropical River Plumes in the Great Barrier Reef: Application and Performance of an Airborne Sea Surface Salinity Mapping System. *Remote Sensing of Environment*, *85*, 204–220.

Burrage, D. M., Wesson, J., Martinez, C., Pérez, T., Möller, O., & Piola, A. (2008). Patos Lagoon Outflow within the Río de la Plata Plume using an Airborne Salinity Mapper: Observing an Embedded Plume. *Continental Shelf Research*, *28*, 1625–1638.

Caponi, E. A., Crawford, D. R., Yuen, H. C., & Saffman, P. G. (1988). Modulation of Radar Backscatter from the Ocean by a Variable Surface Current. *Journal of Geophysical Research*, *93*(C10), 12249–12263.

Carsey, F. D., & Garwood, R. W. (1993). Identification of Modeled Ocean Plumes in Greenland Gyre ERS-1 SAR Data. *Geophysical Research Letters*, *20*(20), 2207–2210.

Chapron, B., Garello, R., & Weissman, D. E. (2008). Ocean Remote Sensing: Challenges for the Future. Proceedings of *OCEANS '08*; Kobe (Japan), 08-11/04/2008.

Chubb, S. R., Askari, F., Donato, T. F., Romeiser, R., Ufermann, S., Cooper, A. L., Alpers, W. R., & Mango, S. A. (1999). Study of Gulf Stream Features with a Multifrequency Polarimetric SAR from the Space Shuttle. *IEEE Transactions on Geoscience and Remote Sensing, 37*(5), 2495–2507.

Chubb, S. R., Cooper, A. L., Jansen, R. W., Fusina, R. A., Lee, J.-S., & Askari, F. (1999). Radar Backscatter from Breaking Waves in Gulf Stream Current Convergence Fronts. *IEEE Transactions on Geoscience and Remote Sensing, 37*(4), 1951–1966.

Clemente-Colón, P., & Yan, X.-H. (2000). Low-Backscatter Ocean Features in Synthetic Aperture Radar Imagery. *John Hopkins APL Technical Digest, 21*(1).

Coleman, G. N., & Sandberg, R. D. (2010). *A Primer on Direct Numerical Simulation of Turbulence - Methods, Procedures and Guidelines; Technical Report AFM-09/01a.*

Cooper, A. L., Shen, C. Y., Marmorino, G. O., & Evans, T. (2005). Simulated Radar Imagery of an Ocean "Spiral Eddy". *IEEE Transactions on Geoscience and Remote Sensing, 43*(10), 2325–2331.

Davidson, P. A. (2004). *Turbulence: An Introduction for Scientists and Engineers.* Oxford, UK: Oxford University Press:

Dickey, T. D. (1990). Physical-Optical-Biological Scales Relevant to Recruitment in Large Marine Ecosystems. In K. Sherman, L. M. Alexander, & B. D. Gold (Eds.), *Large Marine Ecosystems: Patterns, Processes and Yields.* Washington DC, USA: American Association for the Advancement of Science.

DiGiacomo, P. M., & Holt, B. (2001). Satellite Observations of Small Coastal Ocean Eddies in the Southern California Bight. *Journal of Geophysical Research, 106*(C10), 22521–22543.

Dohan, K., & Maximenko, N. (2010). Monitoring Ocean Currents with Satellite Sensors. *Oceanography, 23*(4), 94–103.

Drennan, W. M., Donelan, M., Terray, E. A., & Katsaros, K. B. (1997). On Waves, Oceanic Turbulence, and Their Interaction. *Ocean Engineering, 33*, 17–27.

Drinkwater, M., & Rebhan, H. (2005). *Sentinel-3: Mission Requirements Document* (ESA).

Elfouhaily, T., Chapron, B., & Katsaros, K. B. (1997). A Unified Directional Spectrum for Long and Short Wind-Driven Waves. *Journal of Geophysical Research, 102*(97).

Emery, W. J., Thomas, A. C., Collins, M. J., Crawford, W. R., & Mackas, D. L. (1986). An Objective Method for Computing Advective Surface Velocities from Sequential Infrared Satellite Images. *Journal of Geophysical Research, 91*(C11), 12865–12878.

Emery, W. J., Matthews, D., & Baldwin, D. (2005). Mapping Surface Coastal Currents with Satellite Imagery and Altimetry. Proceedings of *IEEE Geoscience and Remote Sensing Symposium*; Anchorage AL (USA), 20-24/09/2004.

Fischer, K. W., & Shuchman, R. A. (1996). *Satellite Observations of Deep Water Convection.* Arlington VA, USA: Office of Naval Research.

Fischer, K. W., Russel, C. A., & Shuchman, R. A. (1998). Spatial Characterization of Deep Ocean Convection in the Labrador Sea using ERS-2 SAR Imagery. Proceedings of *IEEE Geoscience and Remote Sensing Symposium*; Seattle WA (USA), 06-10/07/1998.

Fischer, K. W., Legg, S., Munk, W. H., Shuchman, R. A., Garwood, R. W., & Palshook, J. P. (1999). Modeled Radar Surface Signature of Deep Ocean Convection. *IEEE Transactions on Geoscience and Remote Sensing, 37*(4), 2050–2067.

Fish, S., & Von Kerczek, C. (1991). Submerged Vortex Pair Influence on Ambient Free Surface Waves. Proceedings of *Symposium on Naval Hydrodynamics*; Ann Arbor MI (USA), 19/24/08/1990.

Fornshell, J. A., & Criess, W. A. (1979). Anticyclonic Eddy Observations in the Slope Water Aboard CGC Evergreen. *Journal of Physical Oceanography, 9*(9), 992–1000.

Freeman, A., Zlotnicki, V., Liu, T., Holt, B., Kwok, R., Yueh, S. H., Vazquez, J., Siegel, D. A., & Lagerloef, G. S. E. (2010). Ocean Measurements from Space in 2025. *Oceanography, 23*(4), 144–161.

Frew, N. M., Bock, E. J., Schimpf, U., Hara, T., Haussecker, H., Edson, J. B., McGillis, W. R., Nelson, R. K., McKenna, S. P., Uz, B. M., & Jahne, B. (2004). Air-Sea Gas Transfer: Its Dependence on Wind Stress, Small-Scale Roughness, and Surface Films. *Journal of Geophysical Research, 109*(C8), C08S17.

Fu, L.-L., & Holt, B. (1983). Some Examples of Detection of Oceanic Mesoscale Eddies by the SEASAT Synthetic-Aperture Radar. *Journal of Geophysical Research, 88*, 1844–1852.

Fu, L.-L., Chelton, D. B., Le Traon, P. Y., & Morrow, R. (2010). Eddy Dynamics from Satellite Altimetry. *Oceanography, 23*(4), 14–25.

Fujimura, A., Matt, S., Soloviev, A., Maingot, C., & Rhee, S. H. (2011). The Impact of Thermal Stratification and Wind Stress on Sea Surface Features in SAR Imagery. Proceedings of *IEEE Geoscience and Remote Sensing Symposium*; Vancouver (Canada), 24-29/07/2011.

Fujimura, A., & Soloviev, A. (2009). Numerical Simulation of the Wind-Stress Effect on ALOS PALSAR Images of Far Wakes of Ships. Proceedings of *3rd ALOS Joint PI Symposium*; Kona HI (USA), 09-13/11/2009.

Fujimura, A., Soloviev, A., & Kudryavtsev, V. N. (2010). Numerical Simulation of the Wind-Stress Effect on SAR Imagery of Far Wakes of Ships. *IEEE Geoscience and Remote Sensing Letters*, *7*(4), 646–649.

Gargett, A. E. (1989). Ocean Turbulence. *Annual Review of Fluid Mechanics*, *21*, 419–451.

Garrett, C., & Munk, W. H. (1979). Internal Waves in the Ocean. *Annual Review of Fluid Mechanics*, *11*(1), 339–369.

Garwood, R. W., Isakari, S. M., & Gallacher, P. C. (1994). Thermobaric Convection. In O. M. Johannessen, R. D. Muench, & J. E. Overland (Eds.), *Geophysical Monograph 85 - The Polar Oceans and their Role in Shaping the Global Environment* (Vol. 85, pp. 199–207). Washington DC, USA: American Geophysical Union.

Gascard, J.-C., Watson, A. J., Messias, M.-J., Olsson, K. A., Johannessen, T., & Simonsen, K. (2002). Long-Lived Vortices as a Mode of Deep Ventilation in the Greenland Sea. *Nature*, *416*(6880), 525–7.

Gasparovic, R. F., Apel, J. R., & Kasischke, E. S. (1988). An Overview of the SAR Internal Wave Signature Experiment. *Journal of Geophysical Research*, *93*(C10), 304–316.

George, S. G., & Tatnall, A. R. L. (2011). Measurement Of Turbulence in the Oceanic Mixed Layer Using Synthetic Aperture Radar (SAR). Proceedings of *Earth Observation for Ocean-Atmosphere Interactions Science*; Frascati (Italy), (29/11)-(02/12)/2011.

George, S. G., & Tatnall, A. R. L. (2012). Simulation of SAR Ocean Turbulence Signatures using Direct Numerical Simulation and Radar/Hydrodynamic Modelling. Proceedings of *European Conference on Synthetic Aperture Radar*; Nuremberg (Germany), 23-26/04/2012.

Gibson, C. H. (1986). Internal Waves, Fossil Turbulence, and Composite Ocean Microstructure Spectra. *Journal of Fluid Mechanics*, *168*.

Gibson, C. H. (1988). Evidence and Consequences of Fossil Turbulence in the Ocean. *Elsevier Oceanography Series*, *46*, 319–334.

Gibson, C. H., Bondur, V. G., Keeler, R. N., & Leung, P. T. (2006). Remote Sensing of Submerged Oceanic Turbulence and Fossil Turbulence. *International Journal of Dynamics of Fluids*, *2*(2), 171–212.

Gower, J. F. R., Denman, K. L., & Holyer, R. J. (1980). Phytoplankton Patchiness Indicates the Fluctuation Spectrum of Mesoscale Oceanic Structure. *Nature*, *288*, 157–159.

Green, T., Medwin, H., & Paquin, J. E. (1972). Measurements of Surface Wave Decay due to Underwater Turbulence. *Nature Physical Science*, *237*, 115–117.

Greidanus, H., Calkoen, C. J., Hennings, I., Romeiser, R., Vogelzang, J., & Wensink, G. J. (1997). Intercomparison and Validation of Bathymetry Radar Imaging Models. Proceedings of *IEEE Geoscience and Remote Sensing Symposium*; Singapore, 03-08/08/1997.

Hagan, D., Rogers, D., Friehe, C., Weller, R., & Walsh, E. (1997). Aircraft Observations of Sea Surface Temperature Variability in the Tropical Pacific. *Journal of Geophysical Research*, *102*(C7), 15733.

Hasselmann, K. (1967). *Weak-Interaction Theory of Ocean Waves*.

Hayward, T. L., & Mantyla, A. W. (1990). Physical, Chemical and Biological Structure of a Coastal Eddy near Cape Mendocino. *Journal of Marine Research*, *48*(4), 825–850.

Henderson, F. M., & Lewis, A. J. (Eds.). (1998). *Principles & Applications of Imaging Radar: Manual of Remote Sensing, Volume 2* (3rd ed.). New York, USA: John Wiley & Sons.

Hennings, I., Romeiser, R., Alpers, W. R., & Viola, A. (1999). Radar Imaging of Kelvin Arms of Ship Wakes. *International Journal of Remote Sensing*, *20*(13), 2519–2543.

Hennings, I., & Lurin, B. (1999). Radar Imaging of the Sea Bed during the C-STAR Experiment in 1996: On the Determination of the Relaxation Rate Parameter of Short Gravity Waves due to Current Variations from In Situ Measurements and Theory. Proceedings of *IEEE Geoscience and Remote Sensing Symposium*; Hamburg (Germany), (28/06)-(02/07)/1999.

Hennings, I., Lurin, B., & Didden, N. (2001). Radar Imaging Mechanism of the Seabed: Results of the C-STAR Experiment in 1996 with Special Emphasis on the Relaxation Rate of Short Waves due to Current Variations. *Journal of Physical Oceanography*, *31*(7), 1807–1827.

Hennings, I., & Herbers, D. (2007). The Expected Potential of TerraSAR-X High Resolution Spotlight Mode Data for Shallow Sea Bottom Topography Imaging: A Preview. Proceedings of *EARSeL Symposium*; Bolzano/Bozen (Italy), 04-07/06/2007.

Herrmann, M., Bouffard, J., & Béranger, K. (2009). Monitoring Open-Ocean Deep Convection from Space. *Geophysical Research Letters*, *36*(3), 1–5.

Hochberg, E., & Atkinson, M. J. (2003). Capabilities of Remote Sensors to Classify Coral, Algae, and Sand as Pure and Mixed Spectra. *Remote Sensing of Environment*, 85(2), 174–189.

Hogan, G. G., Chapman, R. D., Watson, G., & Thompson, D. R. (1996). Observations of Ship-Generated Internal Waves in SAR Images from Loch Linnhe, Scotland, and Comparison with Theory and In Situ Internal Wave Measurements. *IEEE Transactions on Geoscience and Remote Sensing, 34*(2).

Holliday, D., St-Cyr, G., & Woods, N. E. (1986). A Radar Ocean Imaging Model for Small to Moderate Incidence Angles. *International Journal of Remote Sensing, 7*(12), 1809–1834.

Holt, B. (2004). SAR Imaging of the Ocean Surface. In C. R. Jackson & J. R. Apel (Eds.), *SAR Marine User's Manual* (pp. 25–79). Available online: http://www.sarusersmanual.com

Howe, M. S. (2007). *Hydrodynamics and Sound.* New York, USA: Cambridge University Press.

Hsiao, S. V., & Shemdin, O. H. (1983). Measurements of Wind Velocity and Pressure with a Wave Follower during MARSEN. *Journal of Geophysical Research, 88*(C14), 9841–9849.

Hughes, B. A. (1978). The Effect of Internal Waves on Surface Wind Waves 2. Theoretical Analysis. *Journal of Geophysical Research, 83*(7).

IOCCG. (2000). Reports of the International Ocean-Colour Coordinating Group Remote Sensing of Ocean Colour in Coastal, and Other Optically-Complex, Waters.

Isern-Fontanet, J., Turiel, A., García-Ladona, E., & Font, J. (2007). Microcanonical Multifractal Formalism: Application to the Estimation of Ocean Surface Velocities, *Journal of Geophysical Research, 112.*

Isern-Fontanet, J., Lapeyre, G., Klein, P., Chapron, B., & Hecht, M. W. (2008). Three-Dimensional Reconstruction of Oceanic Mesoscale Currents from Surface Information. *Journal of Geophysical Research, 113*(C9), 1–17.

Ivanov, A. Y., & Ginzburg, A. I. (2002). Oceanic Eddies in Synthetic Aperture Radar Images. *Journal of Earth System Science, 111*(3), 281–295.

Jackson, C. R., & Apel, J. R. (Eds.). (2004). *SAR Marine User's Manual.* Washington DC, USA: NOAA NESDIS Office of Research and Applications. Available online: http://www.sarusersmanual.com

Jacobs, G. A., Barron, C. N., Carnes, M. R., Fox, D. N., Hurlburt, H. E., Pistek, P., Rhodes, R. C., et al. (1999). *Navy Altimeter Data Requirements.* Hancock County MS, USA: Naval Research Laboratory.

Jansen, R. W., Chubb, S. R., Fusina, R. A., & Valenzuela, G. R. (1993). *Modeling of Current Features in Gulf Stream SAR Imagery.* Washington DC, USA: Naval Research Laboratory.

Jansen, R. W., Ainsworth, T. L., Fusina, R. A., Chubb, S. R., & Valenzuela, G. R. (1994). Hydrodynamic and Radar Modelling of Surface Features Observed in Gulf Stream Boundary Regions. Proceedings of *IEEE Geoscience and Remote Sensing Symposium*; Pasadena CA (USA), 08-12/08/1994.

Jansen, R. W., Shen, C. Y., Chubb, S. R., & Cooper, A. L. (1998). Subsurface, Surface, and Radar Modeling of a Gulf Stream Current Convergence. *Journal of Geophysical Research*, *103*, 723–743.

Janssen, P. A. E. M., Wallbrink, H., Calkoen, C. J., Halsema, D. van, Oost, W. A., & Snoeij, P. (1998). VIERS-1 Scatterometer Model. *Journal of Geophysical Research*, *103*(C4), 7807–7831.

Johannessen, J. A., Shuchman, R. A., Johannessen, O. M., Davidson, K. L., & Lyzenga, D. R. (1991). Synthetic Aperture Radar Imaging of Upper Ocean Circulation Features and Wind Fronts. *Journal of Geophysical Research*, *96*(C6), 411–422.

Johannessen, J. A., Shuchman, R. A., Digranes, G., Lyzenga, D. R., Wackerman, C. C., Johannessen, O. M., & Vachon, P. W. (1996). Coastal Ocean Fronts and Eddies Imaged with ERS-1 Synthetic Aperture Radar. *Journal of Marine Research*, *101*(C3), 6651–6667.

Johannessen, J. A. (2000). Coastal Observing Systems: The Role of Synthetic Aperture Radar. *John Hopkins APL Technical Digest*, *21*(1), 41–48.

Johannessen, J. A., Kudryavtsev, V. N., Akimov, D., Eldevik, T., Winther, N., & Chapron, B. (2005). On Radar Imaging of Current Features: 2. Mesoscale Eddy and Current Front Detection. *Journal of Geophysical Research*, *110*(C7), 1–14.

Johannessen, J. A., Chapron, B., Collard, F., Kudryavtsev, V. N., Mouche, A., Akimov, D., & Dagestad, K.-F. (2008). Direct Ocean Surface Velocity Measurements from Space: Improved Quantitative Interpretation of Envisat ASAR Observations. *Geophysical Research Letters*, *35*(22), 1–6.

Johannessen, O. M., Lygre, K., & Eldevik, T. (1991). Convective Chimneys and Plumes in the Northern Greenland Sea. *The Nordic Seas: An Integrated Perspective; Geophysical Monograph Series 158*: American Geophysical Union.

Johannessen, O. M., Sandven, S., Jenkins, A. D., Durand, D., Pettersson, L. H., Espedal, H. A., Evensen, G., et al. (2000). Satellite Earth Observation in Operational Oceanography. *Coastal Engineering*, *41*(1-3), 155–176.

Johnson, D. L. (2003). *Airborne Synthetic Aperture Radar Images of an Upwelling Filament*. University of Hawaii: MSc thesis.

Jones, C. E., Minchew, B., Holt, B., & Hensley, S. (2011). Studies of the Deepwater Horizon Oil Spill With the UAVSAR Radar. In Y. Liu, Z.-G. MacFadyen, & R. H. Weisberg (Eds.), *Monitoring and Modeling the Deepwater Horizon Oil Spill: A Record-Breaking Enterprise; Geophysical Monograph Series 195*. Washington DC, USA: American Geophysical Union.

Joseph, A. (2014). *Measuring Ocean Currents: Tools, Technologies and Data. Measuring Ocean Currents: Tools, Technologies and Data.* Waltham MA, USA: Elsevier.

Joyce, T. M. (1984). Velocity and Hydrographic Structure of a Gulf Stream Warm-Core Ring. *Journal of Physical Oceanography*, *14*(5), 936–947.

Kanevsky, M. B. (2009). *Radar Imaging of the Ocean Waves*. Elsevier Science Publishers.

Keller, W. C., & Wright, J. W. (1975). Microwave Scattering and the Straining of Wind-Generated Waves. *Radio Science*, *10*(2), 139–147.

Khatiwala, S., Primeau, F., & Hall, T. (2009). Reconstruction of the History of Anthropogenic CO_2 Concentrations in the Ocean. *Nature*, *462*, 346–350.

Kitaigorodskii, S. A., & Lumley, J. L. (1983). Wave-Turbulence Interactions in the Upper Ocean. Part I: The Energy Balance of the Interacting Fields of Surface Wind Waves and Wind-Induced Three-Dimensional Turbulence. *Journal of Physical Oceanography*, *13*(11), 1977–1987.

Kitaigorodskii, S. A., Donelan, M., Lumley, J. L., & Terray, E. A. (1983). Wave-Turbulence Interactions in the Upper Ocean. Part II: Statistical Characteristics of Wave and Turbulent Components of the Random Velocity Field in the Marine Surface Layer. *Journal of Physical Oceanography*, *13*(11), 1988–1999.

Kitaigorodskii, S. A. (1984). On the Fluid Dynamical Theory of Turbulent Gas Transfer Across an Air-Sea Interface in the Presence of Breaking Wind-Waves. *Journal of Physical Oceanography*, *14*(5), 960–972.

Klein, P., & Lapeyre, G. (2009). The Oceanic Vertical Pump Induced by Mesoscale and Submesoscale Turbulence. *Annual Review of Marine Science*, *1*(1), 351–375.

Klemas, V. (2011). Remote Sensing of Sea Surface Salinity: An Overview with Case Studies. *Journal of Coastal Research*, *276*, 830–838.

Koblinsky, C. J., Gaspar, P., & Lagerloef, G. S. E. (Eds.). (1992). *The Future of Spaceborne Altimetry Oceans and Climate Change - A Long-Term Strategy*. Washington DC, USA.

Kudryavtsev, V. N., Akimov, D., Johannessen, J. A., & Chapron, B. (2005). On Radar Imaging of Current Features: 1. Model and Comparison with Observations. *Journal of Geophysical Research*, *110*(C7), 1–27.

Kudryavtsev, V. N., Shrira, V., Dulov, V., & Malinovsky, V. (2008). On the Vertical Structure of Wind-Driven Sea Currents. *Journal of Physical Oceanography*, *38*(10), 2121–2144.

Lacombe, H., Tchernia, P., Ribet, M., Bonnot, J., Frassetto, R., Swallow, J. C., Miller, A. R., et al. (1970). Observation of Formation of Deep Water in the Mediterranean Sea, 1969. *Nature*, *227*, 1037–1040.

Lagerloef, G. S. E., Swift, C. T., & Le Vine, D. M. (1995). Sea Surface Salinity - The Next Remote Sensing Challenge. *Oceanography*, *8*(2).

Lamb, H. (1932). *Hydrodynamics* (6th Edition). Cambridge, UK: Cambridge University Press.

Lavrova, O. (2005). Slicks as Indicators of Vorticity in Coastal Zones. Proceedings of *International Symposium on Remote Sensing of Environment*; Saint Petersburg (Russian Federation), 20-24/06/2005.

Le Traon, P. Y. (2006). *Report from the Working Group on Space Infrastructure for the GMES Marine Core Service*. GMES.

LeBlond, P. H., & Mysak, L. A. (1978). *Waves in the Ocean*. Norwich, UK: Elsevier Science Publishers.

Lee, J.-S., Jansen, R. W., Schuler, D. L., Ainsworth, T. L., Marmorino, G. O., & Chubb, S. R. (1998). Polarimetric Analysis and Modeling of Multifrequency SAR Signatures from Gulf Stream Fronts. *IEEE Journal of Oceanic Engineering*, *23*(4), 322–333.

Legeckis, R., Brown, C. W., & Chang, P. S. (2002). Geostationary Satellites Reveal Motions of Ocean Surface Fronts. *Journal of Marine Systems*, *37*, 3–15.

Legg, S., McWilliams, J. C., & Gao, J. (1998). Localization of Deep Ocean Convection by a Mesoscale Eddy. *Journal of Physical Oceanography*, *28*(5), 944–970.

Lehner, S., Pleskachevsky, A. L., & Bruck, M. (2012). Sea State Variability and Coastal Interaction Processes Observed by High Resolution TerraSAR-X Satellite Radar Images. Proceedings of *IEEE International Geoscience and Remote Sensing Symposium*; Munich (Germany), 22-27/07/2012.

Leung, P. T., & Gibson, C. H. (2004). Turbulence and Fossil Turbulence in Oceans and Lakes. *Chinese Journal of Oceanology and Limnology*, *22*(1), 1–23.

Li, X., Clemente-Colón, P., & Friedman, K. S. (2000). Estimating Oceanic Mixed-Layer Depth from Internal Wave Evolution Observed from Radarsat-1 SAR. *John Hopkins APL Technical Digest*, *21*(1).

Lilly, J. M., Rhines, P. B., Visbeck, M., Davis, R., Lazier, J. R. N., Schott, F., & Farmer, D. (1999). Observing Deep Convection in the Labrador Sea during Winter 1994/95. *Journal of Physical Oceanography*, *29*(8), 2065–2098.

Lilly, J. M., & Rhines, P. B. (2002). Coherent Eddies in the Labrador Sea Observed from a Mooring. *Journal of Physical Oceanography*, *32*(2), 585–598.

Lindstrom, E. J., Ebbesmeyer, C. C., & Owens, W. B. (1986). Structure and Origin of a Small Cyclonic Eddy Observed during the POLYMODE Local Dynamics Experiment. *Journal of Physical Oceanography*, *16*(3), 562–570.

Liu, A. K., Peng, C. Y., & Schumacher, J. D. (1994). Wave-Current Interaction Study in the Gulf of Alaska for Detection of Eddies by Synthetic Aperture Radar. *Journal of Geophysical Research*, *99*(C5).

Lyden, J. D., Lyzenga, D. R., Shuchman, R. A., & Swanson, C. V. (1985). *SAR Detection of Ship-Generated Turbulent and Vortex Wakes.* Ann Arbor MI, USA: Environmental Research Institute of Michigan.

Lyden, J. D., Hammond, R., Lyzenga, D. R., & Shuchman, R. A. (1988). Synthetic Aperture Radar Imaging of Surface Ship Wakes. *Journal of Geophysical Research*, *93*(8), 12,293–12,303.

Lyzenga, D. R. (1986). Numerical Simulation of Synthetic Aperture Radar Image Spectra for Ocean Waves. *IEEE Transactions on Geoscience and Remote Sensing*, *GE-24*(6), 863–872.

Lyzenga, D. R., & Bennett, J. R. (1988). Full-Spectrum Modeling of Synthetic Aperture Radar Internal Wave Signatures. *Journal of Geophysical Research*, *93*(C10), 12345–12354.

Lyzenga, D. R. (1991). Interaction of Short Surface and Electromagnetic Waves with Ocean Fronts. *Journal of Geophysical Research*, *96*(C6), 10,765–10,772.

Lyzenga, D. R., & Wackerman, C. C. (1997). Detection and Classification of Ocean Eddies using ERS-1 and Aircraft SAR Images. Proceedings of *ERS Symposium on Space at the Service of Our Environment*; Florence (Italy), 14-21/03/1997.

Lyzenga, D. R. (1998). Effects of Intermediate-Scale Waves on Radar Signatures of Ocean Fronts and Internal Waves. *Journal of Geophysical Research*, *103*(C9), 18759–18768.

Lyzenga, D. R., Marmorino, G. O., & Johannessen, J. A. (2004). Ocean Currents and Current Gradients. *SAR Marine User's Manual.* Available online: http://www.sarusersmanual.com

Marmorino, G. O., Jansen, R. W., Valenzuela, G. R., Trump, C. L., Lee, J.-S., & Kaiser, J. A. C. (1994). Gulf Stream Surface Convergence Imaged by Synthetic Aperture Radar. *Journal of Geophysical Research*, *99*(C9), 18315–18328.

Marshall, J., & Schott, F. (1999). Open-Ocean Convection: Observations, Theory, and Models. *Reviews of Geophysics*, *37*(1), 1–64.

Martin, A. P., Wade, I. P., Richards, K. J., & Heywood, K. J. (1998). The PRIME Eddy. *Journal of Marine Research*, *56*(2), 439–462.

McCandless, S. W., & Jackson, C. R. (2004). Principles of Synthetic Aperture Radar. In C. R. Jackson & J. R. Apel (Eds.), *SAR Marine User's Manual* (pp. 1–23). Available online: http://www.sarusersmanual.com

McKee, W. D. (1987). Water Wave Propagation across a Shearing Current. *Wave Motion*, *9*, 209–215.

McKee, W. D. (1996). A Model for Surface Wave Propagation across a Shearing Current. *Journal of Physical Oceanography*, *26*(2), 276–278.

McKenna, S. P., & McGillis, W. R. (2004). The Role of Free-Surface Turbulence and Surfactants in Air-Water Gas Transfer. *International Journal of Heat and Mass Transfer*, *47*, 539–553.

Melsheimer, C., Bao, M., & Alpers, W. R. (1998b). Imaging of Ocean Waves on Both Sides of an Atmospheric Front by the SIR-C/X-SAR Multifrequency Synthetic Aperture Radar. *Journal of Geophysical Research*, *103*(C9), 18839–18849.

Migliaccio, M., Nunziata, F., & Gambardella, A. (2009). On the Co-Polarized Phase Difference for Oil Spill Observation. *International Journal of Remote Sensing*, *30*(6), 1587–1602.

Milgram, J. H., Skop, R. A., Peltzer, R. D., & Griffin, O. M. (1993). Modeling Short Sea Wave Energy Distributions in the Far Wakes of Ships. *Journal of Geophysical Research*, *98*(C4), 7115–7124.

Mittal, R., & Iaccarino, G. (2005). Immersed Boundary Methods. *Annual Review of Fluid Mechanics*, *37*(1), 239–261.

Mobley, C. D., Sundman, L. K., Davis, C. O., Bowles, J. H., Downes, T. V., Leathers, R. A, Montes, M. J., Bissett, W. P., Kohler, D. D. R., Reid, R. P., Louchard E. M., & Gleason, A. (2005). Interpretation of Hyperspectral Remote-Sensing Imagery by Spectrum Matching and Look-Up Tables. *Applied Optics*, 44(17), 3576–92.

Moin, P., & Mahesh, K. (1998). Direct Numerical Simulation: A Tool in Turbulence Research. *Annual Review of Fluid Mechanics*, *30*(1), 539–578.

Monin, A. S., & Ozmidov, R. V. (1985). *Turbulence in the Ocean.* Dordrecht, The Netherlands: D. Riedel Publishing Company.

Morawitz, W. M. L., Sutton, P. J., Worcester, P. F., Cornuelle, B. D., Lynch, J. F., & Pawlowicz, R. (1996). Three-Dimensional Observations of a Deep Convective Chimney in the Greenland Sea during Winter 1988/89. *Journal of Physical Oceanography*, *26*(11), 2316–2343.

Morris, J. T., Anderson, S. J., & Parfitt, A. (2002). Polarimetric Mapping of Ship Wakes. Proceedings of *IEEE Geoscience and Remote Sensing Symposium*; Toronto (Canada), 24-28/06/2002.

Morrow, R., & Le Traon, P. Y. (2006). 15 Years of Satellite Altimetry and Mesoscale Ocean Dynamics. Proceedings of *15 Years of Progress in Radar Altimetry Symposium*. Venice (Italy), 13-18/03/2006.

Mumby, P. J., Green, E. P., Edwards, A. J., & Clark, C. D. (1997). Coral Reef Habitat Mapping: How Much Detail can Remote Sensing Provide? *Marine Biology*, 130(2), 193–202.

Munk, W. H., Scully-Power, P., & Zachariasen, F. (1987). Ships from Space. *Proceedings of the Royal Society A: Mathematical, Physical and Engineering Sciences*, *412*(1843), 231–254.

Nadai, A., Umehara, T., Matsuoka, T., Satake, M., Kobayashi, T., & Uratsuka, S. (2011). Dependency of Backscattering from Ocean Surface on Wind Direction by using Airborne SAR - Low Wind Speed Case. Proceedings of *IEEE Geoscience and Remote Sensing Symposium*; Vancouver (Canada), 24-29/07/2011.

NASA GEO-CAPE. (2012). GEO-CAPE Oceans Science Team Meeting requirements document (Draft v4.1, 01/02/2012). Available online: http://geo-cape.larc.nasa.gov/docs/Ocean_STM_v4_1-1Feb2012_rev.pdf

Ölmez, H. S., & Milgram, J. H. (1992). An Experimental Study of Attenuation of Short Water Waves by Turbulence. *Journal of Fluid Mechanics*, *239*, 133–156.

Ouchi, K., Stapleton, N. R., & Barber, B. C. (1997). Multi-Frequency SAR Images of Ship-Generated Internal Waves. *International Journal of Remote Sensing*, *18*(18), 3709–3718.

Oumansour, K., Wang, Y., & Saillard, J. (1996). Multifrequency SAR Observation of a Ship Wake. *IEE Proceedings F: Communications, Radar and Signal Processing*, *143*(4), 275–280.

Paluszkiewicz, T., Garwood, R. W., & Denbo, D. W. (1994). Deep Convective Plumes in the Ocean. *Oceanography*, *7*(2), 37–44.

Pascual, A., Pujol, M., Larnicol, G., Letraon, P., & Rio, M. (2007). Mesoscale Mapping Capabilities of Multisatellite Altimeter Missions: First Results with Real Data in the Mediterranean Sea. *Journal of Marine Systems*, *65*(1-4), 190–211.

Pascual, A., Ruiz, S., & Tintoré, J. (2010). Combining New and Conventional Sensors To Study the Balearic Current. *Sea Technology*, *51*(7).

Phillips, O. M. (1958a). The Equilibrium Range in the Spectrum of Wind-Generated Waves. *Journal of Fluid Mechanics*, *4*(4), 426–434.

Phillips, O. M. (1958b). The Scattering of Gravity Waves by Turbulence. *Journal of Fluid Mechanics*, *5*(02), 177–192.

Phillips, O. M. (1966). *The Dynamics of the Upper Ocean*. (G. K. Batchelor & J. W. Miles, Eds.) (1st ed.). Cambridge, UK: Cambridge University Press.

Phillips, O. M. (1977). *The Dynamics of the Upper Ocean*. (G. K. Batchelor & J. W. Miles, Eds.) (2nd ed.). Cambridge, UK: Cambridge University Press.

Phillips, O. M. (1985). Spectral and Statistical Properties of the Equilibrium Range in Wind-Generated Gravity Waves. *Journal of Fluid Mechanics*, *156*, 505–531.

Pickart, R. S., Torres, D. J., & Clarke, R. A. (2002). Hydrography of the Labrador Sea during Active Convection. *Journal of Physical Oceanography*, *32*(2), 428–457.

Pingree, R. (1996). A Shallow Subtropical Subducting Westward Propagating Eddy (Swesty). *Transactions of the Royal Society of London A*, *354*, 979–1026.

Plant, W. J. (1982). A Relationship Between Wind Stress and Wave Slope. *Journal of Geophysical Research*, *87*(C3), 1961–1967.

Platonov, A., Tarquis, A., Sekula, E., & Redondo, J. M. (2007). SAR Observations of Vortical Structures and Turbulence in the Ocean. *Models, Experiments and Computation in Turbulence*.

Pollard, R. T., Read, J. F., Allen, J. T., Griffiths, G., & Morrison, A. I. (1995). On the Physical Structure of a Front in the Bellingshausen Sea. *Deep Sea Research II: Topical Studies in Oceanography*, *42*(4-5), 955–982.

Pope, S. B. (2000). *Turbulent Flows*. Cambridge, UK: Cambridge University Press.

Redondo, J. M., Matulka, A., Platonov, A., Sekula, E., & Fraunie, P. (2011). Eddy Measurements, Coastal Turbulence and Statistics in the Gulf of Lions. *Ocean Science Discussion*, *8*, 1–19.

Reed, A. M., Beck, R. F., Griffin, O. M., & Peltzer, R. D. (1990). Hydrodynamics of Remotely Sensed Surface Ship Wakes. *SNAME Transactions*, *98*, 319–363.

Reed, A. M., & Milgram, J. H. (2002). Ship Wakes and Their Radar Images. *Annual Review of Fluid Mechanics*, *34*(1), 469–502.

Remedios, J. J., Leigh, R. J., & Monks, P. S. (2007). *Challenge Workshop: Challenges in Earth Observation of Oceans challenges in Ocean Science - Meeting Report.* Centre for Earth Observation Instrumentation.

Robinson, I. S. (2004). *Measuring the Oceans from Space: The Principles and Methods of Satellite Oceanography* (p. 669). Berlin, Germany: Springer-Praxis.

Robinson, I. S. (2010). *Discovering the Ocean from Space: The Unique Applications of Satellite Oceanography.* Berlin, Germany: Springer-Verlag.

Rogers, B. D., Baumgartner, S. V., Krieger, G., Nottensteiner, A., Horn, R., Steinbrecher, U., Metzig, R., et al. (2008). Bistatic Spaceborne-Airborne Experiment TerraSAR-X/F-SAR: Data Processing and Results. *IEEE Geoscience and Remote Sensing Symposium* (pp. 3–6).

Rojanaratanangkule, W., Thomas, T. G., & Coleman, G. N. (2011). Numerical Study of Turbulent Manoeuvring-Body Wakes: Interaction with a Free Surface. Proceedings of *7th International Symposium on Turbulence and Shear Flow Phenomena*; Ottawa (Canada), 28-31/07/2011.

Rojanaratanangkule, W., Thomas, T. G., & Coleman, G. N. (2012). Numerical Study of Turbulent Manoeuvring-Body Wakes: Interaction with a Non-Deformable Free Surface. *Journal of Turbulence*, *13*(17), 1–22.

Romeiser, R., Schmidt, A., & Alpers, W. R. (1994). A Three-Scale Composite Surface Model for the Ocean. *Journal of Geophysical Research*, *99*(C5), 9785–9801.

Romeiser, R., Alpers, W. R., & Wismann, V. (1997). An Improved Composite Surface Model for the Radar Backscattering Cross Section of the Ocean Surface 1. Theory of the Model and Optimization/Validation by Scatterometer Data. *Journal of Geophysical Research*, *102*(C11), 25237–25250.

Romeiser, R., & Alpers, W. R. (1997). An Improved Composite Surface Model for the Radar Backscattering Cross Section of the Ocean Surface 2. Model Response to Surface Roughness Variations and the Radar Imaging of Underwater Bottom Topography. *Journal of Geophysical Research*, *102*(C11), 25251–25267.

Romeiser, R., Ufermann, S., & Alpers, W. R. (2001). Remote Sensing of Oceanic Current Features by Synthetic Aperture Radar - Achievements and Perspectives. *Annals of Telecommunications*, *56*(11-12), 661–671.

Romeiser, R., Ufermann, S., Rubino, A., Androsov, A., Kern, S., & Mitnik, L. (2002). Interpretation of Convection Cell Signatures in Radar Images of the Greenland Sea. Proceedings of *IEEE Geoscience and Remote Sensing Symposium*; Toronto (Canada), 24-28/06/2002.

Romeiser, R., Ufermann, S., & Kern, S. (2003). Status Report on the Remote Sensing of Current Features by Spaceborne Synthetic Aperture Radar. Proceedings of *Coastal and Marine Applications Synthetic Aperture Radar (SAR) Workshop;* Svalbard (Norway).

Romeiser, R., Ufermann, S., Androsov, A., Wehde, H., Mitnik, L., Kern, S., & Rubino, A. (2004). On the Remote Sensing of Oceanic and Atmospheric Convection in the Greenland Sea by Synthetic Aperture Radar. *Journal of Geophysical Research*, *109*(C3), 1–14.

Romeiser, R. (2008). *M4S 3.2.0 User's Manual.*

Rozenberg, A., Matusov, P., & Melville, W. K. (1998). Polarised Microwave Scattering by Surface Water Waves and Turbulence. Proceedings of *IEEE Geoscience and Remote Sensing Symposium*; Seattle WA (USA), 06-10/07/1998.

Rozenberg, A. (2004). Laboratory Measurements of Wave-Turbulence Interaction for Scatterometry Application. Proceedings of *IEEE Geoscience and Remote Sensing Symposium*; Anchorage AL (USA), 20-24/09/2004.

Sabine, C. L., Feely, R. A., Gruber, N., Key, R. M., Lee, K., Bullister, J. L., Wanninkhof, R., et al. (2004). The Oceanic Sink for Anthropogenic CO2. *Science*, *305*, 367–371.

Schiller, A., & Brassington, G. B. (Eds.). (2011). *Operational Oceanography in the 21st Century*. Dordrecht, The Netherlands: Springer.

Shemer, L., & Kit, E. (1991). Simulation of an Interferometric Synthetic Aperture Radar Imagery of an Ocean System Consisting of a Current and a Monochromatic Wave. *Journal of Geophysical Research*, *96*(C12), 22063–22073.

Shemer, L., & Kagan, L. (1995). Simulation of Ship Wake Image by an Along Track Interferometric SAR. *IEEE Geoscience and Remote Sensing Symposium*, 213–215.

Shen, C. Y., & Evans, T. E. (2002). Inertial Instability and Sea Spirals. *Geophysical Research Letters*, *29*(23), 2124.

Shuchman, R. A., Lyzenga, D. R., & Meadows, G. A. (1985). Synthetic Aperture Radar Imaging of Ocean-Bottom Topography via Tidal-Current Interactions: Theory and Observations. *International Journal of Remote Sensing*, *6*(7), 1179–1200.

Siegmund, R., Lehner, S., Niedermeier, A., & Mayerle, R. (2001). Surface Currents Imaged with Hybrid Along and Cross Track Interferometry. Proceedings of *IEEE Geoscience and Remote Sensing Symposium*; Sydney (Australia), 09-13/07/2001.

Siegmund, R., Bao, M., Lehner, S., & Mayerle, R. (2004). First Demonstration of Surface Currents Imaged by Hybrid Along- and Cross-Track Interferometric SAR. *IEEE Transactions on Geoscience and Remote Sensing*, *42*(3), 511–519.

Skoelv, A., Wahl, T., & Eriksen, S. (1988). Simulation of SAR Imaging of Ship Wakes. Proceedings of *IEEE Geoscience and Remote Sensing Symposium;* Edinburgh (UK), 12-16/09/1988

Skoelv, A. (1991). Simulations of SAR Imaging of Ship Wakes, Comparing Different Wind Growth Rate Models. Proceedings of *IEEE Geoscience and Remote Sensing Symposium*; Espoo (Finland), 03-06/06/1991

Skolnik, M. I. (1980). *Introduction to Radar Systems* (2nd ed.). McGraw-Hill, Inc.

Skolnik, M. I. (1990). *Radar Handbook* (2nd ed.). McGraw-Hill, Inc.

Skop, R. A., Griffin, O. M., & Leipold, Y. (1990). Modification of Directional Wave Spectra by Currents in the Wake of a Surface Ship. *Journal of Ship Research*, *34*, 69–78.

Smyth, W. D., & Moum, J. N. (2001). *3D Turbulence.*

Soloviev, A., Donelan, M., Graber, H. C., Haus, B., & Schlussel, P. (2007). An Approach to Estimation of Near-Surface Turbulence and CO2 Transfer Velocity from Remote Sensing Data. *Journal of Marine Systems*, *66*(1-4), 182–194.

Soloviev, A., Gilman, M., Young, K., Brusch, S., & Lehner, S. (2010a). Sonar Measurements in Ship Wakes Simultaneous With TerraSAR-X Overpasses. *IEEE Transactions on Geoscience and Remote Sensing*, *48*(2), 841–851.

Soloviev, A., Maingot, C., Fujimura, A., Fenton, J., Gilman, M., Matt, S., Lehner, S., Velotto, D., & Brusch, S. (2010b). Fine Structure of the Upper Ocean from High-Resolution TerraSAR-X Imagery and In-Situ Measurements. Proceedings of *IEEE Geoscience and Remote Sensing Symposium*; Honolulu HI (USA), 25-30/07/2010.

Srokosz, M. A. (1995). Ocean Surface Salinity - The Why, What and Whether. *Consultative Meeting on Soil Moisture and Ocean Salinity Measurement Requirements and Radiometer Techniques (SMOS)*, 49–56.

Stammer, D. (1997). Global Characteristics of Ocean Variability Estimated from Regional TOPEX/POSEIDON Altimeter Measurements. *Journal of Physical Oceanography*, *27*(8), 1743–1769.

Steffen, E. L., & D'Asaro, E. A. (2002). Deep Convection in the Labrador Sea as Observed by Lagrangian Floats. *Journal of Physical Oceanography*, *32*(2), 475–492.

Steffen, E. L., & D'Asaro, E. A. (2004). Meso- and Submesoscale Structure of a Convecting Field. *Journal of Physical Oceanography*, *34*(1), 44–60.

Strub, P. T. (2001). High-Resolution Ocean Topography Science Requirements for Coastal Studies. In D. B. Chelton (Ed.), *Report of the High-Resolution Ocean Topography Science Working Group Meeting*. College of Oceanic and Atmospheric Sciences.

Swanson, C. V. (1984). *Radar Observability of Ship Wakes*. Falls Church VA, USA.

Swift, C. T., & McIntosh, R. E. (1983). Considerations for Microwave Remote Sensing of Ocean-Surface Salinity. *IEEE Transactions on Geoscience and Remote Sensing*, *GE-21*(4), 480–491.

Tabata, S. (1982). The Anticyclonic, Baroclinic Eddy off Sitka, Alaska, in the Northeast Pacific Ocean. *Journal of Physical Oceanography*, *12*(11), 1260–1282.

Teixeira, M. A. C., & Belcher, S. E. (2002). On the Distortion of Turbulence by a Progressive Surface Wave. *Journal of Fluid Mechanics*, *458*, 229–267.

Terray, E. A., Donelan, M. A., Agrawal, Y. C., Drennan, W. M., Kahma, K. K., Williams III, A. J., Hwang, P. A., et al. (1996). Estimates of Kinetic Energy Dissipation under Breaking Waves. *Journal of Physical Oceanography*, *26*(5), 792–807.

Thomann, G. C. (1976). Experimental Results of the Remote Sensing of Sea-Surface Salinity at 21-cm Wavelength. *IEEE Transactions on Geoscience Electronics*, *14*(3), 198–214.

Thomas, T. G., & Williams, J. J. R. (1997). Development of a Parallel Code to Simulate Skewed Flow over a Bluff Body. *Journal of Wind Engineering and Industrial Aerodynamics*, *67-68*, 155–167.

Thompson, D. R. (1985). Intensity Modulations in Synthetic Aperture Radar Images of Ocean Surface Currents and the Wave/Current Interaction Process. *John Hopkins APL Technical Digest*, *6*(4).

Thompson, D. R., & Gasparovic, R. F. (1986). Intensity Modulation in SAR Images of Internal Waves. *Nature*, *320*(27).

Thompson, D. R. (1988). Calculation of Radar Backscatter Modulations From Internal Waves. *Journal of Geophysical Research*, *93*, 12371–12380.

Thompson, D. R., Gotwols, B. L., & Sterner, R. E. (1988). A Comparison of Measured Surface Wave Spectral Modulations with Predictions from a Wave-Current Interaction Model. *Journal of Geophysical Research*, *93*(C10), 12339–12343.

Thompson, D. R., & Jensen, J. R. (1993). Synthetic Aperture Radar Interferometry Applied to Ship-Generated Internal Waves in the 1989 Loch Linnhe Experiment. *Journal of Geophysical Research*, *98*(C6), 259–269.

Thorpe, S. A. (2004). Recent Developments in the Study of Ocean Turbulence. *Annual Review of Earth and Planetary Sciences*, *32*(1), 91–109.

Thorpe, S. A. (2005). *The Turbulent Ocean*. Cambridge, UK: Cambridge University Press.

Thorpe, S. A. (2007). *An Introduction to Ocean Turbulence*. Cambridge, UK: Cambridge University Press.

Tokmakian, R., Strub, P. T., & McClean-Padman, J. (1990). Evaluation of the Maximum Cross-Correlation Method of Estimating Sea Surface Velocities from Sequential Satellite Images. *Journal of Atmospheric and Oceanic Technology*, *7*(6), 695–721.

Tolman, H. L., & Chalikov, D. (1996). Source Terms in a Third-Generation Wind Wave Model. *Journal of Physical Oceanography*, *26*(11), 2497–2518.

Toporkov, J. V., Hwang, P. A., Sletten, M. A., Farquharson, G., Perkovic, D., & Frasier, S. J. (2011). Surface Velocity Profiles in a Vessel's Turbulent Wake Observed by a Dual-Beam Along-Track Interferometric SAR. *IEEE Geoscience and Remote Sensing Letters*, *8*(4), 602–606.

True, M. A., Lyzenga, D. R., & Lyden, J. D. (1993). *Centreline Wake Modeling*. Ann Arbor MI, USA: Environmental Research Institute of Michigan.

Turiel, A., Isern-Fontanet, J., Garcia-Ladona, E., & Font, J. (2005). Multifractal Method for the Instantaneous Evaluation of the Stream Function in Geophysical Flows. *Physical Review Letters*, *95*(10), 104502.

Ufermann, S., & Romeiser, R. (1999). A New Interpretation of Multifrequency/Multipolarisation Radar Signatures of the Gulf Stream Front. *Journal of Geophysical Research*, *104*(C11).

Ufermann, S., Robinson, I. S., & Da Silva, J. C. B. (2001). Synergy Between Synthetic Aperture Radar and Other Sensors for the Remote Sensing of the Ocean. *Annals of Telecommunications*, *56*(11), 672–681.

Vastano, A. C., Schmitz, J. E., & Hagan, D. E. (1980). The Physical Oceanography of Two Rings Observed by the Cyclonic Ring Experiment. Part I: Physical Structures. *Journal of Physical Oceanography*, *10*(4), 493–513.

Veron, F., Melville, W. K., & Lenain, L. (2011). The Effects of Small-Scale Turbulence on Air–Sea Heat Flux. *Journal of Physical Oceanography*, *41*(1), 205–220.

Vesecky, J. F., & Stewart, R. H. (1982). The Observation of Ocean Surface Phenomena Using Imagery From the SEASAT Synthetic Aperture Radar: An Assessment. *Journal of Geophysical Research*, *87*(C5), 3397–3430.

Wadhams, P. (2002). A Deep Convective Chimney in the Winter Greenland Sea. *Geophysical Research Letters*, *29*(10), 3–6.

Walker, B., Sander, G., Thompson, M., Burns, B., Fellerhoff, R., & Dubbert, D. (1996). A High-Resolution, Four-Band SAR Testbed with Real-Time Image Formation. Proceedings of *IEEE Geoscience and Remote Sensing Symposium*; Lincoln NE (USA), 27-31/05/1996.

Waugh, D. W., Abraham, E. R., & Bowen, M. M. (2006). Spatial Variations of Stirring in the Surface Ocean: A Case Study of the Tasman Sea. *Journal of Physical Oceanography*, *36*(3), 526–542.

Whitham, G. B. (1965). A General Approach to Linear and Non-Linear Dispersive Waves using a Lagrangian. *Journal of Fluid Mechanics*, *22*(2), 273–283.

Wood, S. (2008). Autonomous Underwater Gliders. In A. V. Inzartsev (Ed.), *Underwater Vehicles*. Vienna, Austria: InTech publishers.

Wright, J. W. (1968). A New Model for Sea Clutter. *IEEE Transactions on Antennas and Propagation*, *16*(2), 217–223.

Wu, S. Y., Liu, A. K., Leonard, G., & Pichel, W. G. (2000). Ocean Feature Monitoring with Wide Swath Synthetic Aperture Radar. *John Hopkins APL Technical Digest*, *21*(1), 122–129.

Yang, J., Xiao, Q., Huang, W., Fu, B., Chen, P., & Yao, L. (2005). Multifrequency SAR Remote Sensing of Ocean Internal Waves. Proceedings of *IEEE Geoscience and Remote Sensing Symposium*; Seoul (South Korea), 25-29/07/2005.

Yoder, J. A., Antoine, D., Del Castillo, C. E., Evans, R. H., Mobley, C., Sarmiento, J. L., Sathyendranath, S., Schueler, C. F., Siegel, D. A., & Wilson, C. (2011). *Assessing Requirements for Sustained Ocean Color Research and Operations*. National Academies Press.

Zappa, C. J., & Jessup, A. T. (2005). High-Resolution Airborne Infrared Measurements of Ocean Skin Temperature. *IEEE Geoscience and Remote Sensing Letters*, *2*(2), 146–150.

Zappa, C. J., McGillis, W. R., Raymond, P. A., Edson, J. B., Hintsa, E. J., Zemmelink, H. J., Dacey, J. W. H., et al. (2007). Environmental Turbulent Mixing Controls on Air-Water Gas Exchange in Marine and Aquatic Systems. *Geophysical Research Letters*, *34*(10), 1–6.

Appendix A

A.1

Abstract

Turbulence in the surface layer of the ocean contributes to the transfer of heat, gas and momentum across the air-sea boundary. As such, study of turbulence in the ocean surface layer is becoming increasingly important for understanding its effects on climate change. Direct Numerical Simulation (DNS) techniques were implemented to examine the interaction of small-scale wake turbulence in the upper ocean layer with incident electromagnetic radar waves. Hydrodynamic-electromagnetic wave interaction models were invoked to demonstrate the ability of Synthetic Aperture Radar (SAR) to observe and characterise surface turbulent wake flows. A range of simulated radar images are presented for a turbulent surface current field behind a moving surface vessel, and compared with the surface flow fields to investigate the impact of turbulent currents on simulated radar backscatter. This has yielded insights into the feasibility of resolving small-scale turbulence with remote-sensing radar and highlights the potential for extracting details of the flow structure and characteristics of turbulence using SAR.

A.2

Oral paper presented at 9th European Conference on Synthetic Aperture Radar (EUSAR), Nuremberg, Germany; 23rd-26th April 2012. 4-page preliminary paper peer-reviewed and accepted; final paper published in VDE conference proceedings.

Abstract

Synthetic Aperture Radar (SAR) has shown remarkable ability to resolve turbulent phenomena such as eddies, breaking waves and ship wakes. Ship-wake turbulence was simulated using Direct Numerical Simulation (DNS) techniques and translated to simulated Normalised Radar Cross-Section (NRCS) and SAR imagery through use of existing radar/hydrodynamic models. Simulated remote-sensing signatures are presented and analysed for the ability to resolve turbulent structure from the resulting imagery and improve understanding of the relationships between small-scale turbulence and radar backscattering. The results obtained indicate that turbulent structure embedded in ship wakes can be translated to and resolved by changes in radar backscatter.

A.3

George, S. G., Tatnall, A. R. L.; *Measurement of Turbulence in the Oceanic Mixed Layer using Synthetic Aperture Radar*; 2012; in Proceedings of the ESA, SOLAS & EGU Joint Conference 'Earth Observation for Ocean-Atmosphere Interactions Science' (Eds. L. Ouwehand), ESA SP-703 (CD-ROM), ESA Communications, European Space Agency, Noordwijk, The Netherlands.

Abstract

Improved understanding of the cause and character of turbulence is increasingly important for applications such as climate change: Turbulent processes near the surface layer of the ocean contribute greatly to momentum, heat and flux transfers across the air-sea boundary. Such processes are most commonly observed in Synthetic Aperture Radar (SAR) imagery as the turbulent wake present behind a moving surface vessel or ship, but also in the radar backscatter signatures of breaking surface & internal waves, convection, eddies, etc. Fine-resolution turbulent wake flows were computed numerically using Direct Numerical Simulation and the interaction of small-scale wake turbulence with the free surface studied using a hydrodynamic interaction model. The resulting modulated surface currents were subsequently processed through radar simulation algorithms to generate simulated radar images of the wake and demonstrating the ability of SAR to observe and characterise surface turbulent flows which contribute to exchange processes at the air-sea interface.

A.4

George, S. G., Tatnall, A. R. L.; *Generation of a Turbulent Surface Wake using Direct Numerical Simulation and Visibility of Flow Structure in Radar Backscattering Signatures*; 2013; International Journal of Remote Sensing (in revision).

Abstract

Turbulence and mixing in the surface layer of the ocean contributes to the transfer of heat, gas and momentum across the air-sea boundary. As such, an understanding of turbulence and turbulent flows at the ocean surface is becoming increasingly important for role in exchange processes and hence climate change. Direct Numerical Simulation was used to derive a hypothetical wake flow, subsequently processed using ocean radar image modelling techniques to investigate the interaction of simple wake profiles with incident electromagnetic radar waves. The results obtained demonstrate the potential to observe and characterise surface turbulent wake flows in terms of radar backscattering, and hence the potential for imaging radar to resolve wake structure at the ocean surface and its interaction with short waves. A range of simulated backscatter images are presented for a turbulent surface current field derived from flow moving past a towed sphere, yielding investigation of the impact of turbulent currents on simulated radar backscattering. This has developed insights into the feasibility of resolving small-scale turbulence with remote-sensing radar and highlights the potential for extracting details of the flow structure and characteristics of turbulence near the surface of the ocean using current and future SAR capability.

Appendix B

B.1 Ocean Colour (i)

Parameter	Range	Accuracy (Case 1 Water)	Accuracy (Case 2 Water)
Marine Reflectance [at 442 nm]	0.001-0.04	5×10^{-4}	5×10^{-4}
Water-leaving radiance $L_w(\lambda)$ (atmospherically-corrected) [mW/cm²/μm/Sr]	0.0-1.0	5 %	5 %
Photosynthetically available radiation PAAR [μmol quanta/m²s]	0-1400	5 %	5 %
Diffuse attenuation coefficient (or turbidity), K [m⁻¹]	0.001-0.1	5 %	5 %
Chlorophyll, Chl [mg/m³]	0.001-150	30 % (threshold) 10 % (goal)	70 % (threshold) 10 % (goal)
Total suspended matter [g/m³]	0.0-100	30 % (threshold) 10 % (goal)	70 % (threshold) 10 % (goal)
Coloured dissolved organic material CDOM, a_{412} [m⁻¹]	0.01-2	50 % (threshold) 10 % (goal)	70 % (threshold) 10 % (goal)
Harmful Algae bloom [mg/m³]	0.1-100	30 % (threshold) 20 % (goal)	70 % (threshold) 30 % (goal)

Table B1. Geophysical Parameters and Accuracies for Ocean Colour (clear daytime conditions); from Drinkwater & Rebhan (2005).

B.2 Ocean Colour (ii)

Source	Phenomena/Process	Colour Variation	Horizontal Scale [km]	Additional Info.
Buranapratheprat et al. (2010)	Eddy	0.1 mgm^{-3}	25 km	
Robinson (2010)	Eddy	0.2-0.5mg^{-3}	30-40 km	Chlorophyll concentration

Table B2. Ocean colour characteristics of ocean phenomena, collected from a variety of sources.

B.3 Sea-Surface Temperature

Source	Phenomena/Process	Temperature Variation [°K]	Horizontal Scale [km]	Additional Info.
Androsov et al. (2005)	Deep Convection	1.2 (A) , 0.7 (B)	75	A – strong atmospheric forcing B – weak atmospheric forcing
Askari et al. (1993) Fronts selected which had large temperature contrasts	Ocean Fronts	2-6	2-5	
	Ocean Front	14	40	Max. variation 4C/km
	Ocean Front	16	40	Max. variation 6C/km
	Ocean Front	9	30	Max. variation 6°C/km
	Ocean Front	9	30	Max. variation 6°C/km
	Ocean Front	6	30	Max. variation 3°C/kmv
Buranapratheprat et al. (2010)	Eddy	0.5	150	
Fischer et al. (1999)	Deep Convection (plume)	0.02-0.03	6	Max gradient 0.02°C /50 m; 6 km span, 50 m grid spacing
	Deep convection (mesoscale)	0.1	1	Total temperature contrast across a chimney, based on hydrodynamic models by Garwood, Isakari & Gallacher (1994)

Table B3. Sea-surface temperature characteristics of ocean phenomena, collected from a variety of sources.

B.3 Sea-Surface Temperature (contd.)

Source	Phenomena/Process	Temperature Variation [°K]	Horizontal Scale [km]	Additional Info.
Gower, Denman & Holyer (1980)	Eddy	2-6	100	Mesoscale eddy
	Open-Ocean	0.1-0.5		Open-ocean thermal contrast
Hayward & Mantyla (1990)	Coastal Eddy	1-1.5	10	
Ivanov & Ginzburg (2002)	Rings	2-3	100-300	
Johannessen et al. (1996)	Coastal Ocean Front	1	20	Gradients up to 0.2°C/km
Johannessen, Lygre, & Eldevik (2005)	Submesoscale Structure			
	Temp. difference between "cold & warm anomalies"	0.01-.04		
	Plumes	0.02-0.05	0.1-0.3	
	Deep Convection	2-3	100-200	Max gradient 0.2°C/km
	\<unknown\>	1	20	
Legg, McWilliams, & Gao (1998)	Evolving Deep Convective Chimney	0.5	10 (0.8 days) 15 (3 days) 20 (6 days)	

B.3 Sea-Surface Temperature (contd.)

Source	Phenomena/Process	Temperature Variation [°K]	Horizontal Scale [km]	Additional Info.
Marshall & Schott (1999)	Deep Convective Patch	0.03		
Martin et al. (1998)	Eddy	0.3-1	40	
Morawitz et al. (1996)	Gyre	0.2		
Pingree (1996)	Eddy	19.9 (A) 18.35 (B)		A – Core B – External
Robinson (2010)	Gulf Stream Front	10		Steep frontal gradient 1°C/km
	Cold-Core Eddy	5		
	Mesoscale Variability; Eddy	1	40 km	
Steffen & D'Asaro (2004)	Basin Scale	2 (2.6-4.6)	100 km	Pickart, Torres & Clarke (2002)
		2.5 (3-5.5)	100 km	Steffen & D'Asaro (2002)
	Mesoscale	0.3	20 km	Lilly et al. (1999), Lilly & Rhines (2002)
		0.47	20 km Eddy	Lilly et al. (1999), Lilly & Rhines (2002)

B.3 Sea-Surface Temperature (contd.)

Source	Phenomena/Process	Temperature Variation [°K]	Horizontal Scale [km]	Additional Info.
Steffen & D'Asaro (2004)	Submesoscale Variability	0.3	5	
	Plume Scale	0.02	1	Steffen & D'Asaro (2002)
Vastano, Schmitz, & Hagan (1980)	Ocean Ring	0.2-0.5	100	
Wadhams (2002)	Deep Convective Chimney	0.1		
Zappa & Jessup (2005)	Eddy Standard Deviation	1.04		
	Eddy Gradient	0.12 [*]	3 m [*]	Meriadonal/zonal variability ~ 0.23°C/km, 0.27°C/km; horizontal gradients > 2°C in 10 km. Observed with airborne IR sensor with 1 m spatial resolution and 0.02°C thermal resolution. [*] Read from Figure 6.
Hagan et al. (1997)	Eddy			Horizontal gradients > 1°C in 10 km. Observed with airborne IR sensor with 100 m spatial resolution and 0.1°C thermal resolution.

B.4 Sea-Surface Salinity

Source	Phenomena/Process	Salinity Variation psu]	Horizontal Scale [km]	Additional Info.
Androsov et al. (2005)	Deep Convective Chimney	0.003	10	
Buranapratheprat et al. (2010)	Eddy	1-2	150	
Burrage (2003)	Coast			~ 1 psu per km
	Open ocean			0.5 psu per 10 km
Burrage et al. (2008)	Front			10 psu per 33 km
Gascard et al. (2002)	Eddy	0.02		
Johannessen et al. (1996)	Coastal Ocean Front	1.5-2	40	Max. gradient 0.1 psu/km
Johannessen et al. (2005)	Deep Convection	0.03	10-20	
	Deep Convection	0.06	10-20	
	Deep Convection	0.03	2-10	
Lagerloef, Swift, & Le Vine (1995)	Gulf Stream	5	160	Max. gradient 2 psu/km
Marshall & Schott (1999)	Deep Convective Patch	0.004		

Table B4. Sea-surface salinity characteristics of ocean phenomena, collected from a variety of sources.

B.4 Sea-Surface Salinity (contd.)

Source	Phenomena/Process	Salinity Variation psu]	Horizontal Scale [km]	Additional Info.
Pingree (1996)	Swesty	37.06 core 36.71 external		
Steffen & D'Asaro (2004)	Mesoscale Variability; Eddy	0.1	40 km	
	Submesoscale Variability	0.04	5 km	
	Basin Scale	0.1 (34.8-34.9)	100 km	Pickart et al. (2002)
		0.15 (34.74-34.91)		Steffen & D'Asaro (2002)
	Mesoscale	0.03	20 km	Lilly et al. (1999), Lilly & Rhines (2002)
		0.059	20 km Eddy	Lilly et al. (1999), Lilly & Rhines (2002)

B.4 Sea-Surface Salinity (contd.)

Source	Phenomena/Process	Salinity Variation psu]	Horizontal Scale [km]	Additional Info.
Srokosz (1995)	Eddy	1.0	10	Hayward & Mantyla (1990)
	Eddy	0.7	20	Hayward & Mantyla (1990)
	Eddy	0.75	100	Fornshell & Criess (1979)
	Eddy	1.7	150	Joyce (1984)
	Eddy	0.4	50-75	Lindstrom, Ebbesmeyer & Owens (1986)
	Eddy	0.5	50-100	Tabata (1982)
	Eddy	0.4	75	Tabata (1982)
	Eddy	0.25	75-100	Vastano et al. (1980)
	Eddy	0.1	50	Vastano et al. (1980)
	Eddy	0.5	10.5	Allen, Smeed, & Chadwick (1994)
	Eddy	0.3	7.3	Allen, Smeed, & Chadwick (1994)
	Eddy	0.7	9.9	Allen, Smeed, & Chadwick (1994)
	Eddy	0.05-0.1	10-20	Pollard, Read, Allen, Griffith & Morrison (1995)

B.5 Sea-Surface Height

Source	Phenomena/Process	Height Variation [cm]	Horizontal Scale [km]	Additional Info.
Drinkwater & Rebhan (2005)	Mesoscale Eddy	4-8		rms height
	High Eddy-Energy Regions	20-40		rms height
Koblinsky, Gaspar, & Lagerloef (1992)	Ocean Gyres (> 300 days)	100 (A) 10 (B)	> 1000 km	A – Mean B - Variation
	Mesoscale Eddies	25	~ 50	
	Western Boundary Currents (> 10 days)	100 (A) 100 (B)	100	A – Mean B – Meanders, variations
	Eastern Boundary Currents (> 10 days)	20 (A) 10 (B)	500	A – Mean B – Meanders, variations
	Equatorial Currents (> 50 days)	20 (A) 10 (B)	> 500	A – Mean B – Meanders, variations
	El Nino Response of Equatorial Sea Level	20	> 500	(~ 1000 days)

Table B5. Sea-surface height characteristics of ocean phenomena, collected from a variety of sources
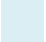
B.5 Sea-Surface Height (contd.)

Source	Phenomena/Process	Height Variation [cm]	Horizontal Scale [km]	Additional Info.
Herrmann, Bouffard, & Béranger (2009)	Deep Convection	2-3		
Jacobs et al. (1999)	Mesoscale Features	5-50		
Strub (2001)	Energetic Coastal Currents	2-10		

Appendix C

C.1 Review of Previous Simulation Studies

The following table(s) represent a large sample of the available literature associated with radar backscatter simulation of ocean at a range of scales and processes. The tables attempt to document, as far as possible, the range of conditions considered in the study and the set-up of the simulation, but are by no means comprehensive. In some cases, information has been extracted from graphs or read from figures by eye, and so may be subject to some element of inaccuracy.

The table is listed chronologically by year, and the alphabetically (by first author). Rows which are highlighted in a light blue tone ⬚ represent particular studies/sources which hold particular relevance for this current study, or which significant reference has been made to in the main thesis.

Source	Phenomena/ Process	Applied Radar Model	Flow Feature Data	Additional Info.
Lyden et al. (1985)	Ship Wake	*ERIM*	Max. current 0.12 ms^{-1}; max. gradient 0.03 s^{-1}	Simulations performed for of 5 kT military ship and 500 kT supertanker. 800 m horizontal distance, 180 m (cross-wake cut of vortex model); 3 m grid spacing. Considers 0/1.5/3/6/12 ms^{-1} winds, X/C/L/P-band. Measures radar intensity above minimum intensity level at wake centre; spectral perturbation.
Shuchman, Lyzenga & Meadows (1985)	Ocean Bottom Topography	*ERIM* forerunner	Max. current 0.72 ms^{-1}	Spatial grid 2.5 x 2.5 km; 20 m grid spacing. Measured outputs include change in NRCS across the ocean floor feature, compared with actual *Seasat* SAR data. Measures maximum/minimum NRCS; modulation depth.
Thompson (1985)	Internal Waves		Max. current 0.3-0.6 ms^{-1}; max. gradient 0.002-8 s^{-1}	Surface currents represented by **sech**^{2} function; 6 ms^{-1} wind speed at 145° to internal wave propagation direction
Thompson & Gasparovic (1986)	Internal Waves		Max. current 0.3-0.6 ms^{-1}; max. gradient 0.002-8 s^{-1}	<conditions believed identical to Thompson (1985> . 2500 m horizontal distance. Considers X/L-band simulation in 6 ms^{-1} wind
Caponi et al. (1988)	Ocean Current	Bragg Model; HSW model	Max. current 0.3 ms^{-1}	(HSW) Holliday, St-Cyr & Woods (1986) model

Table C1. Details of previous simulation studies, collected from a variety of sources.

Source	Phenomena/ Process	Applied Radar Model	Flow Feature Data	Additional Info.
Lyden et al. (1988)	Ship Wake	ERIM	Ship velocity 8 ms⁻¹	Simulations performed to explain the observed modulation of internal waves in SAR data
Lyzenga & Bennett (1988)	Internal Waves	ERIM	Max. current 0.42 ms⁻¹	Spatial grid 500 m, 120 grid points; 150-k wavenumber grid, 24-θ directional grid
Skoelv, Wahl & Eriksen (1988)	Ship Wake	Bragg Model; Holliday, St-Cyr & Woods (1986) model		Passage of a full 2-D wave spectrum through a vortex pair of (locally) constant circulation; same approach as Swanson (1984). Spatial grid 300 m. Considers C/L-band at 23° incidence, in 2-15 ms⁻¹ wind speeds
Thompson (1988)	Internal Waves		Max. current 0.5 ms⁻¹.	X/L-band at 23°/35°/50° incidence angles in 2.5/5/10 ms⁻¹ winds
Thompson, Gotwols & Sterner (1988)	Internal Waves		Max. current 0.5 ms⁻¹; max. gradient 0.001-0.006 s⁻¹	Wind speed 3.5/7 ms⁻¹
Johannessen et al. (1991)	Current Jet		Current jet 0.3 ms⁻¹ (shear 0.3 x 10⁻³ s⁻¹)	Max. jet speed 0.37 ms⁻¹
Lyzenga (1991)	Ocean Front/ Convergence	ERIM	Max. gradient 0.01-0.001 s⁻¹	Spatial grid 120 m, grid spacing (approx.) 20 m

Source	Phenomena/ Process	Applied Radar Model	Flow Feature Data	Additional Info.
Shemer & Kit (1991)	Ocean Current			Ocean system consisting of a current and a monochromatic wave; also considers InSAR simualtion
Skoelv (1991)	Ship Wake	Bragg Model; Holliday, St-Cyr & Woods (1986) model		Combines two imaging models and seven relaxation rate models; spatial domain 160 m. Considers *Seasat/ERS-1* configuration: C/L-band, 20 ° /23 ° , VV-polarisation; 5ms⁻¹ wind speed
Jansen et al. (1993)	Ocean current	*ERIM*	Max. solition-like current 0.1 ms⁻¹; max. gradient -0.0038 s⁻¹	Current rip formed by subduction of Gulf Stream under shelf water. Spatial domain unknown, 145 grid points (y), 4 m grid spacing; 82-k wavenumber grid (0.001 < λ_w < 50); 24-θ directional grid. X-band, 37 ° incidence angle, HH-polairsation; 5 ms⁻¹ wind speed
			Current rip 0.4 ms⁻¹; max. gradient 0.03 s⁻¹	1-D solition-like current. Spatial domain unknown, 95 grid points (x), 4 m grid spacing; 62-k wavenumber grid (0.001 < λ_w < 50); 36- θ directional grid. X-band, 37 ° incidence angle, HH-polairsation; 3 ms⁻¹

Source	Phenomena/ Process	Applied Radar Model	Flow Feature Data	Additional Info.
True, Lyzenga & Lyden (1993)	Ship Wake	*ERIM*		1-D simulations (cross-wale cut); ship velocity 9.26 ms^{-1}. Spatial grid 150 m (1-dimensional); 300 grid points (x), 128 (y); 48-k wavenumber grid (0.01 < λ_w < 50); 12-θ directional grid. Airborne case: 30 °/40 °/50 °/60 ° incidence angles, 0 °/45 °/90 ° heading direction with respect to wake centreline; wind speeds 2.6/5.1/7.7/10.3 ms^{-1} at directions 0 °/45 °/90 ° to wake centreline
Liu, Peng & Schumacher, (1994)	Ocean Eddy		Max. current 0.3 ms^{-1}	Spatial domain 30 x 30 km
Marmorino et al. (1994)	Ocean Front		Max. current 0.1 ms^{-1}, max. gradient 0.002 s^{-1}	Gulf Stream surface convergence; slope water 0.7-0.8 ms^{-1}, low salinity filament 1.2 ms^{-1}, Gulf Stream 1.2-1.4 ms^{-1}. Wind speed 8 ms^{-1}
Jansen et al. (1994)	Ocean Current		Max. gradient 0.002 s^{-1}	Current rip formed by subduction of Gulf Stream under shelf water. Convergence speed 0.2-0.6 ms^{-1}. Wind speeds 3/6/9/12 ms^{-1}
Shemer & Kagan (1995)	Ship Wake			Wigley ship length 30 m, width 10 m, beam 2m; speed 10 ms^{-1}; also considers interferometric simulation. Airborne L-band case, 200 ms^{-1} flight velocity, 20 m InSAR baseline

Source	Phenomena/ Process	Applied Radar Model	Flow Feature Data	Additional Info.
Fischer & Shuchman (1996)	Oceanic Convection	*ERIM*		Convection depths 1000 m, 2000 m; surface heat fluxes 200/400 Wm⁻²; LES model of Garwood, Isakari & Gallacher (1994), and mesoscale model. Spatial domain 6 x 6 km (LES), 50 x 50 km (mesoscale); grid spacing 50 m (LES), 200 m (mesoscale). *ERS-1/RADARSAT-1/JERS-1* cases ; airborne case 30°/40 ° /50 ° incidence angles, 3000 m altitude, 200 ms⁻¹ flight velocity, HH/VV-polarisation. 1/3.5/10 ms⁻¹ wind speed. Measures mean NRCS; NRCS contrast
Johannessen et al. (1996)	Ocean Front / Ocean Eddy	*ERIM*	Max. gradient 0.002 s⁻¹	Considers convergence/divergence at the front feature
Oumansour, Wang & Saillard (1996)	Ship Wake	Two-scale Bragg model		Airborne L- and X-band simulation; range/azimuth resolution 3 m / 0.75 m.

Source	Phenomena/ Process	Applied Radar Model	Flow Feature Data	Additional Info.
Greidanus et al. (1997)	Ocean Bottom Topography	6 models tested and compared ~ \<see 'additional info'\>		Study to compare performance of different radar models to "more extreme" case ocean bottom topography interaction. L-, C- and X-band simulations examining cross-cuts of backscatter. Models tested: 1. ARGOSS // Phillips eqbm. Spectrum, fitted relaxation rate, Bragg backscatter model; 2. GEOMAR // Phillips eqbm. Spectrum, Hughes (1978) relaxation rate, Bragg backscatter model; 3. RWS // Apel (1994) eqbm. spectrum, Hsiao & Shemdin (1983) relaxation rate, Holliday, St-Cyr & Woods (1986) backscatter model; 4. TNO-C // VIERS eqbm. spectrum of Janssen et al. (1998), Plant (1982) relaxation rate, composite surface backscatter model; 5. TNO-B // VIERS eqbm. Spectrum, Plant (1982) relaxation rate, Bragg backscatter model 6. M4S // Romeiser, Alpers & Wismann (1997) eqbm. spectrum, Plant (1982) relaxation rate, composite surface backscatter model

Source	Phenomena/ Process	Applied Radar Model	Flow Feature Data	Additional Info.
Ouchi, Stapleton & Barber (1997)	Internal Waves			Ship-generated internal waves. P/C/L-band; 2.5/5/10 ms^{-1} wind speed
Jansen et al. (1998)	Current Rip		Max. current 0.4 ms^{-1}, max. gradient 0.019 s^{-1}	Gulf Stream surface convergence; current width 4 km. Also considers turning on/off wave-breaking effects, surfactant damping etc. X-band, 37° incidence angle, HH-polarisation
Lee et al. (1998)	Ocean Front			Gulf Stream surface convergence. P/C/L-band, 45° incidence angle
Lyzenga (1998)	Oceant Front / Internal Wave	*ERIM*	Max. current 0.2 ms^{-1}	
Ufermann & Romeiser (1999)	Ocean Front	*M4S*		100-k wavenumber grid, 24-θ directional grid. X/C/L-band; 3.5 ms^{-1} wind speed
Hennings & Lurin (1999)	Underwater Bottom Topography	*M4S*		Study performed to match data from the *C-STARS* campaign. X/C/L/P-band; 0.8/3.8/7.4 ms^{-1}

Source	Phenomena/ Process	Applied Radar Model	Flow Feature Data	Additional Info.
Chubb et al. (1999)	Ocean Front	*ERIM, M4S*	Max. current 1.1 ms⁻¹; max. gradient 0.005 s⁻¹	Gulf Stream features. C/L-band
Hennings et al. (1999)	Ship Wake			Focuses on Kelvin arms of a ship wake. Considers examination of the ability to resolve the wake with different wake/heading alignments. *ERS-1/RADARSAT-1/JERS-1*, 8 hearing directions; 5 ms⁻¹ wind speed
Fischer et al. (1999)	Oceanic Convection	*ERIM*		Convection depths 1000 m, 2000 m; surface heat fluxes 200/400 Wm⁻²; LES model of Garwood, Isakari & Gallacher (1994), and mesoscale model. Spatial domain 6 x 6 km (LES), 50 x 50 km (mesoscale); grid spacing 50 m (LES), 98 m (mesoscale). *ERS-1/RADARSAT-1/JERS-1* cases; airborne case 30°/40°/50° incidence angles, 3000 m altitude, 200 ms⁻¹ flight velocity, HH/VV-polarisation. 1/3.5/10 ms⁻¹ wind speed. Mean NRCS; NRCS contrast.

Source	Phenomena/ Process	Applied Radar Model	Flow Feature Data	Additional Info.
Romeiser, Ufermann & Alpers (2001)	Ocean Current	*M4S*	Max. gradient 0.0025 s^{-1}; current divergence 0.005 s^{-1}	100-k wavenumber grid ; 24-θ directional grid
Romeiser et al. (2004)	Oceanic & Atmospheric Convection	*M4S*	Max. current up to 0.5 ms^{-1}, cyclonic and/or anti-cyclonic rotation. Max. current shear 1.3 x 10^{-5} s^{-1}.	Examines modulation depth of ERS-2 and RADARSAT-1 simulated signatures. Mean wind speeds applied up to 5 ms^{-1}. Oceanic convection simulation propagated using General Non-hydrostatic Ocean Model. Mesoscale simulation: spatial domain 25 x 25 km domain; 62.5 m grid spacing. Small-scale simulation: spatial domain 5.5 x 5.5 km; grid spacing 62.5 m
Androsov et al. (2005)	Ocean Convection	*M4S*		Non-hydrostatic 3-D model; coupled atmosphere-ocean 3-D model. Spatial grid 40 x 40 km; 55 m grid spacing
Yang et al. (2005)	Internal Waves			Spatial grid 1000 m. Simulation study proposed to consider the optimal conditions for internal wave imaging using SAR. X/C/L/P-band

Source	Phenomena/ Process	Applied Radar Model	Flow Feature Data	Additional Info.
Cooper et al. (2005)	Ocean Eddies			Spiral eddy originally captured by DiGiacomo & Holt (2001); "spiral eddy" hydrodynamic model of Shen & Evans (2002). Spatial domain 10 x 10 km; 256 grid points (x), 192 grid points (y); 62-k wavenumber grid ($0.01 < \lambda_w < 100$), 24-θ directional grid. Considerable focus in surfactant distribution at the surface for use as a tracer for spiral eddy dynamics. X/C/L/P-band, 37° incidence angle; 3/5/8 ms⁻¹
Fujimura & Soloviev (2009)	Ship Wake	*M4S*	Max. current 0.3 ms⁻¹; max. gradient 0.08 s⁻¹	Nominally examining the wind-stress effect. FLUENT non-hydrostatic model Detached Eddy Simulation: 18750000 cells; 10 ms⁻¹ ship (length 6 m), model based on hull and propeller study of Rhee (unknown). Spatial grid 50 x 50 m; 0.5 m grid spacing (x), 0.2 m grid spacing (y). L-band, 35° incidence angle, HH-polarisation
Fujimura, Soloviev & Kudryavtsev (2010)	Ship Wake	*RIM*	Uncertain. "Less than 0.1 ms⁻¹"	Nominally examining the wind-stress effect. FLUENT non-hydrostatic model: 240000 cells; 5.14 ms⁻¹ ship (length 7.5 m, beam 10 m). Pair of counter-rotating vortices of radius 2.5 m, 0.08 rads⁻¹ angular rotation. Details of radar backscatter grid not stipulated.

| Fujimura et al. (2011) | Ship Wake | M4S | Max. current 0.3 ms⁻¹; max. gradient ~0.08 s⁻¹ | Nominally examining the wind-stress effect. FLUENT non-hydrostatic model Detached Eddy Simulation: 18750000 cells; 10 ms⁻¹ ship (length 6 m), model based on hull and propeller study of Rhee (unknown). Spatial grid 50 x 50 m; 0.5 m grid spacing (x), 0.2 m grid spacing (y). X-band, 35° incidence angle, HH-polarisation |

Appendix D

D.1 Influence of Fine-Scale Turbulence on Wave Energy Dissipation: Application in Wave Propagation Models

The effect of fine-scale turbulent velocity fluctuations on surface wave energy has previously been examined by a number of authors (e.g. Milgram et al. [1993], True et al. [1993]), and remarks on this have previously been made in various portions of this thesis. In these previous studies, the effects of turbulence on surface wave energy have been implemented through manipulation of the source term in the right-hand side of the wave action balance formulation of Equations (xiv-xv) presented in Chapter 4. As discussed previously discussed in §4.3.2, most ocean radar imaging models perform on the principle of Conservation of Wave Action (CWA), in which wave-current interaction is driven by application of a set of source function parameters describing the balance of wave energy within the ocean surface layer. This balance is dependent on a number of factors; primarily the surface wave spectrum, the effect of the wind-sea interaction and breaking of waves. In the wave propagation equation (i.e. Equation [xv]), the source term(s) $S(\mathbf{k})$ are those which represent the rate of change in wave energy at the ocean surface, i.e.

$$\frac{dE(\mathbf{k})}{dt} = S(\mathbf{k}) \tag{D.1}$$

Compared with the influence of the wind on surface wave energy of the wind, the extraction of wave energy by turbulence is likely to play a minor role, but the exact role that it plays is still not well-understood. In comparison with other influences on wave energy (such as wind, wave-wave interactions, viscosity, etc.), there has been limited research into energy dissipation by turbulence, limited analysis of the wave energy dissipation on radar backscattering from short waves, and the relationship(s) between turbulence and radar backscatter are therefore still open to some debate.

A dissipative process is one that causes energy to be extracted from a wave system, leading to a source term contribution which is negative in sign convention. Dissipation of wave energy by the effects of viscosity is commonly applied to wave action models in the form (Lamb, 1932) according to

$$S_v(k) = -\frac{4\nu k^2}{\omega} N(k) \tag{D.2}$$

where $S_\nu(k)$ is the source term representing the removal wave energy from the wave system through the effects of viscosity. Energy dissipation may also be generated by other sources such as breaking waves or whitecapping of surface waves. Observed effects of (turbulence) dissipation are described as follows, using the findings of True et al. (1993):

o   Reduction of energy in surface wave system and reduction of action spectral density due to turbulent dissipation;

o   Reduction in amplitude of short, surface waves;

o   Reduction of wave relaxation rate;

o   Linear increase in modulation depth with turbulent damping rate;

o   Reduction in the equilibrium wave height spectrum.

Application of turbulence wave energy dissipation source terms for ocean radar imaging models has not been widely pursued in recent years since the studies by True et al. (1993) and Milgram et al. (1993) who considered the effects of turbulence dissipation on cross-wake profiles of NRCS. There has been no considerable discussion of the approaches of different authors to the problem of turbulence dissipation of wave energy (and its inclusion in source term models), therefore a review of this research is presented in this Appendix, culminating in some future perspectives.

D.1.1   Review of Previous Research: Early Works

The basis for studies of wave-current interaction involving turbulence was forged by the efforts of O. M. Phillips (1966), A. G. Boyev (1971) and S. A. Kitaigorodskii et al. (1983). First steps in this field were progressed by Phillips (1966), who discussed two mechanisms of decay of surface waves due to interaction with turbulent motions, dependent on the length scale of the observed turbulence.

1.   Scattering due to turbulent convective distortion of wave fronts causing a broadening of the wave spectrum. This effect is primarily observed when the scale of turbulence is equal to, or larger than, that of the waves: in these cases, turbulence assists in scattering short waves to different wavenumbers in addition to being diffracted by the strong mean currents causing the wave energy to be redistributed between wavenumbers, leading to reduced energy density (and thus wave amplitude) at the Bragg wavenumber. The effect of scattering of waves due to ship-generated currents is discussed by Skop et al. (1990)

2. Dissipation of wave energy due to straining of small turbulent eddies by mean wave motions when the scale of turbulence is much less than those of the waves, as observed by experimental studies such as Green et al. (1972), Ölmez & Milgram (1992) and Rozenberg (2004): "dissipation (whereby mean wave motions strain turbulent vortex filaments, thus increasing turbulent energy at the expense of wave energy) is a second-order process in ka, which is effective when the scale of the turbulence is much less than that of the waves. The decay law associated with this mechanism is not known but is probably nonlinear in wave amplitude (in the differential form)."

The theory of turbulent interaction with surface waves through the concept of downward convection of wave energy was first introduced by Boyev (1971) and later developed further in the companion papers by Kitaigorodskii & Lumley (1983) and Kitaigorodskii et al. (1983). This theory proposed how turbulence in the surface layer (of thickness k^{-1}), which contains energy of the surface wave system, may extract wave energy from the surface by convecting fluid into the (comparatively) quiescent fluid below. Energy is transferred across the boundary through vertical fluctuations which ultimately act to remove kinetic (i.e. wave) energy from the surface layer and hence leads to a reduction of surface wave amplitudes. Following their studies, Kitaigorodskii & Lumley (1983) concluded that "rapid fluctuations [of turbulence] can interact with periodic wave motion, since for them the latter appears as a slowly-varying shear current," observing that, while short- and rapid-scale turbulence may act as an effective eddy viscosity on the wave-induced velocity field, its role in the dissipation of energy is negligible within the total wave energy balance. Where turbulence intensity is much smaller than the rms wave velocity, they concluded that waves are "not appreciably distorted by their interaction with the turbulence".

The theory of dissipation of kinetic energy beneath surface waves was later expanded upon by Agrawal et al. (1992), who drew comparison with a wall layer with frictional wind stress and publishing measurements of enhanced levels of dissipation in the turbulent surface layer of Lake Ontario. Anis & Moum (1995) also examined the role of turbulent dissipation, ε, below the surface layer, and proposed two acting mechanisms: the first was transport of high levels of TKE (created by wave breaking at the surface) downward by the motion of swell; the second mechanism "requires a rotational wave field and significant wave stresses that balance the turbulence Reynolds stresses," such that energy is delivered to the mean flow from the wave field through wave stresses. In both cases, the transport of energy is balanced by turbulent dissipation through ε. Similarly, Borue et al. (1995) conducted a DNS study examining the interaction of surface waves and free-surface turbulence, confined to infinitesimally small waves. In their study, turbulence arising from

both bottom-shear and externally-imposed stress at the free surface (most relevant) was considered, and indicated a weak relationship between the turbulence and surface waves; although the operation of infinitesimally small waves may not be representative of real-world wave conditions responsible or surface radar backscattering.

D.1.2 Review of Previous Research: Experimental Studies

Green et al. (1972) conducted experiments using paddle-generated waves of 1 cm amplitude along with grid-generated turbulence causing wave amplitudes less than 1 mm; estimated turbulent rms velocity, u', of 1.2 cms[-1] (according to Teixeira & Belcher [2002]), measuring the decay of surface waves due to the presence of turbulence. Where turbulence interacted with the paddle-generated waves, the "turbulence energy is comparable with the wave energy," indicating that the presence of a dissipative decay mechanism proportional to the square of the wave amplitude (although in a natural environment, wave motions are likely to dominate). In a similar vein, studies by Reed et al. (1990) and Ölmez & Milgram (1992) involved experiments measuring the dissipation of short water waves by turbulence in a wave tank: a relationship was discovered between the amplitude decay rate, β_{Turb}, of waves of small steepness and characteristics of turbulent mixing, where

$$\beta_{Turb} = 0.103 \frac{u'}{(L')^{1/3}} \left(\frac{k}{2\pi}\right)^{2/3} \qquad (D.3)$$

$$L' = \frac{\pi}{2} \frac{\Phi(0)}{(u')^2} \qquad (D.4)$$

where u' is the rms horizontal turbulent level, L' is the horizontal integral length scale (or mixing scale length) and $\Phi(0)$ is the one-sided power density spectrum of the velocity component. This approximation was found to be relatively close to the measured wave decay rate in cases where the horizontal component of turbulence was close to homogeneous through the depth of wave energy. Their observations also confirmed the theory of downward convection of wave energy, noting that "most of it [the wave energy] may be convected downward and out of the wave zone by the vertical turbulent velocities," as opposed to transfer of energy in the normal energy-containing depth of the waves. Their results found that the decay rate of waves in turbulence is mainly dependent on the amplitude A_w, wavenumber k and frequency ω_0 of the waves, and on the relevant conditions of the fine-scale turbulence.

The conclusions drawn by Ölmez & Milgram (1992) suggest that wave energy dissipation due to turbulence plays only a minor role on short surface waves, at least when compared to the effect of

interaction with gravity waves and surface currents, but can affect "short-wave energy over substantial length scales such as remote measurement of ship wakes and estimation of wind speed by backscattered microwave intensity from the sea." The wave amplitude decay rate (β_{Turb}) derived from this research was later applied to ship wake remote-sensing studies by Milgram et al. (1993) and True et al. (1993); discussed later in this section. The region of effect of turbulent wave damping is later described by Reed & Milgram (2002): "the strong turbulence immediately behind the ship dissipates or scatters the short waves (Phillips, 1958b). However, as the turbulence rapidly reduces with increasing aft distance, it has little additional effect on the waves in the wake that are more than approximately one ship length behind the ship." These findings indicate that, on short scales, the effect of turbulent velocity fluctuation of wave energy dissipation could have some significance, however in the context of gravity waves and mean currents, its influence may quickly be masked by stronger surface motions.

However, the true role that turbulence plays in influencing radar backscattering signatures is often contested: in observations of the effect of ocean underwater topography on surface currents, Alpers & Hennings (1984) have previously observed that positive/negative deivations from the ambient NRCS either side of a subsurface feature are typically symmetric; implying that "turbulent interaction of the current with the ripple waves cannot be significant, because this process would always lead to an attenuation of the short waves and thus a reduction in the spectral energy density of the Bragg waves, but never to an enhancement." Of course, intensity of the observed turbulence may play a role, and thus account for differing observations made in regions of a ship wakes associated with higher turbulence intensity.

Experimental study by Rozenberg (2004) has shown further evidence that interaction of short surface waves with subsurface turbulence may cause attenuation of wave energy and the broadening of directional propagation spectra. These experiments considered interaction of gravity-capillary waves in the presence of turbulence, conducted in a wave channel using mechanically-generated waves and a multi-jet manifold to derive turbulent flow. The experiments demonstrated both a scattering and dissipation of surface waves by the turbulence, as well as a "pronounced distortion effect on the short waves due to scattering by submerged turbulence." The primary finding of the study was that turbulence reduced the energy of short waves and broadened their directional propagation spectra, however variations in the observed result were discovered for different scales of the disturbing turbulence: "if there is a separation of scales (turbulence scales larger than wave scales), the Doppler effect leads to a broadening of the dispersion relationship, which may be easy to interpret. If the turbulence scales are much smaller than those of the waves, then the main influence of turbulence may be an increase in wave dissipation. If the waves and turbulence are of

comparable length and time scales (our case), then turbulence influenced water waves through both scattering and dissipations." It was also found that strong turbulence (with Reynolds' numbers greater than 1000) had a dampening effect on surface waves.

D.1.3 Review of Previous Research: Remote-Sensing Applications

Following the launch of *ERS-1* (1991), the field saw renewed interest in the effect of dissipation of wave energy due to turbulent energy fluctuations was examined in order to explain the appearance of dark 'scars' of radar backscattering observed for many kilometres of a ship's wake, particularly at low frequencies such as L-band: it was found that the dark wake region indicated more damping than was predicted by interaction with the mean surface current alone. Research on dissipation of wave energy by turbulent interactions was performed using ocean radar imaging models to compare simulated radar imagery with those obtained operationally.

Milgram et al. (1993) used the findings of Ölmez & Milgram (1992) to define a new source term to include in the wave action balance calculation. Their approach was to apply an additional energy dissipation term to the source parameterisation, $S_{Turb,Milgram}(\mathbf{k})$, defined as the energy decay rate due to turbulence,

$$S_{Turb,Milgram}(\mathbf{k}) = 0.06 \frac{u'k^{2/3}}{(L')^{1/3}} N(\mathbf{k}) = 2\beta_{Turb} N(\mathbf{k}) \tag{D.5}$$

choosing a wave amplitude decay rate a factor of two beyond that derived by Ölmez & Milgram (1992). Milgram et al. (1993) concluded that reduced radar return leading to a dark centreline wake image is undoubtedly associated with reduced short-wave energy in the centreline ship wake. A similar parameterisation was employed by True et al. (1993) for a similar study, $S_{Turb,True}(\mathbf{k})$; differing from Milgram's parameterisation only by the size of the numerical coefficient and matching the Ölmez & Milgram (1992) decay rate.

$$S_{Turb,True}(\mathbf{k}) = 0.03 \frac{u'k^{2/3}}{(L')^{1/3}} N(\mathbf{k}) = \beta_{Turb} N(\mathbf{k}) \tag{D.6}$$

Equation (D.6) may also be rewritten in terms of the turbulent dissipation rate, ε:

$$S_{Turb,True}(\mathbf{k}) = 0.10\varepsilon^{1/3} k^{2/3} N(\mathbf{k}) \tag{D.7}$$

The presence of turbulence (and application of its effects in the wave energy balance through use of Equation (D.7) was discovered to cause a reduction in action spectral density of surface waves. An

almost linear relationship was observed between the measured modulation depth of NRCS and reduction of the relaxation rate (with increasing wavenumber) with increasing value of turbulence damping rate, ε. Both turbulence and concentration of surfactants in longitudinal bands caused by passage of the ship play a certain role in attenuating short waves, and that it may be difficult to isolate one from the other. True et al. (1993) also comment on selection of the numerical coefficient applied by different authors to a similar source term parameterisation: "a 50% increase of the damping rate can be achieved by doubling the constant of proportionality in the damping formula or increasing the dissipation rate, ε, by a factor of 8. In other words, the modulation depth is not sensitive to the dissipation rate." For a ship-wake application, True et al. (1993) computed cross-wake transects of ship wake with, and without, a turbulent dissipation source term in the wave action model, demonstrating a significant decrease in radar backscattering in the vicinity of the turbulent wake; as reproduced in Figure D1.
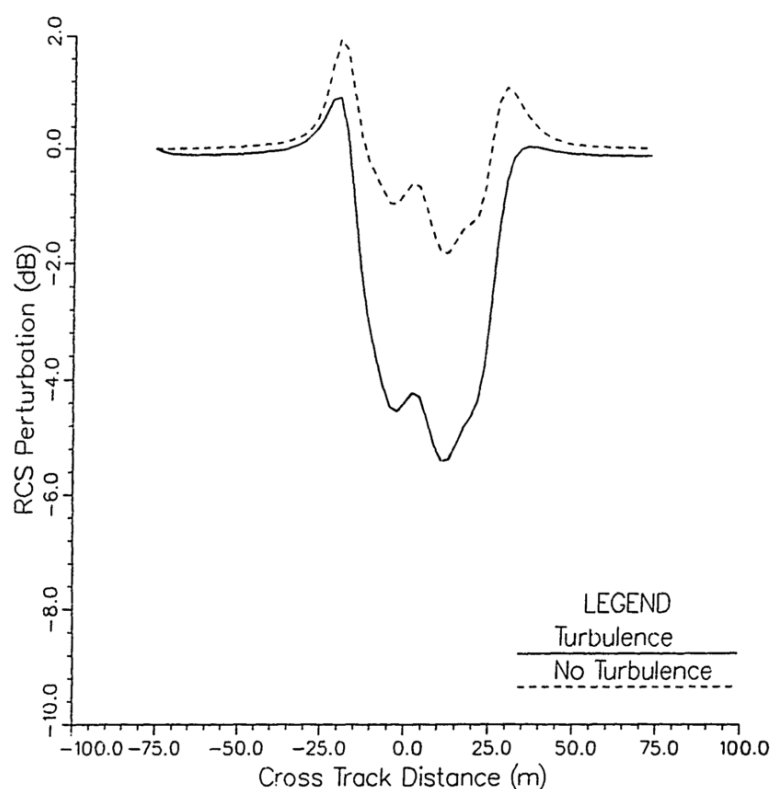

Figure D1. Transect taken across the radar signature of modelled ship wake, computed with, and without, application of turbulent dissipation of short waves in the wave energy balance; from True et al. (1993).

Fish & von Kerczek (1991) performed simulations of a two-dimensional vortex pair (generated by a typical ship operating characteristics) near a free surface with monochromatic ambient waves. Their analysis showed that submerged vortices can generate Bragg radar images with a dark centre region and that the ambient surface waves undergo spectral modification when encountering the surface wake current.

D.1.4 Review of Previous Research: Recent Developments

There has, in recent times, been renewed interest in understanding the role of turbulence on wave propagation; in particular, work published and presented by Teixeira & Belcher (2002) and Ardhuin & Jenkins (2006) has done much to advance the field, albeit with respect to swell wave propagation. In their work, Teixeira & Belcher (2002) developed a new theory to study interaction of turbulence and wave systems based on rapid distortion, engaged to provide a direct estimate of the wave attenuation coefficient. The Rapid Distortion Theory (RDT) is valid in cases where the wave orbital velocity "is larger than the turbulence and the slope of the wave is sufficiently high that the straining of the turbulence by waves dominates over the straining of the turbulence itself." The theory assumes that the turbulence is of a scale (integral length scale $'$) much smaller than that of the waves (wavelength λ_w) and wave slopes are "sufficiently high that the straining of the turbulence by the wave[s] is stronger than the straining of the turbulence by itself". It was discovered that waves propagating in a turbulent field locally generate TKE, causing change to local wave energy at the rate of $\beta_{TB2002}(\mathbf{k})$, representing the work done by the Stokes shear against the turbulent flux. Teixeira & Belcher (2002) found that they were able to "account for the turbulence-induced wave decay observed in the experimental studies of Ölmez & Milgram (1992) and Green et al. (1972)," arriving at a result for wave amplitude decay (which occurs exponentially in time due to turbulence) with an attenuation rate of

$$\beta_{TB2002} = A \left(\frac{u'}{c_p}\right)^2 \omega \tag{D.8}$$

where c_p is the phase velocity of the ocean waves under scrutiny, ω is wave angular frequency and A is a numerical constant of $O(1)$. It is noted that this wave decay rate is only important at wavenumbers for which viscous dissipation does not dominate.

In similar work investigating the interaction of surface waves with upper ocean turbulence, Ardhuin & Jenkins (2006) developed theory regarding how the production of TKE in the near-surface layer may be equated to the change in (i.e. loss of) energy by the surface waves, given that the majority of

wave energy is not directly dissipated into heat. Equating the production of TKE in the surface layer with the loss of wave energy based on the conservation of energy, Ardhuin & Jenkins (2006) arrive at the source term for wave energy loss, $S_{Turb,AJ2006}(\mathbf{k})$, given in deep water by

$$S_{Turb,AJ2006}(\mathbf{k}) = -\frac{2\mathbf{k}\omega(\mathbf{k})}{\mathbf{g}}\tau(0)\cdot\mathbf{k} \qquad (D.9)$$

where τ is the horizontal distribution of Reynolds' stress.

The conclusions drawn by Ardhuin & Jenkins (2006), and the application of Equation (D.9), imply that turbulence has a dampening effect on waves which are propagating in the direction of the wind stress, and that waves which propagating against the wind extract energy from turbulence. They found that wave interaction with oceanic (fine-scale) turbulence can explain swell attenuation rates when compared with viscous wind-caused damping. Breaking of surface waves is the main source of TKE in the surface layer, but may also be generated by surface shearing processes.

Furthermore, Kudryavtsev et al. (2008) have developed theory and modelling of wave energy balance; in particular considering the interaction(s) of wind waves, turbulence and surface shear currents. They propose a new, semi-empirical model for the ocean surface layer which develops the theories Kitaigorodskii (1984) and Terray et al. (1996) regarding the injection of momentum and energy into the body of the ocean by breaking waves.

D.1.5   Summary

Appendix D has so far presented a review of the previous research associated with understanding and modelling the effect of fine-scale turbulence on dissipation of wave energy of short surface waves and regarding operation of alternative modelling procedures. Whilst the effects of turbulence on low-frequency gravity waves are more well-developed (and have also seen developments in recent years in publications such as Tolman & Chalikov [1996]), this review has focussed on the effects of fine-scale turbulence on short, backscattering waves, with the aim of collating the various ideas and previous research into this problem into a single, unified review relevant to (Bragg-scale) backscattering of radar waves.

As a first step, it is recommended that future work should consider further experimental study on the phenomenon of wave energy dissipation arising from small-scale turbulence: a natural progression from previous studies, and the research presented in this thesis, lies in conducting a range of laboratory experiments to further understand the influence of fine-scale turbulence on short ocean surface waves. A target application would lie in generating short waves and surface

mixing in wind/wave tank and observing radar backscatter measurements using Radio Frequency (RF) antennas at multiple frequencies, along with accurate observation of wave amplitudes and measurement of amplitude decay. Ideally, this would produce results which allow comparison with previous experiments conducted by Green et al. (1972) and Ölmez & Milgram (1992), to further understand the wave amplitude decay rate β_{Turb} due to turbulence and therefore application of the S_{Turb} source term parameterisation in wave-current interaction models. Addition of an airborne remote-sensing campaign and in-situ instrument to measure this effect would add significant weight to the results and verify this effect in geophysical conditions.

In addition, there has currently been only limited study on the effects of turbulence dissipation on two-dimensional simulated surface signatures, since work by True et al. (1993) and Milgram et al. (1993) considered only one-dimensional simulations (in a transect across the turbulent wake) considering the effect of turbulence dissipation on radar backscattering. Recommendations are made towards performing a full/expanded simulation study, using results from an experimental study of the wave amplitude decay rate due to turbulence, on a two-dimensional surface wake current profile. Such a simulation study would include comparison of varying parameterisation(s) of the S_{Turb} source term which have been applied previously for inclusion in the surface wave energy balance; a summary of these terms is presented in Table D1.

Equation	Reference	Parameterisation
(D.5)	Milgram et al. (1993)	$$S_{Turb,Milgram}(\mathbf{k}) = 0.06\frac{u^{\prime}k^{2/3}}{(L^{\prime})^{1/3}}N(\mathbf{k})$$
(D.7)	True et al. (1993)	$$S_{Turb,True}(\mathbf{k}) = 0.03\frac{u^{\prime}k^{2/3}}{(L^{\prime})^{1/3}}N(\mathbf{k})$$ $$= 0.10\varepsilon^{1/3}k^{2/3}N(\mathbf{k})$$
N/A	DTI (unpublished)	$$S_{Turb,DTI}(\mathbf{k}) = 6\left[\frac{u^{\prime}k^{2/3}}{(L^{\prime})^{1/3}}N(\mathbf{k})\right]$$
(D.8)	Teixeira & Belcher (2002)	$$\beta_{TB2002} = A\left(\frac{u^{\prime}}{c_p}\right)^2\omega$$
(D.9)	Ardhuin & Jenkins (2006)	$$S_{Turb,AJ2006}(\mathbf{k}) = -\frac{2\mathbf{k}\omega(\mathbf{k})}{\mathbf{g}}\tau(0)\cdot\mathbf{k}$$

Table D1. Parameterisation of turbulent dissipation source term applied by other authors.

Further investigation should also be committed to understanding the limitations of the WKB approximation and, potentially, for implementing alternative wave propagation models which offer reliable computation even in the presence of rapidly-varying currents. In previous studies (which have been cited in this thesis), simulation of radar signatures arising from a turbulent ship wake has been performed by a wide range of scientists, using the established technique of Conservation of Wave Action under the WKB approximation to calculate the modulation of the surface profile in the context of wave-current interaction. Such efforts are in spite of questions regarding the presence of rapidly-varying currents within the wake which may not be computed correctly in the CWA process. There is little in the way of open discussion in the literature regarding the impact that the presence of rapidly-varying currents or 'turbulence' have on the applicability of wave action, and there is no evidence of alternative (wave-current interaction) methods being applied to rectify this shortfall; at least, not with respect to derivation of SAR remote-sensing signatures. In study of ocean bottom topography interactions for SAR applications, Alpers & Vlasenko (2002) have discussed improvements to the ocean wave action balance calculation: "The proper way to study the interaction of a strong internal solitary wave with an underwater bank would be to use a three-dimensional, fully nonlinear and non-hydrostatic system of hydrodynamic equations. But this is practically impossible with modern-day computers." There are, hence, significant challenges towards pursuing developments in this area.

Due to the restrictive conditions that the WKB approximation places on the current fields under question, a handful of alternative theories have been developed to simulate wave propagation over a current without the geometrical optics approximation: McKee (1987) derived the 'Mild-Slope Equation'(MSE) (later expanded to the 'Extended Mild-Slope Equation' [EMSE] described by McKee [1996]) which calculates the propagation of waves over current without the approximation of geometrical optics and the assumption of a "slowly-varying" current. This work was calculated for a shearing current $(0,0,W)$, where an analogue of the 'Mild-Slope Equation' was used to propagate small-amplitude water waves across the shear, deriving the 'Mild-Shear Equation' (McKee, 1996):

$$\frac{d}{dx}\left\{\psi(x)\frac{d\eta}{dx}\right\} + \varepsilon^2(k^2(x) - n^2)\psi(x)\eta = 0 \tag{D.10}$$

$$\psi(x) = \Omega^{-2}(x)\int_0^H \Phi^2(y;x)\,dy \tag{D.11}$$

Even when operating the MSE/EMSE procedure, wave action flux is conserved, revealing a potential alternative to the accepted ray theory/WKB method which may be adapted for operation in radar backscattering simulations.